Two-loop electroweak corrections to Higgs boson pair production

THOMAS WILLIAM STONE

Two-loop electroweak corrections to Higgs boson pair production

Staying in the loop: tools and techniques for higher-order calculations

Thomas Stone

A Thesis presented for the degree of
Doctor of Philosophy

Institute for Particle Physics Phenomenology
Department of Physics
Durham University
United Kingdom

May 2025

Two-loop electroweak corrections to Higgs boson pair production

Staying in the loop: tools and techniques for higher-order calculations

Thomas Stone

Submitted for the degree of Doctor of Philosophy

May 2025

Abstract: Precision calculations are essential for advancing our understanding of fundamental physics. As collider experiments achieve ever-higher accuracy, matching this precision on the theoretical side is increasingly critical. This demands sophisticated computational tools to tackle complex higher-order corrections.

This thesis focuses on techniques for handling Feynman integrals which are central to these corrections. We introduce a method to compute these integrals directly in the Minkowski kinematic regime without contour deformation, demonstrating its efficiency and robustness through multi-loop examples.

We also present a calculation of next-to-leading-order electroweak corrections to Higgs pair production, detailing the computational framework and presenting results for the NLO EW corrections to both total and differential cross sections.

Beyond this specific calculation, the techniques outlined in this thesis have broader applications in precision collider physics. By improving the efficiency and accuracy of multi-loop calculations, they contribute to reducing theoretical uncertainties and enhancing the search for deviations from the Standard Model.

Contents

List of Figures

List of Tables

Declaration

The work in this thesis is based on research carried out in the Department of Physics at Durham University. No part of this thesis has been submitted elsewhere for any degree or qualification.

Research presented in this thesis is based on joint work:

- Chapter 3 is based on [1, 2]: Stephen Jones, Anton Olsson and Thomas Stone, *Evaluating Parametric Integrals in the Minkowski Regime without Contour Deformation*, Proceedings of Science (PoS) LL2024 (2024) **036** and Stephen Jones, Anton Olsson and Thomas Stone, *Positive Integrands from Feynman Integrals in the Minkowski Regime*, **To Appear**.

- Chapter 4 is based on [3]: Gudrun Heinrich, Stephen Jones, Matthias Kerner, Thomas Stone, Augustin Vestner, *Electroweak corrections to Higgs boson pair production: the top-Yukawa and self-coupling contributions*, Journal of High Energy Physics (JHEP) 11 (2024) **040**.

Acknowledgements

My thanks, first and foremost, go to Stephen Jones for always going above and beyond in his role as supervisor. My PhD experience has been thoroughly enjoyable as well as intellectually stimulating, in no small part because of him.

I would also like to thank my parents, Mark and Lesley, my brother, Ben and my wider family for their perpetual encouragement and understanding.

I am deeply grateful to my partner, Rūdolfs Treilis, for making my time in Durham so special.

I must also thank my trusty band of proofreaders, Mălina Roșca, Ery McPartland and Elliot Fox, for their invaluable comments on the draft, as well as all my other friends, both in and out of Durham, for so many good times!

Finally, I would like to thank the IPPP for giving me the opportunity to undertake this PhD, my collaborators at KIT for their support, insights and fruitful discussions and Lorenzo Tancredi at TUM for allowing me to continue on my journey in academia.

"Erst kommt das Denken, dann das Integral."
(Roughly, "First think, then do the integral.")

— *Rudolf Peierls* to a young *Hans Bethe*

This thesis is dedicated to

Mum and Dad

for giving me the best start in life and for
your continued support – I can never thank
you enough.

Chapter 1

Introduction

High-energy physics is firmly in the era of precision, where innovative advancements in computational capability are driving efforts to tackle some of the most pressing challenges in fundamental physics. The pursuit of higher-order corrections in quantum chromodynamics (QCD) and the electroweak (EW) sector is essential for accurately describing the processes observed at current and future particle colliders, such as the high-luminosity Large Hadron Collider (LHC). These corrections are vital for matching theoretical predictions to the unprecedented precision of experimental measurements, enabling the discovery of new physics and the rigorous testing of the Standard Model (SM). However, this frontier comes with significant challenges: for example, both the reduction to and the evaluation of a basis of master Feynman integrals required for higher-order calculations often involve intricate mathematical and computational obstacles. To overcome these hurdles, novel analytic and numerical tools are indispensable for advancing our understanding of these fundamental processes.

In this thesis, we discuss several of the challenges arising in the computation of higher-order corrections, focussing heavily on loop integrals and various techniques employed to handle these complicated objects. The remainder of Chapter 1 motivates the relevance of Higgs pair production as a salient process to investigate in the Standard Model and establishes the framework for the leading-order (LO) calculation.

In Chapter 2, we explore the rich structure of Feynman integrals, providing the relevant background knowledge required to follow the exposition in Chapters 3 and 4. Throughout, we encounter a variety of important concepts including dimensional regularisation, loop integral representations, integration-by-parts (IBP) reduction, sector decomposition and the method of differential of equations, to name a few. In Chapter 3, we introduce a novel approach to directly evaluating Feynman integrals in the Minkowski kinematic regime without recourse to contour deformation by mapping Minkowski integrals to causally-prescribed sums of 'Euclidean' integrals. The benefits of this approach are twofold: firstly, numerical performance is vastly improved compared to standard contour deformation, as demonstrated in a number of multi-loop examples; secondly, from the analytic practitioner's perspective, it renders the continuation to physical kinematics manifestly trivial. The thesis concludes with Chapter 4 which describes, in detail, our recent calculation of a partial subset of next-to-leading-order (NLO) electroweak corrections to di-Higgs production. We discuss a number of the methods adopted in the calculation, such as optimising the basis of master integrals for numerical evaluation, before presenting results for the contribution of this subset of NLO EW corrections to total and differential cross sections.

1.1 Higgs Pair Production

To motivate the study of Higgs pair production, we begin by briefly summarising the relevant SM background[1]. The Standard Model is a quantum field theory based on the gauge group

$$G = \mathrm{SU}(3)_C \times \mathrm{SU}(2)_L \times \mathrm{U}(1)_Y \tag{1.1.1}$$

where the subgroup $\mathrm{SU}(3)_C$ corresponds to QCD and the remaining part of G, $\mathrm{SU}(2)_L \times \mathrm{U}(1)_Y$, describes the electroweak sector. This latter subgroup is spontan-

[1]For a detailed introduction to the Standard Model, consult any of the excellent textbooks which discuss the topic (for example, [4–6]).

eously broken,

$$\mathrm{SU}(2)_L \times \mathrm{U}(1)_Y \;\rightarrow\; \mathrm{U}(1)_Q\,, \tag{1.1.2}$$

as a consequence of the non-zero vacuum expectation value (vev) of the Higgs field. Writing the Higgs doublet as

$$\Phi = \begin{pmatrix} \phi^+ \\ \phi^0 \end{pmatrix} = \frac{1}{\sqrt{2}} \begin{pmatrix} \phi_1 + i\phi_2 \\ \phi_3 + i\phi_4 \end{pmatrix}, \tag{1.1.3}$$

we can parameterise the expansion about the non-zero vev, v, by

$$\Phi = U\,\frac{1}{\sqrt{2}} \begin{pmatrix} 0 \\ v + H \end{pmatrix} \tag{1.1.4}$$

where U is 2×2 unitary matrix which, using the gauge freedom, we can – and will – always take to be the identity matrix. This choice, known as the unitary gauge, decouples the would-be Goldstone bosons from the Standard Model. The physical Higgs boson field is identified with H, where $\langle H \rangle = 0$, resulting in

$$\langle \Phi \rangle = \frac{1}{\sqrt{2}} \begin{pmatrix} 0 \\ v \end{pmatrix}. \tag{1.1.5}$$

The SM Higgs potential is given by the most general (renormalisable) potential built from Φ that is invariant under electroweak gauge transformations:

$$\begin{aligned} V(\Phi) &= -\mu^2 \Phi^\dagger \Phi - \frac{\lambda}{4}\left[\Phi^\dagger \Phi\right]^2, \qquad\qquad \mu^2 > 0\,, \quad \lambda < 0 \\ &= -\frac{\mu^2}{2}\,(v+H)^2 - \frac{\lambda}{16}\,(v+H)^4 \\ &= -\frac{v}{4}\left(4\mu^2 + \lambda v^2\right) H - \frac{1}{8}\left(4\mu^2 + 3\lambda v^2\right) H^2 \\ &\quad - \frac{\lambda v}{4}\,H^3 - \frac{\lambda}{16}\,H^4 + \mathcal{O}\left(H^0\right) \end{aligned} \tag{1.1.6}$$

where we have inserted the expansion about the vev from (1.1.4) and we ignore the constant terms, $\mathcal{O}\left(H^0\right)$, in the potential. Note that the presence of a non-zero vacuum expectation value is itself a consequence of $\mu^2 > 0\,,\ \lambda < 0$. Considering the way the potential appears in the SM Lagrangian, $\mathcal{L} \supset -V(\Phi)$, we can identify the

coefficient of H^2 with $\frac{m_H^2}{2}$. Furthermore, the condition

$$\left.\frac{\partial V(\Phi)}{\partial H}\right|_{H=0} = 0 \tag{1.1.7}$$

implies that $v^2 = -\frac{4\mu^2}{\lambda}$. With these identifications, we can eliminate $\mu^2 = \frac{m_H^2}{2}$ and $\lambda = -\frac{2m_H^2}{v^2}$; the Higgs potential is then given by

$$\begin{aligned} V(\Phi) &= -\frac{m_H^2}{4}(v+H)^2 + \frac{m_H^2}{8v^2}(v+H)^4 \\ &= \frac{m_H^2}{2}H^2 + \frac{m_H^2}{2v}H^3 + \frac{m_H^2}{8v^2}H^4 + \mathcal{O}\left(H^0\right) . \end{aligned} \tag{1.1.8}$$

We make a number of comments about the terms appearing in (1.1.8). Firstly, we note that the term linear in H vanishes after expressing the potential in terms of m_H and v – this occurs due to the condition that the vacuum minimises the potential[1]. Secondly, the cubic and quartic terms in the potential will induce cubic and quartic self-interactions of the Higgs with Feynman rules given by  $= -i\frac{3m_H^2}{v}$ and  $= -i\frac{3m_H^2}{v^2}$ in the Standard Model; the SM cubic and quartic self-couplings are therefore completely fixed by m_H and v. Although experimental measurements have determined the Higgs mass and vev (thereby fixing the numerical value of the cubic and quartic SM self-couplings), direct measurements of the self-couplings remain imprecise[2]. Any deviations from the SM predictions in experimentally derived values for the self-couplings would be a clear signpost for beyond the Standard Model (BSM) physics.

In order to measure the self-couplings directly, we must study processes which act as probes of these couplings. Di-Higgs production is an example of such a process, as sensitivity to the cubic self-coupling already enters at the leading order in the gluon fusion channel – which dominates at the LHC – as shown in Fig. 1.1. In the Standard Model, Higgs pair production via gluon fusion is a loop-induced process meaning that the leading order corresponds to a 1-loop contribution, the NLO correction to a 2-loop contribution and so on. The leading order calculation was performed some

[1] We will revisit this point in Chapter 4 when discussing the handling of tadpole contributions.
[2] See Chapter 4 for current and projected bounds on the cubic Higgs self-coupling.

Figure 1.1: Example 1-loop (LO) box- and triangle-type diagrams contributing to HH-production in the dominant gluon fusion channel. Note the appearance at the leading order of the Higgs cubic self-coupling in the triangle-type diagrams.

time ago [7, 8] with the first NLO QCD result (retaining full top mass dependence) presented in [9][12]. The LO partonic cross section is given by

$$\hat{\sigma}^{(0)} = \frac{1}{2s}\int \frac{\mathrm{d}^3\mathbf{k}_3}{(2\pi)^3\, 2E_{\mathbf{k}_3}} \frac{\mathrm{d}^3\mathbf{k}_4}{(2\pi)^3\, 2E_{\mathbf{k}_4}} \,(2\pi)^4\,\delta^4\left(p_1+p_2-k_3-k_4\right)\left|\overline{\mathcal{M}}^{(0)}\right|^2 \tag{1.1.9}$$

where the integral over the two-particle phase space may be partially performed using the δ-functions. Standard manipulations carried out in the centre-of-momentum frame allow us to write

$$\hat{\sigma}^{(0)} = \frac{1}{16\pi s^2}\int_{t_-}^{t_+} \mathrm{d}t\,\left|\overline{\mathcal{M}}^{(0)}\right|^2 \tag{1.1.10}$$

where s and t are the standard Mandelstam invariants for $2 \to 2$ scattering. The integration limits, $t_\pm$, correspond to the boundary of the physical scattering region in the s-t plane and are explicitly derived in Chapter 4 where we also express the averaged matrix element squared, $\left|\overline{\mathcal{M}}^{(0)}\right|^2$, as a sum over squared scalar form factors. The technology required to perform the loop integrals which appear in the averaged matrix element squared (and higher-order corrections to it) forms the focus of a large portion of this thesis.

To obtain the total cross section from the partonic cross section, we use the collinear factorisation formula with the gluon PDFs (parton distribution functions):

$$\sigma^{(0)}\Big(\bar{s},\mu_r,\mu_f\Big) = \int_0^1 \mathrm{d}x_1\mathrm{d}x_2\, f_g\Big(x_1,\,\mu_f^2\Big) f_g\Big(x_2,\,\mu_f^2\Big)\hat{\sigma}^{(0)}\Big(s=x_1x_2\bar{s},\mu_r,\mu_f\Big)\theta\Big(x_1x_2\bar{s}-4m_H^2\Big) \tag{1.1.11}$$

where μ_r is the renormalisation scale, μ_f is the factorisation scale and the Heaviside

[1] For a thorough overview of the available results for this process, see Chapter 4.

[2] The NLO QCD calculation is in the process of being re-performed using improved computational technology and insights gained from the NLO EW calculation presented in Chapter 4.

function explicitly ensures that the integration is over the kinematically-allowed region. Changing variables to $\tau = x_1 x_2$ and $x_1 = x$, we obtain

$$\sigma^{(0)}\Big(\bar{s}, \mu_r, \mu_f\Big) = \int_0^1 \mathrm{d}\tau \int_\tau^1 \frac{\mathrm{d}x}{x} f_g\Big(x,\, \mu_f^2\Big) f_g\Big(\frac{\tau}{x},\, \mu_f^2\Big)\, \hat{\sigma}^{(0)}\Big(s = \tau\bar{s}, \mu_r, \mu_f\Big)\, \theta\left(\tau\bar{s} - 4m_H^2\right). \tag{1.1.12}$$

Defining $\tau_0 = \frac{4m_H^2}{\bar{s}}$ and introducing the (gluon) luminosity function,

$$\frac{\mathrm{d}\mathcal{L}_{gg}}{\mathrm{d}\tau} = \int_\tau^1 \frac{\mathrm{d}x}{x}\, f_g\left(x,\, \mu_f^2\right)\, f_g\left(\frac{\tau}{x},\, \mu_f^2\right), \tag{1.1.13}$$

we can write down the final result for the total cross section:

$$\sigma^{(0)}\Big(\bar{s}, \mu_r, \mu_f\Big) = \int_{\tau_0}^1 \mathrm{d}\tau\, \frac{\mathrm{d}\mathcal{L}_{gg}}{\mathrm{d}\tau}\, \hat{\sigma}^{(0)}\Big(s = \tau\bar{s}, \mu_r, \mu_f\Big). \tag{1.1.14}$$

Comparing theoretical predictions for total and differential cross sections to experimental measurements is essential for testing whether the underlying theory accurately describes reality. With the increasing precision of experimental data, achieving matching theoretical accuracy requires higher-order corrections, along with the refined mathematical and computational techniques required to calculate them.

While the Standard Model remains a remarkably successful theory, it is widely recognized as incomplete. The Higgs self-coupling, due to its direct connection to the shape of the Higgs potential, could play a key role in identifying potential deviations from the Standard Model and signs of new physics. Precise theoretical predictions for Higgs pair production, including electroweak corrections which are $\mathcal{O}\,(5\%)$ and distort the shapes of differential cross sections, are therefore vital.

The remainder of this thesis is devoted to the development of tools and techniques for calculating higher-order corrections, with a strong focus on loop integrals, which are essential ingredients in these computations. A number of these methods are then applied to the case of NLO EW corrections to Higgs pair production, where we spell out in detail some of the material we have presented schematically here. Beyond this specific case, the techniques developed in this thesis have broader applications and can contribute to future studies of processes in precision collider physics.

Chapter 2

Feynman Integrals

Beyond tree-level, Feynman integrals appear in the calculation of quantum field theory observables (for instance, in matrix elements for processes which are then used to derive cross-sections). Therefore, these loop integrals play a significant role both in understanding precise quantum corrections to an observable, where the leading order is a tree-level contribution, as well as in the ability to calculate loop-induced processes where Feynman integral evaluations are required to compute the first term in an asymptotic series (di-Higgs production is a prime example of this). In this chapter, we remind the reader of some of the fundamentals of Feynman integrals before briefly detailing aspects of the rich structure that appears most prominently at the multi-loop level. A comprehensive exposition of the state-of-the-art knowledge in the field of Feynman integrals is beyond the scope of this thesis; we refer the reader to [10] for an excellent overview while we restrict to the relevant topics here.

2.1 Fundamentals

In this chapter, we will focus solely on scalar Feynman integrals; we will assume that some kind of reduction from tensor to scalar integrals has already taken place in the relevant calculation (for example, Passarino-Veltman reduction [11] or use of the projector method, see e.g. [12, 13]). We will allow for 'dots' – propagators which

are doubled, tripled etc. – as well as inverse propagators in the numerator such that, in momentum space, our integrals (which depend implicitly on the spacetime dimension, D and an arbitrary mass scale, μ) will take the following general form:

$$J\left(\boldsymbol{s};\boldsymbol{\nu}\right) = \left(\mu^2\right)^{\nu-\frac{LD}{2}} \int \prod_{l=1}^{L} \left[\mathscr{D}k_l\right] \prod_{i=1}^{N} \frac{1}{\mathcal{D}_i^{\nu_i}\left(\boldsymbol{k},\boldsymbol{p},m_i^2\right)} \,. \tag{2.1.1}$$

Here, our L-loop, N-propagator integral, J, depends on the kinematic invariants, $\boldsymbol{s}$[1], which include the squared masses, $m_i^2 \geq 0$, associated to each inverse propagator $\mathcal{D}_i$ (which themselves depend on the loop ($\boldsymbol{k}$) and external ($\boldsymbol{p}$) momenta). The powers $\nu_i \in \mathbb{Z}$ of the inverse propagators may be positive (with $\nu_i > 1$ corresponding to dots), negative (corresponding to inverse propagators in the numerator) or zero (such that the corresponding propagator does not appear at all in the integrand) and we define $\nu = \sum_{i=1}^{N} \nu_i$. For our purposes, we will take these inverse propagators to be

$$\mathcal{D}_i = q_i^2 - m_i^2 + i0^+ \tag{2.1.2}$$

where q_i is the overall momentum flowing through the propagator (in general, a linear combination of external and loop momenta) and $i0^+$ encodes the causal Feynman prescription. We will also define the measure to be

$$\left[\mathscr{D}k_l\right] = \frac{\mathrm{d}^D k_l}{i\pi^{\frac{D}{2}}} \tag{2.1.3}$$

for the spacetime dimension D such that the overall μ-dependent prefactor renders the integral dimensionless. Note that this is not the physical normalisation from the Feynman rules where the denominator of (2.1.3) would be $(2\pi)^D$; however, conversion between the normalisations is trivial.

As a simple example, let us consider the tadpole integral with $\nu_1 = \nu \in \mathbb{Z}_{>0}$,

$$J_{\text{tad}}\left(m^2;\nu\right) = \left(\mu^2\right)^{\nu-\frac{D}{2}} \int \left[\mathscr{D}k\right] \frac{1}{\left(k^2 - m^2 + i0^+\right)^{\nu}} \,. \tag{2.1.4}$$

We remind the reader that $k^2 = k_0^2 - |\vec{k}|^2$ and so, without the Feynman prescription,

[1] Italicised, boldface characters are a shorthand to denote ordered sets, e.g. $\boldsymbol{c} = \{c_1, c_2, \ldots, c_{|\boldsymbol{c}|}\}$.

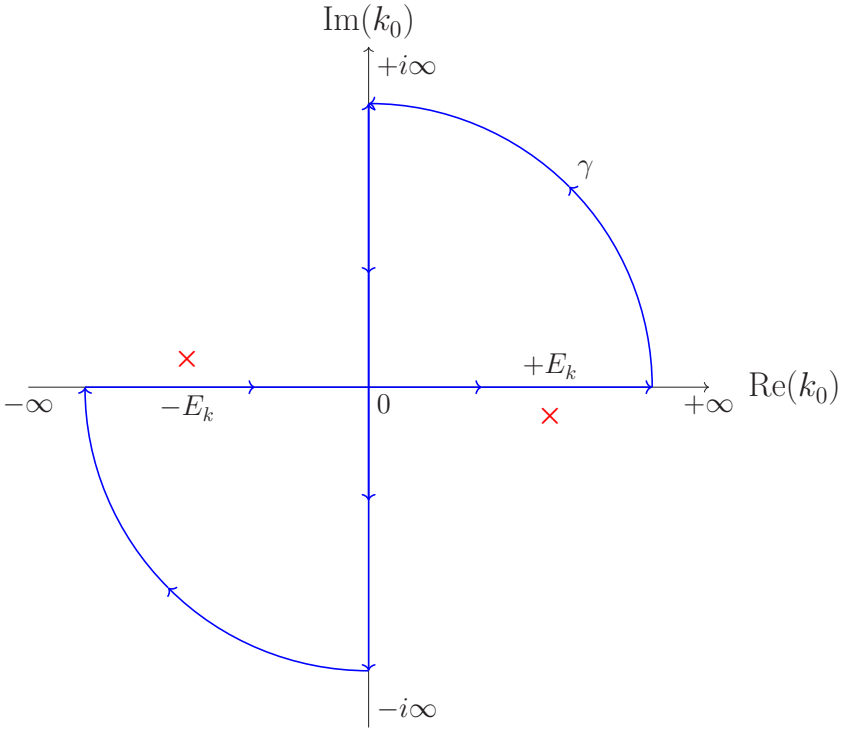

Figure 2.1: The idea behind Wick rotation. Once the poles (in red) have been shifted off the original contour of integration according to the Feynman prescription, the contour is closed in the complex k_0 plane generating the overall contour, γ. Since this contour encloses no poles, the integral can be evaluated with Cauchy's theorem. Contributions from the arcs of this contour vanish in the infinite-radius limit.

there would be poles on the k_0 integration contour for

$$k_0 = \pm\sqrt{|\vec{k}|^2 + m^2} = \pm E_k \,. \tag{2.1.5}$$

The causal Feynman prescription shifts the poles off the contour of integration (or, equivalently, deforms the contour away from the real axis to avoid the poles) as in Fig. 2.1. The contour can be closed in the complex k_0 plane such that it does not enclose any poles and hence, by Cauchy's theorem,

$$\int_\gamma \mathrm{d}k_0 \, \frac{1}{\left(k_0^2 - |\vec{k}|^2 - m^2 + i0^+\right)^\nu} = 0 \,. \tag{2.1.6}$$

Given that the contributions from the quarter-circular arcs can also be shown to

vanish in the limit that their radii go to infinity, we obtain

$$\int_{-\infty}^{+\infty} \mathrm{d}k_0 \, \frac{1}{\left(k_0^2 - |\vec{k}|^2 - m^2 + i0^+\right)^\nu} + \int_{+i\infty}^{-i\infty} \mathrm{d}k_0 \, \frac{1}{\left(k_0^2 - |\vec{k}|^2 - m^2\right)^\nu} = 0 \qquad (2.1.7)$$

where we have neglected the $i0^+$ prescription in the second integrand as the contour along the imaginary axis in Fig. 2.1 avoids any poles irrespective of its presence. Using (2.1.7), we can change variables – a process known as Wick rotation owing to the idea that the integration contour has been rotated as in Fig. 2.1 – to Euclidean momenta,

$$k_0 = ik_{0,E}\,, \qquad \vec{k} = \vec{k}_E\,, \qquad (2.1.8)$$

such that

$$\int_{-\infty}^{+\infty} \mathrm{d}k_0 \, \frac{1}{\left(k_0^2 - |\vec{k}|^2 - m^2 + i0^+\right)^\nu} = i\,(-1)^\nu \int_{-\infty}^{+\infty} \mathrm{d}k_{0,E} \, \frac{1}{\left(k_{0,E}^2 + |\vec{k}_E|^2 + m^2\right)^\nu}\,. \qquad (2.1.9)$$

Note that $k_{0,E}^2 + |\vec{k}_E|^2 = k_E^2$ (the standard Euclidean norm squared) and our original tadpole becomes

$$J_{\text{tad}}\left(m^2;\nu\right) = i\,(-1)^\nu \left(\mu^2\right)^{\nu-\frac{D}{2}} \int [\mathscr{D}k_E] \, \frac{1}{\left(k_E^2 + m^2\right)^\nu}\,. \qquad (2.1.10)$$

The integrand of (2.1.10) depends only on the norm of the Euclidean D-vector so we may naturally adopt D-dimensional spherical polar coordinates and perform the angular integrations trivially, using $\Omega_D = \frac{2\pi^{D/2}}{\Gamma(D/2)}$:

$$\begin{aligned} J_{\text{tad}}\left(m^2;\nu\right) &= \frac{(-1)^\nu}{2\pi^{\frac{D}{2}}} \left(\mu^2\right)^{\nu-\frac{D}{2}} \int \mathrm{d}\Omega_D \int_0^\infty \mathrm{d}k_E^2 \, \frac{\left(k_E^2\right)^{\frac{D}{2}-1}}{\left(k_E^2 + m^2\right)^\nu} \\ &= \frac{(-1)^\nu}{\Gamma\left(\frac{D}{2}\right)} \left(\mu^2\right)^{\nu-\frac{D}{2}} \int_0^\infty \mathrm{d}k_E^2 \, \frac{\left(k_E^2\right)^{\frac{D}{2}-1}}{\left(k_E^2 + m^2\right)^\nu} \\ &= \frac{(-1)^\nu}{\Gamma\left(\frac{D}{2}\right)} \left(\frac{m^2}{\mu^2}\right)^{\frac{D}{2}-\nu} \int_0^\infty \mathrm{d}\tau \, \frac{\tau^{\frac{D}{2}-1}}{(\tau+1)^\nu} \end{aligned} \qquad (2.1.11)$$

where, in the final line, we have made the simple change of variables $\tau = k_E^2/m^2$.

This brings the integral into the familiar form of an Euler beta function:

$$B(z_1, z_2) = \int_0^1 \mathrm{d}t\; t^{z_1-1}(1-t)^{z_2-1} = \int_0^\infty \mathrm{d}t\; \frac{t^{z_1-1}}{(t+1)^{z_1+z_2}} = \frac{\Gamma(z_1)\,\Gamma(z_2)}{\Gamma(z_1+z_2)} \tag{2.1.12}$$

where the second and third equalities follow from the first (defining) equality. We can use the representations of the Euler beta function in (2.1.12) to identify our integral in (2.1.11) and, by direct inspection, we find that

$$J_{\text{tad}}\left(m^2;\nu\right) = \frac{(-1)^\nu\,\Gamma\left(\nu-\frac{D}{2}\right)}{\Gamma(\nu)}\left(\frac{m^2}{\mu^2}\right)^{\frac{D}{2}-\nu}. \tag{2.1.13}$$

It is useful to examine (2.1.13) in various limits. If we try and take the standard tadpole ($\nu = 1$) in $D = 4$, we find that the formula in (2.1.13) diverges. In general, due to the simple poles of $\Gamma(z)$ at $z \in \mathbb{Z}_{\leq 0}$ (and under our assumption that ν is a positive integer), the tadpole will diverge when D is a positive even number greater than or equal to 2ν.

Superficially, this poses a serious issue: the simplest possible (non-zero) Feynman integral is infinite in our number of spacetime dimensions! To handle this divergence (and the vastly many others appearing in loop integrals) formally, we will need to adopt a regularisation scheme. If we consider (2.1.11) with $\nu = 1$ and $D = 4$, we see that the origin of this divergence comes from the upper limit of integration (that is to say, $k_E^2 \to \infty$). We call this an ultraviolet (UV) divergence – in contrast to an infrared (IR) divergence which stems from low-momentum, long-distance behaviour. Generally, both types of divergence can appear in a given Feynman integral.

There are a number of commonly-used regularisation schemes, each with their own advantages and disadvantages. To regulate UV divergences, one may employ cut-off regularisation where the norms of the Euclidean loop momenta are restricted to be between zero and some hard cut-off scale, Λ. One can then show that physical observables are independent of the choice of cut-off and therefore Λ may freely be taken to infinity. One of the disadvantages of this approach is that a hard cut-off is generally not Lorentz invariant and can also violate gauge invariance (although there are intriguing approaches inspired by smoothed asymptotics to remedy this,

see [14, 15], for example). Another UV regularisation scheme, first introduced in [16], is Pauli-Villars regularisation which, in the case of a photon propagator, for example, involves the following modification:

$$\frac{1}{k^2 + i0^+} \quad \longrightarrow \quad \frac{1}{k^2 + i0^+} - \frac{1}{k^2 - \Lambda^2 + i0^+} \,. \tag{2.1.14}$$

The physical theory is again recovered in the limit that the regulator Λ (which acts like a large fictitious mass) is taken to infinity. This scheme is gauge invariant in abelian theories such as QED but this feature no longer holds at the non-abelian level and is therefore less suited to calculations in theories such as QCD. Furthermore, in many computations, numerous additions of these fictitious heavy particle propagators are required (see [17]) rendering this procedure unwieldy in general. To regulate IR divergences, it is often possible to add a small mass term to the propagator of massless particles but, for example, explicit photon mass terms in the QED Lagrangian are forbidden by gauge invariance so this may be undesirable (even though the small mass only appears at intermediate steps in the calculation and is formally taken to zero at the end for physical observables) depending on one's taste.

Instead, throughout this thesis, we adopt a unified framework for regulating both UV and IR divergences simultaneously while retaining both Lorentz and gauge invariance. This framework, first comprehensively presented in [18], is known as dimensional regularisation.

2.1.1 Dimensional Regularisation

Dimensional regularisation[1] is a procedure through which divergences in quantum field theory calculations are regulated by extending the theory away from some integer dimension $D = D_0$ (often taken to be $D_0 = 4$) to general complex D. Let us consider how this procedure affects a generic loop integral appearing in the

[1] By dimensional regularisation, we will always be implicitly referring to conventional dimensional regularisation (CDR) and not to other related schemes such as 't Hooft-Veltman scheme (HV) and so on.

calculations in this theory. By simple power counting analysis of the loop momenta present in the measure (2.1.3) and the integrand, it is clear that the UV divergences in D_0 arising from high-momentum behaviour will be cured for $\mathrm{Re}(D) \leq D^{\mathrm{UV}} < D_0$ while the IR divergences, related to low-momentum behaviour, will be cured for $\mathrm{Re}(D) \geq D^{\mathrm{IR}} > D_0$, for some D^{UV} and D^{IR}.

It is clear that both conditions cannot be simultaneously satisfied so, instead, we assume initially that the IR divergences are regulated by some other method (such as the small mass regulator previously mentioned) and consider the theory in $D = D_0 - 2\epsilon$. For sufficiently large $\epsilon > 0$, the integrals appearing in a generic calculation in the theory are individually free of UV divergences (which would reappear in the limit that the regulator goes to zero as $1/\epsilon^n$ poles in a Laurent expansion). At this point, UV renormalisation takes place to remove these divergences completely from the calculation such that the result may be analytically continued to the entire complex D-plane. Then, the IR regulator can be removed and the calculation is convergent for sufficiently large $\epsilon < 0$ with the IR divergences now appearing again as poles in ϵ as $\epsilon \to 0$. These IR poles would then cancel among each other for the calculation of a sufficiently inclusive observable – a fact which, for IR poles stemming from final states, is guaranteed within the Standard Model by the Kinoshita–Lee–Nauenberg (KLN) theorem [19, 20]. Practically, it is often preferable to avoid the initial IR regularisation and simply compute straightforwardly in $D = D_0 - 2\epsilon$ with the knowledge that, before UV renormalisation, poles in ϵ could correspond to either UV and IR divergences with only the latter remaining after applying a valid renormalisation procedure.

It is important to stress that, in order to obtain correct results, we must extend all the objects that lived in the D_0-space to the D-space consistently (and not merely the loop integrals themselves). For example,

$$g_{\mu\nu}g^{\mu\nu} = g^{\mu}_{\mu} = D = D_0 - 2\epsilon \tag{2.1.15}$$

which implies that the identities satisfied by the γ matrices for $D_0 = 4$ are modified,

such as

$$\gamma^\mu\gamma^\nu\gamma^\rho\gamma_\mu = 4g^{\nu\rho}\mathbb{1}_4 \quad \longrightarrow \quad \gamma^\mu\gamma^\nu\gamma^\rho\gamma_\mu = 4g^{\nu\rho}\mathbb{1}_4 - 2\epsilon\gamma^\nu\gamma^\rho. \tag{2.1.16}$$

In this section, however, we focus on the Feynman integrals themselves and make no further comment about the behaviour of other objects in dimensional regularisation (such as the necessary modifications required to maintain a mass-dimensionless coupling, among other notable complications).

Let us now return to our formula for the tadpole in (2.1.13). For $D = 4 - 2\epsilon$, we have

$$\begin{aligned} J_{\text{tad}}\left(m^2;1\right) &= -\Gamma\left(-1+\epsilon\right)\left(\frac{m^2}{\mu^2}\right)^{1-\epsilon} \\ &= \frac{m^2}{\mu^2}\left[\frac{1}{\epsilon} + 1 - \gamma_{\text{E}} - \ln\left(\frac{m^2}{\mu^2}\right)\right] + \mathcal{O}\left(\epsilon\right) \end{aligned} \tag{2.1.17}$$

where, in the second line, we have expanded about $\epsilon \to 0$ (generating the Euler-Mascheroni constant, $\gamma_{\text{E}} = -\Gamma'(1)$, which is an artefact of dimensional regularisation[1]). The original UV divergence is now manifest as a simple pole in the regulator, ϵ. We stress that this procedure has not removed the divergence (in the context of a physical calculation, this would be done with UV renormalisation); we have merely regularised it such that it can be manipulated formally.

In general, the dimensional regularisation procedure interprets Feynman integrals as meromorphic functions of the dimensional regulator, ϵ, for all points, $\boldsymbol{s}$, in the kinematic space which are non-pathological (that is to say, excluding kinematic thresholds which are divergent independent of the spacetime dimension, for example). In the next section, we will introduce a number of different representations of Feynman integrals commonly used in the field as well as discussing the connections between them.

[1]We could have also redefined the measure in (2.1.3) to ensure this constant is not present in the results of our integrals (as is commonly done in the literature).

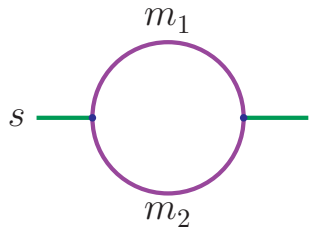

Figure 2.2: The unequal mass bubble with $s = p^2$ and $m_1 \neq m_2$.

2.2 Representations of Feynman Integrals

There are many different representations of a given Feynman integral, each with their own benefits and drawbacks depending on the context in which they are being studied. In this section, we will highlight three of these – namely, the momentum space, Schwinger parameter and Feynman parameter representations – while noting that other, less familiar representations such as the Lee-Pomeransky, Baikov and Mellin-Barnes representations exist and are well-suited to certain applications (see [10] for details). In this section, we will restrict to $\nu_i \in \mathbb{Z}_{>0}$ but we will return to allowing for inverse propagators in the numerator in later sections[1].

To clarify some of the abstract general formulae presented in the section, we will consider the simple example of an unequal mass bubble integral and analyse how this appears in each of the three representations. We depict this integral in diagrammatic form in Fig. 2.2 and state the conventions adopted in this thesis: blue external legs are on-shell ($p_a^2 = 0$), green external legs are off-shell ($p_a^2 \neq 0$), black internal lines are massless propagators ($m_i = 0$), purple internal lines are massive propagators ($m_i > 0$), red dashed lines correspond to propagator deletions, 'dots' are given by filled black circles and vertices are given by filled dark blue circles (these are most useful for depicting non-planar integrals such as those appearing in Chapter 3).

[1]Generalisations of some of the formulae presented in this section which allow for inverse propagators in the numerator exist but we will not discuss them here.

2.2.1 Momentum Space Representation

We begin by looking at the momentum space representation in more detail. We have already seen the general formula for a Feynman integral in momentum space in (2.1.1); we repeat it here for convenience:

$$J\left(\boldsymbol{s};\boldsymbol{\nu}\right)=\left(\mu^2\right)^{\nu-\frac{LD}{2}}\int\prod_{l=1}^{L}\left[\mathscr{D}k_l\right]\prod_{i=1}^{N}\frac{1}{\mathcal{D}_i^{\nu_i}\left(\boldsymbol{k},\boldsymbol{p},m_i^2\right)}\,. \tag{2.2.1}$$

For our prototypical example (the unequal mass bubble in Fig. 2.2), this general formula reduces to

$$J_{\text{bub}}\left(\boldsymbol{s};\boldsymbol{\nu}\right)=\left(\mu^2\right)^{\nu_1+\nu_2-\frac{D}{2}}\int\left[\mathscr{D}k\right]\frac{1}{\left[k^2-m_1^2+i0^+\right]^{\nu_1}\left[(k-p)^2-m_2^2+i0^+\right]^{\nu_2}} \tag{2.2.2}$$

where $\boldsymbol{s}=\{s,m_1^2,m_2^2\}$ and we have routed the momenta as in Fig. 2.3a.

(a) (b)

Figure 2.3: An example of momentum routing for the unequal mass bubble (2.3a) and a depiction of an explicit choice of 'dot' structure: $\nu_1=3,\nu_2=2$ (2.3b).

An important point to stress about the momentum representation is that, due to the integration limits, we can always shift one of the loop momenta by some linear combination of the external and other loop momenta without affecting the result of the integral. For example, a perfectly acceptable momentum routing would be to modify Fig. 2.3a by $k\to k+p$ which would result in

$$J_{\text{bub}}\left(\boldsymbol{s};\boldsymbol{\nu}\right)=\left(\mu^2\right)^{\nu_1+\nu_2-\frac{D}{2}}\int\left[\mathscr{D}k\right]\frac{1}{\left[(k+p)^2-m_1^2+i0^+\right]^{\nu_1}\left[k^2-m_2^2+i0^+\right]^{\nu_2}}\,. \tag{2.2.3}$$

For a simple 1-loop integral like the bubble, it is clear by inspection that the two expressions in (2.2.2) and (2.2.3) are equivalent but for a more complicated multi-

loop example with many external legs and mass scales, this would not be so trivial. Fortunately, there exist efficient algorithms to detect when two integrals are related in this way (and under more general transformations of the loop and external momenta) which are implemented in public packages such as `Reduze` [21] among many others.

In the following section, we will use the momentum representation to derive another useful representation of Feynman integrals called the Schwinger parameter representation.

2.2.2 Schwinger Parameter Representation

In order to introduce the Schwinger parameter representation, we first present the Schwinger trick:

$$\frac{1}{A^{\nu_i}} = \frac{1}{\Gamma(\nu_i)} \int_0^\infty \mathrm{d}t \; t^{\nu_i - 1} e^{-tA}, \quad \mathrm{Re}(A) > 0 \tag{2.2.4}$$

which follows from the definition of the Γ-function. If we replace A in (2.2.4) with $-\mathcal{D}_i = -q_i^2 + m_i^2$ (which is valid in the context of Wick rotation of all the momenta and in the Euclidean kinematic regime where we can drop the $i0^+$ prescription[1]), we can insert the Schwinger trick into the momentum representation in (2.2.1) for all the propagators and find

$$J(\boldsymbol{s};\boldsymbol{\nu}) = \left(\mu^2\right)^{\nu - \frac{LD}{2}} (-1)^\nu \int \prod_{l=1}^{L} [\mathscr{D}k_l] \prod_{i=1}^{N} \frac{1}{\Gamma(\nu_i)} \int_0^\infty \mathrm{d}t_i \; t_i^{\nu_i - 1} e^{-t_i\left(-q_i^2 + m_i^2\right)} . \tag{2.2.5}$$

We can reverse the order of integration and combine the product of exponentials into the exponential of a sum to obtain

$$J(\boldsymbol{s};\boldsymbol{\nu}) = \left(\mu^2\right)^{\nu - \frac{LD}{2}} \frac{(-1)^\nu}{\prod_{i=1}^{N} \Gamma(\nu_i)} \int_0^\infty \prod_{i=1}^{N} \mathrm{d}t_i \; t_i^{\nu_i - 1} \int \prod_{l=1}^{L} [\mathscr{D}k_l] \, e^{-\sum_{i=1}^{N} t_i\left(-q_i^2 + m_i^2\right)} . \tag{2.2.6}$$

[1] Strictly, we could have dropped this assumption and used the modified Schwinger trick $\mathcal{D}_i^{-\nu_i} = i^{-\nu_i} \, \Gamma(\nu_i)^{-1} \int_0^\infty \mathrm{d}t \; t^{\nu_i - 1} e^{it\mathcal{D}_i}$ which holds for $\mathrm{Im}(\mathcal{D}_i) > 0$ (as guaranteed by the Feynman prescription) and invoked ideas from complex analysis but the final result in (2.2.10) would prove to be the same, provided we re-insert the Feynman prescription correctly at the end. Hence, we present the Euclidean case for the derivation here but one can consult [22] for more detail.

The argument of the exponential in (2.2.6) will have terms which are quadratic, linear and constant with respect to the loop momenta and so, by defining a vector $\vec{\mathbf{K}}$ of the L loop momenta k_l, we can always write this as

$$\sum_{i=1}^{N} t_i \left(-q_i^2 + m_i^2\right) = -\vec{\mathbf{K}} \cdot \mathbf{M} \cdot \vec{\mathbf{K}} + 2\vec{\mathbf{V}} \cdot \vec{\mathbf{K}} + C \tag{2.2.7}$$

where the symmetric, positive-definite $L \times L$ matrix $\mathbf{M}$ depends only on the Schwinger parameters, t_i, while the L-vector $\vec{\mathbf{V}}$ and the constant contribution C depend on both the Schwinger parameters and the external kinematics.

Once we have the exponential in this form, we can naturally extend the standard result for the multivariable Gaussian integral to D dimensions and perform the integration over the loop momenta. That is to say,

$$\left(\mu^2\right)^{\nu - \frac{LD}{2}} \int \prod_{l=1}^{L} [\mathscr{D}k_l]\, e^{-\sum_{i=1}^{N} t_i \left(-q_i^2 + m_i^2\right)} = \mathcal{U}(\boldsymbol{t})^{-\frac{D}{2}} \exp\left(-\frac{\mathcal{F}(\boldsymbol{t}, \boldsymbol{s})}{\mathcal{U}(\boldsymbol{t})}\right) \tag{2.2.8}$$

where we have introduced, for the first time, the first and second Symanzik polynomials $\mathcal{U}$ and $\mathcal{F}$ which will play an important role in this thesis. Here, they can be identified with

$$\begin{aligned} \mathcal{U} &= \det \mathbf{M} \\ \mathcal{F} &= \frac{\mathcal{U}}{\mu^2} \left(\vec{\mathbf{V}} \cdot \mathbf{M}^{-1} \cdot \vec{\mathbf{V}} + C\right) \end{aligned} \tag{2.2.9}$$

coming from the solution to the Gaussian integral and we will see a graphical way of deriving them in section 2.2.3. Putting everything together and correctly re-inserting the Feynman prescription required outside of the Euclidean regime, we obtain the Schwinger parameter representation:

$$J(\boldsymbol{s}; \boldsymbol{\nu}) = \frac{(-1)^{\nu}}{\prod_{i=1}^{N} \Gamma(\nu_i)} \int_0^{\infty} \prod_{i=1}^{N} \mathrm{d}t_i\, t_i^{\nu_i - 1} \mathcal{U}(\boldsymbol{t})^{-\frac{D}{2}} \exp\left(-\frac{\mathcal{F}(\boldsymbol{t}, \boldsymbol{s}) - i0^+}{\mathcal{U}(\boldsymbol{t})}\right). \tag{2.2.10}$$

Now we return to our example of the unequal mass bubble and assign Schwinger parameters to each propagator as in Fig. 2.4. The sum in (2.2.7) simplifies to

$$t_1\left(-k^2 + m_1^2\right) + t_2\left(-(k-p)^2 + m_2^2\right) = -(t_1 + t_2)\, k^2 + 2t_2\, p \cdot k - t_2\, p^2 + t_1 m_1^2 + t_2 m_2^2 \tag{2.2.11}$$

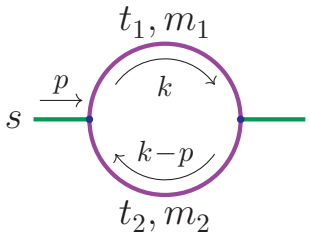

Figure 2.4: The bubble with assigned Schwinger parameters.

and, as this is a 1-loop example, we can easily extract the 1×1 matrix $\mathbf{M}$ and the 1-vector $\vec{\mathbf{V}}$ as $t_1 + t_2$ and $t_2\, p$ respectively as well as $C = -t_2\, p^2 + t_1 m_1^2 + t_2 m_2^2$. Using (2.2.9) and inserting $p^2 = s$, we find

$$\begin{aligned} \mathcal{U}(\boldsymbol{t}) &= t_1 + t_2 \\ \mathcal{F}(\boldsymbol{t}, \boldsymbol{s}) &= \frac{t_1 + t_2}{\mu^2} \left(\frac{t_2^2 s}{t_1 + t_2} - t_2 s + t_1 m_1^2 + t_2 m_2^2 \right) \\ &= -\frac{s}{\mu^2}\, t_1\, t_2 + (t_1 + t_2) \left(\frac{m_1^2}{\mu^2}\, t_1 + \frac{m_2^2}{\mu^2}\, t_2 \right), \end{aligned} \tag{2.2.12}$$

allowing us to write

$$\begin{aligned} J_{\text{bub}}(\boldsymbol{s}; \boldsymbol{\nu}) = \frac{(-1)^{\nu}}{\Gamma(\nu_1)\,\Gamma(\nu_2)} \int_0^{\infty} \mathrm{d}t_1\, \mathrm{d}t_2\; t_1^{\nu_1 - 1}\, t_2^{\nu_2 - 1}\, (t_1 + t_2)^{-\frac{D}{2}} \times \\ \exp\left(-\frac{-s\, t_1\, t_2 + (t_1 + t_2) \left(m_1^2\, t_1 + m_2^2\, t_2 \right) - i0^+}{\mu^2\, (t_1 + t_2)} \right). \end{aligned} \tag{2.2.13}$$

In the next section, the Schwinger parameter representation in (2.2.10) will be used to derive the most important representation for this thesis: the Feynman parameter representation.

2.2.3 Feynman Parameter Representation

We now discuss the Feynman parameter representation – one of the most commonly adopted representations of Feynman integrals. We start with the Schwinger parameter representation[1] in (2.2.10) and insert a factor of 1 under the integral sign

[1] One could instead follow the textbook approach and start from the momentum representation in (2.2.1) and introduce Feynman parameters using Feynman's trick for each of the propagators:

$$\prod_{i=1}^{N} A_i^{-\nu_i} = \frac{\Gamma(\nu)}{\prod_{i=1}^{N} \Gamma(\nu_i)} \int_{\mathbb{R}^N_{\geq 0}} \prod_{i=1}^{N} \mathrm{d}x_i\; x_i^{\nu_i - 1} \delta\left(1 - \sum_{i=1}^{N} x_i \right) \left(\sum_{i=1}^{N} x_i A_i \right)^{-\nu}.$$

(keeping the Feynman prescription implicit for now):

$$J(\boldsymbol{s};\boldsymbol{\nu}) = \frac{(-1)^{\nu}}{\prod_{i=1}^{N}\Gamma(\nu_i)} \int_0^\infty \prod_{i=1}^{N} \mathrm{d}t_i \, t_i^{\nu_i-1} \int_0^\infty \mathrm{d}\lambda \, \delta\left(\lambda - \sum_{i\in S} t_i\right) \mathcal{U}(\boldsymbol{t})^{-\frac{D}{2}} \exp\left(-\frac{\mathcal{F}(\boldsymbol{t},\boldsymbol{s})}{\mathcal{U}(\boldsymbol{t})}\right) \tag{2.2.14}$$

where S is any (non-empty) subset of $\{1, 2, \ldots, N\}$. We change variables to Feynman parameters defined by $t_i = \lambda x_i$ which gives us

$$\begin{aligned} J(\boldsymbol{s};\boldsymbol{\nu}) = \frac{(-1)^{\nu}}{\prod_{i=1}^{N}\Gamma(\nu_i)} \int_0^\infty \prod_{i=1}^{N} \mathrm{d}x_i \, x_i^{\nu_i-1} \, \delta\left(1 - \sum_{i\in S} x_i\right) \times \\ \int_0^\infty \mathrm{d}\lambda \, \lambda^{\nu-1} \, \mathcal{U}(\lambda\boldsymbol{x})^{-\frac{D}{2}} \exp\left(-\frac{\mathcal{F}(\lambda\boldsymbol{x},\boldsymbol{s})}{\mathcal{U}(\lambda\boldsymbol{x})}\right). \end{aligned} \tag{2.2.15}$$

At this stage, we make use of an important property of the $\mathcal{U}$ and $\mathcal{F}$ polynomials. A result of the construction in (2.2.9) is that the $\mathcal{U}$ and $\mathcal{F}$ polynomials are homogeneous of degree L and $L+1$ respectively in their parameters (this is manifest in the graphical construction of the polynomials presented later in this section). Explicitly, this means that

$$\begin{aligned} \mathcal{U}(\lambda\boldsymbol{x}) &= \lambda^L \mathcal{U}(\boldsymbol{x}) \\ \mathcal{F}(\lambda\boldsymbol{x},\boldsymbol{s}) &= \lambda^{L+1} \mathcal{F}(\boldsymbol{x},\boldsymbol{s}) \end{aligned} \tag{2.2.16}$$

which simplifies (2.2.15):

$$\begin{aligned} J(\boldsymbol{s};\boldsymbol{\nu}) = \frac{(-1)^{\nu}}{\prod_{i=1}^{N}\Gamma(\nu_i)} \int_0^\infty \prod_{i=1}^{N} \mathrm{d}x_i \, x_i^{\nu_i-1} \, \delta\left(1 - \sum_{i\in S} x_i\right) \mathcal{U}(\boldsymbol{x})^{-\frac{D}{2}} \times \\ \int_0^\infty \mathrm{d}\lambda \, \lambda^{\nu-\frac{LD}{2}-1} \exp\left(-\frac{\mathcal{F}(\boldsymbol{x},\boldsymbol{s})}{\mathcal{U}(\boldsymbol{x})}\lambda\right). \end{aligned} \tag{2.2.17}$$

Restricting to the Euclidean regime (where $\mathcal{F} > 0$ within the integration domain), we can change variables once more to $\chi = \frac{\mathcal{F}}{\mathcal{U}}\lambda$, obtaining

$$J(\boldsymbol{s};\boldsymbol{\nu}) = \frac{(-1)^{\nu}}{\prod_{i=1}^{N}\Gamma(\nu_i)} \int_0^\infty \prod_{i=1}^{N} \mathrm{d}x_i \, x_i^{\nu_i-1} \delta\left(1 - \sum_{i\in S} x_i\right) \frac{\mathcal{U}(\boldsymbol{x})^{\nu-\frac{(L+1)D}{2}}}{\mathcal{F}(\boldsymbol{x},\boldsymbol{s})^{\nu-\frac{LD}{2}}} \int_0^\infty \mathrm{d}\chi \, \chi^{\nu-\frac{LD}{2}-1} e^{-\chi}. \tag{2.2.18}$$

We recognise the integral over χ to be the Γ-function with argument $\nu - \frac{LD}{2}$ which allows us to write down the Feynman parameter representation (with the Feynman prescription correctly re-inserted):

$$J\left(\boldsymbol{s};\boldsymbol{\nu}\right) = \frac{\left(-1\right)^{\nu}\Gamma\left(\nu-\frac{LD}{2}\right)}{\prod_{i=1}^{N}\Gamma\left(\nu_i\right)}\int_0^{\infty}\prod_{i=1}^{N}\mathrm{d}x_i\; x_i^{\nu_i-1}\,\delta\left(1-\sum_{i\in S}x_i\right)\frac{\mathcal{U}\left(\boldsymbol{x}\right)^{\nu-\frac{(L+1)D}{2}}}{\left[\mathcal{F}\left(\boldsymbol{x},\boldsymbol{s}\right)-i0^{+}\right]^{\nu-\frac{LD}{2}}}\,. \tag{2.2.19}$$

We have therefore shown how it is possible to convert from the more familiar momentum space representation of a given integral to either of the Schwinger or Feynman parameter representations. One may ask, however, whether it is possible to immediately write down the parameter representations without recourse to the picture of loop momenta and their associated routings around a diagram; the answer to this question is an emphatic yes. By inspecting (2.2.10) and (2.2.19), we realise that, for a given choice of dot structure $\boldsymbol{\nu}$ of the propagators, the only objects we need to derive are the Symanzik polynomials $\mathcal{U}$ and $\mathcal{F}$. The graphical method of constructing $\mathcal{U}$ and $\mathcal{F}$ using cuts of the diagram associated to the Feynman integral provides such an algorithm to obtain the polynomials without having to introduce and route loop momenta; the only data required consist of the external kinematics and the graph (in the graph theory sense) itself.

Consider the Feynman diagram representation of a Feynman integral (for example, as in Fig. 2.2); this is a graph, G, with edges labelled by e[1]. The $\mathcal{U}$ and $\mathcal{F}$ polynomials can be derived from this graph using the following equations:

$$\mathcal{U}(\boldsymbol{x}) = \sum_{T^1\in\mathcal{T}^1}\prod_{e\notin T^1}x_e, \qquad \mathcal{F}_0(\boldsymbol{x},\boldsymbol{s}) = \sum_{(T^1,T^2)\in\mathcal{T}^2}\left[-\frac{s_{(T^1,T^2)}}{\mu^2}\prod_{e\notin(T^1,T^2)}x_e\right], \tag{2.2.20}$$

$$\mathcal{F}(\boldsymbol{x},\boldsymbol{s}) = \mathcal{F}_0(\boldsymbol{x},\boldsymbol{s}) + \mathcal{U}(\boldsymbol{x})\sum_{e\in G}\frac{m_e^2}{\mu^2}\,x_e \tag{2.2.21}$$

where $\mathcal{T}^1 = \mathcal{T}^1\left(G\right)$ and $\mathcal{T}^2 = \mathcal{T}^2\left(G\right)$ are the spanning 1-forests (i.e. the spanning trees) and the spanning 2-forests of the graph G respectively[2]. The symbol $s_{(T^1,T^2)}$

[1] In this sense, the graph G does not contain external legs as edges (i.e. $\boldsymbol{e} = \{e_1, e_2, ..., e_N\}$) but we will nevertheless depict them in the diagrams.

[2] If the reader is unfamiliar with the pre-requisite graph theory, we recommend consulting [10]

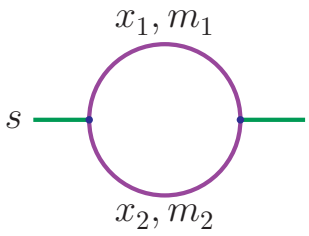

Figure 2.5: The bubble with assigned Feynman parameters.

refers to the square of the total momentum flowing between the two tree components T_1 and T_2 of the spanning 2-forest $\left(T^1, T^2\right)$. By considering (2.2.20), it is manifest in this construction that, in the absence of internal masses, each Feynman parameter appears at most linearly in each monomial of $\mathcal{U}$ and $\mathcal{F}$. We note that the presence of internal masses only modifies the $\mathcal{F}$ polynomial as in (2.2.21) such that, in these additional terms, Feynman parameters associated to massive propagators may appear quadratically in a given monomial. In any case, $\mathcal{U}$ and $\mathcal{F}$ remain homogeneous polynomials of the Feynman parameters of degree L and $L+1$ respectively with all the kinematic dependence retained solely in $\mathcal{F}$. Given that the Feynman parameters are integrated over $\mathbb{R}^N_{\geq 0}$, it is clear that $\mathcal{U} \geq 0$ with the equality only holding on the boundary of the integration domain. The kinematic dependence of $\mathcal{F}$ means that, in general, $\mathcal{F}$ can be positive, negative or zero throughout the integration domain (with the Feynman prescription in (2.2.19) required when $\mathcal{F}$ is zero within the domain of integration, away from the boundary). We will define the Euclidean regime in this thesis to be the kinematic regime such that $\mathcal{F} \geq 0$ in the integration domain with the equality holding only on the boundary as with $\mathcal{U}$. We note that, if momentum conservation is imposed on the kinematic parameters appearing in $\mathcal{F}$ (such that they are not all independent), such a regime is not even guaranteed to exist for a given Feynman integral – we will meet such integrals in Chapter 3.

We will present some simple cases to clarify the graphical construction in (2.2.20) and (2.2.21). Firstly, we return to our familiar example of the unequal mass bubble and assign Feynman parameters to each propagator as in Fig. 2.5. To construct $\mathcal{U}$,

for an introduction relevant for this context. In any case, we hope that the presented diagrammatic examples clarify this construction.

we must sum over all deletions of L propagators which reduce the original L-loop diagram to a tree (here $L = 1$):

$$\mathcal{U}(\boldsymbol{x}) = \quad + \quad . \tag{2.2.22}$$

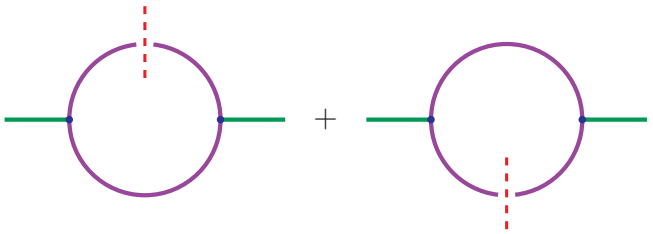

Similarly, to construct $\mathcal{F}_0$, we must sum over all deletions of $L+1$ propagators which reduce the original L-loop diagram into two trees with non-zero squared momentum flowing between them:

$$\mathcal{F}_0(\boldsymbol{x}, \boldsymbol{s}) = -\frac{s}{\mu^2} \quad . \tag{2.2.23}$$

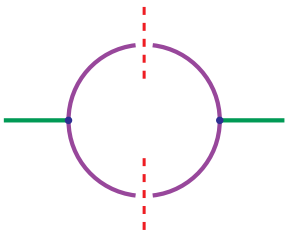

Adding the mass terms from (2.2.21), this yields

$$\begin{aligned} \mathcal{U}(\boldsymbol{x}) &= x_1 + x_2 \\ \mathcal{F}(\boldsymbol{x}, \boldsymbol{s}) &= -\frac{s}{\mu^2}\, x_1 x_2 + (x_1 + x_2)\left(\frac{m_1^2}{\mu^2}\, x_1 + \frac{m_2^2}{\mu^2}\, x_2\right) \end{aligned} \tag{2.2.24}$$

in agreement with (2.2.12) without ever having introduced a loop momentum. This allows us to write down the unequal mass bubble in the Feynman parameter representation:

$$J_{\text{bub}}(\boldsymbol{s}; \boldsymbol{\nu}) = \frac{(-1)^{\nu}\, \Gamma\left(\nu - \frac{D}{2}\right)}{\Gamma(\nu_1)\, \Gamma(\nu_2)} \int_0^\infty \mathrm{d}x_1\, \mathrm{d}x_2\; x_1^{\nu_1 - 1} x_2^{\nu_2 - 1}\, \delta\left(1 - \sum\nolimits_{i=1}^{2} \alpha_i x_i\right) \times \frac{(x_1 + x_2)^{\nu - D}}{\left[-\frac{s}{\mu^2}\, x_1 x_2 + (x_1 + x_2)\left(\frac{m_1^2}{\mu^2}\, x_1 + \frac{m_2^2}{\mu^2}\, x_2\right) - i0^+\right]^{\nu - \frac{D}{2}}} \tag{2.2.25}$$

where the coefficients $\alpha_i \geq 0$ (with at least one of the two non-zero) encode the freedom to choose any non-empty subset of the parameters in the δ-function. Taking the massless limit $m_{1,2} \to 0$ in the Euclidean regime $s < 0$ and integrating out x_2

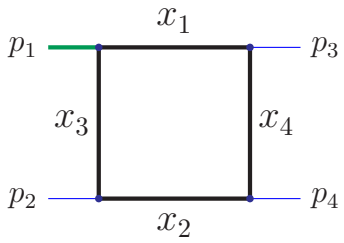

Figure 2.6: The off-shell box with assigned Feynman parameters.

using the δ-function with $\alpha_1 = \alpha_2 = 1$, we obtain

$$J_{\text{bub}}\left(\{s,0,0\};\boldsymbol{\nu}\right) = \frac{(-1)^{\nu}\,\Gamma\left(\nu-\frac{D}{2}\right)}{\Gamma\left(\nu_1\right)\Gamma\left(\nu_2\right)}\left(\frac{-s}{\mu^2}\right)^{\frac{D}{2}-\nu}\int_0^1 \mathrm{d}x_1\; x_1^{\frac{D}{2}-\nu_2-1}\left(1-x_1\right)^{\frac{D}{2}-\nu_1-1} \tag{2.2.26}$$

which we recognise from (2.1.12) as another Euler beta function. This allows us to write

$$J_{\text{bub}}\left(\{s,0,0\};\boldsymbol{\nu}\right) = \frac{(-1)^{\nu}\,\Gamma\left(\nu-\frac{D}{2}\right)\Gamma\left(\frac{D}{2}-\nu_1\right)\Gamma\left(\frac{D}{2}-\nu_2\right)}{\Gamma\left(\nu_1\right)\Gamma\left(\nu_2\right)\Gamma\left(D-\nu\right)}\left(\frac{-s}{\mu^2}\right)^{\frac{D}{2}-\nu} \tag{2.2.27}$$

with the analytic continuation to the physical region given by $s \to s + i0^+$. If we consider the standard case of no dots ($\boldsymbol{\nu} = \{1,1\}$) in $D = 4-2\epsilon$, we have[1]

$$J_{\text{bub}}\left(\{s,0,0\};\{1,1\}\right) = \frac{\Gamma\left(\epsilon\right)\Gamma\left(1-\epsilon\right)^2}{\Gamma\left(2-2\epsilon\right)}\left(\frac{-s}{\mu^2}\right)^{-\epsilon} = \frac{1}{\epsilon} + 2 - \gamma_{\text{E}} - \ln\left(\frac{-s}{\mu^2}\right) + \mathcal{O}\left(\epsilon\right). \tag{2.2.28}$$

We see, once again, that we have a divergent integral as the regulator, ϵ, goes to zero. We note that this pole is purely a result of expanding $\Gamma\left(\epsilon\right)$ which stems from the D-dependent prefactor in (2.2.19); we call such integrals 'quasi-finite'.

As another clarifying example of the graphical construction of the Symanzik polynomials, we now consider the massless box with an off-shell leg shown in Fig. 2.6 (with all the external momenta defined to be incoming and the kinematic invariants given by the standard Mandelstam variables $s = (p_1+p_2)^2$ and $t = (p_1+p_3)^2$ along with

[1] For the physical region ($s > 0$), the analytic continuation gives us $\frac{1}{\epsilon}+2-\gamma_{\text{E}}-\ln\left(\frac{s}{\mu^2}\right)+i\pi+\mathcal{O}\left(\epsilon\right)$.

the off-shellness $p_1^2 \neq 0$). We construct $\mathcal{U}$ with the deletions of 1 propagator,

$\mathcal{U}(\boldsymbol{x}) =$ 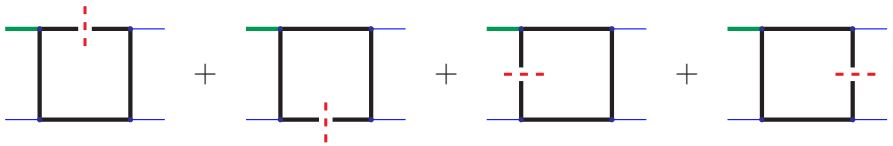 , (2.2.29)

corresponding to the four spanning trees of the graph and we construct $\mathcal{F}_0$ with the deletions of 2 propagators,

$\mathcal{F}_0(\boldsymbol{x},\boldsymbol{s}) = -\frac{s}{\mu^2}$ 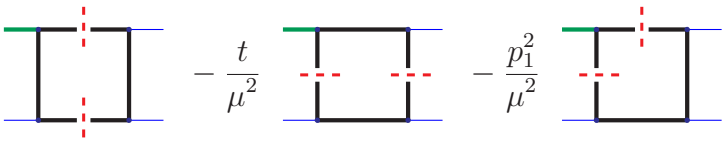 , (2.2.30)

corresponding to the three spanning 2-forests of the graph with non-zero squared momentum flowing between them. Note that if we had allowed all four external legs to be off-shell, each of the six spanning 2-forests of the graph would contribute to $\mathcal{F}_0$ through terms proportional to p_2^2, p_3^2 and p_4^2 (with one of the four p_i being replaced using overall momentum conservation). Since this integral has no massive internal propagators, we have $\mathcal{F} = \mathcal{F}_0$ and so

$$\begin{aligned} \mathcal{U}(\boldsymbol{x}) &= x_1 + x_2 + x_3 + x_4 \\ \mathcal{F}(\boldsymbol{x},\boldsymbol{s}) &= -\frac{s}{\mu^2}\, x_1 x_2 - \frac{t}{\mu^2}\, x_3 x_4 - \frac{p_1^2}{\mu^2}\, x_1 x_3 \end{aligned} \tag{2.2.31}$$

allowing us to write the Feynman parameter representation of the off-shell box:

$$J_{\text{box},p_1^2>0}(\boldsymbol{s};\boldsymbol{\nu}) = \frac{(-1)^{\nu}\,\Gamma\left(\nu-\frac{D}{2}\right)}{\prod_{i=1}^4 \Gamma(\nu_i)} \int_0^\infty \prod_{i=1}^4 \mathrm{d}x_i\; x_i^{\nu_i-1}\, \delta\left(1-\textstyle\sum_{i=1}^4 \alpha_i x_i\right) \times \frac{(x_1+x_2+x_3+x_4)^{\nu-D}}{\left[-\frac{s}{\mu^2}\, x_1x_2 - \frac{t}{\mu^2}\, x_3x_4 - \frac{p_1^2}{\mu^2}\, x_1x_3 - i0^+\right]^{\nu-\frac{D}{2}}}. \tag{2.2.32}$$

Thus, we conclude our discussion of the graphical construction of the Symanzik polynomials through these examples.

The Feynman parameter representation will play a significant role in Chapter 3 where we present an alternative method for integrating these parametric integrands outside the Euclidean regime without requiring an explicit contour deformation.

2.3 Integration-by-Parts Reduction

In state-of-the-art QFT calculations, many thousands of scalar Feynman integrals may appear in the computation of amplitudes. Given the immense difficulty in evaluating these loop integrals (either analytically or numerically), it is advantageous to reduce this number of integrals as far as possible using linear relations between the Feynman integrals themselves. For example, these could be symmetry relations of the kind described in Section 2.2.1 or identities stemming from the Lorentz invariance of the scalar integrals[1]. In this section, we will focus on a special kind of linear relation between Feynman integrals referred to as Integration-by-Parts (IBP) identities. With all the required linear relations, the thousands of integrals may be reduced to a finite basis of so-called 'master' integrals which then need to be evaluated. The vector space structure of Feynman integrals[2] means that this basis choice is not unique and certain choices will be beneficial depending on the method of evaluation.

We will begin by introducing the concept of an integral family and the relevant notation used in the literature of this field, before presenting the IBP identity itself and demonstrating this on our prototypical example of the massive bubble. We conclude this section with an exposition of dimensional recurrence relations (DRRs) which were used in the calculation detailed in Chapter 4.

2.3.1 Integral Families

Consider a process with $P+1$ external legs such that there are P independent external momenta after overall momentum conservation has been applied. The maximal number of kinematic invariants is given by[3]

$$\binom{P}{2} + P = \frac{P\,(P+1)}{2} \tag{2.3.1}$$

[1] We will not discuss these 'LI' identities explicitly as they do not provide additional information to IBP identities (as shown in [23]) which are the focus of this section.

[2] In fact, this vector space structure may even be equipped with an inner product, see [24].

[3] The binomial coefficient ('n choose k') is given by $\binom{n}{k} = \frac{n!}{k!(n-k)!}$.

where the first term on the left-hand-side of (2.3.1) counts the number of ways one can take a scalar product between two of the external momenta ($p_a \cdot p_{b\neq a}$) and the second term counts scalar products of the external momenta with themselves (p_a^2). For the L-loop contribution to the process, scalar products between the L loop momenta and the P external momenta, as well as scalar products among the loop momenta themselves, appear in the Feynman integrals. We can count this number as well:

$$N = \binom{P+L}{2} + L - \binom{P}{2} = \frac{L\,(L+2P+1)}{2}\,. \tag{2.3.2}$$

We define an integral family to be a set of inverse propagators, $\boldsymbol{\mathcal{D}}$, of cardinality $|\boldsymbol{\mathcal{D}}| = N$ such that any scalar product involving at least one of the loop momenta can be written as a linear combination of the inverse propagators appearing in the set.

We make two comments. Firstly, in general, a process at L loops will have Feynman diagrams with multiple topologies leading to multiple integral families being defined. Secondly, not all inverse propagators appearing in $\boldsymbol{\mathcal{D}}$ will correspond to actual propagators of the diagram – they are introduced as so-called 'auxiliary propagators' to ensure the family is complete in the sense of the ability to reproduce all possible scalar products. In the special 1-loop case, we have $N|_{L=1} = P+1$ and, since every 1-loop integral already has $P+1$ propagators, no auxiliary propagators are required.

An integral in the momentum space representation defined with respect to an integral family $\boldsymbol{\mathcal{D}}$ is then given by

$$J\,(\boldsymbol{\nu}) = \left(\mu^2\right)^{\nu - \frac{LD}{2}} \int \prod_{l=1}^{L} [\mathscr{D}k_l] \prod_{i=1}^{N} \frac{1}{\mathcal{D}_i^{\nu_i}} \tag{2.3.3}$$

where, in this section, we allow once more for $\nu_i \in \mathbb{Z}$ (dropping the explicit dependence on $\boldsymbol{s}$ and the Feynman prescription for brevity). Closely adhering to the conventions of [21, 25] and [26, 27], we adopt the following standard notation for a given integral, J:

$$t = \sum_{i=1}^{N} \theta\left(\nu_i - \frac{1}{2}\right) \tag{2.3.4}$$

which counts the number of inverse propagators appearing in the denominator (i.e. inverse propagators with $\nu_i > 0$),

$$r = \sum_{i=1}^{N} \nu_i \, \theta\left(\nu_i - \frac{1}{2}\right) \tag{2.3.5}$$

which is the sum of the powers of the inverse propagators in the denominator[1] and

$$s = \sum_{i=1}^{N} |\nu_i| \, \theta\left(\frac{1}{2} - \nu_i\right) \tag{2.3.6}$$

which is the (negated) sum of the powers of the inverse propagators appearing in the numerator (i.e. inverse propagators with $\nu_i < 0$).

We also introduce the important concept of a sector, $\boldsymbol{\mathcal{S}} \subseteq \boldsymbol{\mathcal{D}}$, which denotes a subset of the inverse propagators in the family. An integral is said to belong to a sector, $\boldsymbol{\mathcal{S}}$, if the set of all inverse propagators appearing in the denominator coincides with $\boldsymbol{\mathcal{S}}$. The notion of a subsector, $\boldsymbol{\mathcal{S}}_1$, of a sector, $\boldsymbol{\mathcal{S}}_2$, is naturally defined through $\boldsymbol{\mathcal{S}}_1 \subset \boldsymbol{\mathcal{S}}_2$. All integrals belonging to the same sector of an integral family share a unique sector ID number, $\mathcal{S}$, given by

$$\mathcal{S} = \sum_{i=1}^{N} 2^{i-1} \, \theta\left(\nu_i - \frac{1}{2}\right) . \tag{2.3.7}$$

The corner integral of a sector is defined to be the unique integral in the sector with $r = t$ and $s = 0$. In other words, it is the only integral in the sector with no dots or inverse propagators in the numerator. It can be shown (see [28]) that all integrals in a given sector will be zero if the corresponding corner integral is scaleless.

To clarify these definitions with an example, consider the somewhat artificial $N = 9$ index structure

$$\boldsymbol{\nu} = \{1, 0, -4, 3, -2, 0, 2, 1, 2\} . \tag{2.3.8}$$

This corresponds to an integral (defined with respect to an integral family) with $t = 5$, $r = 9$ and $s = 6$ in sector 457. The corner integral of this sector has the index structure

$$\boldsymbol{\nu} = \{1, 0, 0, 1, 0, 0, 1, 1, 1\} . \tag{2.3.9}$$

[1] Note that this implies that the total number of dots on an integral is given by $d = r - t$.

In this language of integral families and sectors, symmetry relations can provide identities connecting the integrals within a sector or between sectors (or, in the case of multiple defined integral families, even between sectors in different families). In the next section, we will discuss the most important linear relations between Feynman integrals: IBP identities.

2.3.2 The IBP Identity

We present the IBP identity for dimensionally-regulated integrals [29]:

$$\left(\mu^2\right)^{\nu-\frac{LD}{2}} \int \prod_{l=1}^{L} [\mathscr{D}k_l] \, \frac{\partial}{\partial k_m^\mu} \left[\frac{q_n^\mu}{\prod_{i=1}^{N} \mathcal{D}_i^{\nu_i}} \right] = 0 \tag{2.3.10}$$

where q_n^μ is any linear combination of the loop and external momenta. For a given 'seed' integral of the type in (2.3.3), this generates $L\,(L+P)$ relations – this can be seen by considering $\boldsymbol{q}$ to be the loop and external momenta themselves with $n \in \{1, 2, \ldots, L, L+1, \ldots, L+P\}$ and $m \in \{1, 2, \ldots, L\}$. The IBP identity relates integrals from the same family with differing numbers of propagators; to that end, we introduce the propagator raising and lowering operators, $\mathbb{i}^{\pm}$, defined by

$$\mathbb{i}^{\pm} J\left(\nu_1, \ldots, \nu_i, \ldots, \nu_N\right) = J\left(\nu_1, \ldots, \nu_i \pm 1, \ldots, \nu_N\right) . \tag{2.3.11}$$

Let us return to the unequal mass bubble,

$$J_{\text{bub}}\left(\nu_1, \nu_2\right) = \left(\mu^2\right)^{\nu-\frac{D}{2}} \int [\mathscr{D}k] \, \frac{1}{\left[k^2 - m_1^2\right]^{\nu_1} \left[(k-p)^2 - m_2^2\right]^{\nu_2}} . \tag{2.3.12}$$

Using (2.3.10), we obtain one IBP relation for $q_1 = k$ and another for $q_2 = p$. These are given by

$$\begin{aligned} 0 &= \left[(D - 2\nu_1 - \nu_2) - \nu_2 \mathbb{1}^- \mathbb{2}^+ - 2\frac{m_1^2}{\mu^2}\nu_1 \mathbb{1}^+ - \frac{m_1^2+m_2^2-s}{\mu^2}\nu_2 \mathbb{2}^+ \right] J_{\text{bub}} \\ 0 &= \left[(\nu_2 - \nu_1) + \nu_1 \mathbb{1}^+ \mathbb{2}^- - \nu_2 \mathbb{1}^- \mathbb{2}^+ - \frac{m_1^2-m_2^2+s}{\mu^2}\nu_1 \mathbb{1}^+ - \frac{m_1^2-m_2^2-s}{\mu^2}\nu_2 \mathbb{2}^+ \right] J_{\text{bub}} . \end{aligned} \tag{2.3.13}$$

We can insert different integer values of ν_1 and ν_2 (corresponding to different values of r and s) to build as large a system of equations as we need to reduce any integral in

this family to a basis of master integrals, $\vec{J}$, which we could take to be, for example,

$$\vec{J} = \begin{bmatrix} J_{\text{bub}}(1,1) \\ J_{\text{bub}}(1,0) \\ J_{\text{bub}}(0,1) \end{bmatrix}. \tag{2.3.14}$$

Note that we have a true bubble master integral in the top-level sector ($\mathcal{S} = 3$) and tadpole master integrals in the subsectors ($\mathcal{S} = 1$ and $\mathcal{S} = 2$).

For a general integral family, we can determine the required ranges of r and s demanded by the physics problem and build a system of equations that can be solved such that any integral in the defined range can be expressed as a linear combination of the elements in a finite basis of master integrals. In practice, this reduction process is automated in modern computations using the Laporta algorithm [30] which systematically solves the system of IBP relations by assigning a lexicographic ordering to the integrals and reducing integrals which are higher-ranked with respect to this ordering to lower-ranked ones. Different lexicographic orderings may be chosen, provided they are consistent; for example, we may define one integral to be less complicated than another integral ($J_1 \overset{\text{L.O.}}{<} J_2$) if $t_1 \leq t_2$ then if $s_1 \leq s_2$ then if $r_1 \leq r_2$ then if $\mathcal{S}_1 \leq \mathcal{S}_2$ and so on where the subsequent checks are only carried out at each step if the equality holds.

In its standard form, the Laporta algorithm selects master integrals based purely on the defined lexicographic ordering which may not always lead to an optimal basis. However, in modern applications, the algorithm is often modified to reduce integrals directly to a preferred basis of master integrals. In Chapter 4, we will show how we chose a basis of master integrals by demanding that the most difficult integrals only had to be expanded to leading order in ϵ which drastically improved the numerical evaluation of the integrals with the package `pySecDec`.

The existence of a systematic reduction to a basis guarantees that all integrals within a given topology can be expressed in terms of a well-chosen set of master integrals, greatly simplifying higher-order calculations in perturbative quantum field theory.

2.3.3 Dimensional Recurrence Relations

In this section, we discuss dimensional recurrence relations (DRRs) which relate integrals in a given dimension D to integrals in the same family in some other dimension D' – usually, $D' = D \pm 2$. These DRRs can be used along with IBP relations to rotate a basis of master integrals from one basis, $\vec{J}_1$, in D to another basis, $\vec{J}_2$, which, in general, contains integrals in multiple dimensions. It was shown in [31,32] that such rotations can be constructed which generate a basis of (quasi-)finite[1] integrals. Such bases are highly desirable; for example, they can make the pole structure of an amplitude manifest in the coefficients of the master integrals post-reduction and they can be much simpler to evaluate either analytically or numerically. In Chapter 4, we will demonstrate how such a finite basis – by which we henceforth mean a basis of finite integrals – was used and further improved upon for the calculation of electroweak corrections to di-Higgs production.

In this section, we derive a relation between an integral in D dimensions and integrals from the same integral family with a different dot structure in $D+2$ dimensions; such a relation was first presented in [36] with the reverse direction ($D \to D-2$) stated in [37][2]. We apply this method, along with IBP reduction, to our bubble example to construct the rotation from the basis, $\vec{J}_1$, given in (2.3.14) to a finite basis, $\vec{J}_2$. To that end, in this section, we will explicitly indicate the dimension of our integrals with respect to the reference dimension, D, as well as introducing the dimension raising and lowering operators and the (modified) propagator raising operator:

$$\begin{aligned} \mathbb{D}^{\pm} J^D\left(\nu_1,\ldots,\nu_i,\ldots,\nu_N\right) &= J^{D\pm 2}\left(\nu_1,\ldots,\nu_i,\ldots,\nu_N\right) \\ \hat{\mathbb{1}}^{+} J^D\left(\nu_1,\ldots,\nu_i,\ldots,\nu_N\right) &= -\nu_i J^D\left(\nu_1,\ldots,\nu_i+1,\ldots,\nu_N\right) . \end{aligned} \tag{2.3.15}$$

We begin by acting on the Schwinger parameter representation in (2.2.10) – where

[1] For a thorough discussion on finiteness criteria in the Euclidean regime, see [33]; the Minkowski case is still an open question in general – see discussions in [34,35], for example.

[2] Naturally, after IBP reduction, the reverse direction can also be obtained from the forward result via matrix inversion but computationally it can be convenient to have access to both relations.

$\nu_i > 0$ – with the raising operators in (2.3.15). The result is

$$\begin{aligned}\mathbb{D}^+ J^D(\boldsymbol{\nu}) &= \frac{(-1)^\nu}{\prod_{i=1}^N \Gamma(\nu_i)} \int_0^\infty \prod_{i=1}^N \mathrm{d}t_i \; t_i^{\nu_i - 1} \mathcal{U}(\boldsymbol{t})^{-1} \mathcal{U}(\boldsymbol{t})^{-\frac{D}{2}} \exp\left(-\frac{\mathcal{F}(\boldsymbol{t},\boldsymbol{s}) - i0^+}{\mathcal{U}(\boldsymbol{t})}\right) \\ \hat{\mathbb{i}}^+ J^D(\boldsymbol{\nu}) &= \frac{(-1)^\nu}{\prod_{i=1}^N \Gamma(\nu_i)} \int_0^\infty \prod_{i=1}^N \mathrm{d}t_i \; t_i^{\nu_i - 1} t_i \, \mathcal{U}(\boldsymbol{t})^{-\frac{D}{2}} \exp\left(-\frac{\mathcal{F}(\boldsymbol{t},\boldsymbol{s}) - i0^+}{\mathcal{U}(\boldsymbol{t})}\right).\end{aligned} \tag{2.3.16}$$

By inspecting (2.3.16), we realise that we can construct an identity operator out of $\mathbb{D}^+$ and $\{\hat{\mathbb{i}}\}$ by first considering the effect of $\mathcal{U}\left(\hat{\mathbb{1}}, \ldots, \hat{\mathbb{N}}\right)$[1] on J^D. The action of $\mathcal{U}\left(\hat{\mathbb{1}}, \ldots, \hat{\mathbb{N}}\right)$ brings a factor of $\mathcal{U}(\boldsymbol{t})$ into the numerator of the integrand while, from (2.3.16), $\mathbb{D}^+$ induces a factor of $\mathcal{U}(\boldsymbol{t})$ in the denominator. Clearly then, from the commutativity of the propagator raising operators and the dimension shift operators in (2.3.15) with one another, we obtain

$$J^D(\boldsymbol{\nu}) = \mathcal{U}\left(\hat{\mathbb{1}}, \ldots, \hat{\mathbb{N}}\right) \mathbb{D}^+ J^D(\boldsymbol{\nu}) \tag{2.3.17}$$

which, by definition, implies that

$$J^D(\boldsymbol{\nu}) = \mathcal{U}\left(\hat{\mathbb{1}}, \ldots, \hat{\mathbb{N}}\right) J^{D+2}(\boldsymbol{\nu}) \; . \tag{2.3.18}$$

Hence, we have constructed a way to express integrals in D dimensions in terms of integrals in $D+2$.

Note that, if we merely apply $\mathcal{U}\left(\hat{\mathbb{1}}, \ldots, \hat{\mathbb{N}}\right) \mathbb{D}^+$ to a master integral in D dimensions, we do not, in general, obtain a linear combination of master integrals in $D+2$ immediately. However, the integrals that appear can always be reduced back to the same masters in $D+2$ dimensions using IBP relations (which will, of course, be the same relations as in D dimensions but with $D \to D+2$). Therefore, for some basis of master integrals, $\vec{J}^D$, we can construct the basis rotations

$$\vec{J}^D = \mathbf{R}\, \vec{J}^{D+2} \iff \vec{J}^{D+2} = \mathbf{R}^{-1} \vec{J}^D \tag{2.3.19}$$

for some invertible matrix $\mathbf{R}$ derived using the DRRs and IBP relations.

[1] $\mathcal{U}\left(\hat{\mathbb{1}}, \ldots, \hat{\mathbb{N}}\right)$ is defined naturally; for example, if $\mathcal{U}(\boldsymbol{t}) = t_1 + t_2$, then $\mathcal{U}\left(\hat{\mathbb{1}}, \hat{\mathbb{2}}\right) = \hat{\mathbb{1}} + \hat{\mathbb{2}}$.

To obtain a (quasi-)finite basis from some generic basis of master integrals, one often modifies both the dimensions of some (or even all) of the original integrals as well as their dot structures; the new basis will have the same number of master integrals in each sector as before when employing dots and dimension shifts. For our bubble example, let us derive the relation between our original quasi-finite basis

$$\vec{J}_1^{\,4-2\epsilon} = \begin{bmatrix} J_{\text{bub}}^{4-2\epsilon}(1,1) \\ J_{\text{bub}}^{4-2\epsilon}(1,0) \\ J_{\text{bub}}^{4-2\epsilon}(0,1) \end{bmatrix} \tag{2.3.20}$$

in $D = 4 - 2\epsilon$ and a choice of finite basis given by

$$\vec{J}_2^{\,2-2\epsilon} = \begin{bmatrix} J_{\text{bub}}^{2-2\epsilon}(1,1) \\ J_{\text{bub}}^{2-2\epsilon}(2,0) \\ J_{\text{bub}}^{2-2\epsilon}(0,2) \end{bmatrix} \tag{2.3.21}$$

in $D - 2 = 2 - 2\epsilon$ dimensions with a dot on each of the subsector (tadpole) master integrals. We apply (2.3.18) to each of the integrals in the finite basis, $\vec{J}_2^{\,2-2\epsilon}$:

$$\begin{aligned} J_{\text{bub}}^{2-2\epsilon}(1,1) &= \left[\hat{\mathbb{1}} + \hat{2}\right] J_{\text{bub}}^{4-2\epsilon}(1,1) \\ &= -J_{\text{bub}}^{4-2\epsilon}(2,1) - J_{\text{bub}}^{4-2\epsilon}(1,2) \\ &= R_{1,1}\, J_{\text{bub}}^{4-2\epsilon}(1,1) + R_{1,2}\, J_{\text{bub}}^{4-2\epsilon}(1,0) + R_{1,3}\, J_{\text{bub}}^{4-2\epsilon}(0,1)\ , \end{aligned} \tag{2.3.22}$$

$$\begin{aligned} J_{\text{bub}}^{2-2\epsilon}(2,0) &= \hat{\mathbb{1}}\, J_{\text{bub}}^{4-2\epsilon}(2,0) \\ &= -2\, J_{\text{bub}}^{4-2\epsilon}(3,0) \\ &= R_{2,2}\, J_{\text{bub}}^{4-2\epsilon}(1,0)\,, \end{aligned} \tag{2.3.23}$$

$$\begin{aligned} J_{\text{bub}}^{2-2\epsilon}(0,2) &= \hat{2}\, J_{\text{bub}}^{4-2\epsilon}(0,2) \\ &= -2\, J_{\text{bub}}^{4-2\epsilon}(0,3) \\ &= R_{3,3}\, J_{\text{bub}}^{4-2\epsilon}(0,1) \end{aligned} \tag{2.3.24}$$

where, in the final line for each integral, we have used IBP relations to reduce back

to the quasi-finite basis, $\vec{J}_1^{4-2\epsilon}$. The change of basis matrix,

$$\mathbf{R} = \begin{bmatrix} R_{1,1} & R_{1,2} & R_{1,3} \\ 0 & R_{2,2} & 0 \\ 0 & 0 & R_{3,3} \end{bmatrix}, \tag{2.3.25}$$

contains the non-zero elements

$$\begin{aligned} R_{1,1} &= \frac{2\,(1-2\epsilon)\,s\,\mu^2}{\left(s-\left[m_1+m_2\right]^2\right)\left(s-\left[m_1-m_2\right]^2\right)}\,, \\ R_{1,2} &= \frac{(1-\epsilon)\left(m_2^2-m_1^2-s\right)\mu^4}{m_1^2\left(s-\left[m_1+m_2\right]^2\right)\left(s-\left[m_1-m_2\right]^2\right)}\,, \\ R_{1,3} &= \frac{(1-\epsilon)\left(m_1^2-m_2^2-s\right)\mu^4}{m_2^2\left(s-\left[m_1+m_2\right]^2\right)\left(s-\left[m_1-m_2\right]^2\right)}\,, \\ R_{2,2} &= \epsilon\,(1-\epsilon)\,\frac{\mu^4}{m_1^4}\,, \\ R_{3,3} &= \epsilon\,(1-\epsilon)\,\frac{\mu^4}{m_2^4}\,. \end{aligned} \tag{2.3.26}$$

Hence, we can relate the two bases, $\vec{J}_1^{4-2\epsilon}$ and $\vec{J}_2^{2-2\epsilon}$, using the change of basis matrix and its inverse, $\mathbf{R}^{-1}$:

$$\vec{J}_2^{2-2\epsilon} = \mathbf{R}\,\vec{J}_1^{4-2\epsilon} \iff \vec{J}_1^{4-2\epsilon} = \mathbf{R}^{-1}\vec{J}_2^{2-2\epsilon}\,. \tag{2.3.27}$$

We have shown that the use of dimensional recurrence relations in combination with IBP reduction provides a powerful tool for rotating to finite bases of master integrals, significantly simplifying their evaluation. However, while such basis choices mitigate divergences in the regulator, ϵ, we would wish, in principle, to be able to evaluate any Feynman integral. In cases where a fully finite basis cannot be easily identified or when one simply wants to evaluate an integral without having to first reduce to a basis of master integrals, an approach is required for the divergent integrals where expanding the integrands about $\epsilon \to 0$ and integrating the coefficients to obtain the Laurent expansion fails. One such approach is sector decomposition [38], discussed in the following section, which systematically isolates divergent regions of parameter space and allows for their analytic or numerical evaluation via expansion in ϵ.

2.4 Sector Decomposition

Let us consider a generic loop integral with $\nu_i > 0$ in the Feynman parameter representation, as in (2.2.19) and repeated here for convenience:

$$J(\boldsymbol{s};\boldsymbol{\nu}) = \frac{(-1)^{\nu}\,\Gamma\left(\nu - \frac{LD}{2}\right)}{\prod_{i=1}^{N}\Gamma(\nu_i)} \int_0^{\infty} \prod_{i=1}^{N} \mathrm{d}x_i\; x_i^{\nu_i - 1}\,\delta\left(1 - \sum_{i\in S} x_i\right) \frac{\mathcal{U}(\boldsymbol{x})^{\nu - \frac{(L+1)D}{2}}}{\left[\mathcal{F}(\boldsymbol{x},\boldsymbol{s}) - i0^{+}\right]^{\nu - \frac{LD}{2}}}\,. \tag{2.4.1}$$

In the Euclidean regime[1], the singularities of Feynman integrals stem from either the boundary of the integration domain or a possible overall $1/\epsilon$ from the $D-$dependent prefactor. Sector[2] decomposition (see [39, 40] for comprehensive reviews) is an approach to handling the former type of singularity by first applying parameter transformations which 'factorise' these singularities and then employing suitable subtractions such that any remaining non-trivial integrals are finite. This makes the approach ideally suited to numerical evaluation and, as a result, it is implemented in numerous packages such as `pySecDec` [41] among others [42, 43].

The factorisation step is required when a parametric integral possesses what is known as an 'overlapping' singularity. To illustrate what these are and how to handle them, we consider the archetypal toy example, following [39]:

$$I = \int_0^1 \mathrm{d}x_1\,\mathrm{d}x_2 \frac{1}{x_1^{1+a\epsilon} x_2^{b\epsilon}\left[x_1 + (1-x_1)\,x_2\right]}\,. \tag{2.4.2}$$

There is a singularity stemming from the third factor in the denominator of the integrand in (2.4.2) as $x_1 \to 0$ and $x_2 \to 0$ simultaneously. When a singularity is a result of multiple parameters approaching the boundary of integration at the same time (but strictly not when they individually tend towards it), we call this an overlapping singularity. Sector decomposition is a way of handling an integral with overlapping singularities by mapping it to a sum of sector integrals where none of the singularities are of that nature.

[1] We remind the reader that we define the Euclidean regime to be the kinematic region where $\mathcal{F} \geq 0$ in the integration domain with the equality only holding on the boundary.

[2] NB: 'sector' in this context is unrelated to the notion of a sector defined in the previous section.

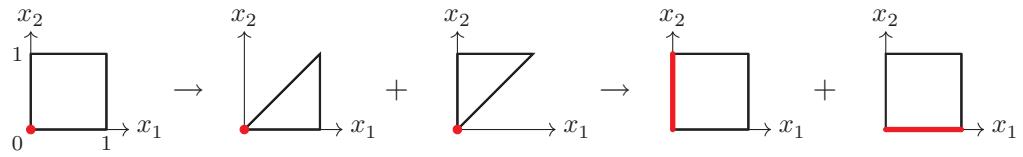

Figure 2.7: Decomposing the original domain of integration into two sectors and then remapping the resulting domains back to the positive unit square. The overlapping singularity is depicted by a filled red circle and its evolution under this procedure is shown.

To sector decompose the integral in (2.4.2), we begin by inserting a factor of 1 under the integral sign in a way which dissects the integration domain into two sectors. We then remap each of the resulting sectors back to the original domain of integration. This proceeds as follows:

$$
\begin{aligned}
I &= \int_{\square} \mathrm{d}x_1 \mathrm{d}x_2 \frac{1}{x_1^{1+a\epsilon} x_2^{b\epsilon} \left[x_1 + (1-x_1)\, x_2\right]} \left[\theta\left(x_1 - x_2\right) + \theta\left(x_2 - x_1\right)\right] \\
&= \int_{\blacktriangle} \mathrm{d}x_1 \mathrm{d}x_2 \frac{1}{x_1^{1+a\epsilon} x_2^{b\epsilon} \left[x_1 + (1-x_1)\, x_2\right]} + \int_{\blacktriangledown} \mathrm{d}x_1 \mathrm{d}x_2 \frac{1}{x_1^{1+a\epsilon} x_2^{b\epsilon} \left[x_1 + (1-x_1)\, x_2\right]} \\
&= \int_{\square} \mathrm{d}x_1 \mathrm{d}x_2 \frac{1}{x_1^{1+(a+b)\epsilon} x_2^{b\epsilon} \left[1 + (1-x_1)\, x_2\right]} + \int_{\square} \mathrm{d}x_1 \mathrm{d}x_2 \frac{1}{x_1^{1+a\epsilon} x_2^{1+(a+b)\epsilon} \left[1 + (1-x_2)\, x_1\right]}
\end{aligned}
\tag{2.4.3}
$$

where the integration domains at each step correspond to those in Fig 2.7. In order to obtain the final line, we have applied the variable transformations $x_2 \to x_1 x_2$ and $x_1 \to x_1 x_2$ for the domain remappings $\blacktriangle \to \square$ and $\blacktriangledown \to \square$ respectively. This procedure has 'factorised' the overlapping singularity; in each of the resulting integrands, there is no additional singularity from the simultaneous limit $x_1 \to 0$ and $x_2 \to 0$ which is distinct from the individual limits. For a generic Feynman integral, there are a number of algorithmic approaches, both iterative and geometric, implemented in various packages which allow for the systematic resolution of these overlapping singularities in the Euclidean regime – see [39,40] for detail on the different methods.

In general, once the overlapping singularities of a Feynman integral have been

factorised in this sense, we are left with sector integrals of the type:

$$I_\sigma = \int_0^1 \prod_{i \in S_\sigma} \mathrm{d}x_i \, x_i^{\alpha_i + \beta_i \epsilon} \, \mathcal{I}_\sigma \left(\{x_j\}_{j \in S_\sigma}, \epsilon \right) . \tag{2.4.4}$$

Here, σ labels the sector and $S_\sigma \subset \{1, \ldots, N\}$ (with $|S_\sigma| = N - 1$) encodes which parameters appear in the sector. $\mathcal{I}_\sigma$ is the remaining part of the integrand which does not lead to singularities in any limit in which the Feynman parameters go to the boundary (either individually or simultaneously). At this stage, we perform the subtractions: if $\alpha_i > -1$, the integral over x_i in (2.4.4) is finite and we may move onto the next variable; if $\alpha_i \leq -1$, we require a subtraction to perform the x_i integration.

For clarity, let us consider the univariate case for the exposition of the subtraction procedure – the generalisation to the multivariable case is simply an iteration of this procedure over all the variables. Consider the integral

$$I_\sigma = \int_0^1 \mathrm{d}x \, x^{\alpha + \beta\epsilon} \, \mathcal{I}_\sigma \left(x, \epsilon \right) \tag{2.4.5}$$

with $\alpha \leq -1$. We can construct a subtraction term by Taylor expanding the integrand about the singular limit $x \to 0$:

$$R_\sigma = \int_0^1 \mathrm{d}x \, x^{\alpha + \beta\epsilon} \sum_{k=0}^{|\alpha|-1} \frac{x^k}{k!} \frac{\partial^k \mathcal{I}_\sigma}{\partial x^k} \bigg|_{x=0} . \tag{2.4.6}$$

By construction, the subtraction term, R_σ, has the same behaviour as I_σ in the singular region of x approaching zero but it is far simpler to evaluate. The result is

$$R_\sigma = \sum_{k=0}^{|\alpha|-1} \frac{1}{k! \left[1 + k + \alpha + \beta\epsilon \right]} \frac{\partial^k \mathcal{I}_\sigma}{\partial x^k} \bigg|_{x=0} \tag{2.4.7}$$

which allows us to write

$$\begin{aligned} I_\sigma &= R_\sigma + I_\sigma - R_\sigma \\ &= \sum_{k=0}^{|\alpha|-1} \frac{1}{k! \left[1 + k + \alpha + \beta\epsilon \right]} \frac{\partial^k \mathcal{I}_\sigma}{\partial x^k} \bigg|_{x=0} + \\ &\quad \int_0^1 \mathrm{d}x \, x^{\alpha + \beta\epsilon} \left[\mathcal{I}_\sigma \left(x, \epsilon \right) - \sum_{k=0}^{|\alpha|-1} \frac{x^k}{k!} \frac{\partial^k \mathcal{I}_\sigma}{\partial x^k} \bigg|_{x=0} \right] . \end{aligned} \tag{2.4.8}$$

The singularity of I_σ has been isolated in the first term of (2.4.8) while the remaining integral is finite by construction. The integrand of this finite integral may be expanded as a series about $\epsilon \to 0$ and each term in the expansion can then be integrated either analytically or numerically. For the common case of $\alpha = -1$, (2.4.8) reduces to the familiar subtraction given by

$$I_\sigma = \frac{\mathcal{I}_\sigma(0,\epsilon)}{\beta\epsilon} + \int_0^1 \mathrm{d}x\, x^{-1+\beta\epsilon} \left[\mathcal{I}_\sigma(x,\epsilon) - \mathcal{I}_\sigma(0,\epsilon)\right] . \tag{2.4.9}$$

Let us apply the subtraction procedure to the sector integrals in our toy example – this is a multivariate case so we will need to iterate the method outlined above over all the parameters (in this example, over x_1 and x_2). We denote the sector integrals appearing in the last line of (2.4.3) by I_A and I_B. It is clear that I_A has a leading $1/\epsilon$ pole (as $\alpha_1 = -1$ and $\alpha_2 = 0$) while I_B has a $1/\epsilon^2$ pole (as $\alpha_1 = -1$ and $\alpha_2 = -1$). This means that I_A only requires a subtraction for the x_1 integration; we will perform this subtraction explicitly and simply state the result for I_B which requires the iterated procedure:

$$\begin{aligned}
I_A &= \int_0^1 \mathrm{d}x_1\,\mathrm{d}x_2\, \frac{1}{x_1^{1+(a+b)\epsilon} x_2^{b\epsilon}\left[1+(1-x_1)\,x_2\right]} \\
&= \int_0^1 \mathrm{d}x_1\,\mathrm{d}x_2\, \frac{1}{x_1^{1+(a+b)\epsilon} x_2^{b\epsilon}\left[1+x_2\right]} + \\
&\quad \int_0^1 \mathrm{d}x_1\,\mathrm{d}x_2 \left[\frac{1}{x_1^{1+(a+b)\epsilon} x_2^{b\epsilon}\left[1+(1-x_1)\,x_2\right]} - \frac{1}{x_1^{1+(a+b)\epsilon} x_2^{b\epsilon}\left[1+x_2\right]}\right] \\
&= \int_0^1 \mathrm{d}x_2\, \frac{-x_2^{-b\epsilon}}{(a+b)\,\epsilon\left[1+x_2\right]} + \int_0^1 \mathrm{d}x_1\,\mathrm{d}x_2\, \frac{x_1^{-(a+b)\epsilon} x_2^{1-b\epsilon}}{\left[1+(1-x_1)\,x_2\right]\left[1+x_2\right]} \\
&= -\frac{\ln 2}{(a+b)}\frac{1}{\epsilon} - \frac{b\,\pi^2}{12\,(a+b)} + \frac{\ln^2 2}{2} + \mathcal{O}(\epsilon)
\end{aligned} \tag{2.4.10}$$

and

$$I_B = \frac{1}{a\,(a+b)}\frac{1}{\epsilon^2} + \frac{\ln 2}{(a+b)}\frac{1}{\epsilon} + \frac{a\,\pi^2}{12\,(a+b)} - \frac{\ln^2 2}{2} + \frac{\pi^2}{12} + \mathcal{O}(\epsilon) . \tag{2.4.11}$$

Summing over the sectors and noting the cancellations, we find that

$$\begin{aligned}
I &= I_A + I_B \\
&= \frac{1}{a\,(a+b)}\frac{1}{\epsilon^2} + \frac{a\,\pi^2}{6\,(a+b)} + \mathcal{O}(\epsilon) .
\end{aligned} \tag{2.4.12}$$

We have seen an example of how sector decomposition systematically handles divergent integrals in the Euclidean regime, allowing for their analytical or numerical evaluation as a Laurent series in the dimensional regulator, ϵ. In the Minkowski regime, where $\mathcal{F}$ can vanish within the integration domain (away from the boundary), other methods are required to supplement this procedure in order to evaluate Feynman integrals – we postpone discussion of this physically significant case to Chapter 3 where we introduce a new procedure to map Minkowski integrals to a sum of 'Euclidean' ones (which can then be handled using the methods outlined in this section).

In the next section, we discuss another way of evaluating Feynman integrals which requires setting up a differential equation system for a basis of master integrals. Sector decomposition can be complementary here, either by providing boundary conditions for the differential equation system or by allowing for an independent check of the solution of the system; we will see both applications in the calculation presented in Chapter 4.

2.5 Differential Equations

The method of differential equations, first introduced in its current form in [44, 45] and later expanded upon in [46, 47], is a technique for evaluating a master basis of Feynman integrals. Derivatives of each integral in the basis are taken with respect to the kinematic invariants and the resulting integrals are then IBP-reduced back to the masters. This enables the construction of a closed system of coupled differential equations which can then be solved using various techniques. In this section, we begin by presenting a general algorithm for explicitly constructing derivative operators which manifestly return integrals from the same family (albeit in shifted dimension)[1]; this allows for the use of IBP relations to reduce back to the basis of masters. We will then show the general form of the differential equation system, commenting on

[1] Other derivative operators are available.

some useful properties which can help to verify a valid construction. Finally, we will apply the method of differential equations to the finite basis in (2.3.21) for our prototypical example of the massive bubble topology.

To construct the derivative operators, we return (as in the derivation of the dimensional recurrence relations) to the Schwinger parameter representation:

$$J\left(\boldsymbol{s};\boldsymbol{\nu}\right)=\frac{\left(-1\right)^{\nu}}{\prod_{i=1}^{N}\Gamma\left(\nu_{i}\right)}\int_{0}^{\infty}\prod_{i=1}^{N}\mathrm{d}t_{i}\;t_{i}^{\nu_{i}-1}\,\mathcal{U}\left(\boldsymbol{t}\right)^{-\frac{D}{2}}\exp\left(-\frac{\mathcal{F}\left(\boldsymbol{t},\boldsymbol{s}\right)-i0^{+}}{\mathcal{U}\left(\boldsymbol{t}\right)}\right). \tag{2.5.1}$$

In this section, we will absorb μ^2 into the definition of our kinematic invariants, $s_j \in \boldsymbol{s}$, such that $s_j/\mu^2 \to s_j$ where the new s_j are dimensionless. By a slight abuse of notation, we implement this by setting $\mu^2 = 1$ (note that the μ-dependence can always be restored). Let us consider the action of the derivative with respect to s_j (having already eliminated dependent kinematic invariants using momentum conservation) on the Schwinger parameter representation in (2.5.1), with $\nu_i > 0$:

$$\begin{aligned}\frac{\partial J}{\partial s_{j}}&=-\frac{\left(-1\right)^{\nu}}{\prod_{i=1}^{N}\Gamma\left(\nu_{i}\right)}\int_{0}^{\infty}\prod_{i=1}^{N}\mathrm{d}t_{i}\;t_{i}^{\nu_{i}-1}\,\mathcal{U}\left(\boldsymbol{t}\right)^{-1}\mathcal{U}\left(\boldsymbol{t}\right)^{-\frac{D}{2}}\frac{\partial\mathcal{F}}{\partial s_{j}}\exp\left(-\frac{\mathcal{F}\left(\boldsymbol{t},\boldsymbol{s}\right)-i0^{+}}{\mathcal{U}\left(\boldsymbol{t}\right)}\right)\\&=-\frac{\left(-1\right)^{\nu}}{\prod_{i=1}^{N}\Gamma\left(\nu_{i}\right)}\int_{0}^{\infty}\prod_{i=1}^{N}\mathrm{d}t_{i}\;t_{i}^{\nu_{i}-1}\,\mathcal{U}\left(\boldsymbol{t}\right)^{-\frac{D+2}{2}}\mathcal{F}_{s_{j}}(\boldsymbol{t})\exp\left(-\frac{\mathcal{F}\left(\boldsymbol{t},\boldsymbol{s}\right)-i0^{+}}{\mathcal{U}\left(\boldsymbol{t}\right)}\right)\end{aligned} \tag{2.5.2}$$

where in the final line we have used that the $\mathcal{F}$ polynomial is linear in the s_j to define the s_j-coefficient of $\mathcal{F}$: $\mathcal{F}_{s_j}(\boldsymbol{t}) = \frac{\partial\mathcal{F}}{\partial s_j}$. It is clear from the graphical construction of $\mathcal{F}$ that $\mathcal{F}_{s_j}$ depends only on the integration parameters and not on the other kinematic invariants. From the linearity of the $\mathcal{F}$ polynomial in all the kinematic invariants (with no constant term), we also have that

$$\mathcal{F}\left(\boldsymbol{t},\boldsymbol{s}\right)=\sum_{s_{j}\in\boldsymbol{s}}\mathcal{F}_{s_{j}}(\boldsymbol{t})\,s_{j}\,. \tag{2.5.3}$$

Similarly to the application of $\mathcal{U}\left(\hat{\mathbb{1}},\ldots,\hat{\mathbb{N}}\right)$ on J in the derivation of dimensional recurrence relations, we can consider the action of $\mathcal{F}_{s_j}\left(\hat{\mathbb{1}},\ldots,\hat{\mathbb{N}}\right)$ on J. This would replicate the second line of (2.5.2), up to a minus sign and a dimension shift. Hence, we obtain

$$\frac{\partial J}{\partial s_{j}}=-\mathcal{F}_{s_{j}}\left(\hat{\mathbb{1}},\ldots,\hat{\mathbb{N}}\right)\mathbb{D}^{+}J\left(\boldsymbol{s};\boldsymbol{\nu}\right)\,. \tag{2.5.4}$$

Using DRRs and IBP relations, we can always reduce the right hand side of (2.5.4) to master integrals. Hence, for a generic basis $\vec{J}$, we can construct

$$\frac{\partial \vec{J}}{\partial s_j} = \mathbf{A}_{s_j} \vec{J} \tag{2.5.5}$$

where $\mathbf{A}_{s_j}$ is the so-called 'partial derivative matrix' for s_j. Treating D and $\boldsymbol{\nu}$ as fixed for each master integral, J, in the basis, $\vec{J}$, we have

$$\mathrm{d}\vec{J} = \sum_{s_j \in \boldsymbol{s}} \frac{\partial \vec{J}}{\partial s_j} \mathrm{d}s_j \,. \tag{2.5.6}$$

Comparing (2.5.5) with (2.5.6), we obtain the following compact expression for the differential equation system:

$$\mathrm{d}\vec{J} = \left[\sum_{s_j \in \boldsymbol{s}} \mathbf{A}_{s_j} \mathrm{d}s_j \right] \vec{J} \,. \tag{2.5.7}$$

We can define the matrix of one-forms $\mathbf{A} = \sum_{s_j \in \boldsymbol{s}} \mathbf{A}_{s_j} \mathrm{d}s_j$ to obtain the even more compact expression

$$\mathrm{d}\vec{J} = \mathbf{A}\vec{J} \tag{2.5.8}$$

which allows us to write the 'integrability condition':

$$\mathrm{d}^2 = 0 \quad \Rightarrow \quad \mathrm{d}\mathbf{A} = \mathbf{A} \wedge \mathbf{A} \,. \tag{2.5.9}$$

This integrability condition on $\mathbf{A}$ is equivalent to a condition on the partial derivative matrices themselves given by

$$\forall s_j, s_k \in \boldsymbol{s} : \quad \frac{\partial \mathbf{A}_{s_j}}{\partial s_k} - \frac{\partial \mathbf{A}_{s_k}}{\partial s_j} + \left[\mathbf{A}_{s_j}, \mathbf{A}_{s_k} \right] = 0 \,. \tag{2.5.10}$$

In multi-loop calculations (such as the one presented in Chapter 4 where each $\mathbf{A}_{s_j}$ was a 494×494 matrix), it is advisable to check the integrability condition is satisfied explicitly; the realisation of the integrability condition in (2.5.10) is often the most practical. Another useful check relates to the fact that not all derivatives of a Feynman integral are independent – they obey the scaling relation

$$\sum_{s_j \in \boldsymbol{s}} s_j \frac{\partial J}{\partial s_j} = \left(\frac{LD}{2} - \nu \right) J \,. \tag{2.5.11}$$

This can easily be seen by considering the action of the derivative operator $\sum_{s_j \in \boldsymbol{s}} s_j \frac{\partial}{\partial s_j}$ on an integral, J, in the Feynman parameter representation. The scaling relation induces the following relation on the partial derivative matrices:

$$\sum_{s_j \in \boldsymbol{s}} s_j \mathbf{A}_{s_j} = \mathbf{\Gamma} \tag{2.5.12}$$

where $\mathbf{\Gamma}$ is a diagonal matrix with elements consisting of the scaling dimension of each master integral. Performing both checks (that is to say, that the integrability condition and the scaling relation are satisfied) is highly recommended when constructing a differential equation system.

Now, we implement this method of differential equations in our example of the unequal mass bubble topology with the master basis

$$\vec{J} = \begin{bmatrix} J_{\text{bub}}^{2-2\epsilon}(1,1) \\ J_{\text{bub}}^{2-2\epsilon}(2,0) \\ J_{\text{bub}}^{2-2\epsilon}(0,2) \end{bmatrix} . \tag{2.5.13}$$

Applying (2.5.4) for $s_j \in \{s, m_1^2, m_2^2\}$ to each integral in $\vec{J}$, we obtain

$$\begin{aligned} \partial_s J_{\text{bub}}^{2-2\epsilon}(1,1) &= \hat{\mathbb{1}}\,\hat{2}\, J_{\text{bub}}^{4-2\epsilon}(1,1) = J_{\text{bub}}^{4-2\epsilon}(2,2) \\ \partial_{m_1^2} J_{\text{bub}}^{2-2\epsilon}(1,1) &= -\hat{\mathbb{1}}\left(\hat{\mathbb{1}} + \hat{2}\right) J_{\text{bub}}^{4-2\epsilon}(1,1) = -2\, J_{\text{bub}}^{4-2\epsilon}(3,1) - J_{\text{bub}}^{4-2\epsilon}(2,2) \\ \partial_{m_2^2} J_{\text{bub}}^{2-2\epsilon}(1,1) &= -\hat{2}\left(\hat{\mathbb{1}} + \hat{2}\right) J_{\text{bub}}^{4-2\epsilon}(1,1) = -J_{\text{bub}}^{4-2\epsilon}(2,2) - 2\, J_{\text{bub}}^{4-2\epsilon}(1,3) , \end{aligned} \tag{2.5.14}$$

$$\begin{aligned} \partial_s J_{\text{bub}}^{2-2\epsilon}(2,0) &= 0 \\ \partial_{m_1^2} J_{\text{bub}}^{2-2\epsilon}(2,0) &= -\hat{\mathbb{1}}^2\, J_{\text{bub}}^{4-2\epsilon}(2,0) = -6\, J_{\text{bub}}^{4-2\epsilon}(4,0) \\ \partial_{m_2^2} J_{\text{bub}}^{2-2\epsilon}(2,0) &= 0 , \end{aligned} \tag{2.5.15}$$

$$\begin{aligned} \partial_s J_{\text{bub}}^{2-2\epsilon}(0,2) &= 0 \\ \partial_{m_1^2} J_{\text{bub}}^{2-2\epsilon}(0,2) &= 0 \\ \partial_{m_2^2} J_{\text{bub}}^{2-2\epsilon}(0,2) &= -\hat{2}^2\, J_{\text{bub}}^{4-2\epsilon}(0,2) = -6\, J_{\text{bub}}^{4-2\epsilon}(0,4) . \end{aligned} \tag{2.5.16}$$

Using IBP relations and DRRs, we can reduce the resulting integrals appearing above back to the masters in $\vec{J}$. This allows us to construct the following differential equation system:

$$\frac{\partial \vec{J}}{\partial s} = \mathbf{A}_s \vec{J}, \qquad \frac{\partial \vec{J}}{\partial m_1^2} = \mathbf{A}_{m_1^2} \vec{J}, \qquad \frac{\partial \vec{J}}{\partial m_2^2} = \mathbf{A}_{m_2^2} \vec{J} \tag{2.5.17}$$

$$\mathbf{A}_s = \begin{bmatrix} \frac{\left(m_1^2+m_2^2-s\right)s+\left([m_1^2-m_2^2]^2-s^2\right)\epsilon}{s\left(s-[m_1+m_2]^2\right)\left(s-[m_1-m_2]^2\right)} & \frac{m_1^2\left(m_1^2-m_2^2-s\right)}{s\left(s-[m_1+m_2]^2\right)\left(s-[m_1-m_2]^2\right)} & \frac{m_2^2\left(m_2^2-m_1^2-s\right)}{s\left(s-[m_1+m_2]^2\right)\left(s-[m_1-m_2]^2\right)} \\ 0 & 0 & 0 \\ 0 & 0 & 0 \end{bmatrix} \tag{2.5.18}$$

$$\mathbf{A}_{m_1^2} = \begin{bmatrix} \frac{\left(s-m_1^2+m_2^2\right)(1+2\epsilon)}{\left(s-[m_1+m_2]^2\right)\left(s-[m_1-m_2]^2\right)} & \frac{s-m_1^2-m_2^2}{\left(s-[m_1+m_2]^2\right)\left(s-[m_1-m_2]^2\right)} & \frac{2m_2^2}{\left(s-[m_1+m_2]^2\right)\left(s-[m_1-m_2]^2\right)} \\ 0 & -\frac{1+\epsilon}{m_1^2} & 0 \\ 0 & 0 & 0 \end{bmatrix} \tag{2.5.19}$$

$$\mathbf{A}_{m_2^2} = \begin{bmatrix} \frac{\left(s+m_1^2-m_2^2\right)(1+2\epsilon)}{\left(s-[m_1+m_2]^2\right)\left(s-[m_1-m_2]^2\right)} & \frac{2m_1^2}{\left(s-[m_1+m_2]^2\right)\left(s-[m_1-m_2]^2\right)} & \frac{s-m_1^2-m_2^2}{\left(s-[m_1+m_2]^2\right)\left(s-[m_1-m_2]^2\right)} \\ 0 & 0 & 0 \\ 0 & 0 & -\frac{1+\epsilon}{m_2^2} \end{bmatrix} \tag{2.5.20}$$

where the set of partial derivative matrices, $\mathbf{A}_{s_j}$, can be shown to explicitly satisfy the integrability condition in (2.5.10) and the scaling relation in (2.5.12).

Finally, we can obtain the Laurent series in ϵ for each master integral in the basis, $\vec{J}$, using the package `DiffExp` [48]. `DiffExp` solves the system using a generalised series solution, expanding in a line parameter, x, which defines a chosen contour in the kinematic space. Truncating the series solution after a large enough number of terms provides a sufficiently precise value of the coefficient of each order in ϵ for a given value of x. In Fig. 2.8, we present results for $J_{\text{bub}}^{2-2\epsilon}(1,1)$ as a function of s obtained using `DiffExp`, having provided the package with an analytic boundary condition at $s = 0$ and having fixed $m_1 = 1$ and $m_2 = 2$.

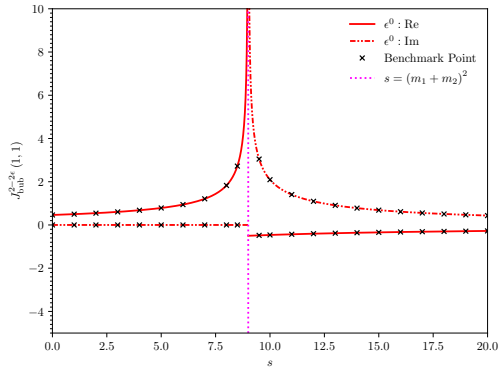

(a) ϵ^0

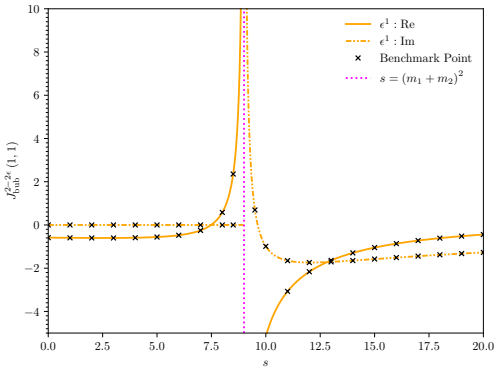

(b) ϵ^1

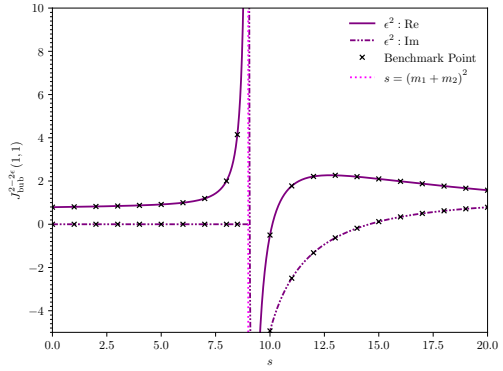

(c) ϵ^2

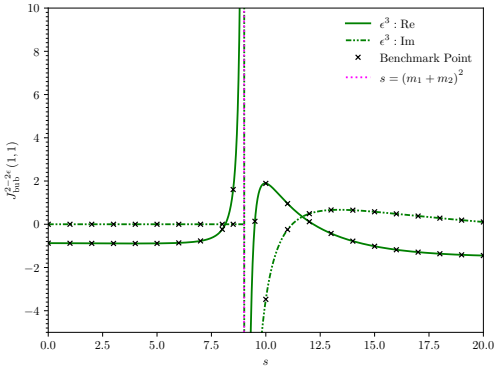

(d) ϵ^3

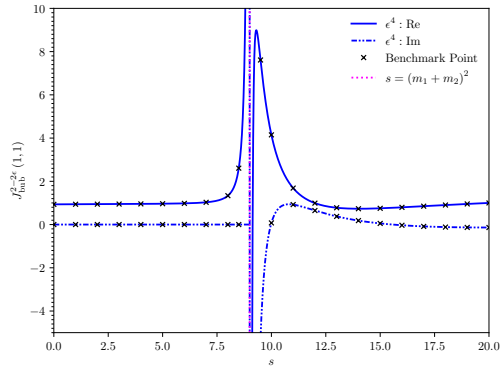

(e) ϵ^4

Figure 2.8: Coefficients of ϵ^n ($n \in \{0, 1, 2, 3, 4\}$) in the Laurent expansion of $J^{2-2\epsilon}_{\text{bub}}(1,1)$ as functions of s with $m_1 = 1$ and $m_2 = 2$ fixed. The threshold at $s = (m_1 + m_2)^2$ is shown in pink and the series solution is verified using `pySecDec` at numerous benchmark points denoted by crosses.

Chapter 3

Avoiding Contour Deformation in Feynman Integrals

In this chapter, we introduce a novel method for integrating directly in the Minkowski regime without recourse to contour deformation. The method maps a Minkowski integral to a causally-prescribed sum of integrals with manifestly non-negative[2] integrands which can then be dealt with using the standard approach of sector decomposition, for example, as discussed in Section 2.4. We begin, in Section 3.1, by reviewing how contour deformation can handle some of the singularities which appear in loop integrals in the Feynman parameter representation. The method for avoiding contour deformation is outlined in Section 3.2 with an algorithm provided for the cases where we know how to automate the procedure. Examples of the method being applied to both massless and massive Feynman integrals are given in Section 3.3 with the effect on performance discussed in Section 3.4.

3.1 Preliminaries

In this section, we will re-introduce our notation for Feynman integrals in Feynman parameter space. We will review the singularities present in dimensionally regulated

[2]The integrands are also strictly positive within the integration domain, away from the boundary.

parameter integrals and summarise the method of contour deformation, which can be used to evaluate parameter integrals outside the Euclidean regime.

3.1.1 Integrands in Parameter Space

In this chapter, an L-loop dimensionally regularised[1] Feynman integral depending on the kinematic invariants, $\boldsymbol{s}$, will be written in terms of Feynman parameters, $\boldsymbol{x}$, as

$$J(\boldsymbol{s}) = \frac{(-1)^{\nu}\,\Gamma\left(\nu - LD/2\right)}{\prod_{i=1}^{N}\Gamma\left(\nu_i\right)} \lim_{\delta\to 0^+}\int_{\mathbb{R}^N_{\geq 0}} \prod_{i=1}^{N} \mathrm{d}x_i x_i^{\nu_i - 1} \frac{\mathcal{U}(\boldsymbol{x})^{\nu-(L+1)D/2}}{\left(\mathcal{F}(\boldsymbol{x},\boldsymbol{s}) - i\delta\right)^{\nu - LD/2}}\,\delta\Big(1-\alpha\left(\boldsymbol{x}\right)\Big) \tag{3.1.1}$$

where $\mathcal{U}(\boldsymbol{x})$ and $\mathcal{F}(\boldsymbol{x},\boldsymbol{s})$ are the homogeneous Symanzik polynomials discussed heavily in Chapter 2. Given its significance in this exposition, we now denote the Feynman prescription explicitly by the limit that the parameter $\delta > 0$ goes to zero from above. In contrast to (2.2.19), we denote the domain of integration by $\mathbb{R}^N_{\geq 0}$ and set $\mu^2 = 1$. The argument of the δ-function defines an arbitrary hyperplane that bounds the integral in this positive domain for at least one $x_i \geq 0$ [10, 49, 50]. Common choices of the function $\alpha(\boldsymbol{x})$ include the N-dimensional simplex $\alpha(\boldsymbol{x}) = \sum_{i=1}^{N} x_i$, or lower dimensional simplices $\alpha(\boldsymbol{x}) = \sum_{i\in S} x_i$, where a non-empty subset of the Feynman parameters, S, is selected as mentioned in Section 2.2.3.

We recall from the graphical construction of the Symanzik polynomials in (2.2.20) and (2.2.21) that $\mathcal{U}(\boldsymbol{x})$ and $\mathcal{F}_0(\boldsymbol{x},\boldsymbol{s})$ are at most linear in a particular Feynman parameter, while $\mathcal{F}(\boldsymbol{x},\boldsymbol{s})$ is at most linear (quadratic) in parameters associated to massless (massive) propagators. Furthermore, we note that $\mathcal{U}(\boldsymbol{x})$ consists purely of positive monomials of Feynman parameters with positive coefficients, it is therefore manifestly positive in $\mathbb{R}^N_{\geq 0}$. The $\mathcal{F}(\boldsymbol{x},\boldsymbol{s})$ polynomial is built from monomials with both positive and negative sign depending on the value of the invariants, $\boldsymbol{s}$.

Both $\mathcal{U}(\boldsymbol{x})$ and $\mathcal{F}(\boldsymbol{x},\boldsymbol{s})$ may vanish on the intersection of the hyperplane defined

[1] Without loss of generality, we will assume $D = 4 - 2\epsilon$ throughout. We stress that the method is agnostic to the specific number of spacetime dimensions.

by the δ-function with the coordinate hyperplanes, or, equivalently, for subsets of $\boldsymbol{x}$ vanishing. Depending on the propagator powers, ν_i, and the space-time dimension, D, this can give rise to UV and IR divergences. When the invariants $\boldsymbol{s}$ are chosen such that $\mathcal{F}(\boldsymbol{x}, \boldsymbol{s})$ contains monomials with different signs, the $\mathcal{F}(\boldsymbol{x}, \boldsymbol{s})$ polynomial can additionally vanish and change sign on hypersurfaces within the integration domain, $\mathbb{R}^N_{>0}$.

For some Feynman integrals, it is possible to define a kinematic region in which all monomials of $\mathcal{F}(\boldsymbol{x}, \boldsymbol{s})$ have the same overall sign, we will refer to this choice of kinematics as being the manifestly same-sign regime. More generally we can encounter Feynman integrals and kinematic regions in which the monomials of $\mathcal{F}(\boldsymbol{x}, \boldsymbol{s})$ do not have the same sign, but for which $\forall \boldsymbol{x} \in \mathbb{R}^N_{>0} : \mathcal{F}(\boldsymbol{x}, \boldsymbol{s}) > 0$ or $\forall \boldsymbol{x} \in \mathbb{R}^N_{>0} : \mathcal{F}(\boldsymbol{x}, \boldsymbol{s}) < 0$, this situation will be referred to as being a same-sign regime[1]. In the most general situation $\mathcal{F}(\boldsymbol{x}, \boldsymbol{s})$ vanishes on hypersurfaces in $\mathbb{R}^N_{>0}$ and has no definite sign, we will refer to this as a mixed-sign (or Minkowski) regime.

3.1.2 Landau Equations

The necessary, but not sufficient, conditions for a dimensionally regulated parameter integral to have a singularity are described by the Landau equations [51–55]. In parameter space they can be written as [56],

$$\mathcal{F}(\boldsymbol{x}, \boldsymbol{s}) = 0, \qquad x_k \frac{\partial \mathcal{F}(\boldsymbol{x}, \boldsymbol{s})}{\partial x_k} = 0, \quad \text{for each } k \in \{1, \ldots, N\}. \tag{3.1.2}$$

As discussed above, the $\mathcal{F}$-polynomial can vanish and potentially give rise to singularities when some subset of Feynman parameters vanish, $x_i \to 0$, i.e. at the boundary of the integration domain, causing each individual monomial in $\mathcal{F}$ to vanish. Such singularities occur independently of the sign of the individual monomials in $\mathcal{F}$ and can be identified algorithmically, for example, by using sector decomposition [40, 57–60].

The cases where both $\mathcal{F}(\boldsymbol{x}, \boldsymbol{s})$ and all $\partial \mathcal{F}(\boldsymbol{x}, \boldsymbol{s})/\partial x_k$ vanish away from the boundary

[1] We define the Euclidean region specifically to be the positive case, $\forall \boldsymbol{x} \in \mathbb{R}^N_{>0} : \mathcal{F}(\boldsymbol{x}, \boldsymbol{s}) > 0$.

of the integration domain can occur when monomials of different sign are present in $\mathcal{F}(\boldsymbol{x}, \boldsymbol{s})$ as well as all partial derivatives with respect to the Feynman parameters. In these cases, the monomials can cancel against each other within the domain of integration and lead to solutions of the Landau equations.

Significant progress in analysing and solving the Landau equations has been made recently, see [61–72], for example. In [35], the analysis of a set of solutions of the Landau equations in parameter space which are present for generic kinematics led to the idea that integrals can be split on hypersurfaces which solve the Landau equations within the integration domain, thus mapping these solutions to the boundary of the new dissected integrals. The advantage of this dissection procedure is that the solutions of the Landau equations are now again solely on the boundary of integration and any resulting singularities can be algorithmically detected in parameter space using sector decomposition algorithms. In this chapter, we will explore this idea in a slightly different context, instead focusing on the variety $\mathcal{F}(\boldsymbol{x}, \boldsymbol{s}) = 0$ but, importantly, not requiring all partial derivatives vanish. Generally, such hypersurfaces are not solutions of the Landau equations and therefore do not give rise to (non-spurious) dimensionally-regulated singularities of the Feynman integral. However, as described in Section 3.1.3, these varieties do introduce a substantial (and computationally-expensive) obstacle.

3.1.3 Contour Deformation

When evaluating integrals in the mixed-sign (Minkowski) regime, the $\mathcal{F}(\boldsymbol{x}, \boldsymbol{s})$ polynomial can vanish within the domain of integration due to cancellation between monomials. When this occurs, the causal $i\delta$ appearing in (3.1.1) acts as a deformation of the integration contour into the complex-plane and provides a prescription for evaluating the integral in a theory with causal propagators. As a result of this, in the mixed-sign regime, the integral can become complex-valued. The values of the kinematic invariants, $\boldsymbol{s}$, at which the integral transitions from a same-sign to

a mixed-sign regime is sometimes called a (pseudo-)threshold and such points can correspond, for example, to internal propagators becoming on-shell. The Feynman prescription defines an analytic continuation of the integral and specifies the branch on which multivalued functions, such as square-roots and logarithms which result from the integration over the Feynman parameters, should be evaluated.

The location (and shape) of the $\mathcal{F}(\boldsymbol{x}, \boldsymbol{s}) = 0$ hypersurface depends on the signs and magnitudes of the kinematic invariants, $\boldsymbol{s}$. In the same-sign regime, the variety of $\mathcal{F}(\boldsymbol{x}, \boldsymbol{s})$ is located in the non-positive domain of $\boldsymbol{x}$ and only touches the integration domain when some x_i vanish. In the mixed-sign regime, the variety enters the domain of integration with portions of the hypersurface strictly within the domain (away from the boundary). To correctly define the causal integral, the integration contour can be deformed into the complex-plane by shifting each Feynman parameter by a vanishingly small imaginary part $i\tau_k$:

$$x_k \;\rightarrow\; z_k = x_k - i\tau_k. \tag{3.1.3}$$

This shift results in the $\mathcal{F}$-polynomial transforming as,

$$\mathcal{F}(\boldsymbol{x}, \boldsymbol{s}) \rightarrow \mathcal{F}(\boldsymbol{z}, \boldsymbol{s}) = \mathcal{F}(\boldsymbol{x}, \boldsymbol{s}) - i \sum_k \tau_k \frac{\partial \mathcal{F}(\boldsymbol{x}, \boldsymbol{s})}{\partial x_k} + \mathcal{O}(\tau^2). \tag{3.1.4}$$

The individual τ_k can then be chosen in accordance with the causal prescription, i.e. to ensure that the deformed $\mathcal{F}(\boldsymbol{z}, \boldsymbol{s})$ develops a negative imaginary part where $\mathcal{F}(\boldsymbol{x}, \boldsymbol{s})$ vanishes. If the τ_k are chosen such that a loop can be formed by connecting the original contour (with the prescribed $i\delta$) and the new integration contour and the τ_k are chosen small enough that this loop does not enclose any additional poles, then Cauchy's integral theorem states that the two integrals are equal up to a minus sign. An example of a choice of shift parameters that achieves all of the above (in the integration domain $x_i \in [0, 1]$) is given by [73–85],

$$\tau_k = \lambda_k \, x_k (1 - x_k) \frac{\partial \mathcal{F}(\boldsymbol{x})}{\partial x_k}, \tag{3.1.5}$$

where λ_k are arbitrary parameters chosen small enough that the loop does not enclose

any additional poles. Inserting the deformation into (3.1.4) gives,

$$\mathcal{F}(\boldsymbol{z},\boldsymbol{s}) = \mathcal{F}(\boldsymbol{x},\boldsymbol{s}) - i\sum_k \lambda_k\, x_k(1-x_k)\left(\frac{\partial \mathcal{F}(\boldsymbol{x},\boldsymbol{s})}{\partial x_k}\right)^2 + \mathcal{O}(\tau^2). \tag{3.1.6}$$

This choice gives a negative imaginary part to $\mathcal{F}(\boldsymbol{z},\boldsymbol{s})$ except at $x_k = 0$ and $x_k = 1$ (chosen as the boundary of integration) and where all $\partial\mathcal{F}(\boldsymbol{x},\boldsymbol{s})/\partial x_k$ vanish. Note that (3.1.4) suggests an interpretation of the Landau equations in the situation where $\mathcal{F}(\boldsymbol{x},\boldsymbol{s})$ and all the partial derivatives, $\partial\mathcal{F}(\boldsymbol{x},\boldsymbol{s})/\partial x_k$, simultaneously vanish. In this case the infinitesimal deformation of the integration contour into the complex-plane according to (3.1.3) does not avoid the variety of $\mathcal{F}(\boldsymbol{x},\boldsymbol{s})$.

The advantage of the deformation procedure given in (3.1.3) and (3.1.5) is that the deformed integral is exactly equal (up to a minus sign) to the original Feynman integral. However, a significant drawback of this procedure is that the integral can become highly oscillatory with a large positive contribution from one part of the contour cancelled by a large negative contribution from elsewhere along the contour. Furthermore, the change of variables from $\boldsymbol{x} \to \boldsymbol{z}$ introduces an $(N-1)\times(N-1)$ Jacobian determinant (after integrating out the δ-function) depending in a non-trivial way on the integration variables and kinematics. In high-dimensional cases, this Jacobian can be significantly more complicated than the integrand itself. Furthermore, the contour depends on the arbitrary parameters λ_k, it is not always trivial to pick valid values and the variance of the integrand depends on the choice of λ_k.

Alternatively, the Feynman integral can be directly evaluated with $i\delta$ set to several small positive (non-zero) numbers. The correct result can then be obtained by performing an extrapolation of these evaluations to $\delta \to 0^+$, see [86–89]. The drawback of this approach is that the value of the integral with non-zero δ only approximates the true result and any error due to the extrapolation to $\delta \to 0^+$ needs to be carefully assessed. Furthermore, the value of δ must always be chosen small enough that no additional poles are crossed in the complex-plane, this can force the integration contour close to the singular surface making the integrand oscillatory.

In Section 3.2, we describe an alternative strategy of evaluating Feynman integrals

in parameter space in the mixed-sign regime without using contour deformation.

3.2 Method

In this section, we propose a procedure for evaluating Feynman parametrised integrals in the mixed-sign (Minkowski) regime, i.e. where $\mathcal{F}(\boldsymbol{x}, \boldsymbol{s})$ has no definite sign for $\boldsymbol{x} \in \mathbb{R}^N_{>0}$, without deforming the integration contour into the complex-plane. After introducing the general concept, we present a constructive algorithm valid for a specific class of Feynman integrals. We show that when this form can be achieved, the resulting integrands are strictly non-negative and the analytic continuation of the resulting integrals becomes trivial.

3.2.1 Overview

The quintessential idea is to construct transformations of the Feynman parameters such that the variety of the $\mathcal{F}$-polynomial (the hypersurface defined by $\mathcal{F}(\boldsymbol{x}, \boldsymbol{s}) = 0$) is mapped to the boundary of the integration domain. After this, $\mathcal{F}$ only vanishes on the integration boundary, any singularities resulting from this can be algorithmically dealt with using existing methods, such as sector decomposition.

The procedure involves splitting the integration domain into regions where $\mathcal{F} > 0$ and $\mathcal{F} < 0$ and integrating these regions separately. We may also further sub-divide the positive and negative regions for technical or computational ease, see the massive examples in Section 3.3.2. For the regions where $\mathcal{F}$ is negative, we factor out a minus sign from $\mathcal{F}$ ensuring the Feynman prescription is respected, after this, we will have only non-negative integrands. The resulting general decomposition for the original Feynman integral, $J(\boldsymbol{s})$, is

$$J(\boldsymbol{s}) = \sum_{n_+=1}^{N_+} J^{+,n_+}(\boldsymbol{s}) + \lim_{\delta \to 0^+} (-1 - i\delta)^{-(\nu - LD/2)} \sum_{n_-=1}^{N_-} J^{-,n_-}(\boldsymbol{s}), \tag{3.2.1}$$

where we have allowed for both the positive and negative regions to be subdivided

into N_+ and N_- sub-regions respectively. After this decomposition, we note that the imaginary part of the original integral $J(\boldsymbol{s})$ is fully determined by the contribution from the negative region(s) in (3.2.1) and, furthermore, is a result of the $(-1-i\delta)^{-(\nu-LD/2)}$ factor multiplying the purely real $J^-(\boldsymbol{s})$ contribution(s). We remark that, in many cases, the division can be chosen such that there is only a single positive and a single negative region (see the algorithm in Section 3.2.2 and many of the massless examples in Section 3.3.1).

It has long been known that, for integrals in a kinematic regime where $\mathcal{F}$ is non-positive in the integration domain, an overall minus sign can be factored out and the resulting non-negative (Euclidean) integrand can be evaluated. As a trivial example, consider the massless bubble in the physical $s > 0$ regime:

$$\begin{aligned} J_{\text{bub},m=0} &= \lim_{\delta\to 0^+} \Gamma(\epsilon) \int_{\mathbb{R}^2_{\geq 0}} \mathrm{d}x_1 \mathrm{d}x_2 \frac{(x_1+x_2)^{-2+2\epsilon}}{(-sx_1x_2-i\delta)^{\epsilon}} \delta\left(1-\sum_{i=1}^2 \alpha_i x_i\right) \\ &= \lim_{\delta\to 0^+} (-1-i\delta)^{-\epsilon} \Gamma(\epsilon) \int_{\mathbb{R}^2_{\geq 0}} \mathrm{d}x_1 \mathrm{d}x_2 \frac{(x_1+x_2)^{-2+2\epsilon}}{(sx_1x_2)^{\epsilon}} \delta\left(1-\sum_{i=1}^2 \alpha_i x_i\right) \\ &= \lim_{\delta\to 0^+} (-1-i\delta)^{-\epsilon} J^-_{\text{bub},m=0} \end{aligned} \tag{3.2.2}$$

where in the final line we have translated this simple manipulation into the language of our decomposition given in (3.2.1). Our procedure essentially generalises this idea by mapping a generic integral into integrals which are already Euclidean (where $\mathcal{F} > 0$ originally) plus cases like this where $\mathcal{F} < 0$ and we can factor out the prescription to generate Euclidean integrands.

In order to construct the integrands appearing in (3.2.1), we must ensure that our transformations do not spoil the non-negativity of $\mathcal{U}$ (nor introduce zeroes of $\mathcal{U}$ within the integration domain) as well as avoiding transformations with Jacobian determinants which break the positivity of the resulting integrand within (but not necessarily on the boundary of) the integration domain. Furthermore, we must check that the transformations applied do not miss any regions from the original integration domain as well as prohibiting transformations that map regions from outside the original integration domain into the new domain.

These demands may initially appear quite constraining and hence, one might assume that the transformations are potentially difficult to construct. However, we will show that for a large number of massless integrals (a sample of which are detailed in Section 3.3.1), the procedure is algorithmic. Additionally, geometric visualisations can prove extremely useful for building an understanding of how the transformations should appear, which aids their construction. We adopt this approach on a case-by-case basis for the resolution of the massive integrals in Section 3.3.2. In its current form, this approach suffers from the disadvantage that it is difficult to visualise beyond four propagators, although this does not present an obstacle to the concept in principle.

The interplay between the positive and negative contributions in our dissection also allows us to obtain an understanding of the structure of the original integral from a new perspective. For example, if we have a finite integral with a complex-valued leading order in the ϵ expansion, we must necessarily have a pole in ϵ in the negative integral contribution which generates an imaginary ϵ^0 term when multiplied with the expansion of $(-1-i\delta)^{-(\nu-LD/2)}$. In order for the full integral to be finite, the positive contribution must have the exact same pole in ϵ such that the poles cancel in the full integral to leave a finite leading order.

3.2.2 Algorithm for Univariate Bisectable Integrals

Here we describe an algorithmic procedure for resolving a class of Feynman integrals which we call univariate bisectable in $\boldsymbol{s}_R$. The algorithm will succeed in mapping an integral in a given mixed-sign (Minkowski) regime, $\boldsymbol{s}_R$, defined by a set of inequalities depending on external kinematics, to a single integral in which $\mathcal{F}(\boldsymbol{x},\boldsymbol{s})$ is non-negative and a single integral in which $\mathcal{F}(\boldsymbol{x},\boldsymbol{s})$ is non-positive if there is a single variable for which the $\mathcal{F}(\boldsymbol{x},\boldsymbol{s})=0$ hypersurface divides the integration domain in two. In Section 3.3 we discuss several non-trivial examples for which this algorithm succeeds and we also solve cases for which this algorithm is not sufficient.

Algorithm 1: Univariate Bisection (UB)

Input: $\mathcal{I}(\boldsymbol{x}, \boldsymbol{s}; \delta)$, $\{\boldsymbol{s}_{\min} < \boldsymbol{s} < \boldsymbol{s}_{\max}\}$
Output: $\mathcal{I}^+(\boldsymbol{x}, \boldsymbol{s})$, $\mathcal{I}^-(\boldsymbol{x}, \boldsymbol{s})$
foreach $x_i \in \boldsymbol{x}$ **do**
  Let $r = \texttt{Reduce}[\{\mathcal{F}(\boldsymbol{x}, \boldsymbol{s}) < 0\} \cup \{0 < \boldsymbol{x}\} \cup \{\boldsymbol{s}_{\min} < \boldsymbol{s} < \boldsymbol{s}_{\max}\}, x_i]$;
  if $r \sim$ (3.2.6) **then**
    Let $\mathcal{I}^-(\boldsymbol{x}, \boldsymbol{s}) = \mathcal{J}(\boldsymbol{x}_{\neq i}, y_i)\, \mathcal{I}(\boldsymbol{x}_{\neq i}, y_i; -\boldsymbol{s}; 0)$
    Let $\mathcal{I}^+(\boldsymbol{x}, \boldsymbol{s}) = \mathcal{J}(\boldsymbol{x}_{\neq i}, y_i')\, \mathcal{I}(\boldsymbol{x}_{\neq i}, y_i'; \boldsymbol{s}; 0)$
    return $\mathcal{I}^+(\boldsymbol{x}, \boldsymbol{s})$, $\mathcal{I}^-(\boldsymbol{x}, \boldsymbol{s})$
  else if $r \sim$ (3.2.7) **then**
    Let $\mathcal{I}^-(\boldsymbol{x}, \boldsymbol{s}) = \mathcal{J}(\boldsymbol{x}_{\neq i}, y_i')\, \mathcal{I}(\boldsymbol{x}_{\neq i}, y_i'; -\boldsymbol{s}; 0)$
    Let $\mathcal{I}^+(\boldsymbol{x}, \boldsymbol{s}) = \mathcal{J}(\boldsymbol{x}_{\neq i}, y_i)\, \mathcal{I}(\boldsymbol{x}_{\neq i}, y_i; \boldsymbol{s}; 0)$
    return $\mathcal{I}^+(\boldsymbol{x}, \boldsymbol{s})$, $\mathcal{I}^-(\boldsymbol{x}, \boldsymbol{s})$
end
return $\neg$UB *in* $\{\boldsymbol{s}_{\min} < \boldsymbol{s} < \boldsymbol{s}_{\max}\}$

We begin by considering a generic Feynman integral of the form Eq. (3.2.3),

$$J(\boldsymbol{s}) = \frac{(-1)^\nu \Gamma\left(\nu - LD/2\right)}{\prod_{i=1}^N \Gamma\left(\nu_i\right)} \lim_{\delta \to 0^+} I(\boldsymbol{s}; \delta), \tag{3.2.3}$$

$$I(\boldsymbol{s}; \delta) = \int_{\mathbb{R}^N_{\geq 0}} \mathrm{d}\boldsymbol{x}\; \mathcal{I}(\boldsymbol{x}, \boldsymbol{s}; \delta)\, \delta\Big(1 - \alpha\left(\boldsymbol{x}\right)\Big) \tag{3.2.4}$$

$$= \int_{\mathbb{R}^N_{\geq 0}} \prod_{i=1}^N \mathrm{d}x_i x_i^{\nu_i - 1} \frac{\mathcal{U}(\boldsymbol{x})^{\nu - (L+1)D/2}}{\left(\mathcal{F}(\boldsymbol{x}, \boldsymbol{s}) - i\delta\right)^{\nu - LD/2}}\, \delta\Big(1 - \alpha\left(\boldsymbol{x}\right)\Big). \tag{3.2.5}$$

Our goal is to cast the integral into the form of (3.2.1) for a specific kinematic region.

We begin by defining some convenient notation, let $\boldsymbol{x} = \{x_1, \ldots, x_N\}$ be the complete set of Feynman parameters and $\boldsymbol{x}_{\neq i} = \boldsymbol{x} \backslash \{x_i\} = \{x_1, \ldots, x_{i-1}, x_{i+1}, \ldots x_N\}$ be the set excluding a single parameter x_i. Let $\boldsymbol{s}_R = \{\boldsymbol{s}_{\min} < \boldsymbol{s} < \boldsymbol{s}_{\max}\}$ be a kinematic region defined by a system of inequalities, this notation should be interpreted as placing minimum and maximum limits on each independent kinematic invariant/mass on which the integral depends (i.e. after applying momentum conservation to eliminate any dependent invariants).

The success of the algorithm depends on the choice of kinematic region, a conservative choice of input region would be to choose a region from one (pseudo-)threshold to the next (pseudo-)threshold in each variable without crossing any intermediate thresholds.

In Algorithm 1, we state the univariate bisection procedure. The input to the algorithm is the integrand of the Feynman integral to be resolved and the kinematic regime of interest. The algorithm iterates over each Feynman parameter and attempts to find a valid bisection. The `Reduce`$[\{\dots\}, x_i]$ function (which is already implemented in this syntax in `Mathematica`) takes a set of inequalities and tries to reduce them to a simpler system with the result including expressions of the type $a < x_i < b$, where possible, for generic functional forms a and b. The forms of the reduced system, r, for which a bisection is valid are given by,

$$\{0 < x_i < f\left(\boldsymbol{x}_{\neq i}\right)\} \quad \cup \quad \{0 < \boldsymbol{x}_{\neq i}\} \quad \cup \quad \{\boldsymbol{s}_{\min} < \boldsymbol{s} < \boldsymbol{s}_{\max}\}, \tag{3.2.6}$$

$$\{f\left(\boldsymbol{x}_{\neq i}\right) < x_i\} \quad \cup \quad \{0 < \boldsymbol{x}_{\neq i}\} \quad \cup \quad \{\boldsymbol{s}_{\min} < \boldsymbol{s} < \boldsymbol{s}_{\max}\}, \tag{3.2.7}$$

where $f(\boldsymbol{x}_{\neq i})$ is a rational function with unit degree of homogeneity. If a valid bisection can be found then we construct a transformation for the bisection parameter, x_i, that maps the variety to an integration boundary. If the reduced system r is of form Eq. (3.2.6) then we map $\mathcal{F} = 0$ to $x_i \to \infty$ while keeping the boundary at $x_i = 0$ fixed. If r is of the form Eq. (3.2.7) then we instead map the variety $\mathcal{F} = 0$ to $x_i = 0$ while keeping the boundary at $x_i \to \infty$ fixed. These mappings can be achieved by replacing x_i with y_i or y_i', given by

$$y_i = \frac{x_i}{x_i + x_j} f\left(\boldsymbol{x}_{\neq i}\right), \tag{3.2.8}$$

$$y_i' = x_i + f\left(\boldsymbol{x}_{\neq i}\right). \tag{3.2.9}$$

In the mapping Eq. (3.2.8) the variable $x_j \neq x_i$ appearing in the denominator is an arbitrary Feynman parameter. The function $\mathcal{J}(\boldsymbol{x}_{\neq i}, y_i)$ appearing in the algorithm is the Jacobian determinant resulting from the change of variables from x_i to y_i. When defining $\mathcal{I}^-(\boldsymbol{x}, \boldsymbol{s})$, we factor a minus sign out of the $\mathcal{F}$-polynomial, we indicate this in our algorithm by calling $\mathcal{I}$ with argument $-\boldsymbol{s}$, this is equivalent as only $\mathcal{F}$ initially depends on the kinematics and it is linear in the kinematic invariants. If the algorithm succeeds then it will return the non-negative integrands $\mathcal{I}^+(\boldsymbol{x}, \boldsymbol{s})$ and

$\mathcal{I}^{-}(\boldsymbol{x},\boldsymbol{s})$, the result for the original integral is then given by,

$$J^{\pm}(\boldsymbol{s}) = \frac{(-1)^{\nu}\,\Gamma\left(\nu - LD/2\right)}{\prod_{i=1}^{N}\Gamma\left(\nu_i\right)} \int_{\mathbb{R}^{N}_{\geq 0}} \mathrm{d}\boldsymbol{x}\; \mathcal{I}^{\pm}(\boldsymbol{x},\boldsymbol{s})\,\delta\Big(1-\alpha\left(\boldsymbol{x}\right)\Big) \tag{3.2.10}$$

$$J(\boldsymbol{s}) = J^{+}(\boldsymbol{s}) + \lim_{\delta\to 0^{+}} \left(-1-i\delta\right)^{-(\nu-LD/2)} J^{-}(\boldsymbol{s}). \tag{3.2.11}$$

If the algorithm fails then the integral is not univariate bisectable in the kinematic region $\{\boldsymbol{s}_{\min} < \boldsymbol{s} < \boldsymbol{s}_{\max}\}$ – a different (more restrictive) choice of region may be necessary or the structure of the integral itself may prevent any univariate bisection from being obtained, we will discuss this case further in Section 3.2.3.

We note that several aspects of the above algorithm are arbitrary. Firstly, there may be multiple possible bisection parameters for a given Feynman integral, in order to obtain the simplest possible integrands it may be beneficial to examine multiple resolutions with different bisection parameters. It is sometimes even possible to select different bisection parameters for constructing $\mathcal{I}^{-}(\boldsymbol{x},\boldsymbol{s})$ and $\mathcal{I}^{+}(\boldsymbol{x},\boldsymbol{s})$. Secondly, the x_j appearing in (3.2.8) can be replaced by a more general function (e.g. a constant), however, we prefer the transformation to be homogeneous such that the resulting integrand retains its homogeneity; any valid linear function of the Feynman parameters would also achieve this.

The univariate bisection algorithm is agnostic to the choice of hyperplane $\alpha(\boldsymbol{x})$ in the δ-function of (3.2.5), such that a choice can be made post-resolution. This is due to the algorithm protecting the projective nature of the resulting integrals by preserving the homogeneity of the integrands throughout the resolution procedure. In contrast to this, for the integrals which we resolve without use of the algorithm, presented in Section 3.3.2, we will often make a specific choice of the δ-function and integrate over one variable before considering the dissection of the integral.

3.2.3 Beyond Univariate Bisectable Integrals

Current work focusses on extending this algorithm to integrals which do not get resolved with a univariate bisection parameter and understanding for which integrals

and regimes the algorithm fails. In Section 3.3.2, several of the presented massive integrals can not be resolved using the univariate bisection algorithm in the full physical region. However, we are also aware of a number of massless integrals for which this algorithm also fails. For example, we use this algorithm to analyse BNP7, a non-planar double-box, in Section 3.3.1 and the algorithm resolves this case but it fails on the planar double-box integral in the same regime when parametrising in terms of s, t. Understanding the fundamental source of the breakdown of this method on examples like this is likely to provide insight on the extension of this procedure to a more general class of Feynman integrals.

One immediate generalisation of Algorithm 1, which we have verified to work on several examples, is to iterate the bisection using several variables until the integral is resolved. The principal complication of this procedure is ensuring that the entire original integration domain is covered without any double counting.

In Section 3.3.2, we will focus on studying individual integrals involving internal masses including integrals known to be elliptic and hyperelliptic. In these cases, we will directly inspect the geometry of the variety of $\mathcal{F}$ and derive a valid decomposition, demonstrating that this principle can be applied for a wide class of Feynman integrals. With our current methods, we will find that, in contrast to Algorithm 1, we often need more than one positive and one negative integrand, motivating the general decomposition formula of (3.2.1).

3.3 Examples

3.3.1 Massless Examples

In this section, we provide a number of examples of massless integrals which are resolved automatically by the algorithm presented in Section 3.2.2. We show that this procedure can be successfully applied to integrals including but not limited to: 1-loop with an off-shell leg, 1-loop 5-point, 2-loop non-planar and 3-loop non-planar

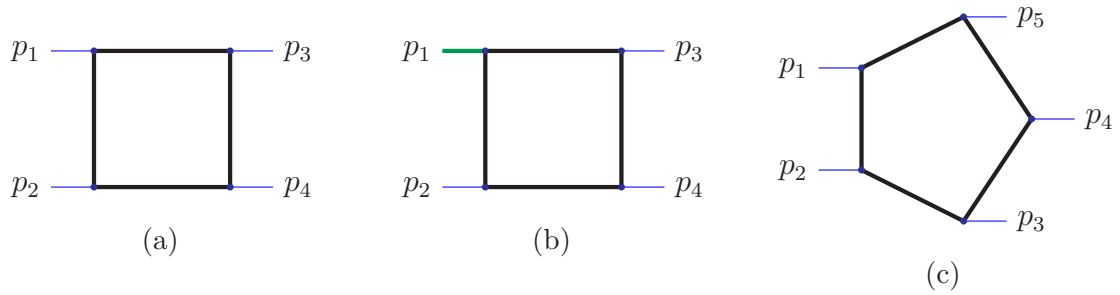

Figure 3.1: The massless box with all on-shell legs (3.1a), an off-shell leg (p_1) (3.1b) and the massless pentagon (3.1c).

integrals. For pedagogical reasons, we apply each step of the algorithm in detail for a simple massless box with on-shell legs before presenting the remaining examples more succinctly.

1-Loop Box with All On-Shell Legs

To clarify the application of the algorithm presented in Section 3.2.2, let us begin by analysing the simple case of a 1-loop massless box with all external legs on-shell, shown in Fig. 3.1a. Each step will be carried out in detail for this simple example in the hope that this illuminates the abstract procedure.

The integral we wish to resolve is

$$J_{\text{box}}(\boldsymbol{s}) = \Gamma(2+\epsilon) \lim_{\delta \to 0^+} I_{\text{box}}(\boldsymbol{s};\delta), \tag{3.3.1}$$

$$I_{\text{box}}(\boldsymbol{s};\delta) = \int_{\mathbb{R}^4_{\geq 0}} \prod_{i=1}^{4} \mathrm{d}x_i \, \frac{\mathcal{U}(\boldsymbol{x})^{2\epsilon}}{\left(\mathcal{F}(\boldsymbol{x},\boldsymbol{s}) - i\delta\right)^{2+\epsilon}} \, \delta\Big(1 - \alpha(\boldsymbol{x})\Big), \tag{3.3.2}$$

where the $\mathcal{U}(\boldsymbol{x})$ and $\mathcal{F}(\boldsymbol{x},\boldsymbol{s})$ polynomials are given by

$$\mathcal{U}(\boldsymbol{x}) = x_1 + x_2 + x_3 + x_4, \tag{3.3.3}$$

$$\mathcal{F}(\boldsymbol{x},\boldsymbol{s}) = -s_{12}x_1x_2 - s_{13}x_3x_4, \tag{3.3.4}$$

with $s_{ij} = (p_i + p_j)^2$. Suppose that we are interested in evaluating this integral for $2 \to 2$ physical scattering kinematics $\{0 < s_{12} < \infty,\ -s_{12} < s_{13} < 0\}$. Usually we would need a contour deformation as this regime is above the threshold at $s_{12} = 0$

and the $\mathcal{F}$ polynomial contains monomials of different sign and can therefore itself be both positive or negative inside the domain of integration. Note that in this kinematic regime $s_{12} > 0$ and $(-s_{13}) > 0$.

Applying Algorithm 1, we begin with the choice $x_i = x_1$. Attempting to reduce with respect to x_1 the set of inequalities,

$$\begin{aligned}&\{-s_{12}x_1x_2 - s_{13}x_3x_4 < 0\} \cup \{0 < x_1,\ 0 < x_2,\ 0 < x_3,\ 0 < x_4\} \cup \\ &\{0 < s_{12} < \infty,\ -s_{12} < s_{13} < 0\},\end{aligned} \tag{3.3.5}$$

we obtain the solution,

$$r = \{\frac{-s_{13}x_3x_4}{s_{12}x_2} < x_1\} \cup \{0 < x_2,\ 0 < x_3,\ 0 < x_4\} \cup \{0 < s_{12} < \infty,\ -s_{12} < s_{13} < 0\}. \tag{3.3.6}$$

We observe that r is of the form Eq. (3.2.7) with

$$f(\boldsymbol{x}_{\neq 1}) = \frac{(-s_{13})x_3x_4}{s_{12}x_2}, \tag{3.3.7}$$

therefore, x_1 is a valid bisection parameter. As dictated by the algorithm, we can now construct the positive and negative contributions by transforming the variable x_1. Applying the transformation given in (3.2.7),

$$x_1 \to y_1' = x_1 + \frac{(-s_{13})x_3x_4}{s_{12}x_2}, \tag{3.3.8}$$

we map the variety $\mathcal{F}(\boldsymbol{x}, \boldsymbol{s}) = 0$ to $x_1 = 0$ while keeping the boundary at $x_1 \to \infty$ fixed. The resulting integrand is given by

$$\begin{aligned}\mathcal{J}^-(\boldsymbol{x}) = 1, \quad \mathcal{U}^-(\boldsymbol{x}) = x_1 + x_2 + x_3 + x_4 + \frac{(-s_{13})x_3x_4}{s_{12}x_2}, \quad \mathcal{F}^-(\boldsymbol{x}, \boldsymbol{s}) = s_{12}x_1x_2,& \\ \mathcal{I}^-_{\text{box}}(\boldsymbol{x}, \boldsymbol{s}) = \mathcal{J}^-(\boldsymbol{x}) \frac{\mathcal{U}^-(\boldsymbol{x})^{2\epsilon}}{\mathcal{F}^-(\boldsymbol{x}, \boldsymbol{s})^{2+\epsilon}}& \\ = x_1^{-2-\epsilon}(s_{12}x_2)^{-2-3\epsilon} \left(s_{12}x_2 \left(x_1 + x_2 + x_3 + x_4\right) - s_{13}x_3x_4\right)^{2\epsilon}.&\end{aligned} \tag{3.3.9}$$

In this example we are not considering an integral with dots (propagators raised to a higher power) or a numerator, in general one would apply the transformation also

to any Feynman parameters appearing in the numerator.

The positive contribution is given by transforming the variable x_1 according to (3.2.8) with the arbitrary choice $x_j = x_N$,

$$x_1 \to y_1 = \frac{x_1}{x_1 + x_4} \frac{(-s_{13}) x_3 x_4}{s_{12} x_2} \tag{3.3.10}$$

which maps the variety $\mathcal{F}(\boldsymbol{x}, \boldsymbol{s}) = 0$ to $x_1 \to \infty$ keeping $x_1 = 0$ fixed. The resulting integrand is given by

$$\begin{aligned}
\mathcal{J}^+(\boldsymbol{x}) &= \frac{(-s_{13}) x_3 x_4^2}{s_{12} x_2 (x_1 + x_4)^2}, \quad \mathcal{U}^+(\boldsymbol{x}) = \frac{x_1}{x_1 + x_4} \frac{(-s_{13}) x_3 x_4}{s_{12} x_2} + x_2 + x_3 + x_4, \\
\mathcal{F}^+(\boldsymbol{x}, \boldsymbol{s}) &= \frac{(-s_{13}) x_3 x_4^2}{x_1 + x_4}, \\
\mathcal{I}^+_{\text{box}}(\boldsymbol{x}, \boldsymbol{s}) &= \mathcal{J}^+(\boldsymbol{x}) \frac{\mathcal{U}^+(\boldsymbol{x})^{2\epsilon}}{\mathcal{F}^+(\boldsymbol{x}, \boldsymbol{s})^{2+\epsilon}} \\
&= (x_1 + x_4)^{-\epsilon} (s_{12} x_2)^{-1-2\epsilon} \left(-s_{13} x_3 x_4^2\right)^{-1-\epsilon} \\
&\quad (s_{12} x_2 (x_1 + x_4) (x_2 + x_3 + x_4) - s_{13} x_1 x_3 x_4)^{2\epsilon}.
\end{aligned} \tag{3.3.11}$$

Sewing the positive and negative contributions together, the final result for the on-shell box integral is given by,

$$J_{\text{box}}(\boldsymbol{s}) = \Gamma(2 + \epsilon) \lim_{\delta \to 0^+} I_{\text{box}}(\boldsymbol{s}; \delta) \tag{3.3.12}$$

$$I_{\text{box}}(\boldsymbol{s}; \delta) = I^+_{\text{box}}(\boldsymbol{s}) + (-1 - i\delta)^{-2-\epsilon} I^-_{\text{box}}(\boldsymbol{s}). \tag{3.3.13}$$

Note that, neglecting the δ-functions, the integrands of both I^+_{box} and I^-_{box} pick up a factor of $\lambda^{-N} = \lambda^{-4}$ under the scaling transformation $\{x_1, \ldots, x_4\} \to \{\lambda x_1, \ldots, \lambda x_4\}$. This stems from the homogeneity of the original $\mathcal{U}$ and $\mathcal{F}$ polynomials and the fact that the algorithm preserves the homogeneity.

1-Loop Box with an Off-Shell Leg

In this example, we extend the previous case to a massless box where we now allow for an off-shell leg as in Fig. 3.1b with $p_1^2 > 0$. For this integral and the remaining

massless examples, we present the resolution procedure more concisely given that the algorithm has been explained and applied in detail already. From now on, we will explicitly denote the hyperplane $\alpha(\boldsymbol{x})$ by $\sum_{i=1}^{N}\alpha_i x_i$. The integral we wish to consider is

$$\begin{aligned} J_{\text{box},p_1^2>0} &= \lim_{\delta\to 0^+}\Gamma\left(2+\epsilon\right) I_{\text{box},p_1^2>0} \\ I_{\text{box},p_1^2>0} &= \int_{\mathbb{R}^4_{\geq 0}}\prod_{i=1}^{4}\mathrm{d}x_i\,\frac{\mathcal{U}(\boldsymbol{x})^{2\epsilon}}{\left(\mathcal{F}(\boldsymbol{x},\boldsymbol{s})-i\delta\right)^{2+\epsilon}}\delta\left(1-\sum_{i=1}^{4}\alpha_i x_i\right) \end{aligned} \tag{3.3.14}$$

where, as we derived explicitly in Section 2.2.3, the $\mathcal{U}$ polynomial remains unchanged and the $\mathcal{F}$ polynomial gets modified by an extra term proportional to the off-shellness, $p_1^2>0$:

$$\begin{aligned} \mathcal{U}(\boldsymbol{x}) &= x_1+x_2+x_3+x_4 \\ \mathcal{F}(\boldsymbol{x},\boldsymbol{s}) &= -sx_1x_2-tx_3x_4-p_1^2x_1x_3. \end{aligned} \tag{3.3.15}$$

We resolve this integral over the Minkowskian kinematic regime given by $s,p_1^2>0$ and $-s<t<0$ (which we note includes the physical scattering kinematics). Following the algorithm, the transformation for the bisection parameter $x_i=x_1$ which resolves the negative contribution is given by

$$\begin{aligned} x_1 &\to x_1+\left(\frac{-tx_3x_4}{sx_2+p_1^2x_3}\right) \\ \mathcal{J} &= 1. \end{aligned} \tag{3.3.16}$$

Given that this transformation resolves the negative ($\mathcal{F}<0$) contribution, we must extract a minus sign from the transformed $\mathcal{F}$ to obtain a manifestly non-negative integrand resulting in

$$\begin{aligned} I^{-}_{\text{box},\mathrm{p}_1^2>0} &= \int_{\mathbb{R}^4_{\geq 0}}\prod_{i=1}^{4}\mathrm{d}x_i\;\mathcal{I}^{-}_{\text{box},p_1^2>0}\;\delta\left(1-\sum_{i=1}^{4}\alpha_i x_i\right) \\ \mathcal{I}^{-}_{\text{box},p_1^2>0} &= \frac{\left[\left(sx_2+p_1^2x_3\right)\left(x_1+x_2+x_3+x_4\right)-tx_3x_4\right]^{2\epsilon}}{x_1^{2+\epsilon}\left(sx_2+p_1^2x_3\right)^{2+3\epsilon}}. \end{aligned} \tag{3.3.17}$$

The positive contribution can naturally be resolved using the same bisection parameter with the transformation (choosing $x_j = x_N = x_4$),

$$\begin{aligned} x_1 &\to \frac{x_1}{x_1 + x_4}\left(\frac{-t x_3 x_4}{s x_2 + p_1^2 x_3}\right) \\ \mathcal{J} &= \frac{-t x_3 x_4^2}{(x_1+x_4)^2\left(s x_2 + p_1^2 x_3\right)}\,, \end{aligned} \tag{3.3.18}$$

which gives us

$$\begin{aligned} I^+_{\text{box},p_1^2>0} &= \int_{\mathbb{R}^4_{\geq 0}} \prod_{i=1}^{4} \mathrm{d}x_i \;\; \mathcal{I}^+_{\text{box},p_1^2>0}\; \delta\left(1 - \textstyle\sum_{i=1}^4 \alpha_i x_i\right) \\ \mathcal{I}^+_{\text{box},p_1^2>0} &= \frac{\left[\left(s x_2 + p_1^2 x_3\right)(x_1+x_4)(x_2+x_3+x_4) - t x_1 x_3 x_4\right]^{2\epsilon}}{x_4^{2+2\epsilon}\,(x_1+x_4)^{\epsilon}\,(-t x_3)^{1+\epsilon}\left(s x_2 + p_1^2 x_3\right)^{1+2\epsilon}}. \end{aligned} \tag{3.3.19}$$

The resulting construction mirrors (3.3.13) and we obtain

$$\begin{aligned} J_{\text{box},p_1^2>0} &= \lim_{\delta\to 0^+} \Gamma(2+\epsilon)\, I_{\text{box},p_1^2>0} \\ I_{\text{box},p_1^2>0} &= I^+_{\text{box},p_1^2>0} + (-1-i\delta)^{-2-\epsilon}\, I^-_{\text{box},p_1^2>0}. \end{aligned} \tag{3.3.20}$$

1-Loop Pentagon

A massless pentagon (see Fig. 3.1c) is minimally parameterised with five kinematic invariants, for example with the set of cyclic scalar products $(s_{12}, s_{23}, s_{34}, s_{45}, s_{51})$, where $s_{ij} = (p_i + p_j)^2$. In Feynman parameterised form the pentagon integral is

$$\begin{aligned} J_{\text{pen}} &= \lim_{\delta\to 0^+} -\Gamma(3+\epsilon)\, I_{\text{pen}} \\ I_{\text{pen}} &= \int_{\mathbb{R}^5_{\geq 0}} \prod_{i=1}^{5} \mathrm{d}x_i\, \frac{\mathcal{U}(\boldsymbol{x})^{1+2\epsilon}}{(\mathcal{F}(\boldsymbol{x},\boldsymbol{s}) - i\delta)^{3+\epsilon}} \delta\left(1 - \textstyle\sum_{i=1}^5 \alpha_i x_i\right) \end{aligned} \tag{3.3.21}$$

where the pentagon $\mathcal{U}$ and $\mathcal{F}$ polynomials are given by

$$\begin{aligned} \mathcal{U}(\boldsymbol{x}) &= x_1 + x_2 + x_3 + x_4 + x_5 \\ \mathcal{F}(\boldsymbol{x},\boldsymbol{s}) &= -s_{45} x_3 x_5 - s_{12} x_2 x_5 - s_{34} x_2 x_4 - s_{51} x_1 x_4 - s_{23} x_1 x_3. \end{aligned} \tag{3.3.22}$$

We consider the kinematic regime where $s_{12}, s_{34}, s_{51} > 0$ and $s_{23}, s_{45} < 0$. Imposing these constraints, the algorithm gives us the transformation to resolve the negative

contribution (where $\mathcal{F} < 0$) for bisection parameter $x_i = x_3$:

$$\begin{aligned} x_3 &\to \frac{x_3}{x_3 + x_5}\left(\frac{s_{51}x_1x_4 + s_{34}x_2x_4 + s_{12}x_2x_5}{-s_{23}x_1 - s_{45}x_5}\right) \\ \mathcal{J} &= \frac{x_5\left(s_{51}x_1x_4 + s_{34}x_2x_4 + s_{12}x_2x_5\right)}{\left(x_3 + x_5\right)^2\left(-s_{23}x_1 - s_{45}x_5\right)} \end{aligned} \tag{3.3.23}$$

where we remind the reader that $-s_{23}, -s_{45} > 0$ in the assumed kinematic regime and we have arbitrarily chosen $x_j = x_N = x_5$ in the transformation. This allows us to obtain, after factoring out a minus sign from the transformed $\mathcal{F}$ and simplifying the resulting integrand,

$$I^-_{\text{pen}} = \int_{\mathbb{R}^5_{\geq 0}} \prod_{i=1}^{5} \mathrm{d}x_i \;\; \mathcal{I}^-_{\text{pen}} \; \delta\left(1 - \textstyle\sum_{i=1}^{5} \alpha_i x_i\right)$$

$$\mathcal{I}^-_{\text{pen}} = \frac{\left[(x_3+x_5)(-s_{23}x_1-s_{45}x_5)(x_1+x_2+x_3+x_4+x_5)+x_3(s_{51}x_1x_4+s_{34}x_2x_4+s_{12}x_2x_5)\right]^{1+2\epsilon}}{x_5^{2+\epsilon}\left(x_3+x_5\right)^{\epsilon}\left(-s_{23}x_1-s_{45}x_5\right)^{2+2\epsilon}\left(s_{51}x_1x_4+s_{34}x_2x_4+s_{12}x_2x_5\right)^{2+\epsilon}}. \tag{3.3.24}$$

Conversely, the positive contribution can be resolved by applying the corresponding transformation of the bisection parameter,

$$\begin{aligned} x_3 &\to x_3 + \left(\frac{s_{51}x_1x_4 + s_{34}x_2x_4 + s_{12}x_2x_5}{-s_{23}x_1 - s_{45}x_5}\right) \\ \mathcal{J} &= 1, \end{aligned} \tag{3.3.25}$$

to the $\mathcal{U}$ and $\mathcal{F}$ polynomials. We find

$$I^+_{\text{pen}} = \int_{\mathbb{R}^5_{\geq 0}} \prod_{i=1}^{5} \mathrm{d}x_i \;\; \mathcal{I}^+_{\text{pen}} \; \delta\left(1 - \textstyle\sum_{i=1}^{5} \alpha_i x_i\right)$$

$$\mathcal{I}^+_{\text{pen}} = \frac{\left[\left(-s_{23}x_1 - s_{45}x_5\right)\left(x_1+x_2+x_3+x_4+x_5\right) + s_{51}x_1x_4 + s_{34}x_2x_4 + s_{12}x_2x_5\right]^{1+2\epsilon}}{x_3^{3+\epsilon}\left(-s_{23}x_1 - s_{45}x_5\right)^{4+3\epsilon}}. \tag{3.3.26}$$

Appropriately combining the positive and negative contributions yields the resolved pentagon integral

$$\begin{aligned} J_{\text{pen}} &= \lim_{\delta \to 0^+} -\Gamma\left(3+\epsilon\right) I_{\text{pen}} \\ I_{\text{pen}} &= I^+_{\text{pen}} + \left(-1 - i\delta\right)^{-3-\epsilon} I^-_{\text{pen}}. \end{aligned} \tag{3.3.27}$$

The resolution described above is valid for one particular sign combination of the

kinematics. In order to evaluate the pentagon for any kinematic point one would have to repeat the procedure above $2^5 = 32$ times. It is possible to reuse resolutions by considering symmetries of the $\mathcal{F}$ polynomial. For example by factoring out a minus sign from $\mathcal{F}$, it is easy to see that half of the sign combinations are related to the other half. Still, it is clear that without an automated implementation of the algorithm, it would be a tedious procedure to fully resolve an integral such as the pentagon, that depends on many kinematic variables. An alternative approach is to instead reduce the pentagon to box integrals with off-shell legs and resolve these instead. A box integral with an off-shell leg has $2^3 = 8$ possible sign combinations, reducing the naive number of required resolutions by a factor of 4. The downside is that the reduction of a pentagon to boxes is only valid up to a finite remainder. This approach is thus only useful if higher orders in ϵ are not needed. The pentagon can be written in terms of boxes [90] as

$$I_{\text{pen}} = -\frac{1}{2}\sum_{l,k=1}^{5} S^{-1}_{lk} I_{\text{box},l} + \mathcal{O}(\epsilon), \tag{3.3.28}$$

where S_{lk} are elements of the matrix

$$S = -\frac{1}{2}\begin{pmatrix} 0 & p_2^2 & s_{23} & s_{51} & p_1^2 \\ p_2^2 & 0 & p_3^2 & s_{34} & s_{12} \\ s_{23} & p_3^2 & 0 & p_4^2 & s_{45} \\ s_{51} & s_{34} & p_4^2 & 0 & p_5^2 \\ p_1^2 & s_{12} & s_{45} & p_5^2 & 0 \end{pmatrix}. \tag{3.3.29}$$

In (3.3.28) each box integral has on off-shell leg corresponding to the pinching of a propagator of the pentagon. While the benefit of reducing the pentagon to boxes is not extremely significant, the same idea can be applied to even higher point functions. For example a hexagon parameterised by 8 invariants has $2^8 = 256$ sign combinations to consider, and so on. Even with an automated implementation of the algorithm, at some point it could become problematic to produce and compile integration code if the number of invariants is too large. In such cases it could be useful to keep these

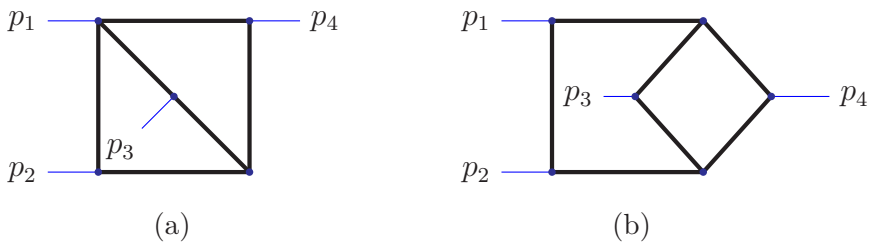

Figure 3.2: Massless non-planar 2-loop boxes with 6 (3.2a: BNP6) and 7 (3.2b: BNP7) propagators respectively.

reduction strategies in mind.

2-Loop Non-Planar 6 Propagator Box

The non planar box with six propagators (BNP6, see Fig. 3.2a) is parameterised by the Mandelstam invariants $s = (p_1 + p_2)^2$ and $t = (p_2 + p_3)^2$ (having applied the momentum conservation rule $s + t + u = 0$) and the integral is given by

$$\begin{aligned} J_{\text{BNP6}} &= \lim_{\delta \to 0^+} \Gamma\left(2 + 2\epsilon\right) I_{\text{BNP6}} \\ I_{\text{BNP6}} &= \int_{\mathbb{R}^6_{\geq 0}} \prod_{i=1}^{6} \mathrm{d}x_i \, \frac{\mathcal{U}(\boldsymbol{x})^{3\epsilon}}{\left(\mathcal{F}(\boldsymbol{x}, \boldsymbol{s}) - i\delta\right)^{2+2\epsilon}} \delta\left(1 - \sum_{i=1}^{6} \alpha_i x_i\right) \end{aligned} \tag{3.3.30}$$

where the $\mathcal{U}$ and $\mathcal{F}$ polynomials for BNP6 are

$$\begin{aligned} \mathcal{U}(\boldsymbol{x}) =& x_1x_2 + x_1x_3 + x_1x_4 + x_1x_5 + x_2x_3 + x_2x_4 + x_2x_6 + \\ & x_3x_5 + x_3x_6 + x_4x_5 + x_4x_6 + x_5x_6 \\ \mathcal{F}(\boldsymbol{x}, \boldsymbol{s}) =& - sx_2x_3x_6 - tx_1x_2x_4 + (s+t)x_1x_3x_5. \end{aligned} \tag{3.3.31}$$

We restrict to the physical kinematic regime for $2 \to 2$ scattering where $s > 0$ and $-s < t < 0$ and apply the algorithm. We find that the negative contribution can be resolved by applying the following transformation (with $x_j = x_N = x_6$) to the bisection parameter $x_i = x_1$:

$$\begin{aligned} x_1 &\to \frac{x_1}{x_1 + x_6} \left(\frac{sx_2x_3x_6}{(s+t)\, x_3x_5 - tx_2x_4} \right) \\ \mathcal{J} &= \frac{sx_2x_3x_6^2}{(x_1 + x_6)^2 \left[(s+t)\, x_3x_5 - tx_2x_4\right]} \end{aligned} \tag{3.3.32}$$

where we remind the reader that we have $s+t>0$ and $-t>0$ in our restricted kinematic regime. This allows us to construct the negative contribution

$$I^{-}_{\text{BNP6}} = \int_{\mathbb{R}^6_{\geq 0}} \prod_{i=1}^{6} \mathrm{d}x_i \;\; \mathcal{I}^{-}_{\text{BNP6}} \; \delta\left(1 - \sum_{i=1}^{6} \alpha_i x_i\right)$$

$$\begin{aligned}\mathcal{I}^{-}_{\text{BNP6}} = &\left(s x_2 x_3 x_6^2\right)^{-1-2\epsilon} (x_1+x_6)^{-\epsilon} \left[(s+t)\, x_3 x_5 - t x_2 x_4\right]^{-1-3\epsilon} \times \\ &\Big[\left[(s+t)\, x_3 x_5 - t x_2 x_4\right](x_1+x_6)\left[(x_3+x_4)(x_2+x_5) + (x_2+x_3+x_4+x_5)\, x_6\right] \\ &+ s x_1 x_2 x_3 x_6 \left(x_2+x_3+x_4+x_5\right)\Big]^{3\epsilon}.\end{aligned} \tag{3.3.33}$$

The positive contribution may be obtained with the corresponding transformation where

$$\begin{gathered} x_1 \to x_1 + \left(\frac{s x_2 x_3 x_6}{(s+t)\, x_3 x_5 - t x_2 x_4}\right) \\ \mathcal{J} = 1 \end{gathered} \tag{3.3.34}$$

giving

$$I^{+}_{\text{BNP6}} = \int_{\mathbb{R}^6_{\geq 0}} \prod_{i=1}^{6} \mathrm{d}x_i \;\; \mathcal{I}^{+}_{\text{BNP6}} \; \delta\left(1 - \sum_{i=1}^{6} \alpha_i x_i\right)$$

$$\begin{aligned}\mathcal{I}^{+}_{\text{BNP6}} = &\, x_1^{-2-2\epsilon} \left[(s+t)\, x_3 x_5 - t x_2 x_4\right]^{-2-5\epsilon} \times \\ &\Big[\left[(s+t)\, x_3 x_5 - t x_2 x_4\right]\Big[(x_3+x_4)(x_2+x_5) + \\ &(x_1+x_6)\left(x_2+x_3+x_4+x_5\right)\Big] + s x_2 x_3 x_6 \left(x_2+x_3+x_4+x_5\right)\Big]^{3\epsilon}.\end{aligned} \tag{3.3.35}$$

We may therefore reconstruct BNP6 using the decomposition formula in (3.2.1):

$$\begin{aligned} J_{\text{BNP6}} &= \lim_{\delta \to 0^+} \Gamma(2+2\epsilon)\, I_{\text{BNP6}} \\ I_{\text{BNP6}} &= I^{+}_{\text{BNP6}} + (-1-i\delta)^{-2-2\epsilon}\, I^{-}_{\text{BNP6}}. \end{aligned} \tag{3.3.36}$$

2-Loop Non-Planar 7 Propagator Box

The non planar box with seven propagators (BNP7, see Fig. 3.2b) depends on the two kinematic invariants $s=(p_1+p_2)^2$ and $t=(p_2+p_3)^2$ and the integral is given

by

$$\begin{aligned} J_{\text{BNP7}} &= \lim_{\delta\to 0^+} -\Gamma\left(3+2\epsilon\right) I_{\text{BNP7}} \\ I_{\text{BNP7}} &= \int_{\mathbb{R}^7_{\geq 0}} \prod_{i=1}^{7} \mathrm{d}x_i \, \frac{\mathcal{U}(\boldsymbol{x})^{1+3\epsilon}}{\left(\mathcal{F}(\boldsymbol{x},\boldsymbol{s})-i\delta\right)^{3+2\epsilon}} \delta\left(1-\textstyle\sum_{i=1}^{7}\alpha_i x_i\right) \end{aligned} \tag{3.3.37}$$

where the $\mathcal{U}$ and $\mathcal{F}$ polynomials for BNP7 are

$$\begin{aligned} \mathcal{U}(\boldsymbol{x}) =& x_1x_4 + x_1x_5 + x_1x_6 + x_1x_7 + x_2x_4 + x_2x_5 + x_2x_6 + x_2x_7 + \\ & x_3x_4 + x_3x_5 + x_3x_6 + x_3x_7 + x_4x_6 + x_4x_7 + x_5x_6 + x_5x_7 \\ \mathcal{F}(\boldsymbol{x},\boldsymbol{s}) =& -s(x_3x_4x_6 + x_2x_5x_7 + x_2x_3x_7 + x_2x_3x_6 + x_2x_3x_5 + x_2x_3x_4) \\ & - tx_1x_5x_6 + (s+t)x_1x_4x_7. \end{aligned} \tag{3.3.38}$$

We consider the kinematic regime where $s > 0$ and $-s < t < 0$ and find that the algorithm gives us the following transformation to resolve the negative contribution (for $x_i = x_1$ and $x_j = x_N = x_7$):

$$\begin{aligned} x_1 &\to \frac{x_1}{x_1+x_7}\left(\frac{s\left[x_3x_4x_6 + x_2x_5x_7 + x_2x_3\left(x_4+x_5+x_6+x_7\right)\right]}{\left(s+t\right)x_4x_7 - tx_5x_6}\right) \\ \mathcal{J} &= \frac{sx_7\left[x_3x_4x_6 + x_2x_5x_7 + x_2x_3\left(x_4+x_5+x_6+x_7\right)\right]}{\left(x_1+x_7\right)^2\left[\left(s+t\right)x_4x_7 - tx_5x_6\right]} \end{aligned} \tag{3.3.39}$$

with $s+t > 0$ and $-t > 0$ in the assumed regime. We may therefore generate

$$I^{-}_{\text{BNP7}} = \int_{\mathbb{R}^7_{\geq 0}} \prod_{i=1}^{7} \mathrm{d}x_i \;\; \mathcal{I}^{-}_{\text{BNP7}} \; \delta\left(1-\textstyle\sum_{i=1}^{7}\alpha_i x_i\right)$$

$$\begin{aligned} \mathcal{I}^{-}_{\text{BNP7}} =& \left(sx_7\right)^{-2-2\epsilon}\left(x_1+x_7\right)^{-\epsilon}\left[\left(s+t\right)x_4x_7 - tx_5x_6\right]^{-2-3\epsilon} \times \\ & \left[x_3x_4x_6 + x_2x_5x_7 + x_2x_3\left(x_4+x_5+x_6+x_7\right)\right]^{-2-2\epsilon} \times \\ & \Big[sx_1\left(x_4+x_5+x_6+x_7\right)\left[x_3x_4x_6 + x_2x_5x_7 + x_2x_3\left(x_4+x_5+x_6+x_7\right)\right] + \\ & \left[(s+t)x_4x_7 - tx_5x_6\right]\left(x_1+x_7\right)\left[\left(x_4+x_5\right)\left(x_6+x_7\right) + \left(x_2+x_3\right)\left(x_4+x_5+x_6+x_7\right)\right]\Big]^{1+3\epsilon}. \end{aligned} \tag{3.3.40}$$

Note that all factors in the integrand of (3.3.40) are positive in this kinematic regime within the integration domain (with zeroes only on the boundary); the algorithm constructively demands this result but it may only be manifest after simplification of the transformed integrand.

The positive contribution to BNP7 can be resolved with the same bisection parameter x_1 using the transformation

$$x_1 \to x_1 + \left(\frac{s\left[x_3 x_4 x_6 + x_2 x_5 x_7 + x_2 x_3 \left(x_4 + x_5 + x_6 + x_7\right)\right]}{\left(s+t\right) x_4 x_7 - t x_5 x_6} \right) \qquad \mathcal{J} = 1 \tag{3.3.41}$$

to obtain

$$I^{+}_{\text{BNP7}} = \int_{\mathbb{R}^7_{\geq 0}} \prod_{i=1}^{7} \mathrm{d}x_i \;\; \mathcal{I}^{+}_{\text{BNP7}} \; \delta\left(1 - \sum_{i=1}^{7} \alpha_i x_i\right)$$

$$\begin{aligned} \mathcal{I}^{+}_{\text{BNP7}} = {} & x_1^{-3-2\epsilon} \left[\left(s+t\right) x_4 x_7 - t x_5 x_6\right]^{-4-5\epsilon} \times \\ & \Big[s\left(x_4 + x_5 + x_6 + x_7\right)\left[x_3 x_4 x_6 + x_2 x_5 x_7 + x_2 x_3\left(x_4 + x_5 + x_6 + x_7\right)\right] + \\ & \left[(s+t) x_4 x_7 - t x_5 x_6\right]\Big[\left(x_4 + x_5\right) x_6 + x_3\left(x_4 + x_5 + x_6\right) + \left(x_3 + x_4 + x_5\right) x_7 + \\ & \left(x_1 + x_2\right)\left(x_4 + x_5 + x_6 + x_7\right)\Big]\Big]^{1+3\epsilon}. \end{aligned} \tag{3.3.42}$$

Combining the positive and negative contributions appropriately gives us the decomposition of BNP7:

$$\begin{aligned} J_{\text{BNP7}} &= \lim_{\delta \to 0^+} -\Gamma\left(3 + 2\epsilon\right) I_{\text{BNP7}} \\ I_{\text{BNP7}} &= I^{+}_{\text{BNP7}} + \left(-1 - i\delta\right)^{-3-2\epsilon} I^{-}_{\text{BNP7}}. \end{aligned} \tag{3.3.43}$$

3-Loop Non-Planar Box, $G_{\bullet\bullet}$

In this section, we consider a massless 3-loop example ($G_{\bullet\bullet}$ in the notation of [35]) where the standard contour deformation implementation in Feynman parameter space breaks down due to the presence of a leading Landau singularity for arbitrary kinematics. We show that, after separately resolving this Landau singularity to decompose the original integral into a sum of six others, we can then apply a combination of shifts and rescalings of the Feynman parameters along with transformations inspired by the algorithm to the two integrals of the resulting six which require a contour deformation in the physical scattering kinematic regime. The massless non-planar 3-loop box (the so-called crown graph, $G_{\bullet\bullet}$, see Fig. 3.3) depends on the

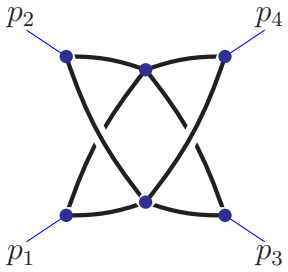

Figure 3.3: Massless non-planar 3-loop box (the crown graph, $G_{\bullet\bullet}$).

Mandelstam invariants s, t and u where we use momentum conservation to eliminate $u = -s - t$. We wish to consider the integral

$$\begin{aligned} J_{G_{\bullet\bullet}} &= \lim_{\delta \to 0^+} \Gamma\left(2 + 3\epsilon\right) I_{G_{\bullet\bullet}} \\ I_{G_{\bullet\bullet}} &= \int_{\mathbb{R}^8_{\geq 0}} \prod_{i=1}^{8} \mathrm{d}x_i \, \frac{\mathcal{U}(\boldsymbol{x})^{4\epsilon}}{\left(\mathcal{F}(\boldsymbol{x}, \boldsymbol{s}) - i\delta\right)^{2+3\epsilon}} \, \delta\left(1 - \sum_{i=1}^{8} \alpha_i x_i\right) \end{aligned} \tag{3.3.44}$$

where the $\mathcal{U}$ and $\mathcal{F}$ polynomials for the crown graph, $G_{\bullet\bullet}$, are given by

$$\begin{aligned} \mathcal{U}(\boldsymbol{x}) = &\left(x_1 + x_2\right)\left(x_3 + x_4\right)\left(x_5 + x_6\right) + \left(x_1 + x_2\right)\left(x_3 + x_4\right)\left(x_7 + x_8\right) + \\ &\left(x_1 + x_2\right)\left(x_5 + x_6\right)\left(x_7 + x_8\right) + \left(x_3 + x_4\right)\left(x_5 + x_6\right)\left(x_7 + x_8\right) \\ \mathcal{F}(\boldsymbol{x}, \boldsymbol{s}) = &- s\left(x_2 x_5 - x_1 x_6\right)\left(x_4 x_7 - x_3 x_8\right) - t\left(x_2 x_3 - x_1 x_4\right)\left(x_6 x_7 - x_5 x_8\right) \end{aligned} \tag{3.3.45}$$

and we restrict to the massless $2 \to 2$ physical scattering regime, $s > 0$ and $-s < t < 0$.

In [35], it was shown that this integral has a solution of the Landau equations within the integration domain for generic physical kinematics, preventing evaluation with the usual contour deformation procedure described in Section 3.1.3. The solution proposed by the authors of [35] was to transform the Feynman parameters such that each factor of $\mathcal{F}(\boldsymbol{x}, \boldsymbol{s})$ is linear. This can be achieved by the transformations

$$x_1 \to x_1 \frac{x_2}{x_8}, \quad x_3 \to x_3 \frac{x_4}{x_8}, \quad x_5 \to x_5 \frac{x_6}{x_8}, \quad x_7 \to x_7 \frac{x_8}{x_8} \tag{3.3.46}$$

with Jacobian $\mathcal{J} = x_2 x_4 x_6 / x_8^3$.

The resulting $\mathcal{F}$-polynomial is given by,

$$\mathcal{F}(\boldsymbol{x}, \boldsymbol{s}) = \frac{x_2 x_4 x_6}{x_8} \left[-s(x_1 - x_5)(x_3 - x_7) - t(x_1 - x_3)(x_5 - x_7)\right]. \tag{3.3.47}$$

The integral can then be dissected into $4! = 24$ regions each defined by a strict ordering of $x_i \geq x_j \geq x_k \geq x_l$ with i, j, k, l all permutations of $1, 3, 5, 7$. Each of the resulting integrals will have polynomials of definite sign multiplying each invariant s, t. Taking into account the symmetry of the integral, $I_{G_{\bullet\bullet}}$ can now be expressed as a sum over six integrals,

$$I_{G_{\bullet\bullet}} = \sum_K I_K,$$

$$I_K = \int_{\mathbb{R}^8_{\geq 0}} \prod_{i=1}^{8} \mathrm{d}x_i \, \frac{\mathcal{U}_K(\boldsymbol{x})^{4\epsilon}}{(x_2 x_4 x_6)^{1+3\epsilon} \, x_8^{1+9\epsilon} \, (\mathcal{F}_K(\boldsymbol{x}, \boldsymbol{s}) - i\delta)^{2+3\epsilon}} \delta\left(1 - \textstyle\sum_{i=1}^{8} \alpha_i x_i\right), \tag{3.3.48}$$

where K is in the set $\{A, B, C, D, E, F\}$ (denoting each of the six integrals from the Landau pole resolution) and we have factored out some monomials into the denominator. The procedure protects the homogeneity of $\mathcal{U}_K$ and $\mathcal{F}_K$ as well as retaining the positive definiteness of the former.

Strictly, not all terms in the sum of (3.3.48) require a δ-prescription; this is clear from examining the resultant $\mathcal{F}_K$ polynomials themselves[1]:

$$\begin{aligned}
\mathcal{F}_A(\boldsymbol{x}, \boldsymbol{s}) &= -\left[s x_3 (x_1 + x_3 + x_5) + (s + t) x_1 x_5\right] \\
\mathcal{F}_B(\boldsymbol{x}, \boldsymbol{s}) &= -\left[(s + t) x_1 x_3 + t x_5 (x_1 + x_3 + x_5)\right] \\
\mathcal{F}_C(\boldsymbol{x}, \boldsymbol{s}) &= -\left[s x_1 (x_1 + x_3 + x_5) - t x_3 x_5\right] \\
\mathcal{F}_D(\boldsymbol{x}, \boldsymbol{s}) &= +\left[(s + t) x_5 (x_1 + x_3 + x_5) + t x_1 x_3\right] \\
\mathcal{F}_E(\boldsymbol{x}, \boldsymbol{s}) &= +\left[s x_3 x_5 - t x_1 (x_1 + x_3 + x_5)\right] \\
\mathcal{F}_F(\boldsymbol{x}, \boldsymbol{s}) &= +\left[s x_1 x_5 + (s + t) x_3 (x_1 + x_3 + x_5)\right].
\end{aligned} \tag{3.3.49}$$

We remind the reader that, in the assumed kinematic regime, we have $s + t > 0$ and $-t > 0$; using this, we can immediately make a number of remarks. Firstly, it is clear that integrals E and F will have manifestly positive integrands (as the $\mathcal{F}_K$ polynomials are the only parts of (3.3.48) that affect whether the individual integrals are Euclidean or not), hence, they do not require a δ-prescription. Secondly, integrals

[1] Note that we have used the symmetry to reduce from 24 integrals to the choice of 6 where all the $\mathcal{F}_K$ depend only on $\{x_1, x_3, x_5\}$ and not x_7.

A and C can be trivially brought into Euclidean form by factoring out $(-1-i\delta)^{-2-3\epsilon}$ from the integrals, similarly to (3.2.2), since $\mathcal{F}_A$ and $\mathcal{F}_C$ are manifestly negative within the domain of integration for the assumed kinematic regime. Finally, we remark that integrals B and D would naively require a contour deformation due to zeroes of the $\mathcal{F}_K$ polynomials within the domain of integration (strictly away from the boundary); this can be traced to the appearance of $+t < 0$ appearing inside the brackets of $\mathcal{F}_B$ and $\mathcal{F}_D$ in (3.3.49). We note that, had we assumed a different kinematic regime, a different subset of the six integrals would be automatically Euclidean but we stress that there is no regime where none of the six naively require a contour deformation.

We therefore focus on integrals B and D and resolve them such that we do not need an explicit contour deformation. In this exposition, instead of straightforwardly applying the algorithm, we present a different resolution procedure to bring the integrals into the required form. We note that each integral may be resolved both with the default application of the univariate bisection algorithm (at the expense of introducing square roots) as well as with an iterated generalisation of the algorithm (the detail of which we leave for further work). Here, we demonstrate an alternative approach based upon shifts and rescalings of the Feynman parameters, focussing on the $\mathcal{F}$ polynomial, which works in this case (and can also be shown to work for many of the other examples presented in this section) but, as of yet, has not been formulated algorithmically. We note that, whenever we shift a variable such that $x_a \to x_a + x_b$, we must consider the converse case $x_b \to x_a + x_b$ to cover the entire original domain. This is justified since we essentially repeatedly insert

$$\theta\left(x_a - x_b\right) + \theta\left(x_b - x_a\right) = 1 \tag{3.3.50}$$

under the integral sign, where the equality above holds. This type of transformation, along with the positive rescaling of a Feynman parameter, is reminiscent of the transformations appearing in sector decomposition; indeed, they are heavily inspired by this procedure. We emphasise, however, that we are still mapping zeroes of the

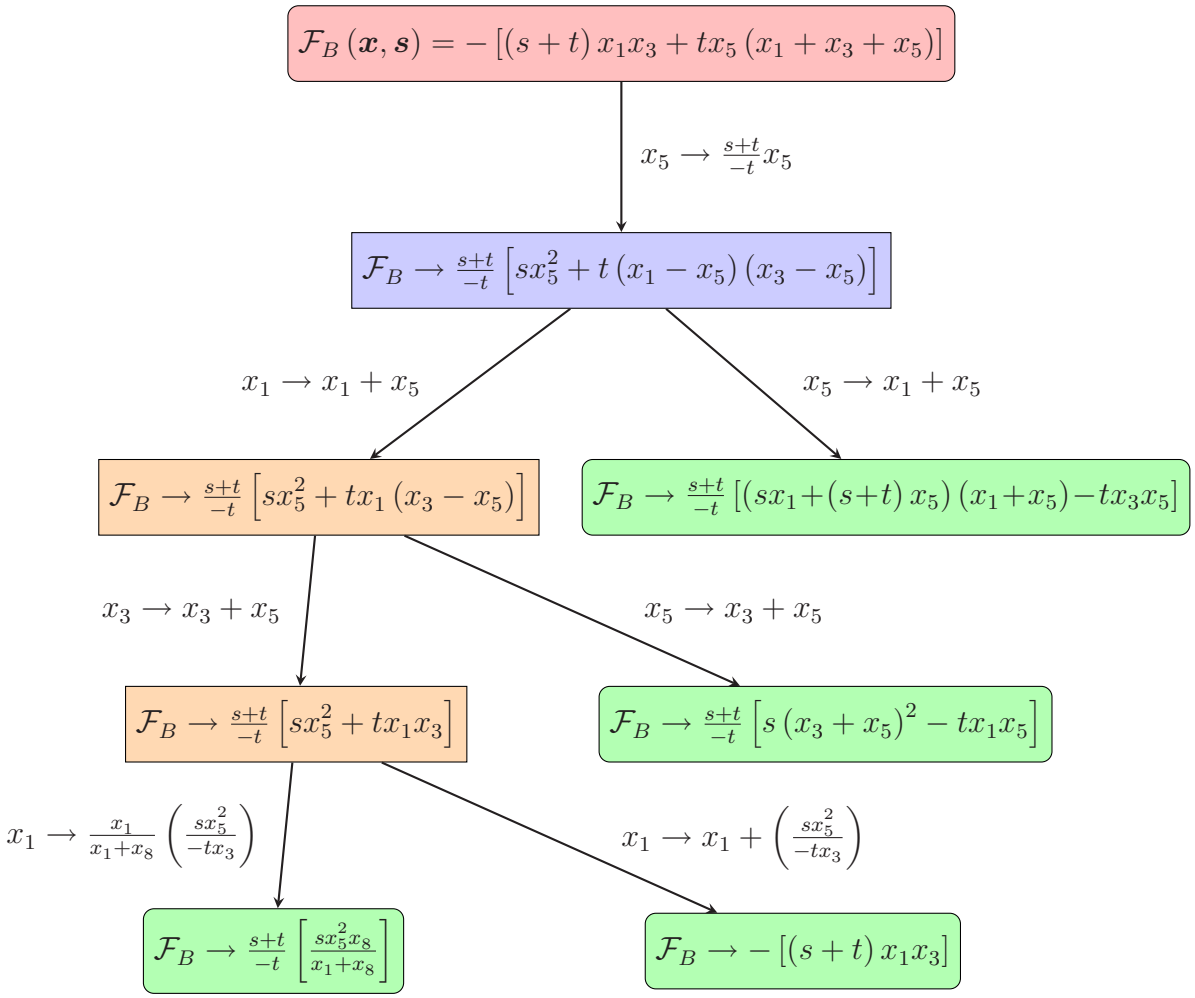

Figure 3.4: A flowchart showing the transformations for an example resolution of integral B in the shifts and rescalings approach; the transformations in the final line are inspired by the algorithmic approach. The initial integral (red) is mapped to four integrals (green) in this resolution, in three of which the transformed $\mathcal{F}_B$ is manifestly positive and in one of which it is manifestly negative. We remind the reader that $s+t>0$ and $-t>0$ in the assumed kinematic regime.

$\mathcal{F}_K$ polynomials from within the domain of integration to the boundary where they can then be dealt with using sector decomposition.

In Fig. 3.4, we show an example of how this approach might be applied to resolve integral B. The integral is mapped to four different integrals (three positive contributions and one negative contribution) such that

$$I_B = \sum_{n_+=1}^{3} I_B^{+,n_+} + (-1 - i\delta)^{-2-3\epsilon} I_B^-. \tag{3.3.51}$$

We note that this approach often generates more integrals than strictly necessary (that is to say, only one positive and only one negative contribution for I_B, for example); however, the transformations at each step are superficially simpler and the resulting integrands are often less involved. In this sense, difficult integrals may be amenable to this less conservative approach if other methods fail.

Integral D may be similarly resolved into three positive contributions and one negative contribution such that our initial integral, $I_{G_{\bullet\bullet}}$, can be expressed as a causally prescribed sum over twelve integrals with manifestly positive integrands:

$$I_{G_{\bullet\bullet}} = \left[\sum_{n_+=1}^{3} I_B^{+,n_+} + \sum_{n_+=1}^{3} I_D^{+,n_+} + I_E^+ + I_F^+ \right] + (-1 - i\delta)^{-2-3\epsilon} \left[I_A^- + I_B^- + I_C^- + I_D^- \right]. \tag{3.3.52}$$

where the positive contributions I_E^+ and I_F^+ are simply I_E and I_F and the negative contributions I_A^- and I_C^- are merely I_A and I_C with $(-1 - i\delta)^{-2-3\epsilon}$ factored out accordingly.

For brevity, we will only state the negative contribution, I_B^-, from the contour-avoided integral, I_B, explicitly:

$$I_B^- = \frac{1}{(s+t)^{1+3\epsilon}(-t)^{1+8\epsilon}} \int_{\mathbb{R}^8_{\geq 0}} \prod_{i=1}^{8} \mathrm{d}x_i \; \mathcal{I}_B^- \; \delta\left(1 - \sum_{i=1}^{8} \alpha_i x_i\right)$$

$$\begin{aligned}
\mathcal{I}_B^- = {} & x_1^{-2-3\epsilon} x_3^{-2-7\epsilon} x_8^{-1-9\epsilon} (x_2 x_4 x_6)^{-1-3\epsilon} \times \\
& \Big[-t x_3 x_4 x_6 x_8 (x_7 + x_8)(x_3 + x_5 + x_7 + x_8)[s x_5 - t(x_3 + x_7 + x_8)] + \\
& x_2 x_6 x_8 (x_7+x_8)[s x_5 (x_3+x_5) - t x_3 (x_1+x_3+x_5+x_7+x_8)][s x_5 - t(x_3+x_7+x_8)] + \\
& x_2 x_4 x_6 (x_3+x_5+x_7+x_8)[s x_5 (x_3+x_5) - t x_3 (x_1+x_3+x_5+x_7+x_8)][s x_5 - t(x_3+x_7+x_8)] \\
& - t x_2 x_4 x_8 (x_7+x_8)(x_3+x_5+x_7+x_8)[s x_5 (x_3+x_5) - t x_3 (x_1+x_3+x_5+x_7+x_8)] \Big]^{4\epsilon}.
\end{aligned} \tag{3.3.53}$$

3.3.2 Massive Examples

In this section, we present 1-, 2- and 3-loop examples of integrals with massive propagators. Understanding how to resolve such integrals would be extremely relevant in applying the method to the calculation of massive phenomenologically-relevant amplitudes, particularly in the case of electroweak corrections, see Chapter 4 for example, where a large number of mass scales may be present in the problem. The primary complication in the massive case is that the $\mathcal{F}$ polynomial gets modified by a term proportional to $\mathcal{U}$ such that each Feynman parameter associated with a massive propagator may appear quadratically in the monomials of $\mathcal{F}$:

$$\mathcal{F} = \mathcal{F}_0 + \mathcal{U} \sum_{j=1}^{N} m_j^2 x_j \tag{3.3.54}$$

where $\mathcal{F}_0$ is the corresponding polynomial of the massless version of the same integral. We analyse the 1-loop massive bubble and triangle initially before applying the method to 2-loop elliptic and 3-loop hyperelliptic examples.

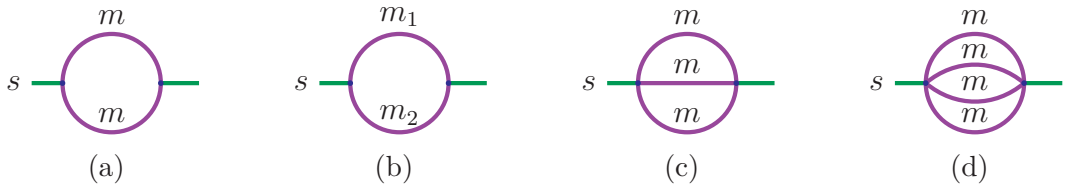

Figure 3.5: The L-loop banana-type integrals resolved in this section ($L \in \{1, 2, 3\}$): the equal mass (3.5a) and unequal mass (3.5b) bubble integrals, the equal mass elliptic sunrise integral (3.5c), and the 3-loop equal mass banana integral (3.5d).

Equal Mass Bubble

To introduce how the method applies to massive integrals, we begin by considering the bubble integral in Fig. 3.5a with internal propagators of equal mass, m:

$$J_{\text{bub}} = \lim_{\delta \to 0^+} \Gamma(\epsilon)\, I_{\text{bub}}$$
$$I_{\text{bub}} = \int_{\mathbb{R}^2_{\geq 0}} \mathrm{d}x_1 \mathrm{d}x_2 \frac{(x_1 + x_2)^{-2+2\epsilon}}{\left(-s x_1 x_2 + (x_1 + x_2)\left(m^2 x_1 + m^2 x_2\right) - i\delta\right)^{\epsilon}} \delta\left(1 - \sum_{i=1}^{2} \alpha_i x_i\right). \tag{3.3.55}$$

We can integrate out x_2 by making the symmetric choice (i.e. $x_1 + x_2$) of hyperplane $\alpha(\boldsymbol{x}) = \sum_{i=1}^{N} \alpha_i x_i$ to obtain

$$I_{\text{bub}} = \int_0^1 \mathrm{d}x_1 \frac{1}{\left(-s x_1 (1 - x_1) + m^2 - i\delta\right)^{\epsilon}}. \tag{3.3.56}$$

The denominator of the integrand in (3.3.56) can develop a zero within the domain of integration above the threshold for the on-shell production of the intermediate pair of massive particles. We wish to consider the integral within this Minkowskian kinematic regime and so we parameterise the above-threshold region with the parameter

$$\beta^2 = \frac{s - 4m^2}{s} \in (0, 1) \tag{3.3.57}$$

and eliminate $s > 0$ for $\beta \in (0, 1)$ to give

$$I_{\text{bub}} = \left(\frac{1 - \beta^2}{m^2}\right)^{\epsilon} \int_0^1 \mathrm{d}x_1 \frac{1}{\left((1 - 2x_1)^2 - \beta^2 - i\delta\right)^{\epsilon}}. \tag{3.3.58}$$

We may exploit the symmetry of the integrand about the point $x_1 = \frac{1}{2}$ (as can be seen in the invariance of the integrand under $x_1 \to 1 - x_1$) to rewrite the integral as

$$I_{\text{bub}} = \left(\frac{1-\beta^2}{m^2}\right)^{\epsilon} \int_0^1 \mathrm{d}x_1 \frac{1}{\Big((1-x_1)^2 - \beta^2 - i\delta\Big)^{\epsilon}} \tag{3.3.59}$$

as this will allow us to resolve the integral into one purely positive contribution (as opposed to two without using the symmetry) and one purely negative contribution. We then split this integral at the point at which the denominator vanishes, $x_1 = 1-\beta$, within the integration domain and remap the resulting domains to the original positive unit interval. That is to say,

$$\begin{aligned}
I_{\text{bub}} &= \left(\frac{1-\beta^2}{m^2}\right)^{\epsilon} \left[\int_0^{1-\beta} \mathrm{d}x_1 \frac{1}{\Big((1-x_1)^2 - \beta^2 - i\delta\Big)^{\epsilon}} + \int_{1-\beta}^1 \mathrm{d}x_1 \frac{1}{\Big((1-x_1)^2 - \beta^2 - i\delta\Big)^{\epsilon}}\right] \\
&= \left(\frac{1-\beta^2}{m^2}\right)^{\epsilon} \left[\int_0^1 \mathrm{d}x_1 \frac{1-\beta}{\Big((1-(1-\beta)\,x_1)^2 - \beta^2\Big)^{\epsilon}} + \int_0^1 \mathrm{d}x_1 \frac{\beta}{\Big(-x_1\,(2-x_1)\,\beta^2 - i\delta\Big)^{\epsilon}}\right] \\
&= \left(\frac{1-\beta^2}{m^2}\right)^{\epsilon} \left[\int_0^1 \mathrm{d}x_1 \frac{1-\beta}{\Big((1-(1-\beta)\,x_1)^2 - \beta^2\Big)^{\epsilon}} + \right. \\
&\qquad\qquad \left. (-1-i\delta)^{-\epsilon} \int_0^1 \mathrm{d}x_1 \frac{\beta}{\Big(x_1\,(2-x_1)\,\beta^2\Big)^{\epsilon}}\right] \\
&= I^{+}_{\text{bub}} + (-1-i\delta)^{-\epsilon}\, I^{-}_{\text{bub}}
\end{aligned} \tag{3.3.60}$$

where the integrands of I^{+}_{bub} and I^{-}_{bub} are manifestly positive inside the domain of integration (and so the prescribed $i\delta$ prescription is dropped within integrals once they no longer require it). These integrals can be easily evaluated analytically and it is interesting to note that, although the entire original integral has the functional form of an incomplete Beta function, the negative contribution is functionally simpler and evaluates to a (normal) Beta function multiplied by a simple prefactor.

Unequal Mass Bubble

To illustrate the applicability of various methods to avoid contour deformation, we present a different way of resolving the massive bubble in the case of unequal masses, m_1 and m_2, depicted in Fig. 3.5b. In this case, we focus solely on the $\mathcal{F}$ polynomial

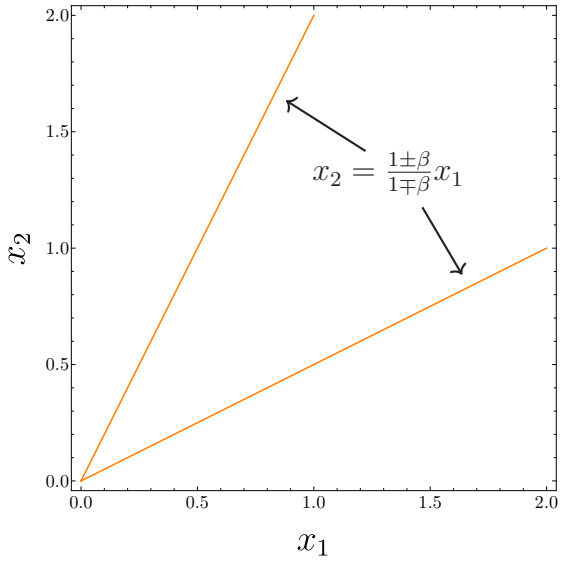

Figure 3.6: The variety of $\widetilde{\mathcal{F}}$ and the three regions of the integration domain which it separates. In the upper left and lower right regions, $\widetilde{\mathcal{F}} > 0$ whereas in the upper right region, $\widetilde{\mathcal{F}} < 0$.

which is given by

$$\mathcal{F} = -sx_1x_2 + (x_1 + x_2)\left(m_1^2x_1 + m_2^2x_2\right). \tag{3.3.61}$$

Analogously to the equal mass bubble, we define

$$\beta^2 = \frac{s - (m_1 + m_2)^2}{s - (m_1 - m_2)^2} \in (0, 1) \tag{3.3.62}$$

which reduces to (3.3.57) in the limit that $m_2 \to m_1 = m$. In the next step, we rescale the Feynman parameters x_1 and x_2 with the transformations $x_i \to x_i/m_i$ such that we can perform the resolution procedure on the dimensionless polynomial

$$\widetilde{\mathcal{F}} = x_1^2 + x_2^2 - 2\frac{1+\beta^2}{1-\beta^2}x_1x_2. \tag{3.3.63}$$

In Fig. 3.6, we plot the variety of $\widetilde{\mathcal{F}}$ (that is to say, the set of points where $\widetilde{\mathcal{F}} = 0$) and find that it separates the integration domain into three regions defined by the sign of $\widetilde{\mathcal{F}}$ – in the upper left and lower right portions of Fig. 3.6, $\widetilde{\mathcal{F}} > 0$, while in the upper right part of the domain, $\widetilde{\mathcal{F}} < 0$.

We need to construct transformations of the Feynman parameters such that we can

convert the unequal mass bubble integral into three integrals each of which is over one of the regions in Fig. 3.6. In order to do this, we first need to solve the variety $\widetilde{\mathcal{F}} = 0$ for one of the Feynman parameters. Trivially, we find that

$$x_2 = \frac{1 \pm \beta}{1 \mp \beta} x_1 \tag{3.3.64}$$

defines the variety $\widetilde{\mathcal{F}} = 0$ in such a form. Once we have this form, the construction of the transformations becomes trivial. For example, we wish to map the upper right region of Fig. 3.6 to the original integration domain which sets the demand that the line $x_2 = \frac{1+\beta}{1-\beta} x_1$ becomes the new axis $x_1' = 0$ and the line $x_2 = \frac{1-\beta}{1+\beta} x_1$ becomes the new axis $x_2' = 0$. These demands, along with the constraint that we want to map a subset of the original integration domain to the full original integration domain (and not to map points from outside the domain) to fix the signs, allow us to write down the transformations immediately:

$$\begin{gathered} x_1' \stackrel{!}{=} -\left(x_2 - \frac{1+\beta}{1-\beta} x_1\right), \quad x_2' \stackrel{!}{=} +\left(x_2 - \frac{1-\beta}{1+\beta} x_1\right) \\ \Downarrow \\ x_1 \to \frac{\left(1-\beta^2\right)(x_1+x_2)}{4\beta}, \quad x_2 \to \frac{(1-\beta)^2 x_1 + (1+\beta)^2 x_2}{4\beta}. \end{gathered} \tag{3.3.65}$$

By construction, this maps the variety of $\widetilde{\mathcal{F}}$ to the boundary of integration and this can be seen explicitly in the effect of the transformations:

$$\widetilde{\mathcal{F}} \to -x_1 x_2 \tag{3.3.66}$$

which is strictly negative within the domain of integration and zero only on the boundary. Naturally, we must also apply the corresponding transformations to the $\mathcal{U}$ polynomial as well as keeping track of the Jacobian determinant. If we carry out the same procedure for the remaining two regions, we find that we can recast our

original integral

$$J_{\text{bub},m_1\neq m_2} = \lim_{\delta\to 0^+} \Gamma(\epsilon)\, I_{\text{bub},m_1\neq m_2}$$
$$I_{\text{bub},m_1\neq m_2} = \int_{\mathbb{R}^2_{\geq 0}} \mathrm{d}x_1\mathrm{d}x_2 \frac{(x_1+x_2)^{-2+2\epsilon}}{\left(-sx_1x_2+(x_1+x_2)\left(m_1^2x_1+m_2^2x_2\right)-i\delta\right)^{\epsilon}} \delta\left(1-\sum_{i=1}^2 \alpha_i x_i\right) \tag{3.3.67}$$

in the regime $s > (m_1+m_2)^2 \Leftrightarrow \beta^2 \in (0,1)$ into a causally-prescribed sum over three integrals with manifestly non-negative integrands:

$$I_{\text{bub},m_1\neq m_2} = I^{+,1}_{\text{bub},m_1\neq m_2} + I^{+,2}_{\text{bub},m_1\neq m_2} + (-1-i\delta)^{-\epsilon} I^{-}_{\text{bub},m_1\neq m_2} \tag{3.3.68}$$

where the constituent integrals are given by

$$I^{+,1}_{\text{bub},m_1\neq m_2} = \frac{1}{m_1m_2}\int_{\mathbb{R}^2_{\geq 0}} \mathrm{d}x_1\mathrm{d}x_2 \left(x_2\left(x_2+\frac{4\beta x_1}{1-\beta^2}\right)\right)^{-\epsilon} \times \left(\frac{x_1}{m_1}+\frac{x_2}{m_2}+\frac{(1+\beta)\,x_1}{(1-\beta)\,m_2}\right)^{-2+2\epsilon} \delta\left(1-\sum_{i=1}^2 \alpha_i x_i\right) \tag{3.3.69}$$

$$I^{+,2}_{\text{bub},m_1\neq m_2} = \frac{1+\beta}{m_1m_2(1-\beta)}\int_{\mathbb{R}^2_{\geq 0}} \mathrm{d}x_1\mathrm{d}x_2 \left(\frac{x_1\left(4\beta x_2+(1+\beta)^2 x_1\right)}{(1-\beta)^2}\right)^{-\epsilon} \times \left(\frac{x_2}{m_2}+\frac{(1+\beta)(x_1+x_2)}{(1-\beta)\,m_1}\right)^{-2+2\epsilon} \delta\left(1-\sum_{i=1}^2 \alpha_i x_i\right) \tag{3.3.70}$$

$$I^{-}_{\text{bub},m_1\neq m_2} = \frac{1-\beta^2}{4m_1m_2\beta}\int_{\mathbb{R}^2_{\geq 0}} \mathrm{d}x_1\mathrm{d}x_2 (x_1x_2)^{-\epsilon} \times \left(\frac{\left(1-\beta^2\right)(x_1+x_2)}{4m_1\beta}+\frac{(1-\beta)^2 x_1+(1+\beta)^2 x_2}{4m_2\beta}\right)^{-2+2\epsilon} \delta\left(1-\sum_{i=1}^2 \alpha_i x_i\right). \tag{3.3.71}$$

Again, these integrals can be analytically evaluated (for example, in `Mathematica`) and we find that they replicate the known result for the unequal mass bubble by checking the coefficients order-by-order in the expansion in ϵ. We note that expanding deeper in ϵ in the contour-avoided form is computationally more efficient than expanding the original integral which may prove useful for multi-loop calculations where the one-loop result may need orders beyond ϵ^0.

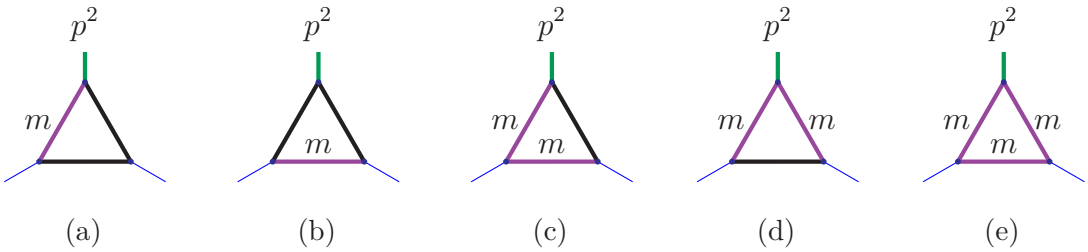

(a) (b) (c) (d) (e)

Figure 3.7: Independent equal mass triangles with an off-shell leg ($p^2 > 0$).

1-Loop Triangle with an Off-Shell Leg

For our final 1-loop massive example, we consider the massive triangle with an off-shell leg (the independent equal-mass configurations of which are shown in Fig. 3.7). Here, we present the resolution of the fully massive triangle (Fig. 3.7e) in detail. We pick this mass configuration for our exposition as it is the most difficult and the analysis of the other examples is carried out almost identically. The integral we wish to consider is

$$J_{\text{tri}} = \lim_{\delta \to 0^+} -\Gamma\left(1+\epsilon\right) I_{\text{tri}}$$
$$I_{\text{tri}} = \int_{\mathbb{R}^3_{\geq 0}} \mathrm{d}x_1 \mathrm{d}x_2 \mathrm{d}x_3 \frac{\left(x_1+x_2+x_3\right)^{-1+2\epsilon}}{\left(-p^2 x_1 x_2 + m^2\left(x_1+x_2+x_3\right)^2 - i\delta\right)^{1+\epsilon}} \delta\left(1 - \sum_{i=1}^3 \alpha_i x_i\right). \tag{3.3.72}$$

It is possible to make multiple choices to parameterise the projective integral and we note that, for example, making different choices of hyperplane $\alpha(\boldsymbol{x}) = \sum_i \alpha_i x_i$ can lead to different solutions of the problem. In our experience, being guided by the symmetry of the problem, where possible, leads to the neatest solutions but one may choose e.g. $\delta\left(1-x_1\right)$ and successfully avoid contour deformation (although not necessarily easily avoiding square roots involving the Feynman parameters). Following this philosophy, we make the symmetric choice – here, $\delta\left(1-x_1-x_2-x_3\right)$ – which is often the optimal choice at 1-loop as it sends the $\mathcal{U}$ polynomial immediately to 1. Defining $\beta^2 = \frac{p^2-4m^2}{p^2} \in (0,1)$ and integrating out the δ-function over x_3, we have

$$I_{\text{tri}} = \left(\frac{1-\beta^2}{m^2}\right)^{1+\epsilon} \int_{\mathbb{R}^2_{\geq 0}} \mathrm{d}x_1 \mathrm{d}x_2\, \theta\left(1-x_1-x_2\right) \left(1-\beta^2-4x_1x_2-i\delta\right)^{-1-\epsilon} \tag{3.3.73}$$

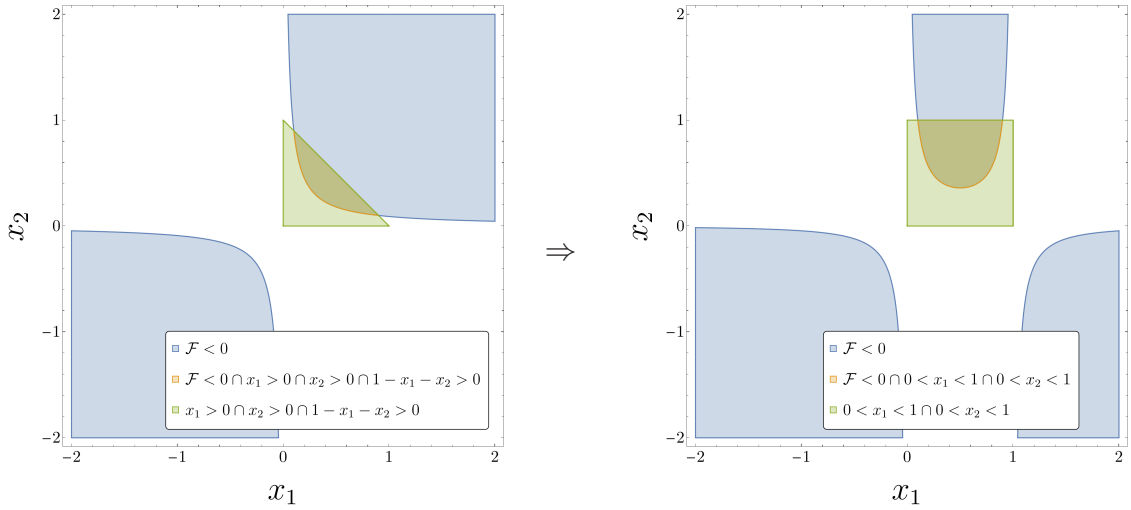

Figure 3.8: Remapping the simplex integration region of the massive triangle (in green) to the positive unit square in $\mathbb{R}^2_{\geq 0}$. Here, $\mathcal{F}$ is to be understood as $\mathcal{F}$ after the δ-function has been integrated out and in the second panel, after the remapping transformation as well.

where the Heaviside function is a result of the symmetric choice of hyperplane and restricts the remaining domain of integration to a simplex. With the foresight that we will wish to integrate this numerically with a standard package like `pySecDec`, we apply a coordinate transformation that remaps this domain to the positive unit square in $\mathbb{R}^2_{\geq 0}$ as in Fig. 3.8. After this mapping, $x_2 \to (1 - x_1)\, x_2$, we have

$$I_{\text{tri}} = \left(\frac{1-\beta^2}{m^2}\right)^{1+\epsilon} \int_0^1 \mathrm{d}x_1 \mathrm{d}x_2\, (1-x_1) \left(1 - \beta^2 - 4\,(1-x_1)\, x_1 x_2 - i\delta\right)^{-1-\epsilon}. \quad (3.3.74)$$

Visualising the variety of the transformed $\mathcal{F}$ allows us to separate the integration domain into a number of regions, the choice (and number) of which is guided by what is practically simpler to deal with. We show this choice of four regions in Fig. 3.9 where we have separated the integration domain (the positive unit square in $\mathbb{R}^2_{\geq 0}$) into three positive regions where $\mathcal{F} > 0$ and one negative one where $\mathcal{F} < 0$ (which will generate the entire imaginary part of the full integral). We will show the chain of transformations which maps the negative region (blue in Fig. 3.9) to the positive unit square and state the result for the remaining positive regions. Firstly, we need to map the orange and red positive regions in Fig. 3.9 outside the square. To do this, we find the x_1-values where the variety of $\mathcal{F}$ intersects with the boundary of

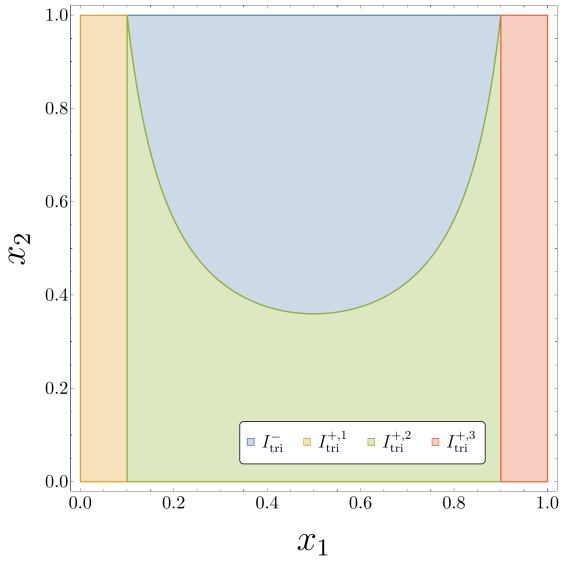

Figure 3.9: The integration domain of the massive triangle separated into one negative and three positive regions.

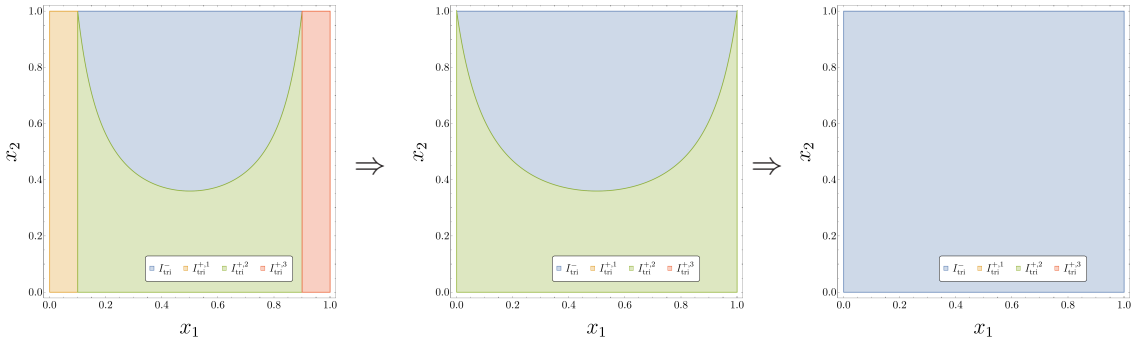

Figure 3.10: The chain of transformations which maps the negative region of the massive triangle (in blue) to the positive unit square.

the domain at $x_2 = 1$. A trivial calculation reveals these values to be $\frac{1\pm\beta}{2}$ and we want to map the x_1-lines defined by these values to the boundaries of integration $x_1 = 0$ and $x_1 = 1$. We can easily construct a transformation which satisfies these demands:

$$x_1' \stackrel{!}{=} \frac{x_1 - \frac{1-\beta}{2}}{\frac{1+\beta}{2} - \frac{1-\beta}{2}} \quad \Rightarrow \quad x_1 \to \frac{1}{2} + \beta\left(x_1 - \frac{1}{2}\right) \tag{3.3.75}$$

and we show the effect of this transformation in the transition from the first to the second panel of Fig. 3.10 with $\mathcal{F} \to 1 - \beta^2 - (1 - (1 - 2x_1)^2\beta^2)\, x_2$. The geometric visualisation helps us to deduce the next logical step which is to map the variety of this transformed $\mathcal{F}$ to the boundary at $x_2 = 0$ while keeping the boundary at $x_2 = 1$

fixed (so as not to map in any points from outside the integration domain). In order to do this, we must first solve $\mathcal{F} = 0$ as $x_2 = f(x_1)$. Trivially, we find:

$$\mathcal{F} = 0 \quad \Rightarrow \quad x_2 = \frac{1-\beta^2}{1-(1-2x_1)^2\beta^2} = f(x_1)\,. \tag{3.3.76}$$

In this form, we can directly construct the transformation which satisfies the demands above:

$$x_1' \stackrel{!}{=} x_1, \quad x_2' \stackrel{!}{=} \frac{x_2 - f(x_1)}{1-f(x_1)} \quad \Rightarrow \quad x_1 \to x_1, \quad x_2 \to x_2 + (1-x_2)\,f(x_1)\,. \tag{3.3.77}$$

This transformation generates the transition between the second and third panels in Fig 3.10 and completes the mapping of the negative region to the positive unit square as required. The final result for the negative contribution after taking into account the Jacobian determinants of the transformations is

$$I_{\text{tri}}^{-} = 2^{-1-2\epsilon}\left(\frac{1-\beta^2}{m^2}\right)^{1+\epsilon}\beta^{1-2\epsilon}\int_0^1 \mathrm{d}x_1\mathrm{d}x_2\,(1-x_1)^{-\epsilon}\,x_1^{-\epsilon}x_2^{-1-\epsilon}\,(1-(1-2x_1)\,\beta)^{-1} \tag{3.3.78}$$

where we have already factored out $(-1-i\delta)^{-1-\epsilon}$. We note that this integral is $\mathcal{O}\left(\frac{1}{\epsilon}\right)$ whereas the full integral I_{tri} is finite. This pole cancels exactly with a corresponding pole in $I_{\text{tri}}^{+,2}$ and, since $I_{\text{tri}}^{+,1}$ and $I_{\text{tri}}^{+,3}$ are free of poles in ϵ, the construction consistently reproduces the full result.

It is illuminating to consider the general structure of this cancellation; if the full result is finite and also has an imaginary part at the leading order (which is true of I_{tri}), the negative contribution must necessarily have a pole in ϵ to generate the imaginary part from multiplying the ϵ^1 term in the expansion of $(-1-i\delta)^{a+b\epsilon}$. Furthermore, the total positive contribution must have an equal pole in ϵ to cancel the pole of the negative contribution leaving a finite result. This type of analysis can be fruitful in predicting a priori the pole structure of the constituent integrals in the decomposition.

For completeness, we state the result for the positive contributions:

$$I_{\text{tri}}^{+,1} = \frac{1}{4}\left(\frac{1-\beta^2}{m^2}\right)^{1+\epsilon}(1-\beta)^{-\epsilon}\int_0^1 \mathrm{d}x_1\mathrm{d}x_2\,(2-(1-\beta)\,x_1)(1+\beta-(2-(1-\beta)\,x_1)\,x_1x_2)^{-1-\epsilon} \tag{3.3.79}$$

$$I_{\text{tri}}^{+,2} = \frac{\beta}{2}\left(\frac{1-\beta^2}{m^2}\right)^{1+\epsilon}\left(1-\beta^2\right)^{-\epsilon}\int_0^1 \mathrm{d}x_1\mathrm{d}x_2\,(1-x_2)^{-1-\epsilon}\,(1-(1-2x_1)\,\beta)^{-1} \tag{3.3.80}$$

$$I_{\text{tri}}^{+,3} = \frac{1}{4}\left(\frac{1-\beta^2}{m^2}\right)^{1+\epsilon}(1-\beta)^{1-\epsilon}\int_0^1 \mathrm{d}x_1\mathrm{d}x_2\,(1-x_1)\,(1+\beta-x_2(1-x_1)(1+\beta+(1-\beta)x_1))^{-1-\epsilon}\,. \tag{3.3.81}$$

This gives the total result

$$I_{\text{tri}} = \sum_{n_+=1}^{3} I_{\text{tri}}^{+,n_+} + (-1-i\delta)^{-1-\epsilon}\,I_{\text{tri}}^{-} \tag{3.3.82}$$

where we stress again that each integrand in the constituent integrals of (3.3.82) is manifestly non-negative in the Minkowskian kinematic region defined by $\beta \in (0,1)$ throughout the entire integration domain. Additionally, all singularities have been mapped to the endpoints where they can be dealt with using standard techniques such as sector decomposition instead of applying a contour deformation prescription as would usually be required in a numerical calculation.

2-Loop Elliptic Sunrise

In this section, we analyse the equal mass sunrise integral – the simplest integral which involves a function class beyond polylogarithms. The sunrise has been studied extensively and it is known to evaluate to elliptic integrals. It is for this reason that we choose to apply the method to the sunrise in order to show that there is no fundamental obstruction to avoiding contour deformation for massive integrals beyond the polylogarithmic class. We find, however, that the sunrise leads us naturally to algebraic transformations of the Feynman parameters instead of purely rational function transformations. To the best of our current knowledge, it seems not to be possible to find a resolution which avoids square roots in the transformations

(we contrast this with initial attempts involving square roots to resolve the massive 1-loop triangles in Fig. 3.7 which were able to be improved upon) but this does not present a problem for our purposes of numerical evaluation.

The analysis of the 2-loop massive sunrise follows similarly to the 1-loop massive triangle detailed in Section 3.3.2 (as they are both cases of integrals with three equal-mass propagators); as a result of this, we focus mainly on the differences to that case in this exposition. The integral we wish to resolve without contour deformation is

$$J_{\text{sun}} = \lim_{\delta \to 0^+} -\Gamma\left(-1+2\epsilon\right) I_{\text{sun}}$$
$$I_{\text{sun}} = \int_{\mathbb{R}^3_{\geq 0}} \mathrm{d}x_1 \mathrm{d}x_2 \mathrm{d}x_3 \frac{\left(x_1x_2+x_2x_3+x_1x_3\right)^{-3+3\epsilon} \delta\left(1-\sum_{i=1}^3 \alpha_i x_i\right)}{\left(-s x_1x_2x_3 + \left(x_1x_2+x_2x_3+x_1x_3\right) m^2 \left(x_1+x_2+x_3\right) - i\delta\right)^{-1+2\epsilon}} \tag{3.3.83}$$

and is depicted in Fig. 3.5c. A plot of the sunrise's $\mathcal{F} = 0$ surface in $\mathbb{R}^3_{>0}$ (which should be rigorously understood in the context of the projective integral, parameterised with the δ-function, for example) is given in Fig. 3.11. It is the shape of this surface that will end up determining the resolution of the integral and we see that its distorted conic-esque geometry divides the integration into an inside and outside; this appears to be intrinsically linked to our inability to use purely rational functions for the resolution transformations. As we will see after a choice of hyperplane in the δ-function, this will force the use of square roots and guide us towards algebraic transformations.

Motivated once again by the symmetry of the problem, we choose $\delta\left(1-x_1-x_2-x_3\right)$ and integrate out x_3 after having parameterised the Minkowskian kinematic regime we are interested in with $\beta^2 = \frac{s-9m^2}{s} \in (0,1)$. We remap the resulting simplex integration domain to the positive unit square (as shown in the transition between the first and second panels of Fig. 3.12) in the same way as for the massive triangle in Section 3.3.2. These manipulations give us

$$I_{\text{sun}} = \left(\frac{1-\beta^2}{m^2}\right)^{-1+2\epsilon} \int_0^1 \mathrm{d}x_1 \mathrm{d}x_2 \frac{\left(1-x_1\right)^{-1+\epsilon} \left(x_1 + \left(1-x_1\right)\left(1-x_2\right)x_2\right)^{-3+3\epsilon}}{\left(\left(1-\beta^2-9x_1\right)\left(1-x_1\right)\left(1-x_2\right)x_2 + \left(1-\beta^2\right)x_1 - i\delta\right)^{-1+2\epsilon}} \tag{3.3.84}$$

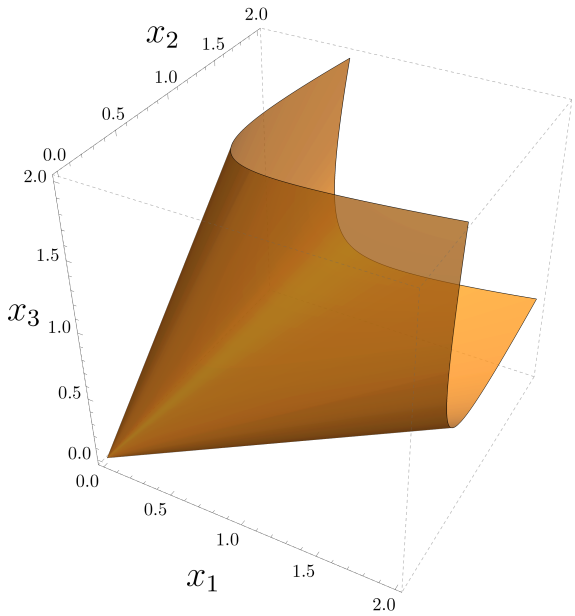

Figure 3.11: The $\mathcal{F} = 0$ surface of the equal mass sunrise in $\mathbb{R}^3_{>0}$ with the caveat that this should properly be understood projectively.

where, by direct inspection of (3.3.84), the integrand can be seen to enjoy a symmetry under $x_2 \to 1 - x_2$ (analogously to the equal-mass bubble in Section 3.3.2). This allows us to integrate x_2 from 0 to $\frac{1}{2}$ instead and then double the result. We remap this halved integration domain back to the positive unit square (as shown in the transition between the second and third panels of Fig. 3.12) and benefit from exploiting this symmetry which reduces the number of regions we will need to resolve. Of course, were this symmetry not present, we would still be able to resolve the integral with more regions. Noting that the Jacobian factor of $\frac{1}{2}$ in this second transformation cancels the doubling from the symmetry, we have

$$I_{\text{sun}} = 4^{2-\epsilon}\left(\frac{1-\beta^2}{m^2}\right)^{-1+2\epsilon} \times \int_0^1 \mathrm{d}x_1 \mathrm{d}x_2 \frac{(1-x_1)^{-1+\epsilon}\left(4x_1 + (1-x_1)(2-x_2)x_2\right)^{-3+3\epsilon}}{\left(\left(1-\beta^2-9x_1\right)(1-x_1)(2-x_2)x_2 + 4\left(1-\beta^2\right)x_1 - i\delta\right)^{-1+2\epsilon}}. \tag{3.3.85}$$

We can define a set of three positive regions where the denominator of (3.3.85),

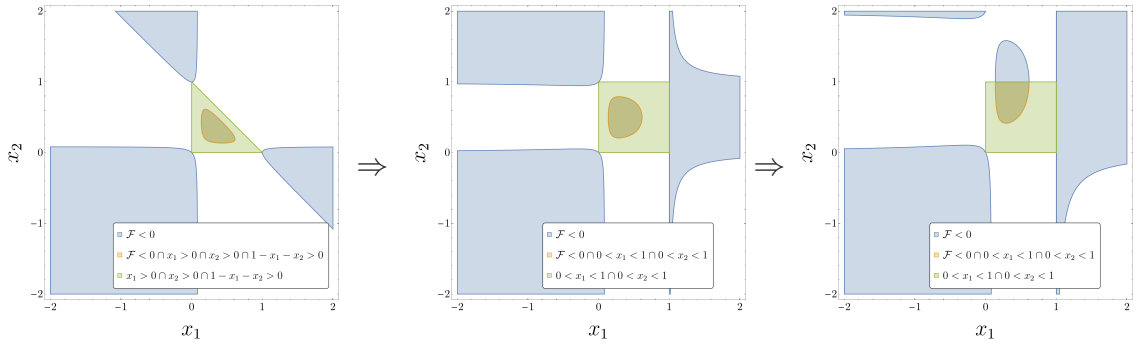

Figure 3.12: Remapping the simplex integration region of the elliptic sunrise (in green) to the positive unit square in $\mathbb{R}^2_{\geq 0}$ then exploiting the symmetry about $x_2 = \frac{1}{2}$. Here, $\mathcal{F}$ is to be understood as $\mathcal{F}$ after the δ-function has been integrated out and in the second and third panels, after their respective remapping transformations as well.

which we will loosely refer to as $\mathcal{F}$ (even though we have factored out $1 - x_1$), is positive (i.e. $\mathcal{F} > 0$) and one where it is negative (i.e. $\mathcal{F} < 0$) which we show in Fig. 3.13. We will resolve the negative region in detail once more as it plays the special role in solely generating the imaginary part of the full integral.

In order to resolve the negative region, we first must map the sides of the variety $\mathcal{F} = 0$ to the boundary. Using the intersection of the variety with the boundary at $x_2 = 1$ to find the associated x_1-values as in the case of the massive triangle in Section 3.3.2, we find the relevant transformation to be

$$\begin{aligned} x_1' &\stackrel{!}{=} \frac{x_1 - \frac{1}{6}\left(2 + \beta^2 - \beta\sqrt{8 + \beta^2}\right)}{\frac{1}{6}\left(2 + \beta^2 + \beta\sqrt{8 + \beta^2}\right) - \frac{1}{6}\left(2 + \beta^2 - \beta\sqrt{8 + \beta^2}\right)} \\ &\Downarrow \\ x_1 &\to \frac{1}{6}\left(2 + \beta^2 - (1 - 2x_1)\,\beta\sqrt{8 + \beta^2}\right). \end{aligned} \tag{3.3.86}$$

The effect of this transformation is shown in the transition from the first to the second panel in Fig. 3.14. It is clear from this geometric picture what the next (and final) step of the resolution should be: mapping the variety to $x_2 = 0$ keeping the boundary at $x_2 = 1$ fixed. The main distinction between this case and the massive triangle in Section 3.3.2 enters here; we want to solve the variety as $x_2 = f(x_1)$ but

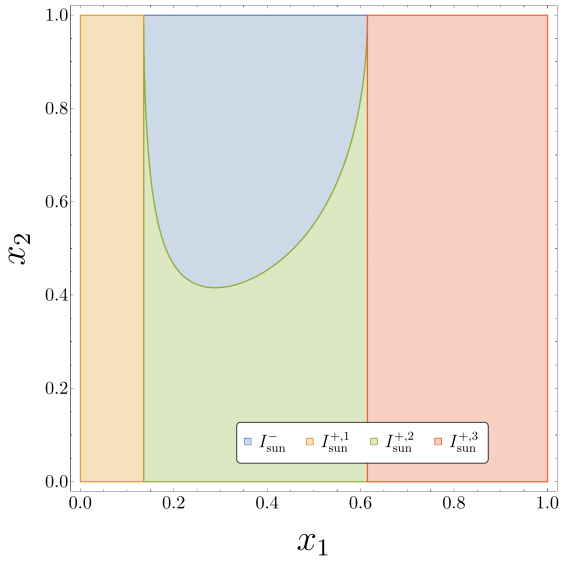

Figure 3.13: The integration domain of the elliptic sunrise separated into one negative and three positive regions.

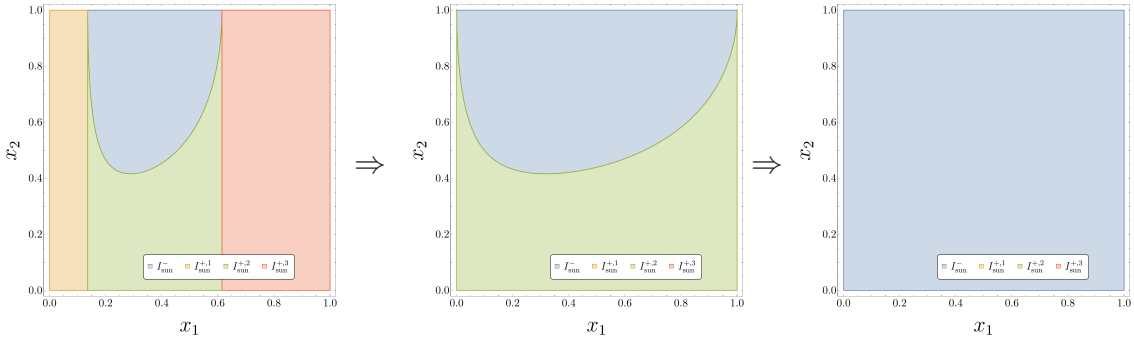

Figure 3.14: The chain of transformations which maps the negative region of the elliptic sunrise (in blue) to the positive unit square.

this gives us a function involving a square root containing x_1 instead of a purely rational function. Nevertheless, we still apply a transformation of the type in (3.3.77) to our transformed $\mathcal{F}$.

Applying the same set of transformations to the $\mathcal{U}$ polynomial and accounting for the corresponding Jacobian determinants, we obtain for our final result for the negative contribution,

$$I^{-}_{\text{sun}} = 2^{7-6\epsilon} 3^{\frac{1}{2}-\epsilon} \left(\beta^2\right)^{2-2\epsilon} \left(8+\beta^2\right)^{2-2\epsilon} \left(\frac{1-\beta^2}{m^2}\right)^{-1+2\epsilon} \times \int_0^1 \mathrm{d}x_1 \mathrm{d}x_2 \, (1-x_1)^{\frac{3}{2}-2\epsilon} x_1^{\frac{3}{2}-2\epsilon} x_2^{1-2\epsilon} R^{-}_{\text{sun}}(x_1, x_2; \beta) \,, \tag{3.3.87}$$

where the finite remainder function is given by,

$$
\begin{aligned}
&R^{-}_{\text{sun}}\left(x_1,x_2;\beta\right) = R_1(x_2;\beta)R_2(x_1;\beta)R_3(x_1;\beta)R_4(x_1,\beta)R_5(x_1,x_2;\beta),\\
&R_1(x_2;\beta) = \bar{x}_2^{1-2\epsilon},\\
&R_2(x_1;\beta) = \left[-\beta^2+\beta\bar{\beta}\tilde{x}_1+4\right]^{3\epsilon-2},\\
&R_3(x_1;\beta) = \left[4-\beta\left(2\beta\left(\beta^2+1\right)-3\beta\bar{\beta}^2x_1\bar{x}_1+2\tilde{\beta}\bar{\beta}\tilde{x}_1\right)\right]^{\frac{3}{2}-\epsilon},\\
&R_4(x_1;\beta) = \left[\beta^2\bar{\beta}^2x_1\bar{x}_1\left(-11\beta^2+3\beta\bar{\beta}\tilde{x}_1+20\right)+4\tilde{\beta}^2\left(\beta^2-\beta\bar{\beta}\tilde{x}_1+4\right)\right]^{1-2\epsilon},\\
&R_5(x_1,x_2;\beta) = \Big[\beta^2\bar{\beta}^2x_1\bar{x}_1\left(x_2\bar{x}_2\left(-\beta^2+\beta\bar{\beta}\tilde{x}_1+4\right)+4\beta\left(3\beta-\bar{\beta}\tilde{x}_1\right)\right)\\
&+4\tilde{\beta}\left(\beta^4+7\beta^2-\left(\beta^2+3\right)\beta\bar{\beta}\tilde{x}_1+4\right)\Big]^{3\epsilon-3},
\end{aligned}
\tag{3.3.88}
$$

with $\bar{x}_1 = 1-x_1,\ \tilde{x}_1 = 1-2x_1,\ \bar{x}_2 = 2-x_2$ and $\bar{\beta} = \sqrt{8+\beta^2},\ \tilde{\beta} = 1-\beta^2$. Each of the factors in the integrand of (3.3.87) can be shown to be positive for $0<x_1<1$, $0<x_2<1$ and $0<\beta<1$, thereby removing the need for a contour deformation.

We can perform similar resolutions for the positive regions to obtain the overall construction:

$$
I_{\text{sun}} = \sum_{n_+=1}^{3} I^{+,n_+}_{\text{sun}} + \left(-1-i\delta\right)^{1-2\epsilon} I^{-}_{\text{sun}}. \tag{3.3.89}
$$

The increase in efficiency of instead integrating the non-negative integrands of the constituent integrals in (3.3.89) with `pySecDec` (as opposed to the standard contour-deformed setup) can be seen in Section 3.4.

3-Loop Hyperelliptic Banana

In this section, we investigate the 3-loop equal mass banana integral. One may associate a geometry to the L-loop massive banana defined by the variety of the $\mathcal{F}$ polynomial in the complex projective space, $\mathbb{CP}^L$; for $L \geq 2$, the corresponding geometry is that of a Calabi-Yau $(L-1)$-fold (see, for example, [91]). In the previous section, we demonstrated that the method works on the sunrise integral (in this language, a 2-loop massive banana) which is associated to an elliptic curve (i.e. a Calabi-Yau 1-fold) at the expense of seemingly inescapably introducing square roots

involving the Feynman parameters. In this section, we show that an integral associated to the more complex geometric structure of a K3 surface (i.e. a Calabi-Yau 2-fold) provides no obstruction to this method of avoiding contour deformation. We make no further comment on the underlying geometry associated to these integrals except to say that this motivates studying these particular examples by proving that these geometric properties are not inherently prohibitive to this procedure. We also acknowledge that it is known that additional non-trivial geometric structure appears for this family of integrals with $L \geq 4$ but resolving fully-massive integrals with more than four propagators is beyond the scope of this thesis.

The 3-loop equal mass banana integral (shown in Fig. 3.5d) is given by

$$\begin{aligned} J_{\text{ban}} &= \lim_{\delta \to 0^+} \Gamma\left(-2+3\epsilon\right) I_{\text{ban}} \\ I_{\text{ban}} &= \int_{\mathbb{R}^4_{\geq 0}} \prod_{i=1}^{4} \mathrm{d}x_i \frac{\left(x_1x_2x_3 + x_1x_3x_4 + x_2x_3x_4 + x_1x_2x_4\right)^{-4+4\epsilon}}{\left(\mathcal{F}\left(\boldsymbol{x},\boldsymbol{s}\right) - i\delta\right)^{2-3\epsilon}} \delta\left(1 - \textstyle\sum_{i=1}^{4} \alpha_i x_i\right) \end{aligned} \tag{3.3.90}$$

where the $\mathcal{F}$ polynomial is

$$\mathcal{F}\left(\boldsymbol{x},\boldsymbol{s}\right) = -sx_1x_2x_3x_4 + \left(x_1x_2x_3 + x_1x_3x_4 + x_2x_3x_4 + x_1x_2x_4\right) m^2 \left(x_1+x_2+x_3+x_4\right). \tag{3.3.91}$$

Having presented the geometric resolution procedure a number of times already, we detail this example more schematically. We begin by integrating out x_4 using the δ-function with the symmetric choice of hyperplane (i.e. $x_1 + x_2 + x_3 + x_4$) and we parameterise the Minkowskian kinematic regime with $\beta^2 = \frac{s-16m^2}{s} \in (0,1)$. Analagously to the elliptic sunrise example, we remap the resulting simplex integration domain to the positive unit hypercube (in this case, the positive unit cube in $\mathbb{R}^3$). The symmetry of the resulting integrand under $x_3 \to 1 - x_3$ allows us once again to reduce the number of integrals into which we will eventually decompose I_{ban} by integrating instead from $x_3 = 0$ up to $x_3 = \frac{1}{2}$, remapping this back to the unit positive cube and doubling the result (however, we remark once more that this is not strictly necessary and one could perform the entire resolution without exploiting

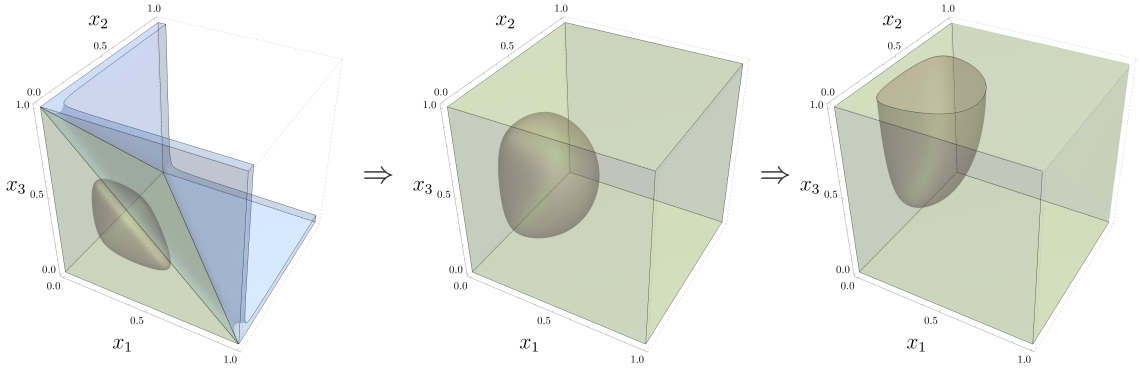

Figure 3.15: Remapping the simplex integration region of the banana (in green) to the positive unit cube in $\mathbb{R}^3_{\geq 0}$ then exploiting the symmetry about $x_3 = \frac{1}{2}$. We omit the legend for clarity but this figure should be understood analagously to Fig. 3.12 with the $\mathcal{F} < 0$ region given in blue outside the domain of integration and in dark orange within. Here, $\mathcal{F}$ is to be understood as $\mathcal{F}$ after the δ-function has been integrated out and in the second and third panels, after their respective remapping transformations as well.

this). This sequence of domain-remapping transformations is depicted in Fig. 3.15 (where this time we focus solely on the positive unit cube) and should be compared and contrasted with the corresponding set of transformations for the elliptic sunrise in Fig. 3.12.

Once the domain has been successfully remapped to the unit positive cube, it may be (somewhat arbitrarily) dissected into regions where the transformed $\mathcal{F}$ polynomial is positive and negative. The art of partitioning the integration domain in general, as we currently understand it, revolves around the balance between minimising the number of integrals in the decomposition (minimally one negative region and one positive region) and producing regions which can all be successfully mapped back to the positive unit hypercube. We show, in Fig. 3.16, an example partitioning of the positive unit cube in $\mathbb{R}^3$ for the resolution of the banana which generates five positive contributions and one negative contribution.

We will focus on the set of transformations which maps the negative region to the original integration domain as shown in Fig 3.17. First, we look at the intersection of the variety of the transformed $\mathcal{F}$ polynomial with the plane $x_3 = 1$ and analyse

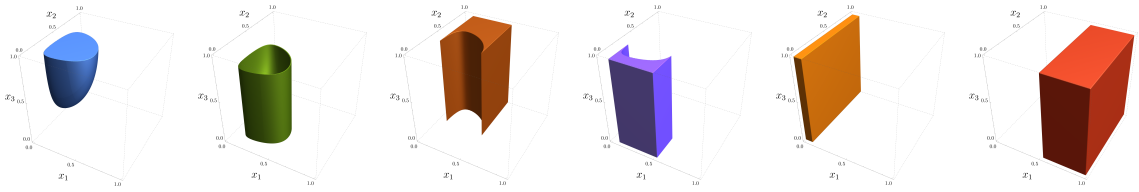

(a) I^{-}_{ban} (b) $I^{+,1}_{\text{ban}}$ (c) $I^{+,2}_{\text{ban}}$ (d) $I^{+,3}_{\text{ban}}$ (e) $I^{+,4}_{\text{ban}}$ (f) $I^{+,5}_{\text{ban}}$

Figure 3.16: The six regions (one negative, 3.16a, and five positive, 3.16b – 3.16f) into which the integration domain of the banana is partitioned in this resolution.

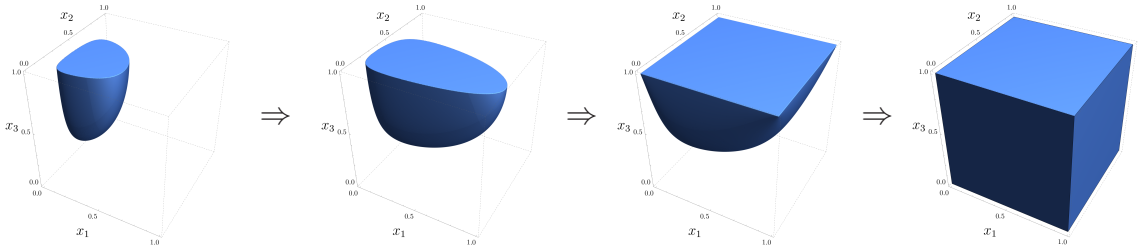

Figure 3.17: The chain of transformations which maps the negative region of the banana (in blue) to the positive unit cube.

the resulting closed curve. It is clear from focussing on the plane $x_3 = 1$ in the first panel of Fig. 3.17 that this curve has four turning points (by which we mean the four points on the curve of maximal and minimal x_1 and x_2 respectively). In the resolution of the negative region shown in Fig. 3.17, we arbitrarily choose to first identify the points of maximal and minimal x_1 on the curve using standard turning point analysis and then map the planes $x_1 = x_1^{\text{min}}$ and $x_1 = x_1^{\text{max}}$ to $x_1 = 0$ and $x_1 = 1$ respectively. This transformation is shown in the transition between the first and second panels of Fig. 3.17. We note that, on the curve, both x_1^{min} and x_1^{max} have a corresponding x_2-value of $x_2 = \frac{1}{3}$ (independent of β) and taking a slice through the integration domain at this value of x_2 (combining all regions in Fig. 3.16) generates a plot which is, superficially, very similar to Fig. 3.12. The next step is to solve the transformed curve at $x_3 = 1$ as $x_2 = f(x_1)$. Clearly, from the second panel of Fig. 3.17, this will have two solutions (the curve is quadratic in x_2) and a square root involving the Feynman parameters – specifically, x_1 – enters at this point. The map which takes $x_2 = f_1(x_1)$ to the plane $x_2 = 1$ and $x_2 = f_2(x_1)$ to the plane $x_2 = 0$ is trivial to construct once f_1 and f_2 are known and we demonstrate the effect of this

transformation in the transition between the second and third panels of Fig. 3.17. Finally, we have to solve the variety of the transformed $\mathcal{F}$ as $x_3 = g(x_1, x_2)$ (which also has two solutions due to the quadratic appearance of x_3 but only one solution which is relevant within the integration domain) and map this to the plane $x_3 = 0$ while keeping $x_3 = 1$ fixed. This transformation is shown in the transition between the third and fourth panels of Fig. 3.17 and concludes the mapping of the original negative region to the positive unit cube.

A similar analysis is carried out for the remaining five positive regions in Fig. 3.16, resulting in[1]

$$I_{\text{ban}} = \sum_{n_+=1}^{5} I_{\text{ban}}^{+,n_+} + (-1 - i\delta)^{1-2\epsilon} I_{\text{ban}}^{-} \tag{3.3.92}$$

where all of the integrands appearing in (3.3.92) are manifestly positive within the domain of integration (and away from the boundary).

3.4 Numerical Benchmarks

The procedure described in the preceding sections produces manifestly positive integrands out of Feynman integrals and, more generally, parameter integrals in mixed-sign regimes. This greatly reduces the complexity of numerically evaluating the remaining integrals and is likely to be beneficial for a variety of parameter space based approaches to evaluating Feynman integrals. For finite integrals, we can numerically integrate the resulting integrands either directly or using `FeynTrop`, for example. For divergent integrals, we still need to factorise any overlapping singularities and perform a suitable subtraction to obtain finite integrals, as described in Section 2.4, for which we can employ sector decomposition as implemented in tools such as `FIESTA` or `pySecDec`.

In this work, we use the public `pySecDec` program to benchmark the integration

[1] We note that, for our numerical evaluation in `pySecDec`, we perform a manual sector decomposition of one of the positive contributions into two constituent integrals but this is implementation-dependent and orthogonal to the resolution procedure for avoiding contour deformation

time of the resolved integrals and compare to the timings we get when using contour deformation. Note that `pySecDec` is not optimised for this new approach and could be greatly improved. For example, parsing large prefactor expressions sometimes dominates evaluation time, due to the usage of inefficient `SymPy` routines. These expressions appear as a result of the resolution procedure, particularly in the massive examples, and have therefore not been a problem in `pySecDec` before. Expanding and loading such expressions in `Mathematica` is practically instant, and we expect the expression parsing in `pySecDec` to be improved in the future. For this reason we subtract the loading time of the prefactors from the results and let the comparisons be strictly on the integration time. This is mainly relevant for the 1-loop massive triangle, where the prefactors were particularly slow to load, relative to the integration time.

Unless otherwise specified, the integration was done with the `Disteval` integrator, run on an NVidia A100 80G GPU. The exceptions are the 2-loop sunrise and 3-loop banana integrals, where an older integrator was used in order to access the feature of user-defined `C++` functions. The resolved versions of these examples contain large positive remainder functions raised to high integer powers that by default get expanded into very large expressions by `FORM` routines within `pySecDec`. This makes it hard to even generate and compile the integration libraries and calls for a better handling of large positive functions in `pySecDec`. This is again something that has only appeared as a result of the resolution procedure and has not been a bottleneck before. Eventually, `pySecDec` should offer the possibility for the user to prevent certain functions from being expanded. For now, this problem can be circumvented by manually defining the remainder expressions as symbolic functions, and provide them directly as `C++` functions. The option of doing this does not yet exist in the `Disteval` interface, but will be included in a release in the near future. These two integration libraries were compiled with `gcc` 7.5.0 and run on one core of an AMD EPYC 7352 CPU.

3.4.1 Timings

In this section, we provide benchmarks of the integration time with the new resolution procedure compared to using contour deformation as implemented in `pySecDec`. Figs. 3.18, 3.19, 3.20, 3.21 and 3.22 show timings for the massless examples described in Section 3.3.1.

For the 1-loop off-shell box it is necessary to go to extreme kinematic configurations before we see noticeable improvement in avoiding contour deformation. However, already for the 1-loop pentagon, there are order of magnitude improvements for all phase space points we test, at a high enough precision.

For the 2-loop and 3-loop non-planar boxes the improvements are even larger which is expected as the computational complexity of the contour deformation grows with the number of propagators.

For certain phase space points in these examples, we do not manage to obtain any digits with contour deformation. The situation is the most extreme for BNP7 where the integration with contour deformation fails to converge at each phase space point we tried.

Fig. 3.23 shows timings for the 1-loop massive triangle described in Section 3.3.2. The triangle can be evaluated to high precision in short time, both with and without contour deformation. The initial lattice size of the QMC integrator is enough to reach about 10 digits of precision and the example is essentially too simple to see any gain from removing contour deformation.

In fact, evaluation of the lattice points is not the bottleneck of this integral which is why we look strictly at the integration time for the benchmarks and ignore the time it takes to load the prefactors. Despite these measures, we still see that the resolved version of the integral evaluates slower than using contour deformation. The reason is that our resolved integrands have singularities at both the upper and the lower integration boundary.

To handle this, `pySecDec` splits the integrals and remaps all singularities to the lower boundary which results in more sectors and thereby increased evaluation time. For the positive contributions, $J_{\text{tri}}^{+,1}$, $J_{\text{tri}}^{+,2}$ and $J_{\text{tri}}^{+,3}$, the singularities are only present at one of the boundaries and the splitting could either be turned off or avoided by applying simple transformations of the type $x \to 1 - x$ before passing them to `pySecDec`.

This reduced the number of sectors significantly and brought the integration time of the resolved integral close to the time of integrating with contour deformation. For the negative contribution, J_{tri}^{-}, singularities are present at both boundaries and splitting the integral is therefore necessary.

The small remaining time difference can mostly be attributed to the extra sector this split generates. Usually, dealing with a few extra sectors due to the resolution procedure is not a major issue, since the resolved integrands typically scale much better. The problem with the triangle is that it is too easy to integrate in either case and we are purely limited by the time it takes to evaluate the initial number of lattice points.

In the other massive examples we also require integral splitting but then the contour deformed integrals are eventually unable to reach higher precision and we are able to access more digits with the resolved integrands.

In Figs. 3.24 and 3.25, we show the timings for the elliptic sunrise and hyperelliptic banana integrals. A black dot indicates a point after which the evaluation time diverged and the integration was terminated after > 10 hours.

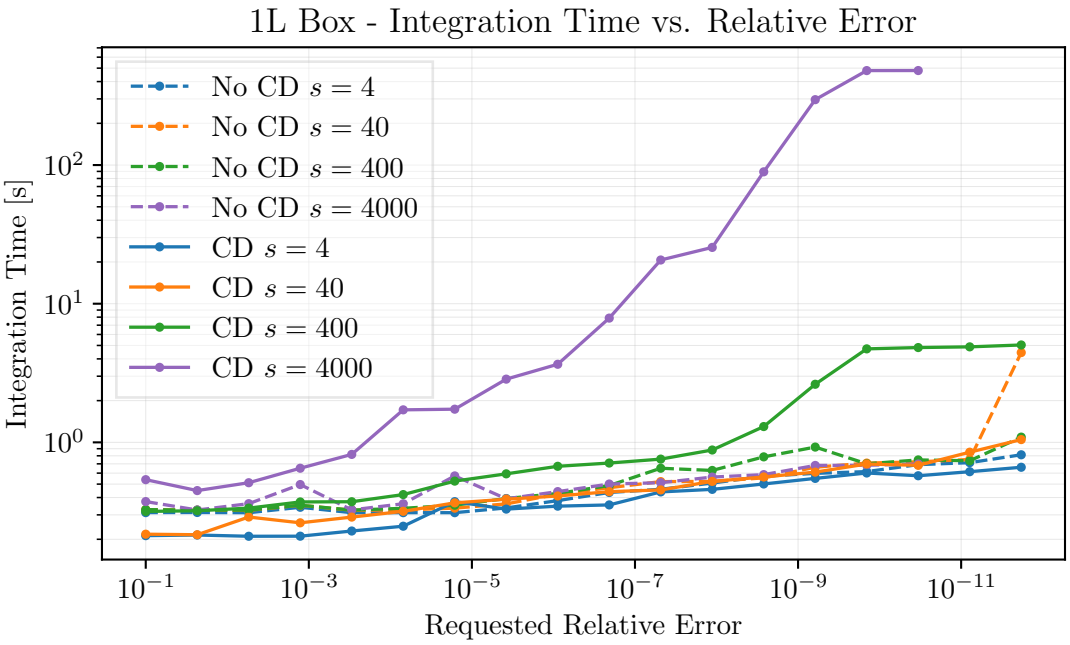

Figure 3.18: Timings with and without contour deformation for the massless 1-loop box with an off-shell leg, expanded up to the finite order. Evaluated for different values of s with $t = -1$ and $p_1^2 = 2$ fixed.

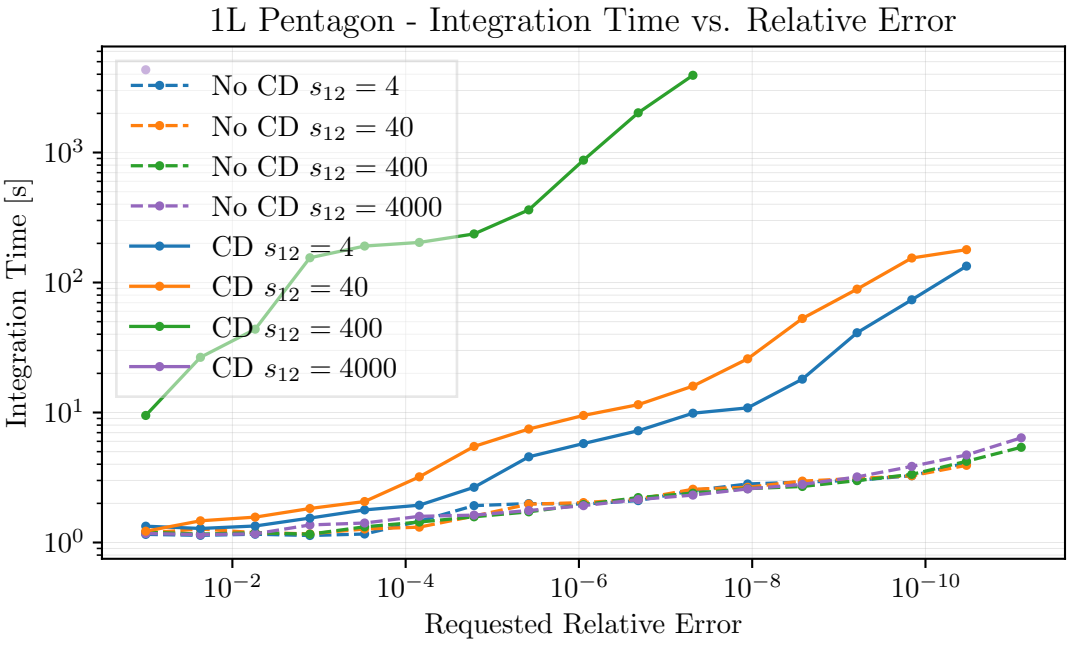

Figure 3.19: Timings with and without contour deformation for the massless 1-loop pentagon, expanded up to the finite order. Evaluated for different values of s_{12} while the other kinematics are fixed at $(s_{23}, s_{34}, s_{45}, s_{51}) = (-3, 2.5, -3, 5)$.

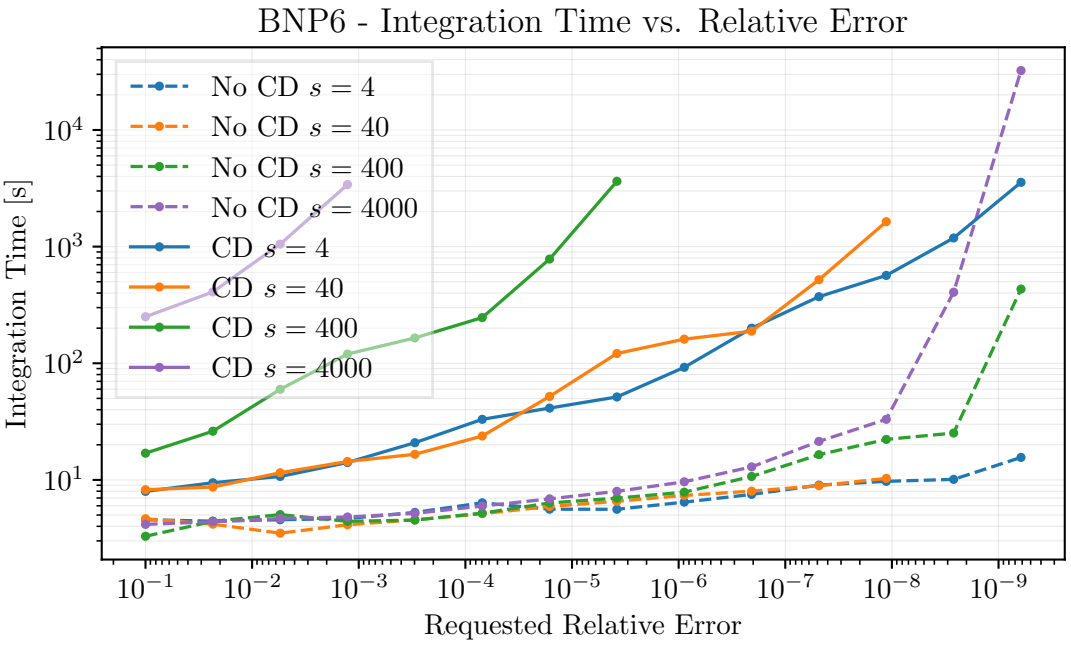

Figure 3.20: Timings with and without contour deformation for the 2-loop non-planar box with 6 propagators, expanded up to the finite order. Evaluated for different values of s with $t = -1$ fixed.

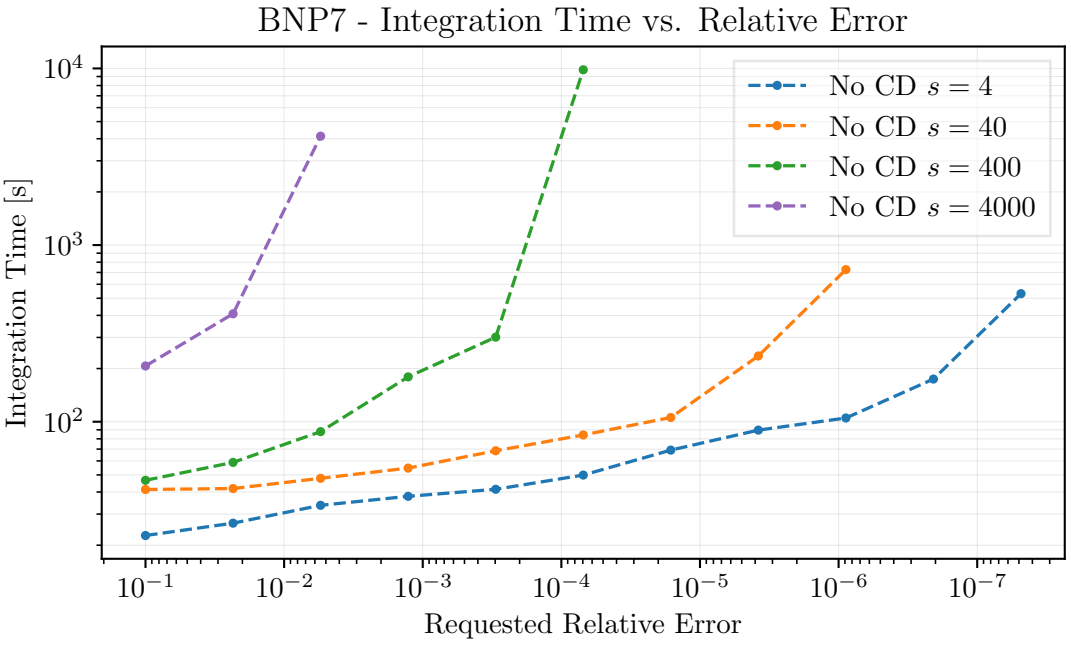

Figure 3.21: Timings with and without contour deformation for the 2-loop non-planar box with 7 propagators, expanded up to the finite order. Evaluated for different values of s with $t = -1$ fixed. In this example no digits could be obtained with contour deformation.

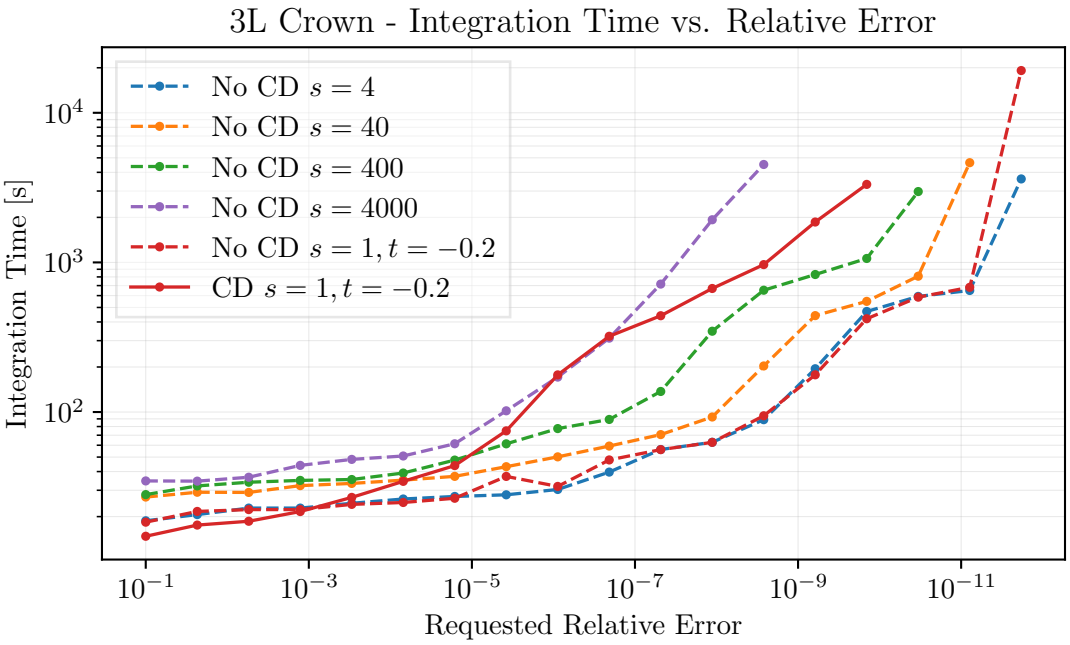

Figure 3.22: Timings with and without contour deformation for the 3-loop non-planar box, with only the leading ϵ^{-4} pole included. Evaluated for different values of s with $t = -1$ fixed, except for the point $s = 1$, where $t = -0.2$. For the benchmarks where $s \geq 4$ no digits could be obtained with contour deformation.

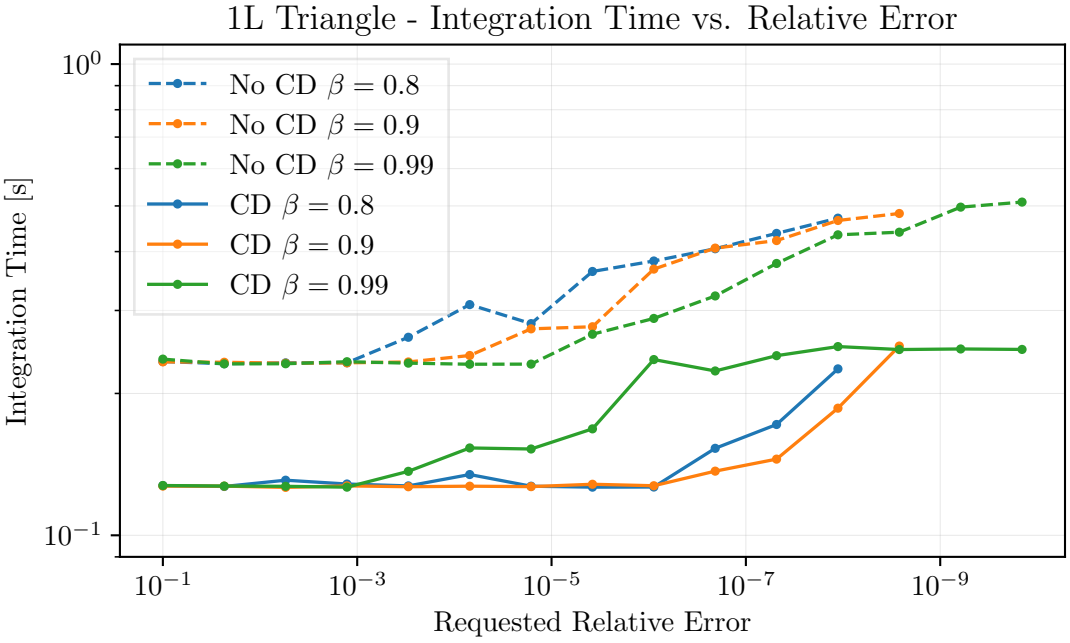

Figure 3.23: Timings with and without contour deformation for the all-massive 1-loop triangle, expanded up to order ϵ^4. Evaluated for different values of β with $m = 1$ fixed.

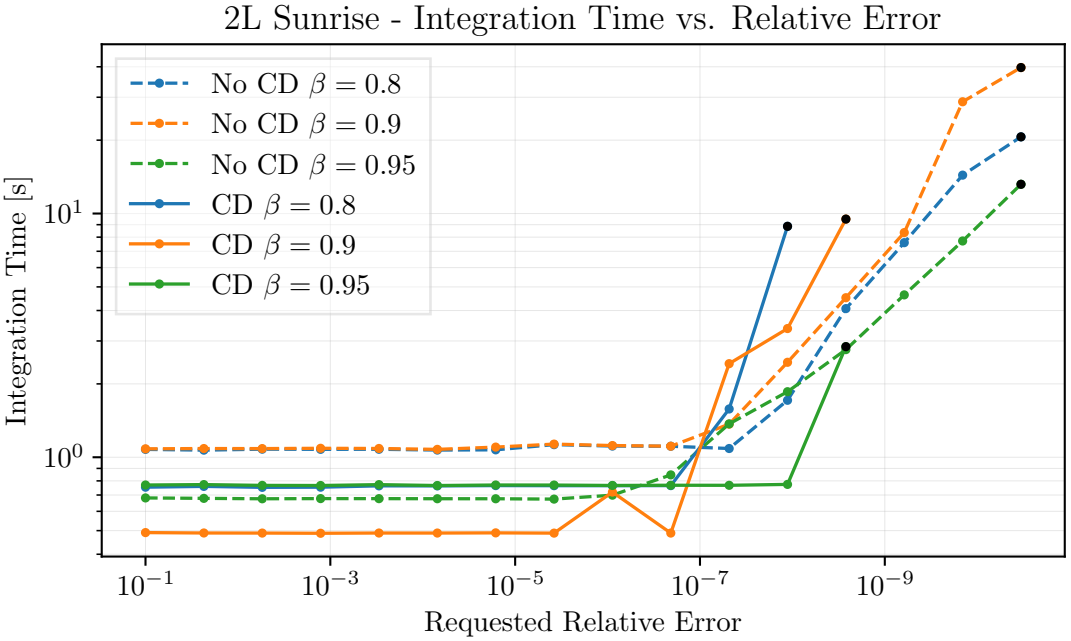

Figure 3.24: Timings with and without contour deformation for the all massive 2L elliptic sunrise, expanded up to order ϵ^4. Evaluated for different values of β with $m = 2$ fixed.

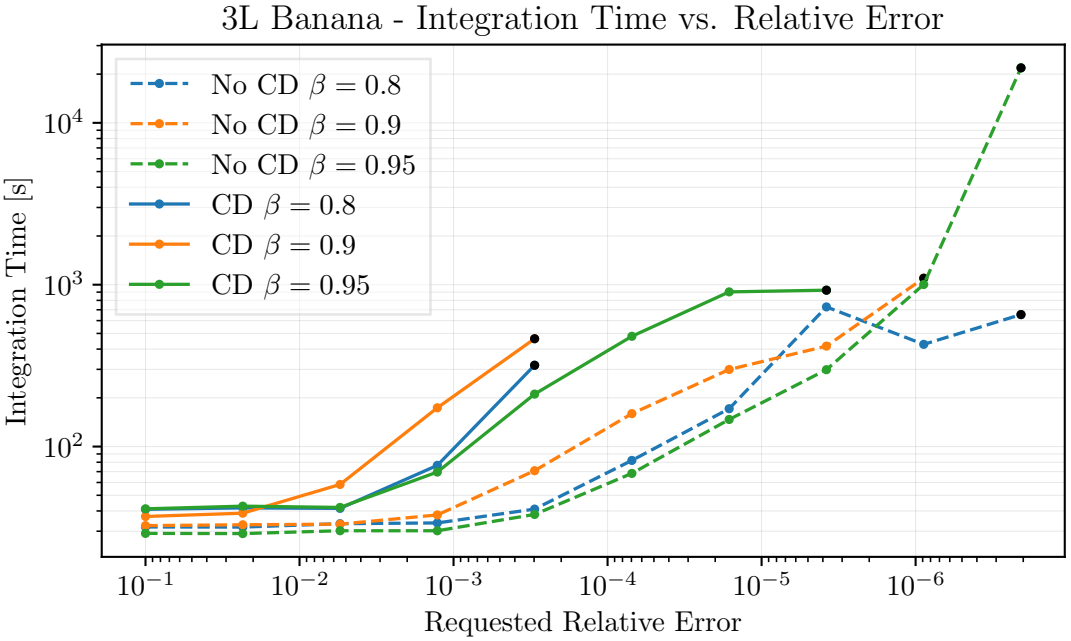

Figure 3.25: Timings with and without contour deformation for the all massive 3L banana, expanded up to order ϵ^4. Evaluated for different values of β with $m = 2$ fixed.

3.4.2 Cancellations

Since the resolved integrals are split up into multiple pieces, there could be a drop in precision on the full integrals due to cancellations. The benchmarks in the previous section already take this into account by considering the relative error on the full integral[1]. We therefore already implicitly see that if there are any cancellations, they are not severe for the phase space points considered so far. In this section we show explicitly that this is the case for larger scans of the phase spaces, by comparing the magnitude of the different contributions against the magnitude of the full integral.

Fig. 3.26 shows the magnitude of the positive and negative contributions to the massless pentagon, compared to the full result, for the real parts of the coefficients to the ϵ^{-3}, ϵ^{-2}, ϵ^{-1} and ϵ^{0} poles. The magnitude of the positive and negative contributions are of the same order of magnitude at each order in ϵ and so the cancellations are small and there is no significant loss in precision. The ϵ^{-3} pole is of course spurious and its coefficient is integrated to 0 within the precision limit. As the pole does not appear when sector decomposing the unresolved pentagon integral, a potential issue with the resolution procedure is highlighted[2]. Spurious poles are difficult to integrate to high relative precision numerically and instead a trigger on absolute precision must be used. For the benchmarks we simply skip integrating the coefficients of poles that are spurious. In practice, however, the order of the leading pole might not be known and in such cases the integration can be terminated based on an absolute error instead.

The cancellations between the positive and negative contributions to the BNP6 and BNP7 examples are shown in Figs. 3.27 and 3.28 respectively. Here there are also spurious ϵ^{-3} poles. The difference to the pentagon is that in these cases they appear as a result of cancellations between the positive and negative contributions, and are therefore a direct consequence of the resolution procedure. In these figures it

[1] This is automated within the `sum_package` module of `pySecDec`.

[2] In this case the spurious pole is actually not a direct consequence of the resolution but of the sector decomposition of the negative piece. Spurious poles can also appear when sector decomposing unresolved integrals.

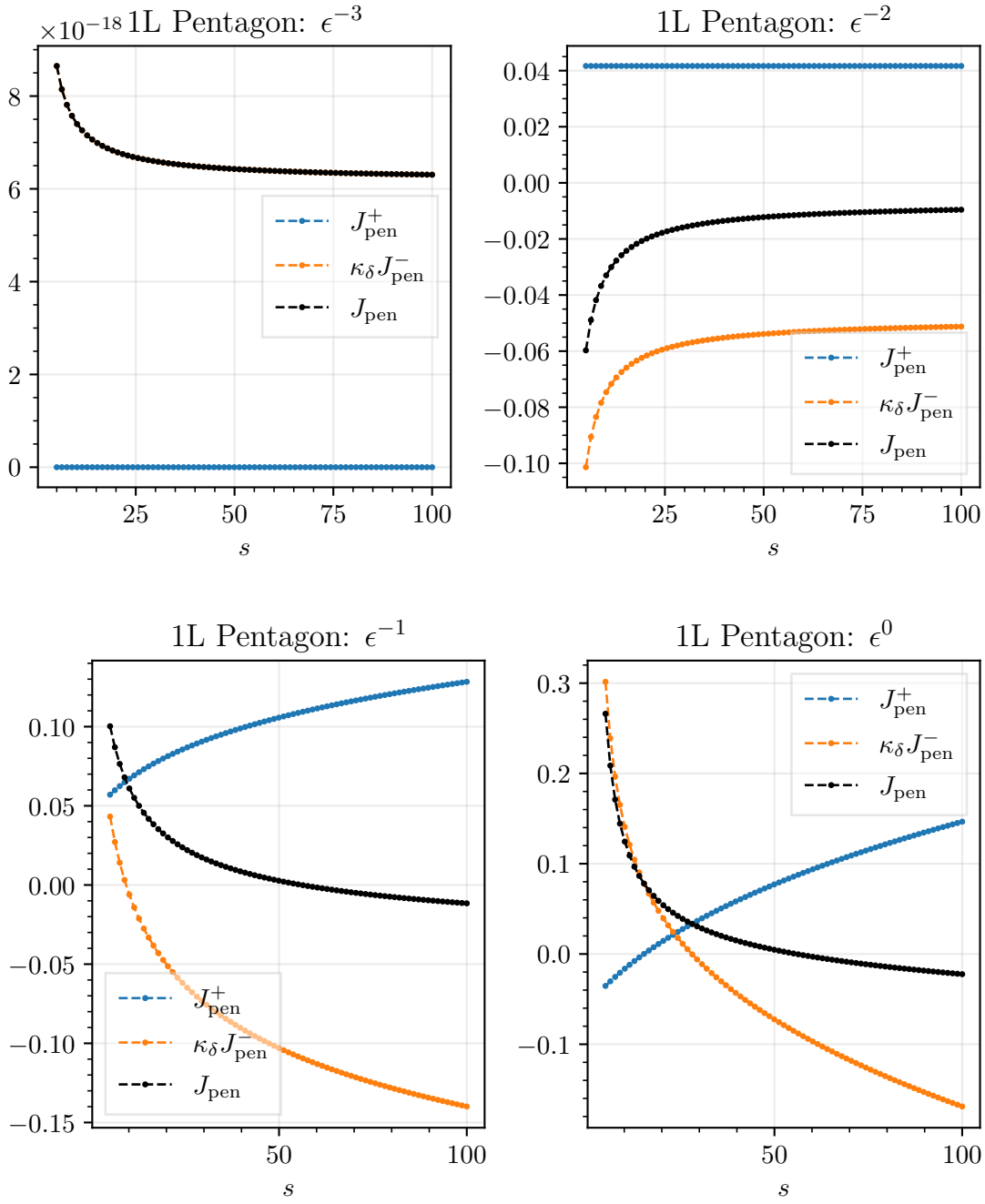

Figure 3.26: Magnitude of the real part of the positive and negative contributions compared to the total integral for the massless pentagon at orders $-3, -2, -1, 0$ in the ϵ expansion. $\kappa_\delta = \lim_{\delta \to 0^+} (-1 - i\delta)^{-3-\epsilon}$. The ϵ^{-3} pole is spurious and is only present as an artefact of the sector decomposition of J^-_{pen}.

is also clear how the cancellations, and thereby the integration performance, gets worse close to threshold. Since in these plots, we fix $t = -1$, the resolution is only

valid when $s > 1$, and the magnitudes of the positive and negative pieces get larger relative to the full integral, closer to this point.

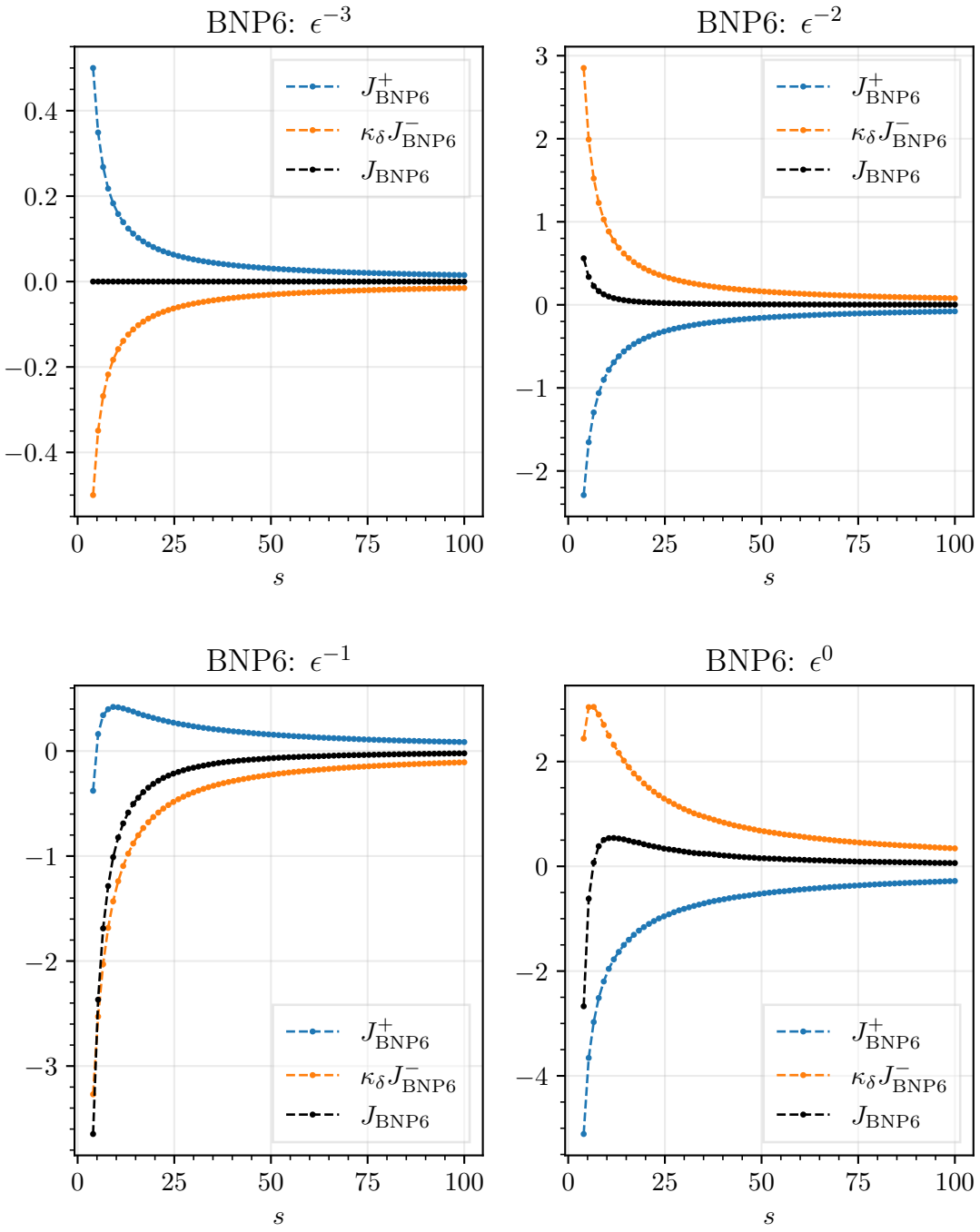

Figure 3.27: Magnitude of the real part of the positive and negative contributions compared to the total integral for BNP6 at orders $-3, -2, -1, 0$ in the ϵ expansion. $\kappa_\delta = \lim_{\delta \to 0^+}(-1 - i\delta)^{-2-2\epsilon}$. The ϵ^{-3} pole is spurious and is a consequence of cancellation between J^{+}_{BNP6} and $\kappa_\delta J^{-}_{\mathrm{BNP6}}$.

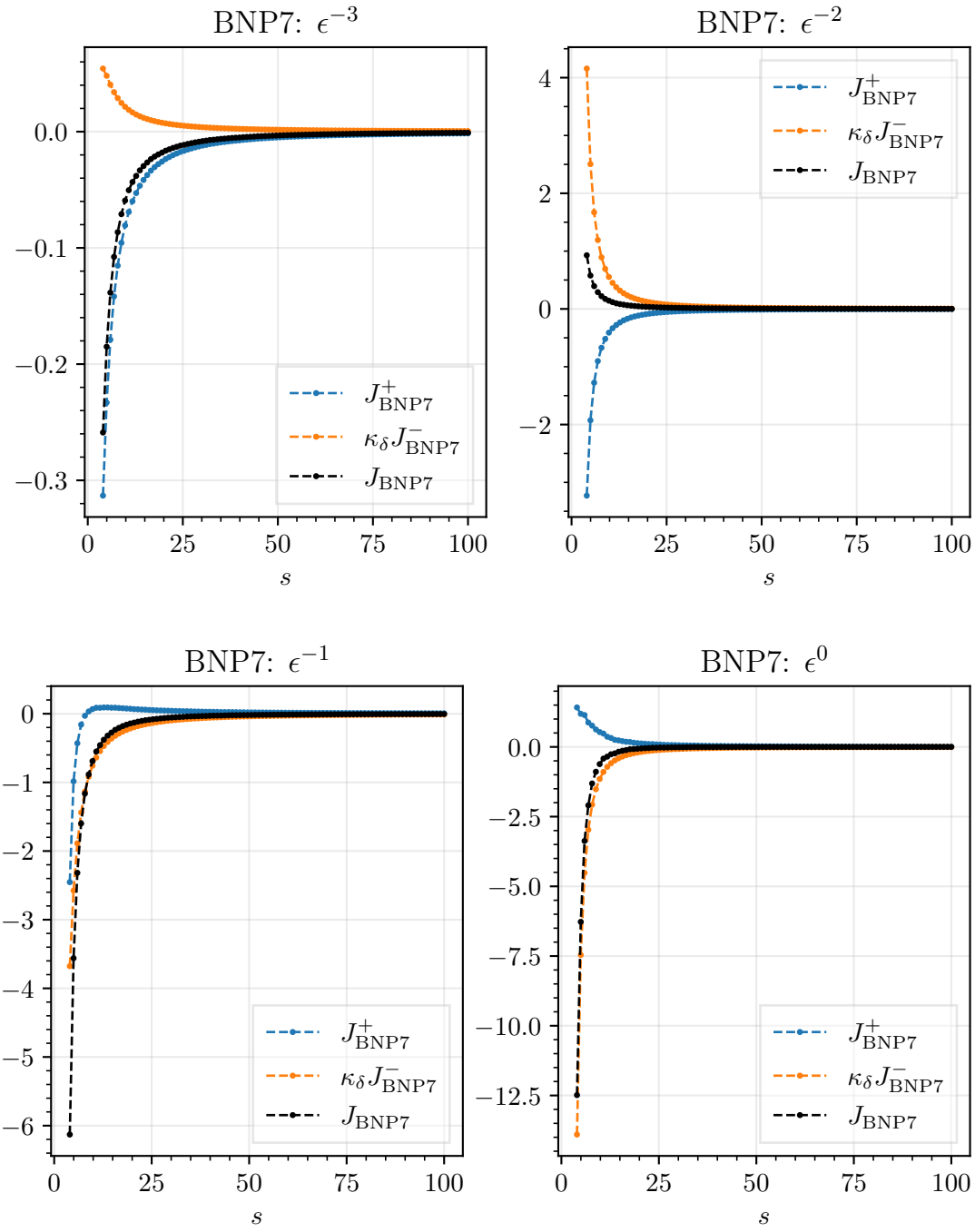

Figure 3.28: Magnitude of the real part of the positive and negative contributions compared to the total integral for BNP7 at orders $-3, -2, -1, 0$ in the ϵ expansion. $\kappa_\delta = \lim_{\delta\to 0^+}(-1-i\delta)^{-3-2\epsilon}$

Fig. 3.29 shows the cancellations between the one negative and three positive contributions to the massive 1-loop triangle. As for BNP6 and BNP7, there is a spurious pole, this time at order ϵ^{-1} which is a direct consequence of the resolution.

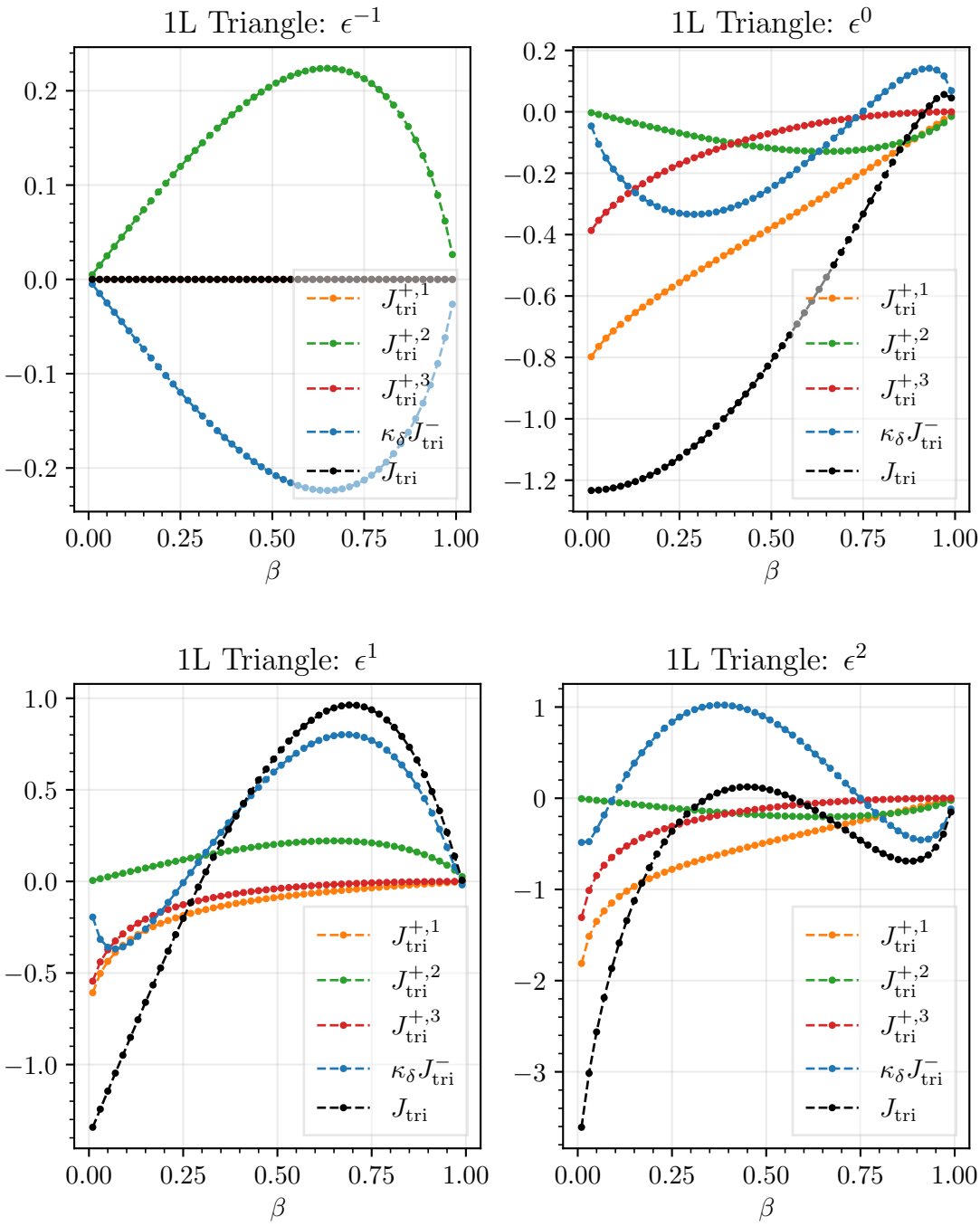

Figure 3.29: Magnitude of the real part of the positive and negative contributions compared to the total integral for the all massive 1L triangle at orders $-1, 0, 1, 2$ in the ϵ expansion. $\kappa_\delta = \lim_{\delta\to 0^+}(-1-i\delta)^{-1-\epsilon}$, $\beta \in (0.01, 0.99)$ and $m = 2$. The $1, 2, 3$ indices corresponds to the different positive regions shown in Fig. 3.9.

Figs. 3.30 and 3.31 show the cancellations between the one negative and three positive contributions to the elliptic sunrise. The ϵ^{-2} pole only has contributions from the

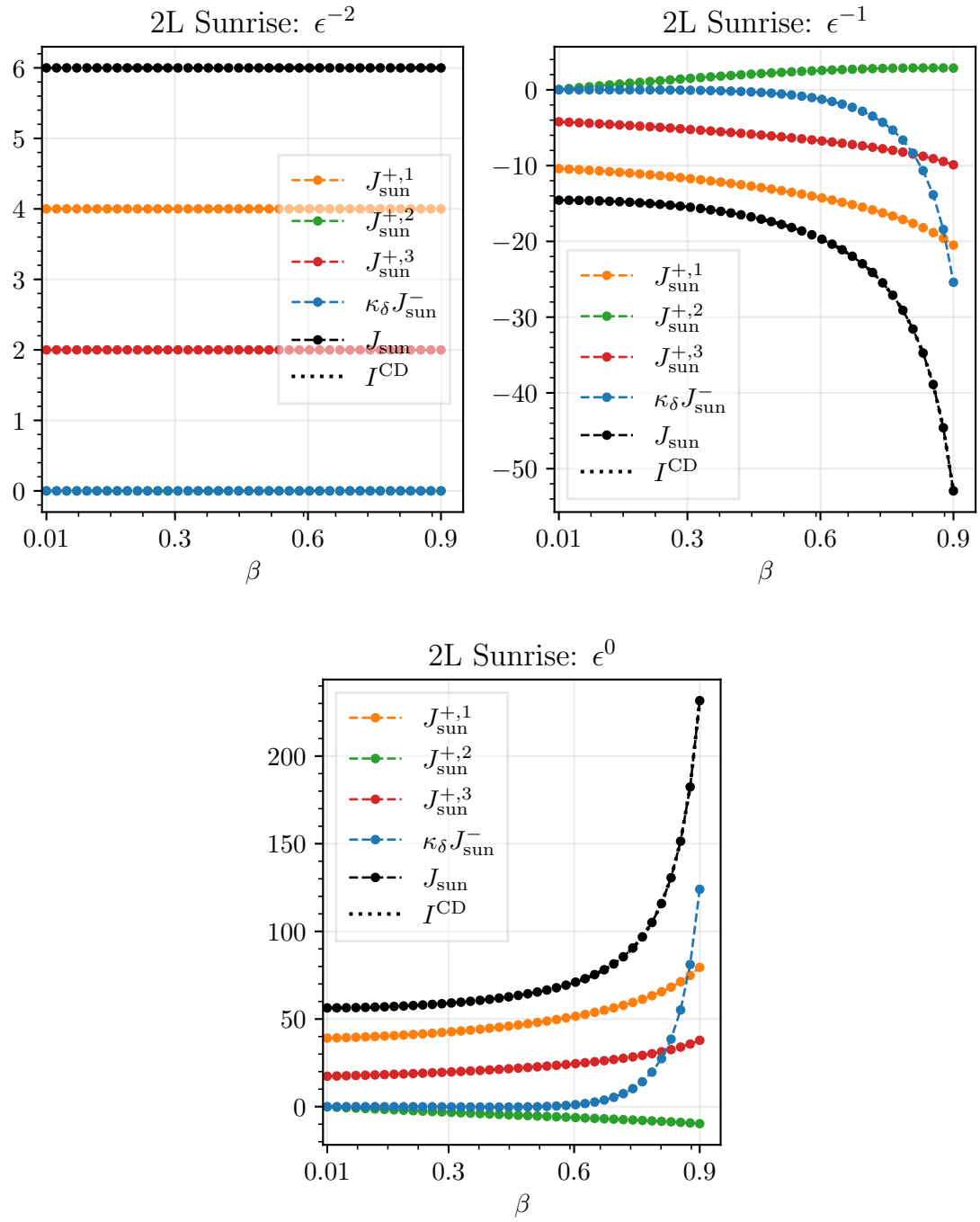

Figure 3.30: Magnitude of the real part of the positive and negative contributions compared to the total integral for the elliptic sunrise at orders $-2, -1, 0$ in the ϵ expansion. $\kappa_\delta = \lim_{\delta\to 0^+}(-1-i\delta)^{-1-2\epsilon}$, $\beta \in (0.01, 0.9)$ and $m = 2$. The $1, 2, 3$ indices corresponds to the different positive regions shown in Fig. 3.13.

$J^{+,1}_{\rm sun}$ and $J^{+,3}_{\rm sun}$ leaving the zero contribution from $J^{+,2}_{\rm sun}$ hidden in Fig. 3.30 under the zero contribution from $\kappa_\delta J^{-}_{\rm sun}$.

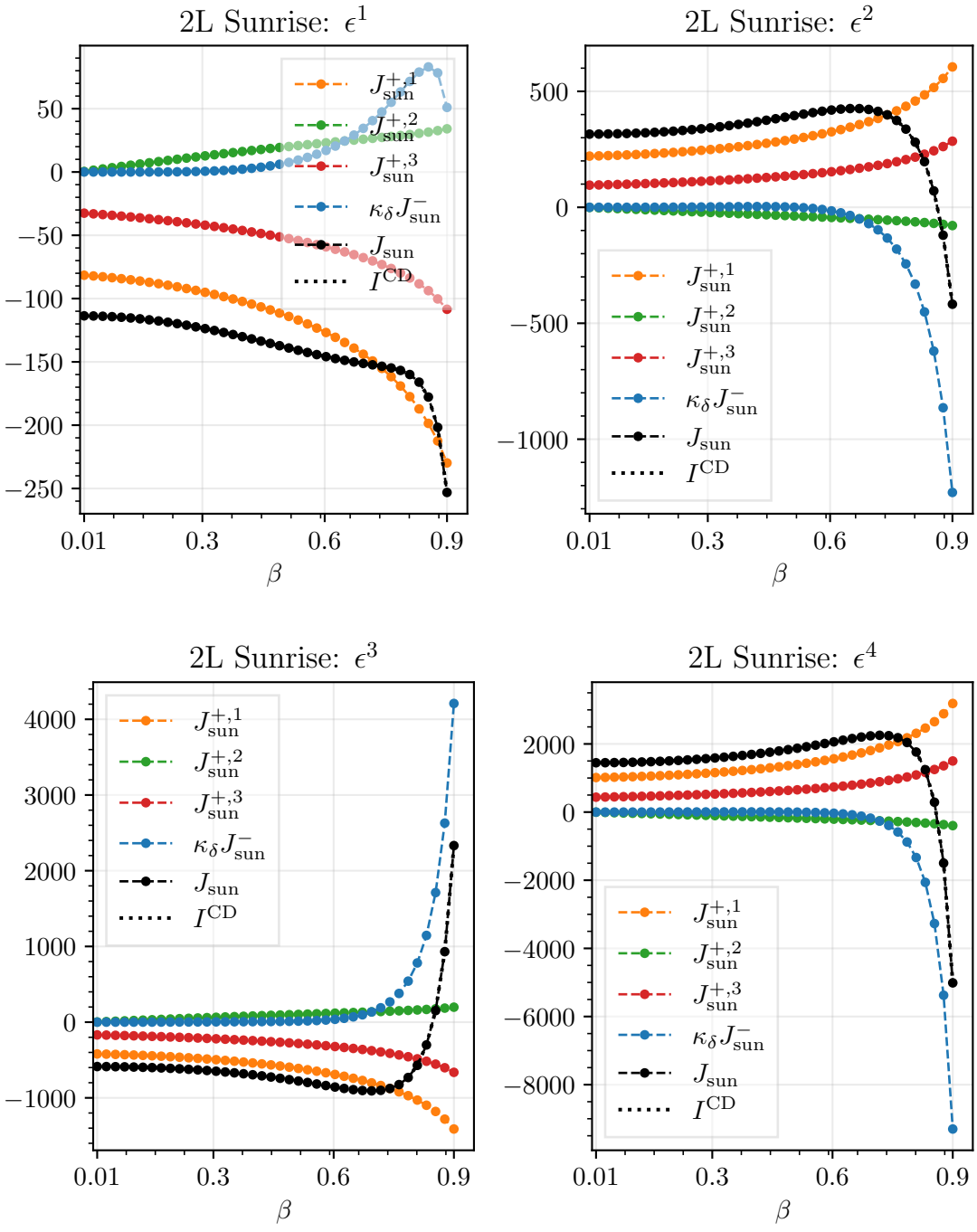

Figure 3.31: Magnitude of the real part of the positive and negative contributions compared to the total integral for the elliptic sunrise at orders $1, 2, 3, 4$ in the ϵ expansion. $\kappa_\delta = \lim_{\delta \to 0^+}(-1 - i\delta)^{-1-2\epsilon}$, $\beta \in (0.01, 0.9)$ and $m = 2$. The $1, 2, 3$ indices corresponds to the different positive regions shown in Fig. 3.13.

Chapter 4

Partial NLO EW Corrections to Higgs Pair Production

In this chapter, we present our recent calculation of next-to-leading order electroweak corrections to Higgs pair production. We begin in Section 4.1 by expanding on the motivation given in Chapter 1 for studying the process $gg \to HH$, summarising the currently available results. In Section 4.2, we describe our calculation in detail, making use of several techniques outlined in Chapter 2. Chronologically, this calculation preceded the development of the methods presented in Chapter 3; however, building on our current understanding, we could, in principle, apply those methods to this and similar calculations, expecting a significant improvement in efficiency and a corresponding reduction in numerical uncertainty – we leave this for future work.

4.1 Invitation

Among the main goals of the current and future runs of the CERN Large Hadron Collider is tightening the constraints on the Higgs boson cubic self-coupling, λ_{HHH}. Measurements of the Higgs boson pair cross section at ATLAS currently set an upper limit of $\mu_{HH} < 2.4$ at 95% confidence level, giving a bound on the self-coupling

modifier, $\kappa_\lambda = \lambda_{HHH}/\lambda_{HHH}^{SM}$, of $-1.4 < \kappa_\lambda < 6.1$ [92, 93] while measurements at CMS place a limit of $\mu_{HH} < 3.4$, giving $-1.24 < \kappa_\lambda < 6.49$ [94]. The high-luminosity LHC run is expected to shrink this constraint to $0.1 < \kappa_\lambda < 2.3$ [95], thereby ruling out the scenario of $\kappa_\lambda = 0$ where the Higgs boson does not couple to itself via a cubic coupling. As discussed in Chapter 1, Higgs boson pair production in gluon fusion is the prime process to consider in order to constrain the trilinear coupling because λ_{HHH} already enters at the leading order and the gluon fusion production channel is dominant at the LHC. Many models of BSM physics predict modified Higgs boson self-couplings, particularly those where electroweak symmetry breaking occurred through a first-order phase transition, which is a prerequisite for generating the observed baryon asymmetry. Therefore, it is crucial to have precise predictions for this process within the SM, such that potential discrepancies between data and theory can be clearly identified as signposts of new physics.

The LO cross section for the process $gg \to HH$ has been calculated in [7,8] and NLO QCD corrections including the full top-quark mass dependence are also available [9, 89, 96–98] as mentioned in Chapter 1, increasing the total cross section by about 60%. The real corrections, entering the NLO QCD cross section, have recently been obtained in a compact analytic form [99]. NLO matching to parton showers has been performed in [100–103], later also including anomalous couplings within an Effective Field Theory (EFT) framework [104–106].

QCD corrections beyond NLO have been calculated in the heavy-top-limit [107–109], or in a combination of large-m_t and high-energy expansions [110]. Partial three-loop results also have been obtained recently [111, 112]. The full NLO QCD corrections have been included in calculations where even higher orders have been evaluated, e.g. including the top mass dependence in the real corrections at NNLO [113], or N^{3}LO corrections [114,115] and N^{3}LO+N^{3}LL corrections [116] in the heavy-top-limit. The N^{3}LO results have a residual scale uncertainty of about 3%, therefore other uncertainties, such as missing electroweak corrections, become an important part in the uncertainty budget.

Currently, the top-mass renormalisation scheme uncertainties are the largest uncertainties for this process [103, 117], they are estimated to be of the order of 20%. However, the electroweak corrections also introduce a renormalisation scheme dependence, and its interplay with the scheme dependence of the QCD corrections is currently unknown. Furthermore, it is well-known that EW corrections can significantly affect the shape of kinematic distributions. For example, the EW corrections to single Higgs boson production are of the order of +5% for $m_H = 125\,\text{GeV}$, dominated by the light fermion contributions, but, for larger values of m_H, the corrections become negative and the light quark contribution ceases to dominate the correction [118–120]. First partial NLO EW corrections to Higgs boson pair production have been calculated in [121–123], the full NLO EW corrections in the large top-quark mass expansion up to $1/m_t^8$ have been calculated in [124]. Total and differential cross sections including the full NLO EW corrections have been presented in [125], finding a decrease by -4% of the total cross section after inclusion of the NLO EW corrections.

As the first order EW corrections to double Higgs production factorise from the NLO QCD corrections to this process, mixed QCD-EW corrections would only play a role at even higher orders. The latter are relevant for single Higgs production, where the experimental uncertainties are very small; contributions to these mixed corrections have been calculated in [126–133].

In this chapter, we calculate the electroweak corrections to the process $gg \to HH$ in the scalar sector, i.e. the corrections which are Yukawa-enhanced or are of Higgs self-coupling type (with the quartic coupling λ_{HHHH} also now entering at NLO), while corrections due to the exchange of virtual electroweak gauge bosons are not included. The calculation involves four-point, two-loop integrals with up to two mass scales (m_t, m_H) and two independent Mandelstam variables (s, t), which we retain fully symbolically in our amplitude. The master integrals are evaluated in two ways: with the method of sector decomposition as explained in Section 2.4 using `pySecDec` [41, 134–136] and by solving differential equations via series expansions

using `DiffExp` [48, 137] as detailed in Section 2.5.

The remainder of this chapter is structured as follows: in Section 4.2, we give details of the calculation, describing the projection onto form factors, the reduction to master integrals and their evaluation; the UV renormalisation of the amplitude is also described in detail. In Section 4.3 we provide values for the bare and renormalised amplitude at a selected phase-space point and present our results for the Higgs boson pair invariant mass and Higgs boson transverse momentum distributions in addition to the impact of these corrections on the total cross section. Our conclusions are presented in Section 4.4.

4.2 Calculation

In this section, we describe the details of our calculation of the NLO electroweak corrections to Higgs boson pair production including only the top-Yukawa and Higgs boson self-coupling contributions. We start by specifying the parts of the SM Lagrangian relevant for computing these corrections in Section 4.2.1, followed by a detailed description of the amplitude structure for $gg \to HH$ in Section 4.2.2. The remaining sections give details of our computational setup, starting from diagram generation in Section 4.2.3, continuing with the reduction to master integrals in Section 4.2.4, and closing with the master integral evaluation in Section 4.2.5. In Section 4.2.6, we describe the renormalisation of our amplitudes. For a review of the standard methods for the computation and renormalisation of one-loop electroweak corrections in the Standard Model, see [138, 139].

4.2.1 Lagrangian and Input-Parameter Scheme

To precisely define the corrections we wish to compute – i.e. only those induced by the Yukawa coupling and Higgs self-couplings – and to derive their renormalisation, we do not start from the general SM Lagrangian. Instead, we start from a more

accessible subset corresponding to a Yukawa model with only one up-type fermion (the top quark) and one scalar field (the Higgs boson). Indeed, employing a series of simplifications, we can see it truly is a subset of the SM: firstly, we remove the Yang-Mills part for the electroweak gauge bosons so that they only appear in the covariant derivative. Additionally, all leptons, light quarks and the bottom quark are dropped since their coupling to the Higgs field is negligibly small compared to that of the top quark. Prior to electroweak symmetry breaking (EWSB), this leads to the bare Lagrangian[1]

$$\begin{aligned}\mathcal{L}_0 = &-\frac{1}{4}\mathcal{G}_{0,\mu\nu}\mathcal{G}_0^{\mu\nu} + (D_\mu\Phi_0)^\dagger(D^\mu\Phi_0) + \mu_0^2\Phi_0^\dagger\Phi_0 + \frac{\lambda_0}{4}(\Phi_0^\dagger\Phi_0)^2 \\ &+ i\bar{Q}_{L,0}\not{D}Q_{L,0} + i\bar{t}_{R,0}\not{D}t_{R,0} - (y_{t,0}\bar{Q}_{L,0}\Phi_0^c t_{R,0} + \text{h.c.}),\end{aligned} \tag{4.2.1}$$

with

$$Q_{L,0} = \begin{pmatrix} t_{L,0} \\ 0 \end{pmatrix}, \tag{4.2.2}$$

and the gluon field strength tensor denoted by $\mathcal{G}_0^{\mu\nu}$. Taking the gaugeless limit for the EW sector corresponds to the limit $(g, g') \to (0, 0)$, which removes the electroweak gauge bosons (as well as their associated ghost fields) entirely, such that the covariant derivatives have the form

$$D_\mu = \partial_\mu - ig_{s,0}G_{0,\mu}^a t^a \tag{4.2.3}$$

where t^a are the generators of $\mathrm{SU(3)_C}$ and $G_{0,\mu}^a$ are the gluon fields. As described in Chapter 1, the Higgs field, Φ_0, acquires a vacuum expectation value, v_0, spontaneously breaking the electroweak symmetry. Expanding the Higgs field around its vev and using unitary gauge to decouple the Goldstone bosons, we obtain the Lagrangian

$$\begin{aligned}\mathcal{L}_0 = &-\frac{1}{4}\mathcal{G}_{0,\mu\nu}\mathcal{G}_0^{\mu\nu} + \frac{1}{2}(\partial_\mu H_0)^\dagger(\partial^\mu H_0) + \frac{\mu_0^2}{2}(v_0 + H_0)^2 + \frac{\lambda_0}{16}(v_0 + H_0)^4 \\ &+ i\bar{t}_0\not{D}t_0 - y_{t,0}\frac{v_0 + H_0}{\sqrt{2}}\bar{t}_0 t_0 + \text{constant}\end{aligned}$$

[1] Objects with a zero subscript are considered bare unless stated otherwise.

$$
\begin{aligned}
&= -\frac{1}{4}\mathcal{G}_{0,\mu\nu}\mathcal{G}_0^{\mu\nu} + \frac{1}{2}(\partial_\mu H_0)^\dagger(\partial^\mu H_0) - \frac{m_{H,0}^2}{2}H_0^2 - \frac{m_{H,0}^2}{2v_0}H_0^3 - \frac{m_{H,0}^2}{8v_0^2}H_0^4 \\
&\quad + i\bar{t}_0 \not{\partial} t_0 - m_{t,0}\bar{t}_0 t_0 - \frac{m_{t,0}}{v_0}H_0\bar{t}_0 t_0 + \text{constant}
\end{aligned}
\tag{4.2.4}
$$

with the identifications,

$$
m_{H,0}^2 = 2\mu_0^2 \ , \ m_{t,0} = \frac{y_{t,0}v_0}{\sqrt{2}} \ \text{ and } \ v_0^2 = -\frac{2m_{H,0}^2}{\lambda_0} \ . \tag{4.2.5}
$$

The constant term in the Lagrangian is neglected from now on as it does not contribute to observables. For later convenience, we also introduce the labels $g_{t,0}, g_{3,0}, g_{4,0}$ (and g_t, g_3, g_4) for the bare (and renormalised) top-Yukawa ($H\bar{t}t$) coupling, cubic Higgs (H^3) self-coupling and quartic Higgs (H^4) self-coupling, respectively. In the SM and in our Yukawa model, they are related to the top-quark mass, Higgs boson mass and vev via

$$
g_{t,0} \equiv \frac{m_{t,0}}{v_0} \ , \qquad g_{3,0} \equiv \frac{3m_{H,0}^2}{v_0} \ , \qquad g_{4,0} \equiv \frac{3m_{H,0}^2}{v_0^2} \ . \tag{4.2.6}
$$

We present the set of Feynman rules for this Lagrangian, relevant to our calculation, in Appendix A.2. For the Yang-Mills part they are equivalent to the standard QCD rules and can be taken from the literature (e.g. from [140] with $\eta_G = 1$, $\eta_s = -1$). Details of the derivation of the electroweak counterterms and renormalisation are presented in Appendix A.

To evaluate our predictions, we must also specify a consistent electroweak input-parameter scheme. We take the top-quark mass and Higgs boson mass in the on-shell (OS) scheme as inputs to our calculation. The renormalised top-quark Yukawa coupling, g_t, depends on the top-quark mass and the vev, it is fixed via the relation given in (4.2.6) after renormalising the top-quark mass and the vev. Similarly, the renormalised cubic, g_3, and quartic, g_4, Higgs boson self-couplings depend on the Higgs mass and the vev and are fixed via (4.2.6) after renormalising the Higgs mass and the vev. In the gaugeless limit, we can consider the Z and W bosons (which do not appear directly in our computation) to be massless particles; therefore, it is natural to pick $M_Z = 0$ and $M_W = 0$ as input parameters. Finally, we must specify

the value of the electromagnetic coupling constant. The most natural choice in our parameterisation would be to specify the value of the vev, v, after renormalisation. However, to simplify the connection to more commonly used input schemes, we instead take G_F as an input parameter and derive from it the value of the vev in the G_μ (a.k.a. α_μ) scheme. That is to say, we require that the relation $v = (\sqrt{2}G_F)^{-\frac{1}{2}}$ holds to all orders in perturbation theory. We circumvent the complication that the muon decay vertex employed for the matching in the G_μ scheme is not present in our model by relying on external calculations (e.g. [141]) to fix the finite parts of the vev renormalisation; for further details, see Section 4.2.6 and Appendix A.1. In summary, the input-parameter scheme of our calculation is therefore $\{M_Z = 0, M_W = 0, G_F\}$ + $\{m_t, m_H\}$, where all masses are specified in the on-shell scheme.

4.2.2 Amplitude Structure

We compute the amplitude for the process $g^a_\mu(p_1)g^b_\nu(p_2) \to H(-p_3)H(-p_4)$, with all momenta defined as incoming. The amplitude may be parametrised in terms of the usual Mandelstam invariants,

$$s = (p_1 + p_2)^2, \qquad t = (p_1 + p_3)^2, \qquad u = (p_2 + p_3)^2, \tag{4.2.7}$$

with $p_1^2 = p_2^2 = 0$ and $p_3^2 = p_4^2 = m_H^2$. Due to momentum conservation, $p_1 + p_2 + p_3 + p_4 = 0$, the invariants obey the additional relation $s + t + u = 2m_H^2$.

As described in Section 4.2.1, we will consider only the subset of electroweak corrections appearing in the SM, involving the top-quark Yukawa coupling and the Higgs boson trilinear and quartic couplings. The electroweak W and Z gauge bosons do not appear in our calculation, therefore, no axial-vector couplings are present in the amplitude. The amplitude may be written as a linear combination of tensor structures

$$\mathcal{M}_{ab} = \varepsilon_{1,\mu}\varepsilon_{2,\nu}M^{\mu\nu}_{ab} = \varepsilon_{1,\mu}\varepsilon_{2,\nu}\delta_{ab}\left[A\, g^{\mu\nu} + \sum\nolimits_{i,j\in\{1,2,3\}} B_{i,j}\, p_i^\mu p_j^\nu\right], \tag{4.2.8}$$

where $\varepsilon_{1,\mu}, \varepsilon_{2,\nu}$ are the gluon polarisation vectors, a, b are colour indices in the adjoint representation and $A, B_{i,j}$ are scalar coefficient functions, depending only on the kinematic invariants and the spacetime dimension. The gluon transversality conditions $\epsilon_1 \cdot p_1 = \epsilon_2 \cdot p_2 = 0$ allow us to set the coefficients $\{B_{1,1}, B_{1,2}, B_{1,3}, B_{2,2}, B_{3,2}\}$ to zero, with five scalar functions remaining (including A). Having applied the transversality condition, the condition that the amplitude obeys the QCD Ward identity, $p_{1,\mu} M_{ab}^{\mu\nu} = p_{2,\nu} M_{ab}^{\mu\nu} = 0$, reduces the independent number of coefficients from five to two. Hence, without loss of generality, the amplitude may be written in terms of only two independent form factors, F_1 and F_2,

$$\mathcal{M}_{ab} = \varepsilon_{1,\mu}\varepsilon_{2,\nu}\delta_{ab}\left(F_1 T_1^{\mu\nu} + F_2 T_2^{\mu\nu}\right). \tag{4.2.9}$$

The tensor structures, $T_1^{\mu\nu}, T_2^{\mu\nu}$, can be chosen to be

$$T_1^{\mu\nu} = g^{\mu\nu} - \frac{p_2^\mu p_1^\nu}{p_1 \cdot p_2}, \tag{4.2.10}$$

$$T_2^{\mu\nu} = g^{\mu\nu} + \frac{1}{p_T^2 (p_1 \cdot p_2)}\left[m_H^2 p_2^\mu p_1^\nu - 2(p_1 \cdot p_3) p_2^\mu p_3^\nu - 2(p_2 \cdot p_3) p_3^\mu p_1^\nu + 2(p_1 \cdot p_2) p_3^\mu p_3^\nu\right], \tag{4.2.11}$$

where $p_T^2 = (ut - m_H^4)/s$ and $T_1 \cdot T_1 = T_2 \cdot T_2 = D-2$, $T_1 \cdot T_2 = D-4$, where $D = 4-2\epsilon$ is the number of spacetime dimensions, such that the individual form factors correspond to helicity amplitudes: $\mathcal{M}^{++} = \mathcal{M}^{--} = -F_1$ and $\mathcal{M}^{+-} = \mathcal{M}^{-+} = -F_2$. The form factors are individually gauge invariant and can be separately renormalised, see Section 4.2.6, meaning that the interference contribution between the renormalised form factors vanishes in the limit $\epsilon \to 0$.

The scalar form factors, F_i, can be extracted from the amplitude, $M_{ab}^{\mu\nu}$, using projectors defined to obey the relations,

$$\sum_{\text{pol}} P_{i,ab}^{\mu\nu}\, \varepsilon_{1,\mu}^* \varepsilon_{2,\nu}^* \varepsilon_{1,\mu'} \varepsilon_{2,\nu'} \delta^{aa'} \delta^{bb'} M_{a'b'}^{\mu'\nu'} = P_{i,ab}^{\mu\nu} M_{\mu\nu}^{ab} = F_i \tag{4.2.12}$$

with $\sum_{\text{pol}} \varepsilon_{1,\mu}^* \varepsilon_{1,\mu'} = -g_{\mu\mu'}$. The projectors are given explicitly by,

$$P_{1,ab}^{\mu\nu} = \frac{\delta_{ab}}{N_c^2 - 1}\, \frac{1}{4(D-3)}\left[(D-2) T_1^{\mu\nu} + (4-D) T_2^{\mu\nu}\right], \tag{4.2.13}$$

$$P_{2,ab}^{\mu\nu} = \frac{\delta_{ab}}{N_c^2 - 1} \frac{1}{4(D-3)} \left[(4-D)T_1^{\mu\nu} + (D-2)T_2^{\mu\nu}\right]. \tag{4.2.14}$$

where the N_c^2-1 (with $N_c = 3$) appearing in the denominator cancels the colour factor appearing from the δ_{ab} in the projector contracting with the δ_{ab} in the decomposed amplitude.

Each of the bare form factors can be expanded in terms of the bare electroweak couplings as follows,

$$F_i = F_i^{(0)} + F_i^{(1)}, \tag{4.2.15}$$

$$F_i^{(0)} = g_{s,0}^2 \Big(g_{3,0}\, g_{t,0}\; F_{i,g_3 g_t}^{(0)} + g_{t,0}^2\; F_{i,g_t^2}^{(0)} \Big), \tag{4.2.16}$$

$$\begin{aligned} F_i^{(1)} = g_{s,0}^2 \Big(& g_{3,0}\, g_{4,0}\, g_{t,0}\; F_{i,g_3 g_4 g_t}^{(1)} + g_{3,0}^3\, g_{t,0}\; F_{i,g_3^3 g_t}^{(1)} + g_{4,0}\, g_{t,0}^2\; F_{i,g_4 g_t^2}^{(1)} \\ & + g_{3,0}^2\, g_{t,0}^2\; F_{i,g_3^2 g_t^2}^{(1)} + g_{3,0}\, g_{t,0}^3\; F_{i,g_3 g_t^3}^{(1)} + g_{t,0}^4\; F_{i,g_t^4}^{(1)} \Big), \end{aligned} \tag{4.2.17}$$

where $g_s = \sqrt{4\pi\alpha_s}$ is the strong coupling. The bare form factors correspond to the coefficients of the bare couplings, we suppress the 0 subscript of the bare couplings in the labels of the form factors for brevity. The form factors $F_{i,j}^{(0)}$ correspond to the leading-order one-loop triangle and box contributions, while $F_{i,j}^{(1)}$ correspond to the 6 possible coupling structure combinations appearing at two loops. We expand our bare form factors in the electroweak coupling, $\alpha_0 \propto 1/{v_0}^2$, such that the products of couplings entering at LO scale as $1/{v_0}^2$ while the products of couplings entering at NLO scale as $1/{v_0}^4$.

The bare form factors may be further decomposed into sets of one-particle-irreducible (1PI) and one-particle-reducible (1PR) diagrams. At leading order, the form factors, split according to combinations of the EW couplings $(g_{t,0}, g_{3,0}, g_{4,0})$, are either entirely 1PI or 1PR,

$$F_{i,g_3 g_t}^{(0)} = F_{i,g_3 g_t}^{(0),\mathrm{1PR}}, \qquad F_{i,g_t^2}^{(0)} = F_{i,g_t^2}^{(0),\mathrm{1PI}}. \tag{4.2.18}$$

Starting from NLO, the form factors contain a mixture of 1PI and 1PR contributions,

$$F_{i,g_3^3 g_t}^{(1)} = F_{i,g_3^3 g_t}^{(1),\mathrm{1PR}}, \qquad F_{i,g_3 g_4 g_t}^{(1)} = F_{i,g_3 g_4 g_t}^{(1),\mathrm{1PR}}, \tag{4.2.19}$$

$$F^{(1)}_{i,g_3^2 g_t^2} = F^{(1),1\text{PI}}_{i,g_3^2 g_t^2} + F^{(1),1\text{PR}}_{i,g_3^2 g_t^2}, \qquad F^{(1)}_{i,g_4 g_t^2} = F^{(1),1\text{PI}}_{i,g_4 g_t^2} + F^{(1),1\text{PR}}_{i,g_4 g_t^2}, \tag{4.2.20}$$

$$F^{(1)}_{i,g_3 g_t^3} = F^{(1),1\text{PI}}_{i,g_3 g_t^3} + F^{(1),1\text{PR}}_{i,g_3 g_t^3}, \qquad F^{(1)}_{i,g_t^4} = F^{(1),1\text{PI}}_{i,g_t^4} + F^{(1),1\text{PR}}_{i,g_t^4}. \tag{4.2.21}$$

We compute each of the bare form factors $F^{(0)}_{i,j}$ and $F^{(1)}_{i,j}$ separately and obtain results for both the 1PI and 1PR contributions separately.

As discussed in Chapter 1, the LO partonic cross section can be written as

$$\hat{\sigma}^{(0)} = \frac{1}{16\pi s^2}\int_{t_-}^{t_+} \mathrm{d}t \left|\overline{\mathcal{M}}^{(0)}\right|^2 = \frac{1}{512\pi s^2}\int_{t_-}^{t_+} \mathrm{d}t \left(\left|F_1^{(0)}\right|^2 + \left|F_2^{(0)}\right|^2\right) \tag{4.2.22}$$

where

$$t_\pm = m_H^2 - \frac{s}{2}\left[1 \mp \sqrt{1 - \frac{4m_H^2}{s}}\,\right] \tag{4.2.23}$$

are the boundaries in t of the physical region for a given $s > 4m_H^2$. The physical region can be derived from the condition that the Gram matrix, $\mathcal{G} = [2p_i \cdot p_j]$, has a positive determinant [142] (in conjunction with the condition that $\sqrt{s} > 2m_H > 0$). The Gram matrix is given by

$$\mathcal{G} = \begin{bmatrix} 0 & s & t - m_H^2 \\ s & 0 & u - m_H^2 \\ t - m_H^2 & u - m_H^2 & 2m_H^2 \end{bmatrix} \tag{4.2.24}$$

and, after applying momentum conservation to eliminate u, we obtain

$$\det \mathcal{G} > 0 \quad \Rightarrow \quad -2s\left[m_H^4 - 2m_H^2 t + t(s+t)\right] > 0\,. \tag{4.2.25}$$

Along with the physical conditions on s and m_H, this allows us to write down the physical region:

$$m_H > 0, \quad t < 0, \quad s > \frac{\left(m_H^2 - t\right)^2}{-t}\,. \tag{4.2.26}$$

The boundaries, $t^\pm$, of the physical region are then obtained by solving $s = \frac{\left(m_H^2 - t\right)^2}{-t}$ for t. The averaged matrix element squared $\left|\overline{\mathcal{M}}^{(0)}\right|^2$ contains a symmetry factor for the two final state Higgs bosons, spin and colour averaging for the incoming gluons, a factor of $D-2$ from the square of the tensor structures ($D-4$ from the interference between the tensor structures does not contribute as explained above) and another

factor of $N_c^2 - 1$ from the sum over the adjoint colour indices of δ_{ab} in (4.2.9). As described in Chapter 1, to obtain the total cross section, the partonic cross section must be combined with the parton distribution functions (PDFs) as in (1.1.14).

At NLO in the electroweak expansion, the bare form factors can have UV divergences which give rise to poles of order $1/\epsilon$ which are treated by renormalising the masses and fields of the Higgs boson and top quark along with the vacuum expectation value. We perform the UV renormalisation by computing explicit counterterm amplitudes, separated on couplings structures, as described in Section 4.2.6. In this way, we retain the complete dependence of our amplitudes on the individual couplings which facilitates changing the electroweak input scheme or supplementing our calculation with higher-dimensional effective field theory operators. The subset of corrections that we consider here consists of corrections involving the emission of additional massive particles from massive particle lines and is therefore free of IR singularities.

4.2.3 Diagram and Amplitude Generation

We generate Feynman diagrams using `QGRAF` [143] and find a total of 168 diagrams, after excluding tadpole diagrams and diagrams present in the full Standard Model but not in our reduced Yukawa Model. We generate the amplitude using two independent tool chains based on either a) `alibrary` [144], a `Mathematica` and `FORM` [145] package for computing multi-loop amplitudes, or b) `Reduze 2` [21]. The resulting amplitudes agree up to sector relations and symmetries before applying integration-by-parts identities (see Section 2.3.1 and Section 2.3.2).

Type	$g_3 g_4 g_t$	$g_3^3 g_t$	$g_4 g_t^2$	$g_3^2 g_t^2$	$g_3 g_t^3$	g_t^4
1PI	0	0	3	6	24	60
1PR	12	6	1	6	24	26
Total	12	6	4	12	48	86

Table 4.1: Number of Feynman diagrams (one-particle-irreducible, one-particle-reducible and total), excluding tadpole diagrams, which contribute to each of the bare coupling structures at NLO.

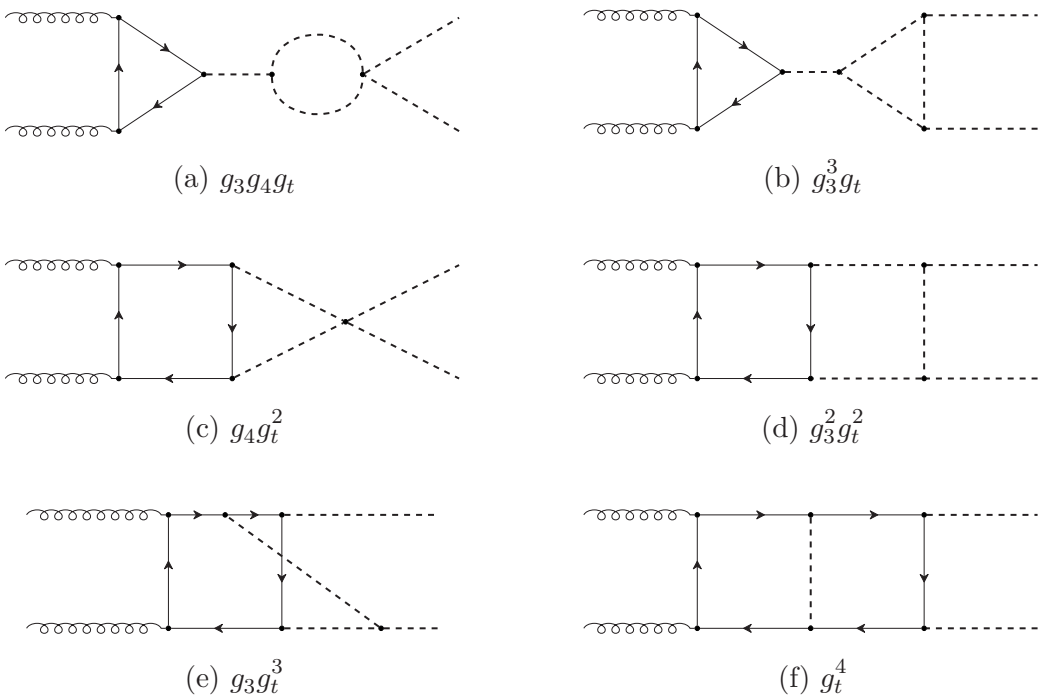

(a) $g_3 g_4 g_t$ (b) $g_3^3 g_t$

(c) $g_4 g_t^2$ (d) $g_3^2 g_t^2$

(e) $g_3 g_t^3$ (f) g_t^4

Figure 4.1: Example diagrams contributing to each of the 6 coupling structures on which we separate the bare two-loop amplitude.

The number of diagrams contributing to each of the coupling structures entering our subset of NLO EW corrections are given in Table 4.1, and example Feynman diagrams for each of these structures are shown in Fig. 4.1. The coupling structures $g_3 g_4 g_t$ and $g_3^3 g_t$ have only a single Yukawa coupling and therefore consist of diagrams that contain loop corrections to the Higgs propagator or trilinear vertex, they are therefore entirely 1PR (see Figs. 4.1a and 4.1b). The 1PR contribution to the $g_4 g_t^2$ coupling structure consists of a diagram containing a triple gluon vertex with a single gluon connected to the fermion loop and thus has a vanishing colour factor. The $g_4 g_t^2$ coupling structure, therefore, receives only a 1PI contribution, see Fig. 4.1c. The remaining coupling structures receive contributions from both 1PI and 1PR diagrams.

The complete EW corrections, obtained using the large-m_t limit in [124] and fully using `AMFlow` in [125], contain within them all coupling structures presented in this work, as well as additional contributions from diagrams containing W and Z bosons and their ghosts, as well as the Goldstone bosons. The coupling structures

$g_3 g_4 g_t$ and $g_3^3 g_t$ consist of factorisable one-loop contributions and are comparatively straightforward to compute, they have appeared previously in the literature [121,146, 147]. The coupling structure $g_4 g_t^2$ contains only three-point integrals, the relevant integrals are known analytically in a large top mass expansion [119,148], the complete structure was computed numerically in [121]. The $g_3^2 g_t^2$ coupling structure was also computed numerically in [121]. To the best of our knowledge, the $g_3 g_t^3$ contribution has not been computed separately so far. The 1PI contribution to g_t^4 was computed in the high-energy limit in [123].

As a cross-check of one of the more challenging pieces of our calculation, we compare the 1PI piece of our bare g_t^4 structure to [123][1] and find good agreement for points at sufficiently high energy $s \gtrsim 4m_t^2$, with points at $s \gtrsim 9m_t^2$ differing by less than 2% and less than 1% for $s \gtrsim 16m_t^2$. The other parts of our calculation are performed systematically using an identical setup to this structure and so are partially checked by this comparison. Further checks on our final result are described in Section 4.3.

4.2.4 Reduction

In this chapter, we modify our notation slightly such that loop integrals are written as a list of exponents ν_i for the denominators $\mathcal{D}_i$ of the corresponding integral family f as defined in Table 4.2. In our calculation each loop integral is defined as

$$\mathcal{I}^f_{\vec{\nu}}(s,t) = \left(\mu^{4-D}\right)^L \int \prod_{l=1}^{L} [\mathscr{D}k_l] \prod_{i=1}^{N} \frac{1}{\mathcal{D}_i^{\nu_i}\left(\boldsymbol{k}, \boldsymbol{p}, m_i^2\right)}, \tag{4.2.27}$$

in a general dimension D, where, as before, L is the number of loops and N is the number of propagators. When reporting bare form factors, our integrals are multiplied by an additional factor of $C_D = \left(i\pi^{D/2}/(2\pi)^D\right)$ per loop. This factor is required to recover the physical normalisation dictated by the Feynman rules as noted in Section 2.1.

After identifying momentum mapping symmetries of the kind described in Sec-

[1] We thank the authors of [123] for performing a detailed comparison of our results.

F1	F2	F3	F4
$l_1^2 - m_t^2$	$l_1^2 - m_t^2$	$l_1^2 - m_H^2$	$l_1^2 - m_t^2$
$l_2^2 - m_t^2$	$l_2^2 - m_t^2$	$(l_1 - l_2)^2 - m_t^2$	$l_2^2 - m_H^2$
$(l_1 - l_2)^2 - m_H^2$	$(l_1 - l_2)^2 - m_H^2$	$(l_1 + p_1)^2 - m_H^2$	$(l_1 - l_2)^2 - m_t^2$
$(l_1 + p_1)^2 - m_t^2$	$(l_1 + p_1)^2 - m_t^2$	$(l_2 + p_1)^2 - m_t^2$	$(l_1 + p_1)^2 - m_t^2$
$(l_2 + p_1)^2 - m_t^2$	$(l_2 + p_1)^2 - m_t^2$	$(l_1 - p_2)^2 - m_H^2$	$(l_2 + p_1)^2 - m_H^2$
$(l_1 - p_2)^2 - m_t^2$	$(l_1 - p_3)^2 - m_t^2$	$(l_2 - p_2)^2 - m_t^2$	$(l_1 - p_2)^2 - m_t^2$
$(l_2 - p_2)^2 - m_t^2$	$(l_2 - p_3)^2 - m_t^2$	$(l_2 - p_2 - p_3)^2 - m_t^2$	$(l_2 - p_2)^2 - m_H^2$
$(l_1 - p_2 - p_3)^2 - m_t^2$	$(l_1 - p_2 - p_3)^2 - m_t^2$	$(l_1 + p_1 + p_3)^2 - m_H^2$	$(l_1 - p_2 - p_3)^2 - m_t^2$
$(l_2 - p_2 - p_3)^2 - m_t^2$	$(l_2 - p_2 - p_3)^2 - m_t^2$	$(l_2 + p_1 - p_2)^2 - m_H^2$	$(l_2 - p_2 - p_3)^2 - m_H^2$

F5	F6	F7
$l_1^2 - m_H^2$	$l_1^2 - m_H^2$	$l_1^2 - m_t^2$
$l_2^2 - m_t^2$	$l_2^2 - m_t^2$	$l_2^2 - m_t^2$
$(l_1 - l_2)^2 - m_t^2$	$(l_1 - l_2)^2 - m_t^2$	$(l_1 - l_2)^2 - m_H^2$
$(l_1 + p_1)^2 - m_H^2$	$(l_1 - p_3)^2 - m_H^2$	$(l_1 + p_1)^2 - m_t^2$
$(l_2 + p_1)^2 - m_t^2$	$(l_2 - p_3)^2 - m_H^2$	$(l_2 + p_1)^2 - m_t^2$
$(l_1 - p_3)^2 - m_H^2$	$(l_2 + p_2)^2 - m_t^2$	$(l_1 - p_2)^2 - m_t^2$
$(l_2 - p_3)^2 - m_t^2$	$(l_1 + p_1 + p_2)^2 - m_H^2$	$(l_2 - p_2)^2 - m_t^2$
$(l_1 - p_2 - p_3)^2 - m_H^2$	$(l_1 - l_2 + p_1)^2 - m_t^2$	$(l_1 - l_2 + p_3)^2 - m_H^2$
$(l_2 - p_2 - p_3)^2 - m_t^2$	$(l_1 - l_2 - p_2 - p_3)^2 - m_H^2$	$(l_2 - p_2 - p_3)^2 - m_t^2$

Table 4.2: Integral families used in the reduction (up to permutations of the external legs).

tion 2.2.1 with `Feynson` [149], we use a total of 7 integral families (along with permutations of the external legs for 5 of the families) to encode the scalar integrals appearing in all form factors. The two-loop families used in this calculation are shown in Table 4.2.

To perform the integration-by-parts reduction [29] procedure outlined in Section 2.3, we begin by identifying a suitable basis of master integrals. Retaining all masses, we find that at two-loop a total of 494 master integrals are required to represent both the NLO amplitude and a closed system of differential equations. We observe that up to 11 master integrals are required within a single sector, namely, a 6-propagator non-planar sector belonging to family F7 (sector 413 using the ID notation of `Reduze 2` introduced in Section 2.3.1).

Initially, we choose a finite basis of integrals [31], as explained in Section 2.3.3, preferring dots over inverse propagators in the numerator. The basis is chosen such that we have D-factorising denominators [150, 151], meaning that, post-reduction (such that $F_i^{(1)} = \sum_{k=1}^{494} c_i^k(\boldsymbol{s}, D)\, \mathcal{I}_k$), the denominator of each of the rational function master coefficients factorises into a product of purely kinematic- and spacetime-dependent functions:

$$c_i^k(\boldsymbol{s}, D) = \frac{g_i^k(\boldsymbol{s}, D)}{h_i^k(\boldsymbol{s}, D)} \to \frac{g_i^k(\boldsymbol{s}, D)}{h_{i,\boldsymbol{s}}^k(\boldsymbol{s})\, h_{i,D}^k(D)}\,. \tag{4.2.28}$$

Using this basis, the time to numerically evaluate all form factors to a precision of 10^{-3} using `pySecDec` is $\mathcal{O}(100h)$ on a single GPU. The evaluation time can be decreased by 2-3 orders of magnitude by further optimising the basis choice. Focusing on the integrals dominating the run time, specifically, the top-level sectors in all integral families and especially those in the most complicated non-planar families (F6 and F7), we searched for a basis in which the masters in the top level ($t = 7$, in the notation of Section 2.3.1) sectors and, where possible, next-to-top level ($t = 6$) sectors had coefficients free of poles in the dimensional regulator, ϵ. To obtain a basis with the required properties we found it necessary to employ both dots and dimensional recurrence relations [36, 37, 152] of the type discussed in Section 2.3.3.

During the basis search, we found it of practical use to reduce individual sectors neglecting subsectors, thereby avoiding the reconstruction of the vastly more complicated subsector master coefficients, for a large number of different possible basis choices. With the pole-free coefficient criterion satisfied, we only need to expand the top-level master integrals to leading order in the regulator, vastly reducing the time required to evaluate them numerically. Furthermore, since we will use the same basis for the evaluation with `pySecDec` and for the differential equations, we must also avoid poles of the regulator in the "diagonal" elements of the differential equation system (as these cannot be removed by similarity transformations of the partial derivative matrices $\mathbf{A}_{s_j}$ later).

Our final basis choice consists of integrals with up to three dots expressed in $D \pm 2n$ in the set $\{2-2\epsilon, 4-2\epsilon, 6-2\epsilon, 8-2\epsilon\}$. We could eliminate $1/\epsilon$ poles in the amplitude coefficients for all $t = 7$ master integrals and many of the $t = 6$ integrals while retaining finiteness and D-factorising coefficients for the new basis of integrals[1]. Crucially, to obtain a basis with these properties, we found it necessary to select integrals in different numbers of dimensions within a single sector.

Having settled on an improved basis, we generate the dimensional recurrence relations and differential equations of the master integrals using `Reduze 2`, firstly with all in $D = 4 - 2\epsilon$. We generate IBP equations with `Kira` [26, 27] covering all integrals appearing in the amplitude, differential equations and dimensional recurrence relations, again in D. Next, we replicate these equations with the relevant shifts of D (that is to say, $\pm 2n$) to cover the entire system, such that we have enough information to express integrals in any of our equations in terms of masters in any of the relevant dimensions. We can load this entire set of equations along with the unreduced amplitude split on coupling structures into `Ratracer` [153] and, defining

[1] In our final basis, we have a total of 25 6-propagator master integrals (+25 obtained by crossing) belonging to `F1`, `F2` and `F4` with a $1/\epsilon$ present in their coefficient in the amplitude. The integrals $\mathcal{I}^{\texttt{F5},D=6-2\epsilon}_{(0,1,1,1,1,0,2,1,0)}(s,t)$ and $\mathcal{I}^{\texttt{F5},D=6-2\epsilon}_{(0,1,1,1,1,0,2,1,0)}(s,u)$ are also present in our final basis, though they are neither finite nor quasi-finite, starting at order $1/\epsilon$. We find that these integrals do not contribute significantly to the evaluation time and did not attempt to improve our basis of master integrals further. However, this would be possible in principle.

our choice of masters, we can solve this system of equations using `Kira`, `Ratracer`, and `Firefly` [154, 155] to express our amplitude and differential equations in terms of our preferred basis of integrals.

We stress that the reduction is obtained fully symbolically, retaining all masses and invariants (m_t is set to 1 in our reduction, but can be restored by dimensional analysis). Using the same setup, we also obtain a reduction with $m_H^2/m_t^2 = 12/23$. We find the total size of the rational coefficients in the reduced amplitude to be 99Gb for the fully symbolic reduction and 8.5Gb with the numeric mass ratio inserted, when separated on coupling structures as in (4.2.17).

As a cross-check of the reduction and our amplitude, we independently perform a reduction to a different set of masters with the Higgs boson mass set to a numerical constant and confirm the value of our amplitude after the numerical evaluation of the master integrals. We further checked the integral reduction by obtaining reductions for individual phase-space points, by substituting all kinematic invariants and masses with randomly selected rational values.

4.2.5 Evaluation of the Master Integrals

To evaluate the master integrals appearing in our two-loop amplitudes, we rely on the method of sector decomposition discussed in Section 2.4, as implemented in the latest version of `pySecDec`. We first generate expressions for the reduced amplitudes in terms of the 494 master integrals, as described in Section 4.2.4. The amplitudes along with the definitions of the integral families are passed to `pySecDec`, which generates a single code capable of evaluating all bare form factors $F_{i,j}^{(1)}$, with $i = 1, 2$ and $j = \{g_3 g_4 g_t,\, g_3^2 g_t,\, g_4 g_t^2,\, g_3^2 g_t^2,\, g_3 g_t^3,\, g_t^4\}$. The code is automatically generated such that the master integrals are numerically evaluated only once per phase-space point and then used to generate results for each of the form factors and coupling structures.

Our amplitude code is generated by retaining the full symbolic dependence on s, t,

m_t, m_H and expanding in ϵ. When evaluating phase-space points, in order to obtain numerically stable coefficients, it is necessary to insert the Mandelstam invariants and masses in a precision higher than the usual floating point double precision. In our code, the input values for the Mandelstam invariants and masses are cast to rational numbers by picking the smallest fraction which reproduces s/m_t^2 and t/m_t^2 to a precision of 10^{-5}, we also set $m_H^2 = 12/23$, with $m_t^2 = 1$. We stress, however, that since we have retained the full symbolic dependence on the masses in the integral reduction and the generation of our code, we can therefore arbitrarily vary the value of the Higgs boson and top-quark masses.

Due to the significant size of the rational coefficients present in our fully symbolic amplitude, the evaluation of the master integral coefficients can itself be time-consuming, taking a few minutes to obtain the numeric value of all of the master integral coefficients. We, therefore, find it beneficial to generate a second code with the specific value for the Higgs boson mass pre-inserted into the coefficients, this reduces the time taken to evaluate the master integral coefficients significantly.

Upon integration, with the master integral basis we have chosen, we observe spurious poles up to order ϵ^{-4} in the coupling structures $g_3^2 g_t^2$, $g_3 g_t^3$ and g_t^4. Upon integration, the coefficient of the $\epsilon^{-4}, \epsilon^{-3}$ and ϵ^{-2} poles vanish within the precision of the numerical integration, leaving a non-zero ϵ^{-1} pole (for structures $\{g_3 g_4 g_t, g_3^3 g_t, g_3 g_t^3, g_t^4\}$ in form factor $F_1^{(1)}$ and for g_t^4 in $F_2^{(1)}$) and finite part. The remaining UV ϵ^{-1} pole is cancelled against the corresponding counter-term amplitude only after integration.

When evaluating the amplitude, `pySecDec` adaptively adjusts the precision with which each integral is obtained in order to reach a given precision for the amplitude (more specifically, each form factor, $F_{i,j}^{(k)}$) in the minimum time. This means that complicated (slow to evaluate or slow to converge) integrals are typically sampled less by the algorithm unless they dominate the uncertainty estimate on the amplitude. In contrast, the algorithm may spend more time evaluating simple integrals precisely, if their contribution to the amplitude is large. In our production runs, we request a relative precision of 10^{-3} on the finite part of each two-loop form factor for each

coupling structure, $F^{(1)}_{i,j}$.

For a typical bulk phase-space point, with $s \approx 561/130 \cdot m_t^2$ and $t \approx -566/217 \cdot m_t^2$, the integration takes approximately five minutes on four GPUs[1]. For the selected phase-space point, the algorithm spends the most time evaluating the integrals $\mathcal{I}^{\texttt{F4}}_{(1,0,1,1,1,1,1,0,1)}(s,t)$ and $\mathcal{I}^{\texttt{F4}}_{(1,0,1,1,1,2,0,0,1)}(s,t)$ and uses the most integrand evaluations for $\mathcal{I}^{\texttt{F4}}_{(1,0,1,1,1,1,1,0,1)}(s,t)$ and $\mathcal{I}^{\texttt{F4}}_{(1,0,1,1,1,1,1,0,1)}(s,u)$. The least precisely known integrals are $\mathcal{I}^{\texttt{F4}}_{(1,0,1,1,1,1,1,0,0)}(s,t)$ with an uncertainty of 3×10^{-4} and $\mathcal{I}^{\texttt{F1}}_{(1,0,1,1,1,1,1,0,0)}(s,t)$ with an uncertainty of 1×10^{-4}, followed by $\mathcal{I}^{\texttt{F4}}_{(1,0,0,1,2,1,1,0,0)}(s,t)$ with an uncertainty around 6×10^{-5}. For a point in the high energy regime with $s \approx 123 \cdot m_t^2$ and $t \approx -7/5 \cdot m_t^2$ we find that the integrals $I^{\texttt{F4}}_{(1,0,1,0,2,1,0,1,1)}(s,t)$ and $I^{\texttt{F4}}_{(1,0,1,0,2,1,0,1,1)}(s,t)$ are the least precisely known after an integration time of two hours. Up to this point, the most time was spent on the integrals $\mathcal{I}^{\texttt{F4}}_{(1,0,1,1,1,2,0,0,1)}(s,u)$ and $\mathcal{I}^{\texttt{F1}}_{(0,1,1,1,1,1,0,2,1,0)}(s,u)$, which are also sampled the most. We remark that all of these integrals are planar.

As a cross-check of the numerical evaluation of our master integrals, we have also obtained a set of differential equations, using the methods outlined in Section 2.5, which are symbolic in s and t and have the aforementioned numeric values for the masses. The differential equations are obtained for the same master integral basis as selected for the numerical evaluation described above and are therefore not in canonical form. They are then rescaled by rational functions of ϵ to eliminate poles in ϵ in the differential equation matrices. To verify our numerical evaluation, we use `pySecDec` to generate a number of boundary points at high precision along a contour of increasing s in the s-t plane as in Fig. 4.2. We then run smaller contours in `DiffExp` between these boundary points to obtain results for the entire contour (except for the $t\bar{t}H$ threshold where we run very close to the threshold above and below without ever crossing it). Similarly to Fig. 2.8, we check at given benchmark points that the evaluations from `DiffExp` and `pySecDec` are consistent and plots of a selection of rescaled master integrals are shown in Fig. 4.3. The real and imaginary parts of the coefficients of the required orders of ϵ in the expansion of the rescaled

[1] Nvidia A100-PCIE-40GB, CUDA v12040

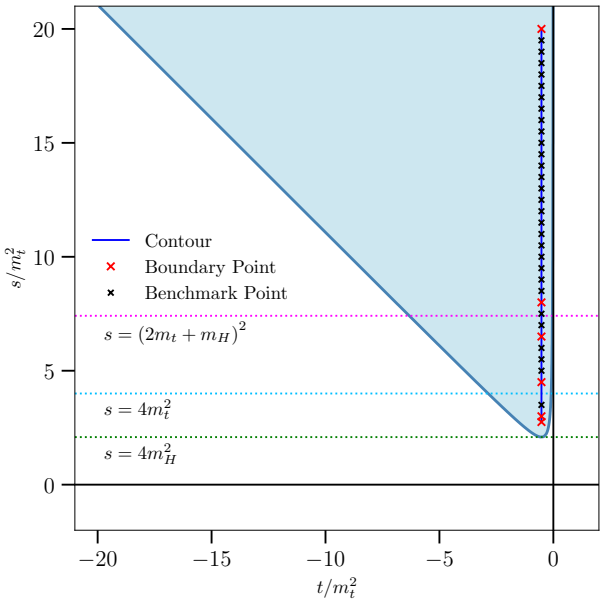

Figure 4.2: The physical region in the s-t plane, given by (4.2.26), with the physical thresholds corresponding to s-channel cuts shown with dotted lines. Our test contour increasing in s is shown in blue with boundary points plotted along with benchmark points verified in `pySecDec`.

master integrals are plotted along with the corresponding boundary and benchmark points. A ratio of the `pySecDec` result to the `DiffExp` result is given in the lower subplot. For completeness, we list the rescalings of the selected master integrals here:

$$c_5(\epsilon) = \frac{\epsilon}{(\epsilon-1)^2(2\epsilon-3)(2\epsilon-1)^2(2\epsilon+1)(3\epsilon-2)(3\epsilon-1)(4\epsilon-3)(4\epsilon-1)},$$
$$c_{155}(\epsilon) = \frac{\epsilon^2}{2\epsilon-1}, \qquad c_{353}(\epsilon) = \frac{\epsilon^4}{2\epsilon-1}, \qquad c_{464}(\epsilon) = \frac{\epsilon^4}{2\epsilon-1}.$$

In order to determine how we should perform the analytic continuation of the master integrals from the unphysical region to the physical region, we first recall that the Feynman prescription in momentum space corresponds, in Feynman parameter space, to the following replacement in the second Symanzik polynomial $\mathcal{F}$:

$$\mathcal{F} \longrightarrow \mathcal{F} - i\delta \tag{4.2.29}$$

where we have used the postive-definiteness of the first Symanzik polynomial $\mathcal{U}$.

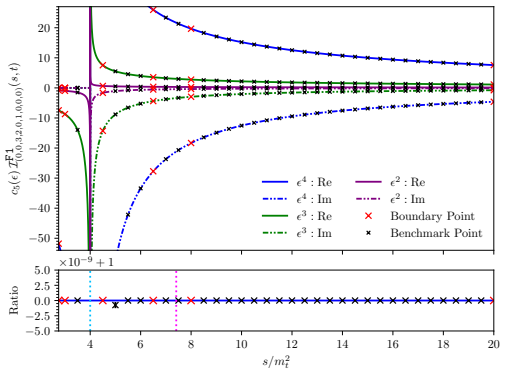

(a) An integral which diverges at the $t\bar{t}$ threshold.

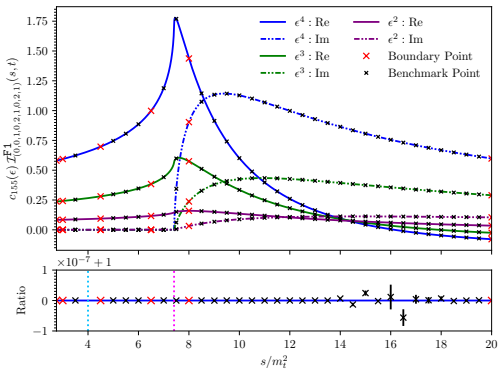

(b) An integral with a $t\bar{t}H$ threshold.

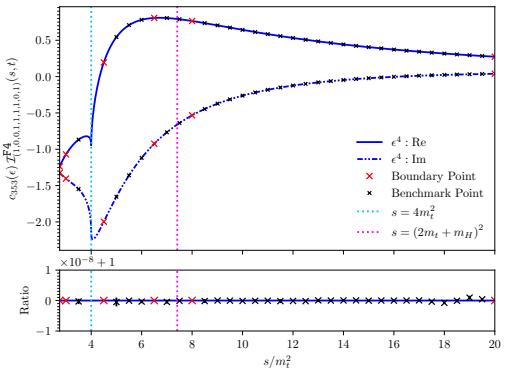

(c) An integral with a $t\bar{t}$ threshold.

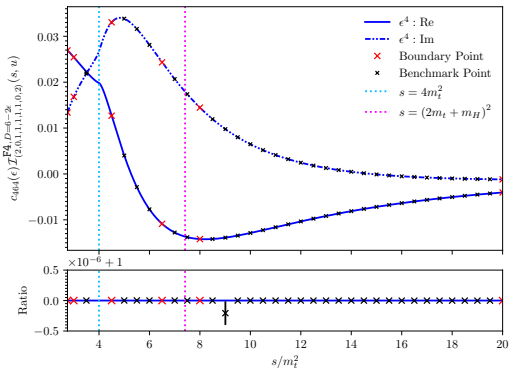

(d) A $t = 7$ top-level integral.

Figure 4.3: Real and imaginary parts of coefficients in the ϵ-expansion of selected rescaled master integrals taken along the contour shown in Fig. 4.2. a) Rescaled master #5: $c_5(\epsilon)\,\mathcal{I}^{\texttt{F1}}_{(0,0,3,2,0,1,0,0,0)}(s,t)$, b) rescaled master #155: $c_{155}(\epsilon)\,\mathcal{I}^{\texttt{F1}}_{(0,0,1,0,2,1,0,2,1)}(s,t)$, c) rescaled master #353: $c_{353}(\epsilon)\,\mathcal{I}^{\texttt{F4}}_{(1,0,0,1,1,1,1,0,1)}(s,t)$ and d) rescaled master #464: $c_{464}(\epsilon)\,\mathcal{I}^{\texttt{F4},D=6-2\epsilon}_{(2,0,1,1,1,1,1,0,2)}(s,u)$. The lower panel of each figure shows the ratio of the `pySecDec` result to the `DiffExp` result for the real part of the coefficient of ϵ^4 which contributes to the amplitude at finite order.

This prescription must be applied consistently in order to obtain valid results when crossing threshold singularities. From the graphical construction of the second Symanzik polynomial $\mathcal{F}$ introduced in Section 2.2.19, this corresponds to sending all the (squared) momenta flowing between two 2-forests, $s_{(T^1,T^2)}$, to $s_{(T^1,T^2)} + i\delta$ and internal masses squared, m_i^2, to $m_i^2 - i\delta$ [48].

In `DiffExp`, we encounter segments centred on thresholds and their expansions may involve multi-valued functions such as logarithms or square roots. At these points, the δ-prescription supplied as an input by the user is applied. Given that $s_{(T^1,T^2)}$ are linear combinations of the Mandelstam variables and external masses (which obey conservation relations), `DiffExp` instead takes as input a list of irreducible polynomials ("DeltaPrescriptions") in the kinematic invariants of the problem which are zero on these thresholds and an additional term $\pm i\delta$ to prescribe the branch choice. For physical thresholds, the correct choice of $\pm i\delta$ is essential to obtain accurate results but `DiffExp` also requires a choice to be made for polynomials which go to zero in the denominators of entries in the partial derivative matrices which do not correspond to physical thresholds – this choice can be freely made without affecting results.

In practice, similarly to [156], we construct the power sets of both the external momenta and the internal masses and generate a list of δ-prescriptions of the form $s - m^2 + i\delta$ where s is a generalised squared sum of momenta and m^2 is a generalised squared sum of internal masses. We obtain a list of irreducible polynomials appearing in the denominators of entries in our partial derivative matrices $\mathbf{A}_{s_j}$ and then see which correspond directly to prescriptions in our constructed list and give them the correct sign of $i\delta$ by expanding the given irreducible polynomial about that point. The remaining denominator polynomials are non-physical and we arbitrarily assign $+i\delta$. This method generates correct results for all points checked with `pySecDec` and changing the sign of a prescription for a polynomial corresponding to a physical threshold can be explicitly seen to give the wrong result.

4.2.6 Electroweak Renormalisation

At higher orders in electroweak theory, a tadpole renormalisation has to be performed on top of the usual field, mass and vertex renormalisation. Since the gaugeless limit removes the coupling α from the theory, conventional input parameter schemes that involve α cannot be used. As described in Section 4.2.1, we fix the input parameters m_H and m_t in the on-shell scheme and use the G_μ scheme for the vev. Tadpole contributions are treated within the Fleischer-Jegerlehner tadpole scheme (FJTS) [157].

The G_μ scheme imposes the renormalisation condition that the expression for muon decay corresponds at all orders to the effective four-fermion tree-level interaction in Fermi's theory, thereby fixing the relation between G_μ and the renormalised vev, and determining the relation between the bare, v_0, and renormalised vev, v, at each order. In the Yukawa model utilised here, the vertex required for muon decay is not present, therefore it is not possible to directly derive the G_μ scheme relation between the bare and renormalised vev.

In principle, the renormalisation constant for the vev can be fixed from any electroweak vertex in the theory, for example, the triple and quartic Higgs self-interaction vertices or the Yukawa vertex, by requiring that the higher order electroweak corrections to the vertices are finite. The consistency of the electroweak theory means that the pole part of the vev renormalisation constant matches in all schemes and independently of which vertex is used to fix it, only the finite part differs. However, to facilitate the use of our result and its interpretation, we present our main results using the G_μ scheme, we obtain the finite parts of the vev counter term using the complete expression for the vev counterterm presented in [141] in the limit $M_W \to 0, M_Z \to 0$. In Appendix A.1 we derive the vev renormalisation constants from each of the vertices in our theory and discuss this point in further detail. With the chosen schemes and conditions, the renormalised quantities and counterterms

$$H_0 = \sqrt{Z_H} H = \sqrt{1+\delta_H} H, \tag{4.2.30}$$

$$t_0 = \sqrt{Z_t} t = \sqrt{1+\delta_t} t, \tag{4.2.31}$$

$$m^2_{H,0} = m^2_H (1+\delta m^2_H), \tag{4.2.32}$$

$$m_{t,0} = m_t (1+\delta m_t), \tag{4.2.33}$$

$$v_0 + \Delta v = v(1+\delta_v) + \Delta v, \tag{4.2.34}$$

can be fixed. Note that the vev renormalisation condition contains one contribution, Δv, from the FJTS for the shift of the vev and another contribution, δ_v, from the vertex correction. For a detailed description of the procedure, please refer to Appendix A. The explicit expressions used in this work are listed in Appendix A.2 and a comparison to expressions in the literature is presented in Appendix A.3.

A gluon field renormalisation factor, Z_g, or strong coupling renormalisation is not needed, since it would only receive electroweak corrections at a higher order in the strong interaction as a mixed correction.

The renormalised amplitude $\mathcal{M}_{\text{ren}}$ can now be calculated from the sum of the LO matrix element $\mathcal{M}^{(0)}$, with the bare fields and parameters expressed in terms of the renormalised quantities, and the NLO matrix element $\mathcal{M}^{(1)}$:

$$\begin{aligned}\mathcal{M}_{\text{ren}} = Z_H \cdot \Big[\mathcal{M}^{(0)} \left(m_t \left(1+\delta m_t\right), m^2_H \left(1+\delta m^2_H\right), v\left(1+\delta_v\right) + \Delta v \right) + \\ \mathcal{M}^{(1)} \left(m_t, m^2_H, v \right) \Big]\end{aligned} \tag{4.2.35}$$

where we have suppressed the gluon colour indices of the matrix element appearing in (4.2.9). The matrix element $\mathcal{M}^{(0)}$ contains all one-loop contributions as well as diagrams with counterterm insertions. All occurring parameters are the renormalised ones. Expanding to first order in δX with $X = \{H, t, m^2_H, m_t, v\}$ and including the tadpole corrections to the vev, Δv, we may rewrite the renormalised amplitude as,

$$\mathcal{M}_{\text{ren}} = \mathcal{M}^{(0)}(m_t, m^2_H, v) + \mathcal{M}^{(1)}_{\delta \text{X}}(m_t, m^2_H, v) + \mathcal{M}^{(1)}(m_t, m^2_H, v) + \mathcal{O}(\delta X^2), \tag{4.2.36}$$

with

$$\begin{aligned}\mathcal{M}^{(1)}_{\delta\mathrm{X}} =&\delta_H\mathcal{M}^{(0)}(m_t, m_H^2, v) + \delta m_t\mathcal{M}^{(0)}_{\delta m_t}(m_t, m_H^2, v) + \delta m_H^2\mathcal{M}^{(0)}_{\delta m_H^2}(m_t, m_H^2, v)\\ &+ \delta v\mathcal{M}^{(0)}_{\delta v}(m_t, m_H^2, v) + \Delta v\mathcal{M}^{(0)}_{\Delta v}(m_t, m_H^2, v).\end{aligned} \tag{4.2.37}$$

In practice, we separate the counterterm amplitudes, $\mathcal{M}^{(1)}_{\delta\mathrm{X}}$, according to the form factor, $i = 1, 2$, and the coupling structure, $j = g_3g_t, g_t^2$, appearing in the amplitude as well as the additional coupling structures appearing in the counterterms δX themselves. We obtain the finite one-loop and two-loop renormalised form factors by taking the combination,

$$F_i^{(0),\mathrm{fin}} = F_i^{(0)}, \tag{4.2.38}$$

$$F_i^{(1),\mathrm{fin}} = F_i^{(1)} + F_i^{(1),\delta X}, \tag{4.2.39}$$

respectively, where $F_i^{(1),\delta X}$ collects the counterterm contribution obtained by applying the projectors (given in (4.2.13) and (4.2.14)) to the counterterm amplitude in (4.2.37). The counterterm amplitudes are generated by inserting the counterterm vertices given in Appendix A.2 into the one-loop amplitude, leaving the counterterms δX and Δv symbolic, then factoring them out of the amplitude. The counterterms δX and the tadpole terms Δv contain $1/\epsilon$ divergences, therefore, the counterterm amplitudes must be expanded up to and including $\mathcal{O}(\epsilon)$ in order to obtain correct results for $\mathcal{M}^{(1)}_{\delta\mathrm{X}}$ at finite order. We evaluate the counterterm amplitudes numerically in `pySecDec` and insert the A_0 and B_0 (tadpole and bubble) integrals appearing in the counterterms symbolically.

We remark that, when considering the form factors separated by individual coupling structures, the sum of the two-loop and corresponding counter term contribution is not finite for all form factors, i.e. the sums $F_{i,j}^{(1)} + F_{i,j}^{(1),\delta X}$ are not individually finite. The reason for this is that, in the SM, the couplings g_t, g_3, and g_4 are not independent quantities, they must obey the relations given in (4.2.6) for the ϵ poles of the renormalised amplitude to cancel. As a result, the Higgs boson cubic, g_3, and quartic, g_4, couplings can not be naively varied without also modifying the

underlying theory, for example by adding mass dimension-6 (and/or dimension-8) operators (see [158], for example) or by imposing additional particles/symmetries.

A further complication arises when considering the renormalised form factors separated by individual coupling structures in G_μ scheme. As described above, in this scheme the δ_v counterterm is derived using the muon decay process, which requires the presence of W and Z bosons and their associated couplings in the theory. Using results from the literature for this counter term, it is not straightforward to separate the contributions to δ_v in the G_μ scheme according to the couplings g_3, g_4 and g_t. The contributions of different coupling structures to the δ_v counterterm also depend on the choice of the renormalisation conditions, as described in Appendix A.1. In this work, we therefore do not attempt this separation and report only the finite renormalised form factors $F_i^{(1),\text{fin}}$ constructed employing the SM values/relations for the various couplings.

4.3 Results

In this section, we present the results of our computation. We begin by discussing both the bare, F_1 and F_2, and renormalised, F_1^{fin} and F_2^{fin}, form factors, before presenting results for the total cross section and differential distributions at NLO$^{\text{EW}}$, including only the Yukawa and self-coupling contributions.

In Table 4.3, we provide explicit numbers for the NLO$^{\text{EW}}$ contributions of each of the coupling structures to the bare amplitude form factors F_1 and F_2. We note that these numbers are the coefficients of the coupling structures (and so need to be multiplied by the coupling structures themselves as in (4.2.17)). We make a number of comments about these results. Firstly, we note that F_1 and F_2 correspond to the $\mathcal{M}^{++}$ and $\mathcal{M}^{+-}$ helicity amplitudes, respectively. Therefore, contributions to F_1 have an initial state with a total spin of zero, whilst F_2 receives contributions from initial states with total spin two. For the structures $g_3 g_4 g_t$ and $g_3^3 g_t$, the contributions to $F_2^{(1)}$ are zero because these diagrams are entirely one-particle-reducible (1PR)

j: $\epsilon^{\#}$	$F^{(1)}_{1,j}$	$F^{(1)}_{2,j}$
$g_3 g_4 g_t : \epsilon^{-1}$	$+7.317018424938384 \cdot 10^{-5}$ $+3.530994674708006 \cdot 10^{-5}\, i$	0
$g_3 g_4 g_t : \epsilon^{0}$	$+3.273276184619130 \cdot 10^{-4}$ $+2.941949902790170 \cdot 10^{-4}\, i$	0
$g_3^3 g_t : \epsilon^{-1}$	$+4.035301063033099 \cdot 10^{-6}$ $+1.947326866890242 \cdot 10^{-6}\, i$	0
$g_3^3 g_t : \epsilon^{0}$	$+3.494986290012938\mathbf{51} \cdot 10^{-5}$ $-4.477006613201774\mathbf{40} \cdot 10^{-5} i$	0
$g_4 g_t^2 : \epsilon^{0}$	$+1.4701555653754\mathbf{324} \cdot 10^{-4}$ $-3.1468546340616\mathbf{729} \cdot 10^{-4}\, i$	0
$g_3^2 g_t^2 : \epsilon^{0}$	$-3.0041895984\mathbf{712} \cdot 10^{-4}$ $+1.362086184\mathbf{2796} \cdot 10^{-4}\, i$	$-1.06780\mathbf{8312} \cdot 10^{-6}$ $+4.82551\mathbf{0899} \cdot 10^{-6}\, i$
$g_3 g_t^3 : \epsilon^{-1}$	$+9.62086881\mathbf{678} \cdot 10^{-5}$ $-1.15718379\mathbf{579} \cdot 10^{-4}\, i$	0
$g_3 g_t^3 : \epsilon^{0}$	$+7.723391\mathbf{3221} \cdot 10^{-4}$ $+1.229726\mathbf{3623} \cdot 10^{-4}\, i$	$+5.9472\mathbf{2962} \cdot 10^{-5}$ $+6.5464\mathbf{6767} \cdot 10^{-5}\, i$
$g_t^4 : \epsilon^{-1}$	$-4.50970913522\mathbf{3640} \cdot 10^{-3}$ $-1.00902628\mathbf{90534} \cdot 10^{-3}\, i$	$-5.411414\mathbf{11126} \cdot 10^{-5}$ $+7.833751\mathbf{22326} \cdot 10^{-5}\, i$
$g_t^4 : \epsilon^{0}$	$-2.11957\mathbf{55326} \cdot 10^{-2}$ $-8.82776\mathbf{96398} \cdot 10^{-3}\, i$	$-3.365\mathbf{9613} \cdot 10^{-4}$ $+4.633\mathbf{8899} \cdot 10^{-4}\, i$

Table 4.3: Numeric results for the bare form factors, $F^{(1)}_{i,j}$, for each coupling structure on the phase-space point: $\{s = 799/125,\ t = -519/500,\ m_H^2 = 12/23,\ m_t^2 = 1\}$. Boldface digits represent the error on the final two stated digits and where there are none, the stated digits are accurate to the given precision. Missing ϵ orders are understood to be identically zero.

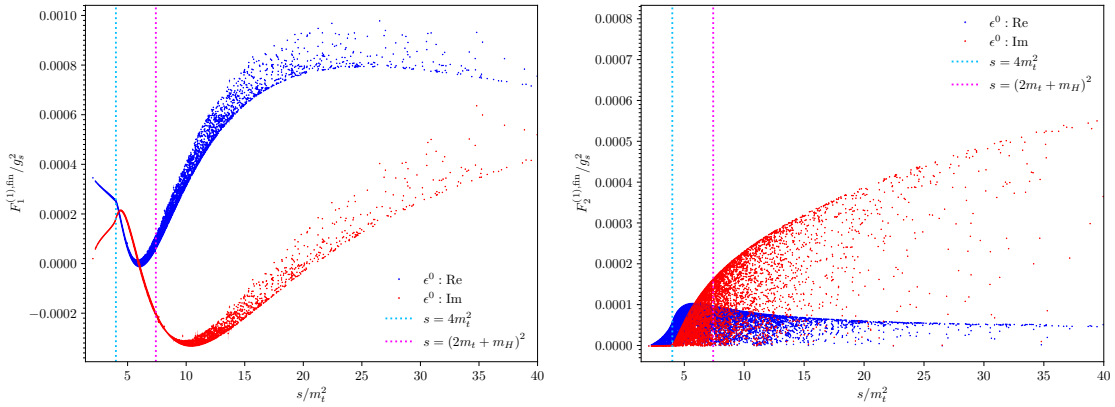

Figure 4.4: The UV-renormalised form factors $F_1^{(1),\text{fin}}$ (left panel) and $F_2^{(1),\text{fin}}$ (right panel) divided by g_s^2. Note that the spread of points, which is due to the t-dependence, is milder in $F_1^{(1)}$ than in $F_2^{(1)}$. The uncertainty of each phase-space point due to the limited precision of the numerical integration is indicated with an error bar.

via a cut through a Higgs boson propagator (see Table 4.1 and Fig. 4.1), therefore the initial states have total spin zero. Similarly, the contribution from structure $g_4 g_t^2$ to $F_2^{(1)}$ is zero since diagrams with this structure can only contribute to spin zero due to their symmetry. Finally, there is no $1/\epsilon$ pole contribution to $F_2^{(1)}$ from structure $g_3 g_t^3$ because the only 1PI counterterm diagrams (which must topologically be LO box diagrams to contribute to $F_2^{(1)}$) which could correspond to this coupling structure have counterterm insertions in the Yukawa vertex, the relevant part of the correction is given in Fig. A.1e in Appendix A.1. This particular contribution to the Yukawa vertex correction is ϵ-finite, hence this structure's contribution to $F_2^{(1)}$ is also finite.

In Fig. 4.4 we display the finite, UV-renormalised, form factors as a function of the Mandelstam invariant s. Examining the $F_1^{(1),\text{fin}}$ form factor we observe that it has both a real and imaginary part for all physically accessible values of s, even close to the HH production threshold, this is because it receives a large contribution from diagrams with a two-particle cut through a pair of Higgs bosons (i.e. with a HH threshold), see e.g. Figs. 4.1a–4.1d. The t-dependence, visible in the spread of points at a given s value, is much milder for $F_1^{(1),\text{fin}}$ than $F_2^{(1),\text{fin}}$. Considering the $F_2^{(1),\text{fin}}$

form factor, we note that it is also complex-valued in the entire physically-accessible region of phase-space. However, only a small imaginary part exists between the HH and $t\bar{t}$ thresholds. As discussed, the $F_2^{(1),\text{fin}}$ form factor receives contributions only from 1PI diagrams, the only class of diagrams contributing with a HH threshold in the s-channel are those of Fig. 4.1d. We find that numerically the contribution of these diagrams to $F_2^{(1),\text{fin}}$ at low invariant mass is much smaller than that of other coupling structures. In Fig. 4.5, we present plots of the finite term of the individual bare form factors, $F_{i,j}^{(1)}$, separated on coupling structures as in (4.2.17). Note again that the spread of points due to the t-dependence is more pronounced in the contributions to $F_2^{(1)}$ than in the contributions to $F_1^{(1)}$.

In order to verify our results, we carried out a number of checks. Firstly, we checked that our two independently generated amplitudes (before reduction to masters) were symbolically identical up to sector relations and symmetries. Secondly, we confirmed that the amplitude is symmetric under the exchange of t and u by comparing the numerical results of multiple pairs of phase-space points wherein the first point's t-value is substituted by $u = 2m_H^2 - s - t$ in the second and observing that these are identical within the stated numerical error. Thirdly, for the two-loop contribution, we observed that before UV renormalisation the only poles appearing were $1/\epsilon$ (spurious poles up to order $1/\epsilon^4$ cancel). After UV renormalisation, all poles cancel which simultaneously corroborates our expectation that there are neither soft nor collinear IR singularities. We also checked that poles of the bare form factors $F_{i,j}^{(1)}$ are purely real below the $t\bar{t}$ threshold for a selection of phase-space points in this kinematic region.

For the presentation of our final results, we use the `PDF4LHC21_40` [159] distribution functions interfaced via `LHAPDF` [160] and set the factorisation and renormalisation scale to $\mu_r = \mu_f = m_{HH}/2$. The masses of the Higgs boson and top quark are set to $m_H = 125$ GeV, $m_t = \sqrt{23/12}\, m_H = 173.055$ GeV, respectively, and we set $G_F = 1.1663787 \cdot 10^{-5}$ GeV^{-2}, corresponding to $v = 246.22$ GeV.

Results for the total and differential cross section at the LHC with a hadronic centre-

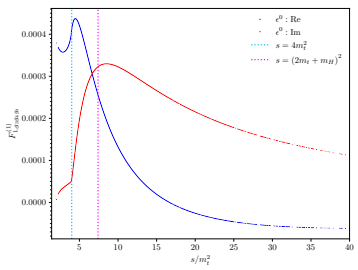

(a) $F^{(1)}_{1,g_3 g_4 g_t}$

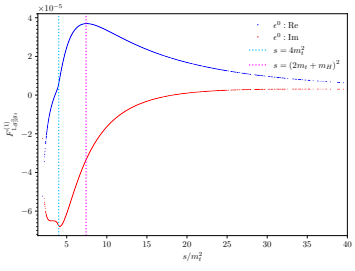

(b) $F^{(1)}_{1,g_3^3 g_t}$

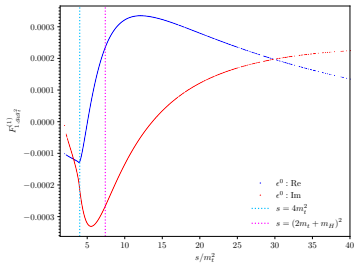

(c) $F^{(1)}_{1,g_4 g_t^2}$

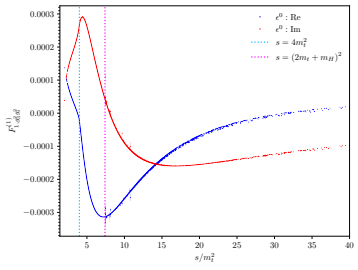

(d) $F^{(1)}_{1,g_3^2 g_t^2}$

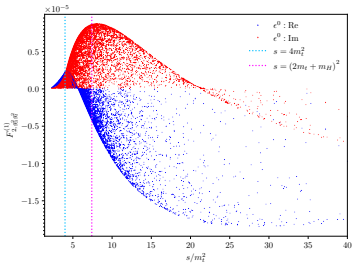

(e) $F^{(1)}_{2,g_3^2 g_t^2}$

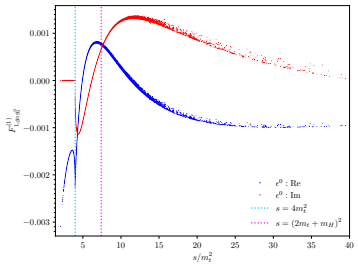

(f) $F^{(1)}_{1,g_3 g_t^3}$

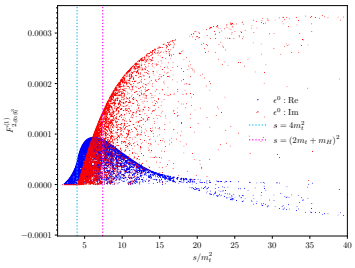

(g) $F^{(1)}_{2,g_3 g_t^3}$

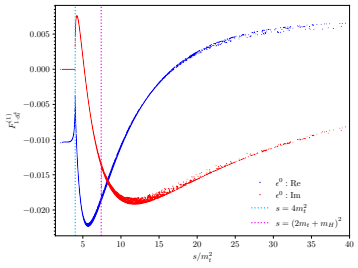

(h) $F^{(1)}_{1,g_t^4}$

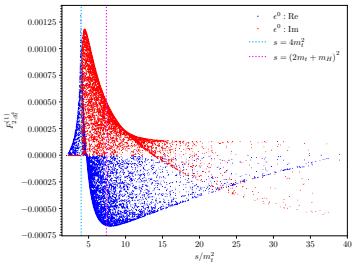

(i) $F^{(1)}_{2,g_t^4}$

Figure 4.5: Plots of the ϵ^0 coefficient of the bare form factors separated on coupling structure, $F^{(1)}_{i,j}$.

$\sqrt{s}$	13 TeV	13.6 TeV	14 TeV
LO [fb]	16.45	18.26	19.52
NLO^{EW} [fb]	16.69	18.52	19.79
$\text{NLO}^{\text{EW}}/\text{LO}$	1.01	1.01	1.01

Table 4.4: Inclusive cross section for Higgs boson pair production for different hadronic centre-of-mass energies, $\sqrt{s}$, at LO and NLO^{EW} including only the Yukawa and self-coupling type corrections. The QCD renormalisation and factorisation scales are set to $\mu_r = \mu_f = m_{HH}/2$.

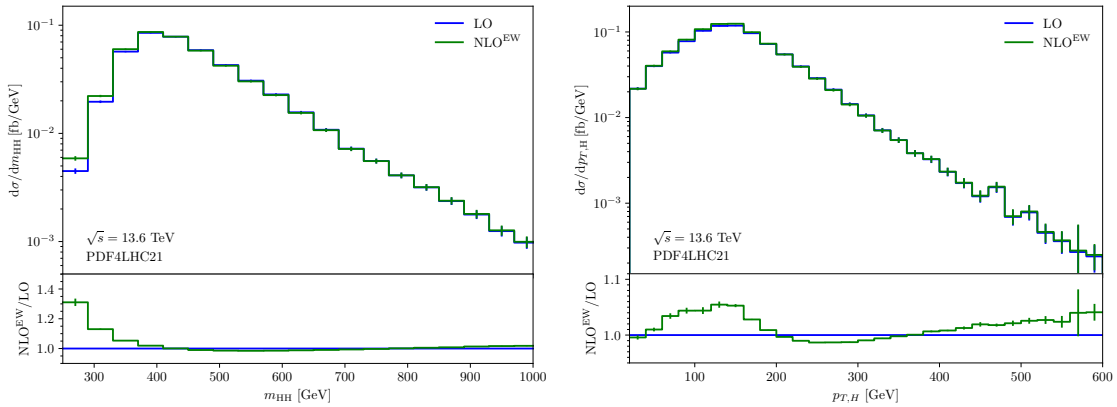

Figure 4.6: Invariant mass and transverse momentum distributions for Higgs boson pair production at LO and NLO^{EW} including only the Yukawa and self-coupling type corrections. The QCD renormalisation and factorisation scales are set to $\mu_r = \mu_f = m_{HH}/2$.

of-mass energy of $\sqrt{s} = 13\,\text{TeV}, 13.6\,\text{TeV}$ and $14\,\text{TeV}$ are given in Table 4.4 and shown differentially in m_{HH} and $p_{T,H}$ in Fig. 4.6, respectively. These results are obtained by reweighting ~ 7000 unweighted LO events with the NLO^{EW} contribution. We observe that the partial NLO^{EW} corrections computed here increase the total cross section by $\sim 1\%$. This is comparable to the size of the QCD scale uncertainty of $\sim 3\%$ obtained at N^3LO in the heavy top-quark limit [114, 115].

For the invariant mass distribution, shown in Fig. 4.6, the corrections introduce very large shape distortions, $\sim 30\%$ with the binning we select, close to the Higgs pair production threshold, compatible with the observations of [122]. In [125], it was found that the full EW corrections lead to an enhancement of the m_{HH} spectrum close to the Higgs boson pair production threshold of up to 15%. Reproducing the binning used in [125] we find an enhancement of $\sim 25\%$, suggesting that the gauge

boson contributions included in their full results partly cancel the enhancement we see at low m_{HH} values. This appears plausible when looking at individual contributions to the EW corrections for single Higgs boson production [118–120]. The shape distortions in the $p_{T,H}$ distribution of our results are less localised, with a significant 5% enhancement just below the top-quark pair production threshold and at high-$p_{T,H}$, along with suppression at the level of 2% just above the top-quark pair production threshold. In our results, we see a general enhancement at high m_{HH} and $p_{T,H}$ not present in the full EW corrections, this suggests that the gauge boson contribution dominates at high-energy and is negative.

We have also evaluated our results using the `NNPDF31_nlo_as_0118` PDF set as used in [125]. Using this PDF set, we obtain a total NLO^{EW} cross section of 20.19 fb including only the Yukawa and self-coupling type corrections, which is a 1% enhancement compared to the LO. In comparison, the full NLO^{EW} total cross section presented in [125] is 19.12(6) fb, which is a 4.2% decrease relative to the LO. This discrepancy suggests that the gauge boson contribution, appearing in the complete EW calculation, dominates the corrections and has the opposite sign to the corrections computed here.

4.4 Conclusions

We have presented the calculation of the electroweak corrections to Higgs boson pair production in gluon fusion in the gaugeless limit. In total, these partial NLO electroweak corrections increase the cross section by about 1 %. The corrections impact the Higgs boson pair production invariant mass and transverse momentum distributions, giving an enhancement of up to 30 % at low m_{HH} values due to the Yukawa-type corrections, which is larger than in the case of the full corrections presented in [125], where the enhancement is found to be 15 %. This suggests that the gauge boson contributions are negative for m_{HH} values below the $2m_t$ threshold. We also observe almost no correction for higher values of m_{HH}, in contrast to

$-10\,\%$ found in [125], suggesting again that this region is dominated by negative contributions from diagrams containing W and Z bosons.

In our calculation, we retain the full symbolic dependence on the top-quark and Higgs boson masses in the reduction to master integrals of the two-loop amplitude. All integrals are calculated using the method of sector decomposition detailed in Section 2.4 and cross-checked by evaluating them using the series expansion of differential equations as outlined in Section 2.5. We provide results for the bare amplitude divided into individual form factors separated according to the Yukawa, Higgs trilinear and quartic couplings. We present results for the UV-renormalised form factors, the di-Higgs invariant mass and the Higgs boson transverse momentum distribution. The renormalisation of partial electroweak corrections in the Yukawa model is discussed in detail, this provides relevant input for the interpretation of results presented elsewhere in the literature for non-Standard Model values of the Higgs boson self-couplings.

The results presented here, and the techniques used to obtain them (a number of which are discussed in Chapter 2), provide an important cross-check and benchmark for further analysing and interpreting the complete electroweak corrections. For example, the fully symbolic reduction to master integrals obtained using several of the ideas presented in Section 2.3 allows for the study of mass scheme uncertainties. Our results also facilitate investigating the effects of anomalous couplings, for example, anomalous trilinear and quartic Higgs boson couplings. These couplings can be varied consistently within an Effective Field Theory framework, for example the non-linear Effective Field Theory (HEFT), where the fact that the Higgs boson is an EW singlet decorrelates the trilinear and quartic Higgs couplings at leading order in the EFT expansion. Although not the main focus of this work, our complete set of differential equations, which can be evaluated using series expansion methods, may also provide useful semi-analytic insights into the structure of the electroweak corrections.

Appendix A

Details of Electroweak Renormalisation

From the Lagrangian of (4.2.4) one arrives at a fully renormalised theory by first including the vev shift $v_0 \to v_0 + \Delta v$ to obtain

$$\begin{aligned}\mathcal{L}' =& \frac{1}{2}(\partial_\mu H_0)^\dagger(\partial^\mu H_0) + \frac{\mu_0^2}{2}(v_0+\Delta v+H_0)^2 + \frac{\lambda_0}{16}(v_0+\Delta v+H_0)^4 \\ &+ i\bar{t}_0 \not{\partial} t_0 - y_{t,0}\frac{v_0+\Delta v+H_0}{\sqrt{2}}\bar{t}_0 t_0 \end{aligned} \tag{A.0.1}$$

$$\begin{aligned}=& \frac{1}{2}(\partial_\mu H_0)^\dagger(\partial^\mu H_0) + H_0\left(\mu_0^2 v_0 + \frac{\lambda_0 v_0^3}{4} + \Delta v(\mu_0^2 + \frac{3}{4}\lambda_0 v_0^2)\right) \\ &+ H_0^2\left(\frac{\mu_0^2}{2} + \frac{3v_0^2\lambda_0}{8} + \frac{3}{4}\lambda_0 v_0 \Delta v\right) + H_0^3\left(\frac{\lambda_0 v_0}{4} + \Delta v\frac{\lambda_0}{4}\right) + H_0^4\frac{\lambda_0}{16} \\ &+ i\bar{t}_0\not{\partial}t_0 - m_{t,0}\bar{t}_0 t_0 - \frac{m_{t,0}}{v_0}\Delta v \bar{t}_0 t_0 - \frac{m_{t,0}}{v_0}H_0\bar{t}_0 t_0 \ . \end{aligned} \tag{A.0.2}$$

This step is required to keep the value of v_0 at the minimum of the Higgs potential, which is shifted at NLO compared to LO. On a diagrammatic level, the shift of the minimum of the Higgs potential is caused by diagrams containing tadpole sub-diagrams.

The definition of the vev upon renormalisation is therefore related to the treatment of tadpole contributions. Tadpole counterterms can be generated in two different ways in the Lagrangian: through parameter renormalisation [138, 161, 162], or via Higgs field redefinitions [157, 161, 163, 164], see [139] for a review. The latter is also

called Fleischer-Jegerlehner scheme (FJTS). A new scheme for tadpole renormalisation, dubbed Gauge-Invariant Vacuum expectation value Scheme (GIVS), has been suggested recently [165], which is a hybrid scheme of the two schemes mentioned above, with the benefits of being gauge independent while avoiding large corrections in $\overline{\text{MS}}$-type schemes. The effects of certain input parameter schemes in SMEFT have been studied in [141].

When using OS renormalisation in unitary gauge, the FJTS is a suitable choice yielding the vev shift prescription and thereby the Lagrangian of (A.0.2). The emerging term linear in the Higgs field is identified with the tadpole counterterm

$$\delta T = \left(\mu_0^2 v_0 + \frac{\lambda_0 v_0^3}{4} + \Delta v(\mu_0^2 + \frac{3}{4}\lambda_0 v_0^2)\right) = -\Delta v m_H^2 \ , \tag{A.0.3}$$

where the first two terms in the brackets cancel upon using (4.2.5) and, in the second equality, the bare quantities have been expressed in terms of their renormalised counterparts, neglecting higher-order terms of $\mathcal{O}(\delta_X^2, \Delta v \delta_X, (\Delta v)^2)$. The renormalisation condition is that the sum of the tadpoles, T^H, and the tadpole counterterm, δT, should vanish at the given order,

$$0 \stackrel{!}{=} \delta T + T^H \quad \Leftrightarrow \quad \delta T = -T^H = -\Big[$$ 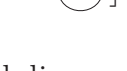 $$+$$ 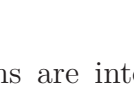 $$\Big] \ . \tag{A.0.4}$$

With this condition, all contributions from tadpole subdiagrams are integrated out and collected in the counterterm δT. Inserting (A.0.3) as well as the field, parameter, and vertex renormalisations from (4.2.30)–(4.2.34) into (A.0.2) yields the fully renormalised Lagrangian

$$\begin{aligned}\mathcal{L} =& \frac{1}{2}(1+\delta_H)(\partial_\mu H)^\dagger(\partial^\mu H) + H\delta T - \left(\frac{m_H^2}{2}\left(1+\delta m_H^2+\delta_H\right) - \frac{3\delta T}{2v}\right)H^2 \\ &- \left(\frac{g_3}{3!}\left(1+\delta m_H^2+\frac{3}{2}\delta_H-\delta_v\right) - \frac{\delta T}{2v^2}\right)H^3 - \frac{g_4}{4!}\left(1+\delta m_H^2+2\delta_H-2\delta_v\right)H^4 \\ &+ i(1+\delta_t)\bar{t}\not{\partial}t - m_t\left(1+\delta m_t+\delta_t-\frac{\delta T}{v m_H^2}\right)\bar{t}t - g_t\left(1+\delta m_t+\frac{\delta_H}{2}+\delta_t-\delta_v\right)H\bar{t}t\end{aligned} \tag{A.0.5}$$

where the couplings g_3, g_4 and g_t are the renormalised counterparts of the bare

couplings, $g_{3,0}, g_{4,0}$ and $g_{t,0}$. They obey (4.2.6) after substituting the bare quantities with their renormalised values. Since the explicit tadpole insertions into each diagram now cancel with the corresponding explicit tadpole counterterm insertions, we can neglect both of these explicit contributions. Tadpole contributions will therefore only appear implicitly due to the terms δT appearing in the counterterm insertions, given in Appendix A.2 (see also Section 3.1.7 of [139] where they use the notation δt to denote what we call δT in the present work).

We perform an on-shell renormalisation, which fixes δ_H, δ_t, δm_H^2 and δm_t via the renormalisation conditions (slashes where applicable)

$$0 = \Big[\Sigma(\not{p})\Big]_{\not{p}=m}, \quad 0 = \left[\frac{\mathrm{d}}{\mathrm{d}\not{p}}\Sigma(\not{p})\right]_{\not{p}=m}. \tag{A.0.6}$$

The masses m and self-energies Σ are those of the top quark and the Higgs boson, respectively. For the top self-energy Σ_t, only the mixed top-Higgs bubble 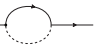 and the counterterm insertion  contribute whereas for the Higgs self-energy Σ_H, there are three diagrams and the counterterm insertion. The resulting renormalisation constants are given in Appendix A.2.

The vev counterterm can be fixed using any of the Yukawa, triple, or quartic Higgs self-interaction vertices. For consistency with much of the literature on EW corrections, we employ the G_μ scheme and use the counterterm as given in [141] in the limit $M_W \to 0, M_Z \to 0$, as detailed in Section A.1.

Finally, we note that the top-quark wave function renormalisation counterterm δ_t enters in multiple vertices, but since there are only closed top loops occurring, the final result should not contain any dependence on this quantity. Every top vertex counterterm insertion $\propto \delta_t$ is cancelled by the top propagator insertion $\propto \delta_t^{-1}$. This also serves as a crosscheck of the renormalised amplitude and, indeed, we do not observe any dependence on δ_t in our final expression.

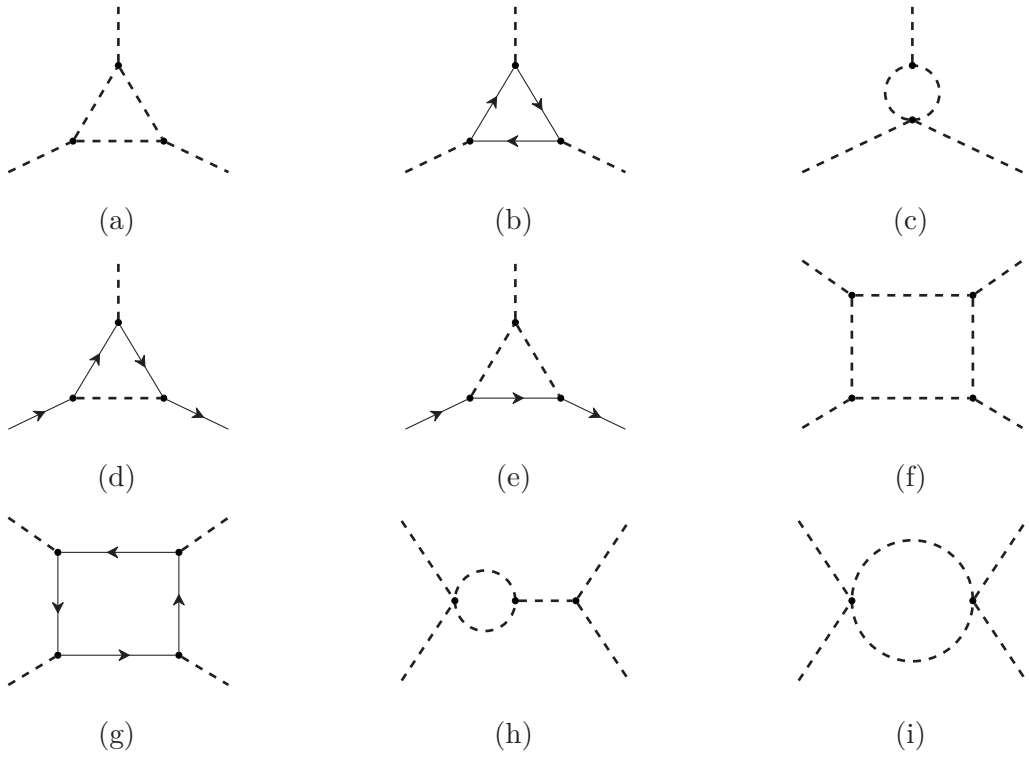

Figure A.1: Example diagrams contributing to the fixing of δ_v from the Higgs cubic vertex (a, b, c), the Yukawa vertex (d, e) and the Higgs quartic vertex (f, g, h, i).

A.1 Vacuum Expectation Value Counterterm

The vev counterterm can be fixed by demanding the finiteness of the higher-order electroweak corrections to an electroweak vertex of the theory. For determining the poles of the counterterm, it does not matter which vertex is picked, and we are free to use either the Yukawa, Higgs cubic or Higgs quartic vertex. By explicit calculation, we find that all three vertices give the same UV divergent part for the vev counterterm,

$$\delta_v|_{\mathrm{UV}} = -\frac{3m_H^4 + 2m_H^2 m_t^2 N_c - 8m_t^4 N_c}{32\pi^2 m_H^2 v^2 \epsilon}, \tag{A.1.1}$$

upon demanding that NLO electroweak virtual contributions do not correct the tree-level expression for the vertex. For example, for the Yukawa coupling, we may require that

$$-ig_t \stackrel{!}{=} \Gamma_{H\bar{t}t}, \tag{A.1.2}$$

at NLO with the diagrams in Figs. A.1d and A.1e contributing to $\Gamma_{H\bar{t}t}$. This fixes the vev counterterm and we find that the divergent part in our theory is given by

$$\delta_v^{g_t}(g_t, g_3, g_4)|_{\text{UV}} = -\frac{g_3 g_t m_H^2 + 2g_t^2 m_t \left(m_H^2 - 4m_t^2\right) N_c}{32\pi^2 m_H^2 m_t \epsilon} \tag{A.1.3}$$

where g_4 is included as an argument because $\delta_v^{g_t}$ can, in principle, have a g_4-dependence at higher-orders (but the UV part at NLO explicitly does not). If instead we fix the vev counterterm from the Higgs cubic self-coupling by requiring that

$$-ig_3 \stackrel{!}{=} \Gamma_{HHH} \tag{A.1.4}$$

holds to NLO in our theory – contributions include the diagrams in Figs. A.1a, A.1b and A.1c – then we obtain,

$$\begin{aligned}\delta_v^{g_3}(g_t, g_3, g_4)|_{\text{UV}} = -\frac{1}{32\pi^2 g_3 m_H^4 \epsilon}\Big[&g_3 g_4 m_H^4 + 8g_4 g_t m_H^2 m_t^3 N_c - 8g_3^2 g_t m_t^3 N_c \\ &+ 2g_3 g_t^2 m_H^2 \left(m_H^2 + 12m_t^2\right) N_c - 48 g_t^3 m_H^4 m_t N_c\Big].\end{aligned} \tag{A.1.5}$$

Similarly, from the requirement

$$-ig_4 \stackrel{!}{=} \Gamma_{HHHH}\ , \tag{A.1.6}$$

we obtain

$$\delta_v^{g_4}(g_t, g_3, g_4)|_{\text{UV}} = -\frac{2g_t g_4 N_c (g_t(m_H^4 + 6m_H^2 m_t^2) - 2g_3 m_t^3) + g_4^2 m_H^4 - 24 g_t^4 m_H^4 N_c}{32\pi^2 g_4 m_H^4 \epsilon} \tag{A.1.7}$$

whose derivation includes contributions from the diagrams in Figs. A.1f, A.1g, A.1h and A.1i. Upon insertion of the SM coupling values of (4.2.6), all of our calculations of the divergent part of δ_v coincide. That is to say,

$$\delta_v^{g_t}\left(\frac{m_t}{v}, \frac{3m_H^2}{v}, \frac{3m_H^2}{v^2}\right)\Big|_{\text{UV}} = \delta_v^{g_3}\left(\frac{m_t}{v}, \frac{3m_H^2}{v}, \frac{3m_H^2}{v^2}\right)\Big|_{\text{UV}} = \delta_v^{g_4}\left(\frac{m_t}{v}, \frac{3m_H^2}{v}, \frac{3m_H^2}{v^2}\right)\Big|_{\text{UV}} \stackrel{!}{=} \delta_v|_{\text{UV}} \tag{A.1.8}$$

as they must since the pole cancellation has to occur independently of the scheme choice. The finite terms, on the other hand, differ. To obtain a result comparable with other authors' works, we choose the G_μ scheme. The pole structure also agrees

in this case; to fix the finite part we use the result of [141] which is obtained from the full SM contributions in G_μ scheme. After application of the same limits as in the Lagrangian, namely $M_W, M_Z \to 0$, we arrive at the counterterm in (A.2.6).

A.2 Feynman Rules and Counterterm Expressions

The Lagrangian of (A.0.5) yields the Feynman rules for renormalised quantities and the counterterm insertions.

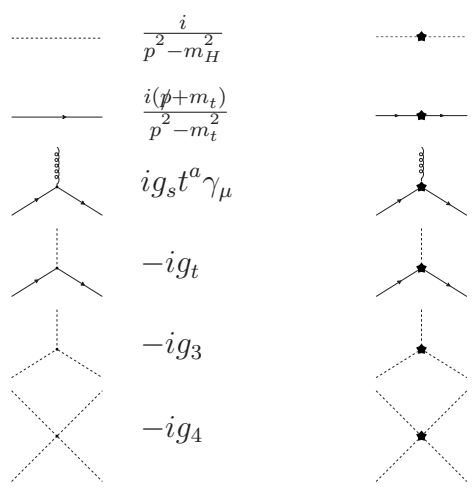

$\frac{i}{p^2-m_H^2}$ $\quad -i\left[(m_H^2-p^2)\delta_H + m_H^2\delta m_H^2 - \frac{g_3}{m_H^2}\delta T\right]$

$\frac{i(\not{p}+m_t)}{p^2-m_t^2}$ $\quad -i\left[(m_t-\not{p})\delta_t + m_t\delta m_t - \frac{g_t}{m_H^2}\delta T\right]$

$ig_s t^a\gamma_\mu$ $\quad ig_s\delta_t t^a\gamma_\mu$

$-ig_t$ $\quad -ig_t\left(\delta m_t + \frac{\delta_H}{2} + \delta_t - \delta_v\right)$

$-ig_3$ $\quad -ig_3\left(\delta m_H^2 + \frac{3}{2}\delta_H - \delta_v\right) + i\frac{g_4}{m_H^2}\delta T$

$-ig_4$ $\quad -ig_4(\delta m_H^2 + 2\delta_H - 2\delta_v)$

We do not list the rules for the gluon self-interactions, since any diagrams involving these vertices are identically zero by colour. The analytic expressions for the counterterm insertions δ_X are as follows:

$$\begin{aligned}\delta m_t = &-\frac{g_t}{2m_t^2}\Big[\Big(\frac{g_3 m_t}{m_H^2} - g_t\Big)\tilde{A}_0(m_H^2) + g_t\Big(1 - 8\frac{m_t^2}{m_H^2}N_c\Big)\tilde{A}_0(m_t^2)\\ &+ g_t(m_H^2 - 4m_t^2)\tilde{B}_0(m_t^2, m_H^2, m_t^2)\Big]\end{aligned} \tag{A.2.1}$$

$$\begin{aligned}\delta_t = &+\frac{g_t^2}{2m_t^2}\Big[\Big((3-2\epsilon) + 4(\epsilon-1)\frac{m_t^2}{m_H^2}\Big)\tilde{A}_0(m_H^2) + (2\epsilon-3)\tilde{A}_0(m_t^2)\\ &+ (2\epsilon-3)(m_H^2 - 2m_t^2)\tilde{B}_0(m_t^2, m_H^2, m_t^2)\Big]\end{aligned} \tag{A.2.2}$$

$$\begin{aligned}\delta m_H^2 = &-\frac{1}{2m_H^2}\Big[\Big(\frac{g_3^2}{m_H^2} - g_4\Big)\tilde{A}_0(m_H^2) + 8g_t N_c\Big(g_t - g_3\frac{m_t}{m_H^2}\Big)\tilde{A}_0(m_t^2)\\ &- g_3^2\tilde{B}_0(m_H^2, m_H^2, m_H^2) - 4g_t^2(m_H^2 - 4m_t^2)N_c\tilde{B}_0(m_H^2, m_t^2, m_t^2)\Big]\end{aligned} \tag{A.2.3}$$

$$\begin{aligned}\delta_H =& + \frac{1}{3m_H^2}\Big[\frac{g_3^2}{m_H^2}(\epsilon-1)\tilde{A}_0(m_H^2) + 12g_t^2N_c(1-\epsilon)\tilde{A}_0(m_t^2)\\ &+ \frac{g_3^2}{2}(2-\epsilon)\tilde{B}_0(m_H^2,m_H^2,m_H^2)\\ &- 6g_t^2((1-\epsilon)m_H^2+2m_t^2)N_c\tilde{B}_0(m_H^2,m_t^2,m_t^2)\Big]\end{aligned} \tag{A.2.4}$$

$$\delta T = -\frac{g_3}{2}\tilde{A}_0(m_H^2) + 4g_tm_tN_c\tilde{A}_0(m_t^2) \tag{A.2.5}$$

$$\delta_v = \frac{1}{2^D\pi^{D/2}}\frac{1}{2v^2}\left(-\frac{m_H^2}{2} + N_cm_t^2 - 2N_cA_0(m_t^2) - 3A_0(m_H^2) + 8N_c\frac{m_t^2}{m_H^2}A_0(m_t^2)\right) \tag{A.2.6}$$

As explained in Appendix A.1, δ_v cannot be split up in different coupling structures, since we obtain the full expression from [141], where this is not provided.

The scalar integrals are defined to be

$$\tilde{A}_0\big(m_1^2\big) := \frac{1}{2^D\pi^{D/2}}A_0\big(m_1^2\big) = \frac{\mu^{4-D}}{2^D\pi^{D/2}}\int\frac{\mathrm{d}^D\ell}{i\pi^{D/2}}\frac{1}{\ell^2-m_1^2} \tag{A.2.7}$$

$$\begin{aligned}\tilde{B}_0\big(p^2,m_1^2,m_2^2\big) :=& \frac{1}{2^D\pi^{D/2}}B_0\big(p^2,m_1^2,m_2^2\big)\\ =& \frac{\mu^{4-D}}{2^D\pi^{D/2}}\int\frac{\mathrm{d}^D\ell}{i\pi^{D/2}}\frac{1}{(\ell^2-m_1^2)((\ell+p)^2-m_2^2)}\end{aligned} \tag{A.2.8}$$

with the t'Hooft scale, μ, to repair the dimensionality and the causal $i\delta$ Feynman prescription understood implicitly.

A.3 Comparison of Counterterms and Renormalization Procedures

In this section, we briefly compare the renormalisation procedure used for the vev in our work, given in (4.2.34) and (A.2.6), to the schemes presented in [141] and [139]. After dropping all non-SM terms, the vev renormalization in (2.18) of [141] reads

$$\frac{1}{v_{T,0}^2} = \frac{1}{v_\mu^2}\Big[1 - \frac{1}{v_\mu^2}\Delta v_\mu^{(4,1,\mu)}\Big] = \frac{1}{v_\mu^2}\Big[1 - \frac{1}{v_\mu^2}\Delta\tilde{v}_\mu^{(4,1,\mu)} - \frac{1}{v_\mu^2}\Delta v_{\mu,\mathrm{tad}}^{(4,1,\mu)}\Big]\,, \tag{A.3.1}$$

where we have used (A.14) of the same reference to collect all contributions not associated with tadpoles in $\Delta\tilde{v}_\mu^{(4,1,\mu)}$ and the remaining tadpole contributions in

$\Delta v^{(4,1,\mu)}_{\mu,\text{tad}}$. Using the relations,

$$v_{T,0}|_{\,[141]} \equiv v_0 + \Delta v, \tag{A.3.2}$$

$$v_\mu|_{\,[141]} \equiv v \tag{A.3.3}$$

and inserting (4.2.34), we obtain,

$$\frac{1}{v^2_{T,0}} = \frac{1}{(v_0+\Delta v)^2} \approx \frac{1}{v^2(1+2\delta_v+2\frac{\Delta v}{v})} \approx \frac{1}{v^2}(1-2\delta_v-2\frac{\Delta v}{v}) \tag{A.3.4}$$

where, in the last two manipulations, we retain only terms linear in δ_v and Δv. By comparison, we can identify

$$\Delta v^{(4,1,\mu)}_{\mu}|_{\,[141]} \equiv 2v^2\Big(\delta_v + \frac{\Delta v}{v}\Big), \tag{A.3.5}$$

$$\Delta v^{(4,1,\mu)}_{\mu,\text{tad}}|_{\,[141]} \equiv 2v\Delta v\ . \tag{A.3.6}$$

The comparison of our counterterms to those given in [139], is less straightforward, as they instead use the renormalisation constants $\delta M^2_W, \delta s_w, \delta Z_e$ to parametrise the renormalisation, where e is the electric charge, $s_w = \sin\theta_w$, and θ_w is the Weinberg angle. Using the tree level relation for the bare vev,

$$\frac{2M_{W,0}s_{w,0}}{e_0} = v_0 \tag{A.3.7}$$

we obtain

$$\frac{\delta M^2_W|_{\,[139]}}{2M^2_W} + \frac{\delta s_w|_{\,[139]}}{s_w} - \delta Z_e|_{\,[139]} = \delta v, \tag{A.3.8}$$

where the extra factors of M_W and s_w in the denominator are due to their definition $M^2_{i,0} = M^2_i + \delta M^2_i$, for $i = W, Z$ rather than e.g. $M^2_{i,0} = M^2_i\,(1+\delta M^2_i)$, see (98) of [139]. This allows us to express our counter terms, given in Section A.2, in terms of their renormalisation constants. To match our counterterm expressions exactly, we additionally set $\delta t_{\text{PRTS}}|_{\,[139]} = 0$ and $\delta t_{\text{FJTS}}|_{\,[139]} = \delta T$ in their expressions, i.e. we select the Fleischer-Jegerlehner tadpole scheme. Finally, to recover the counterterm insertions we give in (A.2.6), the δZ_e expression should be derived in the G_μ scheme, as described in Section 5.1.1 of [139].

Bibliography

[1] S. Jones, A. Olsson and T. Stone, *Evaluating Parametric Integrals in the Minkowski Regime without Contour Deformation*, *PoS* **LL2024** (2024) 036, [2407.06973].

[2] S. Jones, A. Olsson and T. Stone, *Positive Integrands from Feynman Integrals in the Minkowski Regime*, *To Appear* (2025) .

[3] G. Heinrich, S. Jones, M. Kerner, T. Stone and A. Vestner, *Electroweak corrections to Higgs boson pair production: the top-Yukawa and self-coupling contributions*, *JHEP* **11** (2024) 040, [2407.04653].

[4] M. E. Peskin and D. V. Schroeder, *An Introduction to Quantum Field Theory*. Westview Press, 1995.

[5] M. Srednicki, *Quantum Field Theory*. Cambridge University Press, 2007.

[6] M. D. Schwartz, *Quantum Field Theory and the Standard Model*. Cambridge University Press, 3, 2014.

[7] O. J. P. Eboli, G. C. Marques, S. F. Novaes and A. A. Natale, *Twin Higgs Boson Production*, *Phys. Lett. B* **197** (1987) 269–272.

[8] E. W. N. Glover and J. J. van der Bij, *Higgs Boson Pair Production via Gluon Fusion*, *Nucl. Phys. B* **309** (1988) 282–294.

[9] S. Borowka, N. Greiner, G. Heinrich, S. P. Jones, M. Kerner, J. Schlenk et al., *Higgs Boson Pair Production in Gluon Fusion at Next-to-Leading Order with*

Full Top-Quark Mass Dependence, *Phys. Rev. Lett.* **117** (2016) 012001, [1604.06447].

[10] S. Weinzierl, *Feynman Integrals. A Comprehensive Treatment for Students and Researchers*. UNITEXT for Physics. Springer, 2022, 10.1007/978-3-030-99558-4.

[11] G. Passarino and M. J. G. Veltman, *One Loop Corrections for e+ e- Annihilation Into mu+ mu- in the Weinberg Model*, *Nucl. Phys. B* **160** (1979) 151–207.

[12] T. Peraro and L. Tancredi, *Physical projectors for multi-leg helicity amplitudes*, *JHEP* **07** (2019) 114, [1906.03298].

[13] T. Peraro and L. Tancredi, *Tensor decomposition for bosonic and fermionic scattering amplitudes*, *Phys. Rev. D* **103** (2021) 054042, [2012.00820].

[14] A. Padilla and R. G. C. Smith, *Gauge invariance and generalised η regularisation*, 2412.12261.

[15] A. Padilla and R. G. C. Smith, *Smoothed asymptotics: From number theory to QFT*, *Phys. Rev. D* **110** (2024) 025010, [2401.10981].

[16] W. Pauli and F. Villars, *On the invariant regularization in relativistic quantum theory*, *Rev. Mod. Phys.* **21** (Jul, 1949) 434–444.

[17] J. D. Bjorken and S. D. Drell, *Relativistic Quantum Mechanics*. International Series In Pure and Applied Physics. McGraw-Hill, New York, 1965.

[18] G. 't Hooft and M. Veltman, *Regularization and renormalization of gauge fields*, *Nuclear Physics B* **44** (1972) 189–213.

[19] T. Kinoshita, *Mass singularities of feynman amplitudes*, *Journal of Mathematical Physics* **3** (07, 1962) 650–677.

[20] T. D. Lee and M. Nauenberg, *Degenerate systems and mass singularities*, *Phys. Rev.* **133** (Mar, 1964) B1549–B1562.

[21] A. von Manteuffel and C. Studerus, *Reduze 2 - Distributed Feynman Integral Reduction*, 1201.4330.

[22] U.-R. Kim, S. Cho and J. Lee, *The art of Schwinger and Feynman parametrizations*, *J. Korean Phys. Soc.* **82** (2023) 1023–1039.

[23] R. Lee, *Group structure of the integration-by-part identities and its application to the reduction of multiloop integrals*, *Journal of High Energy Physics* **2008** (July, 2008) 031–031.

[24] P. Mastrolia and S. Mizera, *Feynman Integrals and Intersection Theory*, *JHEP* **02** (2019) 139, [1810.03818].

[25] C. Studerus, *Reduze – feynman integral reduction in c++*, *Computer Physics Communications* **181** (2010) 1293–1300.

[26] P. Maierhöfer, J. Usovitsch and P. Uwer, *Kira—A Feynman integral reduction program*, *Comput. Phys. Commun.* **230** (2018) 99–112, [1705.05610].

[27] J. Klappert, F. Lange, P. Maierhöfer and J. Usovitsch, *Integral reduction with Kira 2.0 and finite field methods*, *Comput. Phys. Commun.* **266** (2021) 108024, [2008.06494].

[28] R. N. Lee, *Presenting litered: a tool for the loop integrals reduction*, 2012.

[29] K. G. Chetyrkin and F. V. Tkachov, *Integration by parts: The algorithm to calculate β-functions in 4 loops*, *Nucl. Phys. B* **192** (1981) 159–204.

[30] S. Laporta, *High-precision calculation of multiloop Feynman integrals by difference equations*, *Int. J. Mod. Phys. A* **15** (2000) 5087–5159, [hep-ph/0102033].

[31] A. von Manteuffel, E. Panzer and R. M. Schabinger, *A quasi-finite basis for multi-loop Feynman integrals*, *Journal of High Energy Physics* **2015** (Feb., 2015) .

[32] A. von Manteuffel, E. Panzer and R. M. Schabinger, *Computation of form factors in massless qcd with finite master integrals*, *Physical Review D* **93** (June, 2016) .

[33] E. Panzer, *On hyperlogarithms and feynman integrals with divergences and many scales*, *Journal of High Energy Physics* **2014** (Mar., 2014) .

[34] B. Jantzen, A. V. Smirnov and V. A. Smirnov, *Expansion by regions: revealing potential and glauber regions automatically*, *The European Physical Journal C* **72** (Sept., 2012) .

[35] E. Gardi, F. Herzog, S. Jones and Y. Ma, *Dissecting polytopes: Landau singularities and asymptotic expansions in 2 → 2 scattering*, *JHEP* **08** (2024) 127, [2407.13738].

[36] O. V. Tarasov, *Connection between Feynman integrals having different values of the space-time dimension*, *Physical Review D* **54** (Nov., 1996) 6479–6490.

[37] R. Lee, *Space–time dimensionality D as complex variable: Calculating loop integrals using dimensional recurrence relation and analytical properties with respect to D*, *Nuclear Physics B* **830** (May, 2010) 474–492.

[38] T. Binoth and G. Heinrich, *An automatized algorithm to compute infrared divergent multi-loop integrals*, *Nuclear Physics B* **585** (Oct., 2000) 741–759.

[39] G. Heinrich, *Sector decomposition*, *International Journal of Modern Physics A* **23** (Apr., 2008) 1457–1486.

[40] J. K. Schlenk, *Techniques for higher order corrections and their application to LHC phenomenology*, Ph.D. thesis, Munich, Tech. U., 8, 2016.

[41] G. Heinrich, S. P. Jones, M. Kerner, V. Magerya, A. Olsson and J. Schlenk, *Numerical scattering amplitudes with pySecDec*, *Comput. Phys. Commun.* **295** (2024) 108956, [2305.19768].

[42] A. Smirnov, N. Shapurov and L. Vysotsky, *Fiesta5: Numerical high-performance feynman integral evaluation*, *Computer Physics Communications* **277** (2022) 108386.

[43] C. Bogner and S. Weinzierl, *Resolution of singularities for multi-loop integrals*, *Computer Physics Communications* **178** (Apr., 2008) 596–610.

[44] A. Kotikov, *Differential equations method. new technique for massive feynman diagram calculation*, *Physics Letters B* **254** (1991) 158–164.

[45] A. V. Kotikov, *Differential equation method: The Calculation of N point Feynman diagrams*, *Phys. Lett. B* **267** (1991) 123–127.

[46] E. Remiddi, *Differential equations for feynman graph amplitudes*, *Il Nuovo Cimento A* **110** (Dec., 1997) 1435–1452.

[47] T. Gehrmann and E. Remiddi, *Differential equations for two-loop four-point functions*, *Nuclear Physics B* **580** (July, 2000) 485–518.

[48] M. Hidding, *DiffExp, a Mathematica package for computing Feynman integrals in terms of one-dimensional series expansions*, *Comput. Phys. Commun.* **269** (2021) 108125, [2006.05510].

[49] H. Cheng and T. T. Wu, *EXPANDING PROTONS: SCATTERING AT HIGH-ENERGIES*. 1987.

[50] E. Panzer, *Feynman integrals and hyperlogarithms*, Ph.D. thesis, Humboldt U., 2015. 1506.07243. 10.18452/17157.

[51] L. D. Landau, *On analytic properties of vertex parts in quantum field theory*, *Nucl. Phys.* **13** (1959) 181–192.

[52] J. D. Bjorken, *Experimental tests of Quantum electrodynamics and spectral representations of Green's functions in perturbation theory*, Ph.D. thesis, Stanford U., 1959.

[53] N. Nakanishi, *Ordinary and Anomalous Thresholds in Perturbation Theory*, *Progress of Theoretical Physics* **22** (07, 1959) 128–144, [https://academic.oup.com/ptp/article-pdf/22/1/128/5427385/22-1-128.pdf].

[54] R. E. Cutkosky, *Singularities and discontinuities of Feynman amplitudes*, *J. Math. Phys.* **1** (1960) 429–433.

[55] S. Coleman and R. E. Norton, *Singularities in the physical region*, *Nuovo Cim.* **38** (1965) 438–442.

[56] R. J. Eden, P. V. Landshoff, D. I. Olive and J. C. Polkinghorne, *The analytic S-matrix*. Cambridge Univ. Press, Cambridge, 1966.

[57] C. Bogner and S. Weinzierl, *Resolution of singularities for multi-loop integrals*, *Comput. Phys. Commun.* **178** (2008) 596–610, [0709.4092].

[58] A. V. Smirnov and V. A. Smirnov, *Hepp and Speer Sectors within Modern Strategies of Sector Decomposition*, *JHEP* **05** (2009) 004, [0812.4700].

[59] T. Kaneko and T. Ueda, *A Geometric method of sector decomposition*, *Comput. Phys. Commun.* **181** (2010) 1352–1361, [0908.2897].

[60] T. Kaneko and T. Ueda, *Sector Decomposition Via Computational Geometry*, *PoS* **ACAT2010** (2010) 082, [1004.5490].

[61] F. C. S. Brown, *On the periods of some Feynman integrals*, 0910.0114.

[62] E. Panzer, *Algorithms for the symbolic integration of hyperlogarithms with applications to Feynman integrals*, *Comput. Phys. Commun.* **188** (2015) 148–166, [1403.3385].

[63] C. Fevola, S. Mizera and S. Telen, *Landau Singularities Revisited: Computational Algebraic Geometry for Feynman Integrals*, *Phys. Rev. Lett.* **132** (2024) 101601, [2311.14669].

[64] C. Fevola, S. Mizera and S. Telen, *Principal Landau determinants*, *Comput. Phys. Commun.* **303** (2024) 109278, [2311.16219].

[65] C. Dlapa, M. Helmer, G. Papathanasiou and F. Tellander, *Symbol alphabets from the Landau singular locus*, *JHEP* **10** (2023) 161, [2304.02629].

[66] X. Jiang, J. Liu, X. Xu and L. L. Yang, *Symbol letters of Feynman integrals from Gram determinants*, 2401.07632.

[67] M. Helmer, G. Papathanasiou and F. Tellander, *Landau Singularities from Whitney Stratifications*, 2402.14787.

[68] S. Caron-Huot, M. Correia and M. Giroux, *Recursive Landau Analysis*, 2406.05241.

[69] H. S. Hannesdottir, L. Lippstreu, A. J. McLeod and M. Polackova, *Minimal Cuts and Genealogical Constraints on Feynman Integrals*, 2406.05943.

[70] H. Hannesdottir, A. McLeod, M. D. Schwartz and C. Vergu, *The Landau Bootstrap*, 2410.02424.

[71] S. He, X. Jiang, J. Liu and Q. Yang, *Landau-based Schubert analysis*, 2410.11423.

[72] M. Correia, M. Giroux and S. Mizera, *SOFIA: Singularities of Feynman Integrals Automatized*, 2503.16601.

[73] D. E. Soper, *Talk on QCD calculations by numerical integration*, in *4th International Symposium on Radiative Corrections: Applications of Quantum Field Theory to Phenomenology*, pp. 305–315, 9, 1998, hep-ph/9812324.

[74] D. E. Soper, *Techniques for QCD calculations by numerical integration*, *Phys. Rev. D* **62** (2000) 014009, [hep-ph/9910292].

[75] T. Binoth, G. Heinrich and N. Kauer, *A Numerical evaluation of the scalar hexagon integral in the physical region*, *Nucl. Phys. B* **654** (2003) 277–300, [hep-ph/0210023].

[76] T. Binoth, J. P. Guillet, G. Heinrich, E. Pilon and C. Schubert, *An Algebraic/numerical formalism for one-loop multi-leg amplitudes*, *JHEP* **10** (2005) 015, [hep-ph/0504267].

[77] Z. Nagy and D. E. Soper, *Numerical integration of one-loop Feynman diagrams for N-photon amplitudes*, *Phys. Rev. D* **74** (2006) 093006, [hep-ph/0610028].

[78] C. Anastasiou, S. Beerli, S. Bucherer, A. Daleo and Z. Kunszt, *Two-loop amplitudes and master integrals for the production of a Higgs boson via a massive quark and a scalar-quark loop*, *JHEP* **01** (2007) 082, [hep-ph/0611236].

[79] C. Anastasiou, S. Beerli and A. Daleo, *Evaluating multi-loop Feynman diagrams with infrared and threshold singularities numerically*, *JHEP* **05** (2007) 071, [hep-ph/0703282].

[80] A. Lazopoulos, K. Melnikov and F. Petriello, *QCD corrections to tri-boson production*, *Phys. Rev. D* **76** (2007) 014001, [hep-ph/0703273].

[81] A. Lazopoulos, K. Melnikov and F. J. Petriello, *NLO QCD corrections to the production of $t\bar{t}Z$ in gluon fusion*, *Phys. Rev. D* **77** (2008) 034021, [0709.4044].

[82] C. Anastasiou, S. Beerli and A. Daleo, *The Two-loop QCD amplitude gg —> h,H in the Minimal Supersymmetric Standard Model*, *Phys. Rev. Lett.* **100** (2008) 241806, [0803.3065].

[83] W. Gong, Z. Nagy and D. E. Soper, *Direct numerical integration of one-loop Feynman diagrams for N-photon amplitudes*, *Phys. Rev. D* **79** (2009) 033005, [0812.3686].

[84] S. Becker, C. Reuschle and S. Weinzierl, *Numerical NLO QCD calculations*, *JHEP* **12** (2010) 013, [1010.4187].

[85] S. C. Borowka, *Evaluation of multi-loop multi-scale integrals and phenomenological two-loop applications*, Ph.D. thesis, Munich, Tech. U., 2014. 1410.7939.

[86] E. de Doncker, Y. Shimizu, J. Fujimoto, F. Yuasa, K. Kaugars, L. Cucos et al., *Loop integration results using numerical extrapolation for a non-scalar integral*, *Nucl. Instrum. Meth. A* **534** (2004) 269–273, [hep-ph/0405098].

[87] F. Yuasa, E. de Doncker, N. Hamaguchi, T. Ishikawa, K. Kato, Y. Kurihara et al., *Numerical Computation of Two-loop Box Diagrams with Masses*, *Comput. Phys. Commun.* **183** (2012) 2136–2144, [1112.0637].

[88] E. de Doncker, F. Yuasa, K. Kato, T. Ishikawa, J. Kapenga and O. Olagbemi, *Regularization with Numerical Extrapolation for Finite and UV-Divergent Multi-loop Integrals*, *Comput. Phys. Commun.* **224** (2018) 164–185, [1702.04904].

[89] J. Baglio, F. Campanario, S. Glaus, M. Mühlleitner, J. Ronca, M. Spira et al., *Higgs-Pair Production via Gluon Fusion at Hadron Colliders: NLO QCD Corrections*, *JHEP* **04** (2020) 181, [2003.03227].

[90] T. Binoth, J. P. Guillet and G. Heinrich, *Reduction formalism for dimensionally regulated one loop N point integrals*, *Nucl. Phys. B* **572** (2000) 361–386, [hep-ph/9911342].

[91] S. Pögel, X. Wang and S. Weinzierl, *Bananas of equal mass: any loop, any order in the dimensional regularisation parameter*, *Journal of High Energy Physics* **2023** (Apr., 2023) .

[92] ATLAS collaboration, G. Aad et al., *Constraints on the Higgs boson self-coupling from single- and double-Higgs production with the ATLAS detector using pp collisions at s=13 TeV*, *Phys. Lett. B* **843** (2023) 137745, [2211.01216].

[93] ATLAS collaboration, G. Aad et al., *Combination of searches for Higgs boson pair production in pp collisions at $\sqrt{s} = 13$ TeV with the ATLAS detector*, 2406.09971.

[94] CMS collaboration, A. Tumasyan et al., *A portrait of the Higgs boson by the CMS experiment ten years after the discovery.*, *Nature* **607** (2022) 60–68, [2207.00043].

[95] B. D. Micco, M. Gouzevitch, J. Mazzitelli and C. Vernieri, *Higgs boson potential at colliders: Status and perspectives*, *Reviews in Physics* **5** (Nov., 2020) 100045.

[96] S. Borowka, N. Greiner, G. Heinrich, S. P. Jones, M. Kerner, J. Schlenk et al., *Full top quark mass dependence in Higgs boson pair production at NLO*, *JHEP* **10** (2016) 107, [1608.04798].

[97] J. Baglio, F. Campanario, S. Glaus, M. Mühlleitner, M. Spira and J. Streicher, *Gluon fusion into Higgs pairs at NLO QCD and the top mass scheme*, *Eur. Phys. J. C* **79** (2019) 459, [1811.05692].

[98] J. Davies, G. Heinrich, S. P. Jones, M. Kerner, G. Mishima, M. Steinhauser et al., *Double Higgs boson production at NLO: combining the exact numerical result and high-energy expansion*, *JHEP* **11** (2019) 024, [1907.06408].

[99] J. M. Campbell, G. De Laurentis and R. K. Ellis, *Analytic amplitudes for a pair of Higgs bosons in association with three partons*, 2408.12686.

[100] G. Heinrich, S. P. Jones, M. Kerner, G. Luisoni and E. Vryonidou, *NLO predictions for Higgs boson pair production with full top quark mass dependence matched to parton showers*, *JHEP* **08** (2017) 088, [1703.09252].

[101] S. Jones and S. Kuttimalai, *Parton Shower and NLO-Matching uncertainties in Higgs Boson Pair Production*, *JHEP* **02** (2018) 176, [1711.03319].

[102] G. Heinrich, S. P. Jones, M. Kerner, G. Luisoni and L. Scyboz, *Probing the trilinear Higgs boson coupling in di-Higgs production at NLO QCD including parton shower effects*, *JHEP* **06** (2019) 066, [1903.08137].

[103] E. Bagnaschi, G. Degrassi and R. Gröber, *Higgs boson pair production at NLO in the POWHEG approach and the top quark mass uncertainties*, *Eur. Phys. J. C* **83** (2023) 1054, [2309.10525].

[104] G. Heinrich, S. P. Jones, M. Kerner and L. Scyboz, *A non-linear EFT description of $gg \to HH$ at NLO interfaced to POWHEG*, *JHEP* **10** (2020) 021, [2006.16877].

[105] G. Heinrich, J. Lang and L. Scyboz, *SMEFT predictions for $gg \to hh$ at full NLO QCD and truncation uncertainties*, *JHEP* **08** (2022) 079, [2204.13045].

[106] G. Heinrich and J. Lang, *Combining chromomagnetic and four-fermion operators with leading SMEFT operators for $gg \to hh$ at NLO QCD*, *JHEP* **05** (2024) 121, [2311.15004].

[107] D. De Florian and J. Mazzitelli, *Soft gluon resummation for Higgs boson pair production including finite M_t effects*, *JHEP* **08** (2018) 156, [1807.03704].

[108] D. de Florian, M. Grazzini, C. Hanga, S. Kallweit, J. M. Lindert, P. Maierhöfer et al., *Differential Higgs Boson Pair Production at Next-to-Next-to-Leading Order in QCD*, *JHEP* **09** (2016) 151, [1606.09519].

[109] J. Grigo, J. Hoff and M. Steinhauser, *Higgs boson pair production: top quark mass effects at NLO and NNLO*, *Nucl. Phys. B* **900** (2015) 412–430, [1508.00909].

[110] J. Davies, F. Herren, G. Mishima and M. Steinhauser, *Real corrections to Higgs boson pair production at NNLO in the large top quark mass limit*, *JHEP* **01** (2022) 049, [2110.03697].

[111] J. Davies, K. Schönwald and M. Steinhauser, *Towards $gg \to HH$ at next-to-next-to-leading order: Light-fermionic three-loop corrections*, *Phys. Lett. B* **845** (2023) 138146, [2307.04796].

[112] J. Davies, K. Schönwald, M. Steinhauser and M. Vitti, *Three-loop corrections to Higgs boson pair production: reducible contribution*, 2405.20372.

[113] M. Grazzini, G. Heinrich, S. Jones, S. Kallweit, M. Kerner, J. M. Lindert et al., *Higgs boson pair production at NNLO with top quark mass effects*, *JHEP* **05** (2018) 059, [1803.02463].

[114] L.-B. Chen, H. T. Li, H.-S. Shao and J. Wang, *Higgs boson pair production via gluon fusion at N^3LO in QCD*, *Phys. Lett. B* **803** (2020) 135292, [1909.06808].

[115] L.-B. Chen, H. T. Li, H.-S. Shao and J. Wang, *The gluon-fusion production of Higgs boson pair: N^3LO QCD corrections and top-quark mass effects*, *JHEP* **03** (2020) 072, [1912.13001].

[116] A. A H and H.-S. Shao, *N^3LO+N^3LL QCD improved Higgs pair cross sections*, *JHEP* **02** (2023) 067, [2209.03914].

[117] J. Baglio, F. Campanario, S. Glaus, M. Mühlleitner, J. Ronca and M. Spira, *$gg \to HH$: Combined uncertainties*, *Phys. Rev. D* **103** (2021) 056002, [2008.11626].

[118] U. Aglietti, R. Bonciani, G. Degrassi and A. Vicini, *Two loop light fermion contribution to Higgs production and decays*, *Phys. Lett. B* **595** (2004) 432–441, [hep-ph/0404071].

[119] G. Degrassi and F. Maltoni, *Two-loop electroweak corrections to Higgs production at hadron colliders*, *Phys. Lett. B* **600** (2004) 255–260, [hep-ph/0407249].

[120] S. Actis, G. Passarino, C. Sturm and S. Uccirati, *NLO Electroweak Corrections to Higgs Boson Production at Hadron Colliders*, *Phys. Lett. B* **670** (2008) 12–17, [0809.1301].

[121] S. Borowka, C. Duhr, F. Maltoni, D. Pagani, A. Shivaji and X. Zhao, *Probing the scalar potential via double Higgs boson production at hadron colliders*, *JHEP* **04** (2019) 016, [1811.12366].

[122] M. Mühlleitner, J. Schlenk and M. Spira, *Top-Yukawa-induced corrections to Higgs pair production*, *JHEP* **10** (2022) 185, [2207.02524].

[123] J. Davies, G. Mishima, K. Schönwald, M. Steinhauser and H. Zhang, *Higgs boson contribution to the leading two-loop Yukawa corrections to $gg \to HH$*, *JHEP* **08** (2022) 259, [2207.02587].

[124] J. Davies, K. Schönwald, M. Steinhauser and H. Zhang, *Next-to-leading order electroweak corrections to $gg \to HH$ and $gg \to gH$ in the large-m_t limit*, *JHEP* **10** (2023) 033, [2308.01355].

[125] H.-Y. Bi, L.-H. Huang, R.-J. Huang, Y.-Q. Ma and H.-M. Yu, *Electroweak Corrections to Double Higgs Production at the LHC*, *Phys. Rev. Lett.* **132** (2024) 231802, [2311.16963].

[126] C. Anastasiou, R. Boughezal and F. Petriello, *Mixed QCD-electroweak corrections to Higgs boson production in gluon fusion*, *JHEP* **04** (2009) 003, [0811.3458].

[127] M. Bonetti, K. Melnikov and L. Tancredi, *Two-loop electroweak corrections to Higgs–gluon couplings to higher orders in the dimensional regularization parameter*, *Nucl. Phys. B* **916** (2017) 709–726, [1610.05497].

[128] M. Bonetti, K. Melnikov and L. Tancredi, *Three-loop mixed QCD-electroweak corrections to Higgs boson gluon fusion*, *Phys. Rev. D* **97** (2018) 034004, [1711.11113].

[129] C. Anastasiou, V. del Duca, E. Furlan, B. Mistlberger, F. Moriello, A. Schweitzer et al., *Mixed QCD-electroweak corrections to Higgs production via gluon fusion in the small mass approximation*, *JHEP* **03** (2019) 162, [1811.11211].

[130] M. Bonetti, K. Melnikov and L. Tancredi, *Higher order corrections to mixed QCD-EW contributions to Higgs boson production in gluon fusion*, *Phys. Rev. D* **97** (2018) 056017, [1801.10403].

[131] M. Bonetti, E. Panzer, V. A. Smirnov and L. Tancredi, *Two-loop mixed QCD-EW corrections to $gg \to Hg$*, *JHEP* **11** (2020) 045, [2007.09813].

[132] M. Becchetti, R. Bonciani, V. Del Duca, V. Hirschi, F. Moriello and A. Schweitzer, *Next-to-leading order corrections to light-quark mixed QCD-EW contributions to Higgs boson production*, *Phys. Rev. D* **103** (2021) 054037, [2010.09451].

[133] M. Bonetti, E. Panzer and L. Tancredi, *Two-loop mixed QCD-EW corrections to $q\bar{q} \to Hg$, $qg \to Hq$, and $\bar{q}g \to H\bar{q}$*, *JHEP* **06** (2022) 115, [2203.17202].

[134] S. Borowka, G. Heinrich, S. Jahn, S. P. Jones, M. Kerner, J. Schlenk et al., *pySecDec: a toolbox for the numerical evaluation of multi-scale integrals*, *Comput. Phys. Commun.* **222** (2018) 313–326, [1703.09692].

[135] S. Borowka, G. Heinrich, S. Jahn, S. P. Jones, M. Kerner and J. Schlenk, *A GPU compatible quasi-Monte Carlo integrator interfaced to pySecDec*, *Comput. Phys. Commun.* **240** (2019) 120–137, [1811.11720].

[136] G. Heinrich, S. Jahn, S. P. Jones, M. Kerner, F. Langer, V. Magerya et al., *Expansion by regions with pySecDec*, *Comput. Phys. Commun.* **273** (2022) 108267, [2108.10807].

[137] F. Moriello, *Generalised power series expansions for the elliptic planar families of Higgs + jet production at two loops*, *JHEP* **01** (2020) 150, [1907.13234].

[138] A. Denner, *Techniques for calculation of electroweak radiative corrections at the one loop level and results for W physics at LEP-200*, *Fortsch. Phys.* **41** (1993) 307–420, [0709.1075].

[139] A. Denner and S. Dittmaier, *Electroweak Radiative Corrections for Collider Physics*, *Phys. Rept.* **864** (2020) 1–163, [1912.06823].

[140] J. C. Romao and J. P. Silva, *A resource for signs and Feynman diagrams of the Standard Model*, *Int. J. Mod. Phys. A* **27** (2012) 1230025, [1209.6213].

[141] A. Biekötter, B. D. Pecjak, D. J. Scott and T. Smith, *Electroweak input schemes and universal corrections in SMEFT*, *JHEP* **07** (2023) 115, [2305.03763].

[142] S. Mizera, *Physics of the analytic s-matrix*, *Physics Reports* **1047** (Jan., 2024) 1–92.

[143] P. Nogueira, *Automatic Feynman Graph Generation*, *J. Comput. Phys.* **105** (1993) 279–289.

[144] V. Magerya, "Amplitude library (Alibrary): gluing all the tools needed for computing multi-loop amplitudes in QCD and beyond."

[145] J. Kuipers, T. Ueda and J. A. M. Vermaseren, *Code Optimization in FORM*, *Comput. Phys. Commun.* **189** (2015) 1–19, [1310.7007].

[146] W. Bizoń, U. Haisch and L. Rottoli, *Constraints on the quartic Higgs self-coupling from double-Higgs production at future hadron colliders*, *JHEP* **10** (2019) 267, [1810.04665].

[147] W. Bizoń, U. Haisch, L. Rottoli, Z. Gillis, B. Moser and P. Windischhofer, *Addendum to: Constraints on the quartic Higgs self-coupling from double-Higgs production at future hadron colliders [JHEP 10 (2019) 267]*, *JHEP* **02** (2024) 170, [2402.03463].

[148] G. Degrassi, P. P. Giardino, F. Maltoni and D. Pagani, *Probing the Higgs self coupling via single Higgs production at the LHC*, *JHEP* **12** (2016) 080, [1607.04251].

[149] V. Magerya, "Feynson: finding symmetries between families of Feynman integrals."

[150] A. V. Smirnov and V. A. Smirnov, *How to choose master integrals*, *Nucl. Phys. B* **960** (2020) 115213, [2002.08042].

[151] J. Usovitsch, *Factorization of denominators in integration-by-parts reductions*, 2002.08173.

[152] Z. Bern, L. Dixon and D. A. Kosower, *Dimensionally regulated one-loop integrals*, *Physics Letters B* **302** (Mar., 1993) 299–308.

[153] V. Magerya, *Rational Tracer: a Tool for Faster Rational Function Reconstruction*, 2211.03572.

[154] J. Klappert and F. Lange, *Reconstructing rational functions with FireFly*, *Comput. Phys. Commun.* **247** (2020) 106951, [1904.00009].

[155] J. Klappert, S. Y. Klein and F. Lange, *Interpolation of dense and sparse rational functions and other improvements in FireFly*, *Comput. Phys. Commun.* **264** (2021) 107968, [2004.01463].

[156] M. Hidding and J. Usovitsch, *Feynman parameter integration through differential equations*, *Phys. Rev. D* **108** (Aug, 2023) 036024.

[157] J. Fleischer and F. Jegerlehner, *Radiative Corrections to Higgs Decays in the Extended Weinberg-Salam Model*, *Phys. Rev. D* **23** (1981) 2001–2026.

[158] F. Maltoni, D. Pagani and X. Zhao, *Constraining the Higgs self-couplings at e^+e^- colliders*, *JHEP* **07** (2018) 087, [1802.07616].

[159] PDF4LHC Working Group collaboration, R. D. Ball et al., *The PDF4LHC21 combination of global PDF fits for the LHC Run III*, *J. Phys. G* **49** (2022) 080501, [2203.05506].

[160] A. Buckley, J. Ferrando, S. Lloyd, K. Nordström, B. Page, M. Rüfenacht et al., *LHAPDF6: parton density access in the LHC precision era*, *Eur. Phys. J. C* **75** (2015) 132, [1412.7420].

[161] A. Denner, L. Jenniches, J.-N. Lang and C. Sturm, *Gauge-independent $\overline{MS}$ renormalization in the 2HDM*, *JHEP* **09** (2016) 115, [1607.07352].

[162] A. Denner, S. Dittmaier and J.-N. Lang, *Renormalization of mixing angles*, *JHEP* **11** (2018) 104, [1808.03466].

[163] S. Actis, A. Ferroglia, M. Passera and G. Passarino, *Two-Loop Renormalization in the Standard Model. Part I: Prolegomena*, *Nucl. Phys. B* **777** (2007) 1–34, [hep-ph/0612122].

[164] M. Krause, R. Lorenz, M. Muhlleitner, R. Santos and H. Ziesche, *Gauge-independent Renormalization of the 2-Higgs-Doublet Model*, *JHEP* **09** (2016) 143, [1605.04853].

[165] S. Dittmaier and H. Rzehak, *Electroweak renormalization based on gauge-invariant vacuum expectation values of non-linear Higgs representations. Part I. Standard Model*, *JHEP* **05** (2022) 125, [2203.07236].